

**Correlation between structure, entropy and  
dynamics in multi-species systems**

by

**Palak Patel**

10CC18A26008

A thesis submitted to the  
Academy of Scientific & Innovative Research  
for the award of the degree of  
**DOCTOR OF PHILOSOPHY**

in

**SCIENCE**

Under the supervision of

**Dr. Sarika Maitra Bhattacharyya**



**CSIR-National Chemical Laboratory, Pune**



Academy of Scientific and Innovative Research

AcSIR Headquarters, CSIR-HRDC campus

Sector 19, Kamla Nehru Nagar,

Ghaziabad, U.P. – 201 002, India

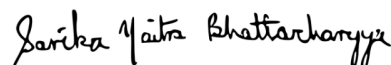
**Oct 2023**

CERTIFICATE

This is to certify that the work in this Ph.D. thesis entitled “Correlation between structure, entropy and dynamics in multi-species systems”, submitted by Palak Patel to the Academy of Science and Innovative Research (AcSIR) in fulfillment of the requirements for the award of the Degree of Doctor of Philosophy in science, embodies original research work carried-out by the student. We, further certify that this work has not been submitted to any other University or Institution in part or full for the award of any degree or diploma. Research material(s) obtained from other source(s) and used in this research work has/have been duly acknowledged in the thesis. Images(s), illustration(s), figure(s), table(s) etc., used in the thesis from other source(s), have also been duly cited and acknowledged.



Palak Patel  
(Student)  
25<sup>th</sup> Oct 2023



Dr. Sarika Maitra Bhattacharyya  
(Supervisor)  
25<sup>th</sup> Oct 2023

## STATEMENT OF ACADEMIC INTEGRITY

I, Palak Patel, a Ph.D. student of the Academy of Scientific and innovative Research (AcSIR) with Registration No. 10CC18A26008 hereby undertake that, the thesis entitled “Correlation between structure, entropy and dynamics in multi-species systems” has been prepared by me and that the document reports original work carried out by me and is free of any plagiarism in compliance with the UGC Regulations on “*Promotion of Academic Integrity and Prevention of plagiarism in Higher Educational Institutions (2018)*” and the CSIR Guidelines for “*Ethics in Research and in Governance (2020)*”.



**Signature of the Student**

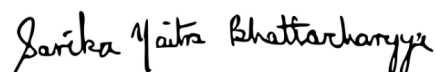
**Name:** Palak Patel

**Date:** 25<sup>th</sup> Oct 2023

**Place:** Pune

---

It is hereby certified that the work done by the student, under my/our supervision, is plagiarism free in accordance with the UGC Regulations on “*Promotion of Academic Integrity and Prevention of plagiarism in Higher Educational Institutions (2018)*” and the CSIR Guidelines for “*Ethics in Research and in Governance (2020)*”.



**Signature of the Supervisor**

**Name:** Dr. Sarika Maitra Bhattacharyya

**Date:** 25<sup>th</sup> Oct 2023

**Place:** Pune

**Dedicated to my family**

(Dada-Dadi, Bade Papa-Maa, Papa-Mummy, Roshan  
Bhaiyya and Chetak)



# Acknowledgments

I would like to take this opportunity to express my deepest gratitude to all those who have contributed to the completion of this Ph.D. thesis.

First and foremost, I would like to express my sincere gratitude to my supervisor, Dr. Sarika Maitra Bhattacharyya for her helpful guidance and constant encouragement throughout the process. Their knowledge, guidance, and dedication to academic success have all been important in determining the direction of my work. I am grateful for the helpful feedback, scientific knowledge, and motivation they have kindly offered at each stage of the research process. Their guidance has improved the caliber of my work while also serving as a source of inspiration for my intellectual development. My deep appreciation for their crucial contribution to the successful completion of this study effort is expressed. I consider myself incredibly fortunate to have had such a committed and experienced guide.

I am also grateful to my Doctoral Advisory Committee members, Dr. Sayan Bagchi, Dr. Durba Sengupta, and Dr. Sailaja Krishnamurty, for their valuable insights, critical evaluation, and helpful suggestions. Their expertise in their respective fields has greatly enriched this study.

I am grateful to Dr. Chandan Dasgupta, Dr. Shiladitya Sengupta, Dr. Prabal Maiti, Dr. Samarjit Karmakar, Dr. Mohd Moid, Dr. Suman Chakrabary to participants of this study, whose willingness to share their time and experiences has been essential to the completion of this research. Their contributions have added depth and richness to the findings.

I acknowledge the former Directors of Dr. Ashwini Kumar Nangia, the present Director, Dr. Ashish Lele, the former HOD of the PSE Division, Dr. Ullas Kharul, Dr. S.K. Asha, and the present HOD of PSE Division, Dr. Suresh Bhat for providing the infrastructure to carry out my research at CSIR-National Chemical Laboratory and for being prompt and responsive to students' requirements. I would like to thank Mr. P.K. Purushothaman, Ms. Komal, Ms. Vaishali, Ms. Vijaya, and other members of the Student Academic Office and Administrative Section of CSIR-NCL who have patiently entertained and guided us through all our queries regarding AcSIR protocols, and fellowship and con-

tingency disbursal. I am thankful to CSIR-HRDG for providing me the JRF and SRF fellowship to continue my research and to AcSIR for providing me the platform to pursue the degree.

Special regards to all of my teachers at different stages of my life (not only educational) because of whose teachings it has become possible for me to reach here.

I am forever and profoundly indebted to my grandparents Jaimangal Prasad Patel and Taramati Patel, my uncle-aunt, Surendra Patel and Ramkumari Patel, my parents, Narendra Patel and Menaka Patel, as well as my brothers, Roshan Patel and Chetak Patel, for the immeasurable impact they have had on shaping the person I am today and the person I aspire to become in the future. The culmination of this thesis stands as a testament to the unwavering determination and countless sacrifices made by my parents and brothers, who have served as unyielding pillars of support throughout this remarkable journey.

I deeply acknowledge the love and support of other family members, my uncle-aunt: Devendra Patel, Kasturba Patel, Mahendra Patel, Anshuiya Patel, my cousins: Bhishm Patel, Harish Patel, Lata Patel, Heena Patel, Shalini Patel, Ashish Patel, Shiva Patel, Dimple, Vijay, Sneha, Dushali, my sister-in-law, Nir-mala Patel, my brother in law, Surendra Patel, Tilak Patel, My nephew/niece Aman, Shradha, Monu, Nurvi has great impacts on my life, I love to spend time with them.

Furthermore, I would like to acknowledge the support and encouragement received from my friends, Shaheena, Chinmayi, Tasneem, Preeti, Asha, Rahul, Anshul, Harish, Gaurav and many more. Their unwavering belief in me, their words of encouragement, and their understanding during challenging times have been a constant source of motivation. Whenever I feel down not only in my professional life but in my personal life, Shaheena and Chinamayi were always there for me. They always stand with me, support me, and encourage me. Without them, I can't complete this journey.

I want to express my gratitude to my amazing lab mates, Manoj Da, Sayantan, Ujjwal, Mohit, Sanket, and Ehtesham, for making my academic journey so much richer. A warm thanks to Manoj Da for his guidance. He is incredibly talented and during study hours, he is committed to his work; outside of work hours, he is a nice and cheerful guy. Sayantan is a master of all trades and brings a wide range of abilities to our team. He has a wide range of skills and is incredibly talented. Ujjwal isn't just a dedicated researcher; he's also a great cook who has spiced up our shared experiences. Mohit is a cool, talented person who approaches the difficulties of life with a smile. When I was down, he always encouraged me and gave me support. Sanket is an honest person. When he sets

his mind to anything, he devotes himself to it. Ehtesham is a hard working guy with good scientific discussion skills. Thanks to everyone for creating such a wonderful environment.

Lastly, I would like to acknowledge the CSIR-HRDG for providing financial support (CSIR-JRF/SRF). This funding has played a crucial role in enabling the execution of this research project.

As I close this chapter of gratitude, I'm reminded of the wisdom of Albert Einstein: "Life is like riding a bicycle. To keep your balance, you must keep moving". To all those who have been my guiding wheels, thank you for ensuring my journey is not only steady but also filled with progress.

# Synopsis

The aim of the thesis is twofold

1. Calculate the effective structure in a continuous-size polydisperse system and correlate the dynamics and structure at the microscopic level.
2. Thermodynamics and its correlation with dynamics in pinned systems: A comparative study using two different methods of entropy calculation, and correlating the dynamics and structure in pinned systems.

The thesis is divided into eight chapters. The outline of each chapter is given below

- Chapter 1 introduces the main research area of this thesis. It provides a short overview of this field and discusses the basics of how dynamics work, particularly when they become slow. The chapter also talks briefly about the connection between thermodynamics and these slow dynamics and mentions the theoretical approaches used to understand them.
- In Chapter 2, a deeper understanding of the glass transition is achieved through an in-depth exploration of its properties. This involves providing detailed explanations of key definitions and the computational techniques utilized to investigate this phenomenon. The chapter's comprehensive approach facilitates a more thorough comprehension of the subject matter.
- In Chapter 3, we conducted a macroscopic analysis of polydisperse systems. Within this chapter, we illustrated that when a polydisperse system is treated as a monodisperse, it exhibits artificial softening. This distortion has repercussions on parameters relying on structural input, leading to inaccurate outcomes. To address this issue, we determined the value of  $M_0$ , representing the optimum number of species required for an accurate description of the system's structure.
- In Chapter 4, a microscopic analysis of polydisperse systems was carried out. We demonstrated that for an accurate depiction of the system's

structure, it is essential to treat it as an  $M_0$ -species system. This chapter presents a noteworthy finding: the dynamics of the system are influenced not solely by its structure, but also significantly by the particle sizes. This revelation underscores the intricate interplay between structure and size in governing particle dynamics.

- In Chapter 5, our investigation revolves around the thermodynamic properties of a pinned system, which is another kind of multispecies glass-forming system. Within this chapter, we employ two distinct methods to calculate excess entropy. Surprisingly, one of the established thermodynamic methods (TI) shows configurational entropy vanishes where single particle dynamics survive, and the Adam-Gibbs relationship is not valid for this. However, when employing the two-phase thermodynamics (2PT) method, we observe that the difference in entropy computed using the two approaches (2PT and TI) grows with an increase in pinning concentration. Additionally, we discover that, for the temperature range under consideration, entropy computed using the 2PT technique satisfies the Adam-Gibbs relationship between the relaxation time and the configurational entropy
- In Chapter 6, we delve into the microscopic analysis of a pinned system. pinned system is generated from the equilibrium configuration of the KA system (which is a binary 80:20 system) and it is expected that the equilibrium properties and the structure of the system do not change. Our exploration revealed that the pinned system structure remains the same when it is treated as a binary system but while treating the pinned system as a modified quaternary system we observe the change in structure with pinning. We observe that when the pinned system is approached from a binary perspective, the correlation between structure order parameters and dynamics is relatively diminished. However, when we consider the pinned system as a modified quaternary system, a notable enhancement in the correlation between structure order parameters and dynamics becomes evident.

# Contents

<b>1</b>	<b>Introduction of glassy dynamics and existing theories</b>	<b>13</b>
1.1	Introduction . . . . .	13
1.2	Dynamical properties . . . . .	15
1.2.1	Dynamical heterogeneity . . . . .	17
1.2.2	Fragility . . . . .	17
1.3	Thermodynamical properties . . . . .	19
1.3.1	Structural arrest in supercooled liquid . . . . .	19
1.3.2	Entropy in supercooled liquid . . . . .	21
1.3.3	Entropy crisis . . . . .	22
1.3.4	Kauzmann paradox or entropy in crisis . . . . .	23
1.4	A summary of theories of the glass transition . . . . .	24
1.4.1	Adam-Gibbs theory . . . . .	24
1.4.2	Free volume theory . . . . .	26
1.4.3	Random first-order transition theory. . . . .	28
1.4.4	Mode coupling theory . . . . .	29
1.5	Conclusion . . . . .	30
<b>2</b>	<b>Definitions, methods and models</b>	<b>32</b>
2.1	Models details . . . . .	32
2.1.1	Polydisperse system . . . . .	33
2.1.2	Pinned system . . . . .	35
2.2	Calculation of dynamic properties . . . . .	36
2.2.1	Relaxation time calculation from overlap function . . . . .	36
2.2.2	Mean square displacement (MSD) . . . . .	38
2.2.3	Non Gaussian parameter . . . . .	38
2.3	Calculation of static properties: Radial distribution function . . . . .	39
2.3.1	Different parameter calculated from macroscopic radial distribution function, $g(r)$ . . . . .	44
2.4	Thermodynamic Properties . . . . .	48
2.4.1	Ideal gas entropy . . . . .	48
2.4.2	Excess entropy . . . . .	50

2.4.3	Vibrational entropy . . . . .	55
2.4.4	Configurational entropy . . . . .	58
2.5	Hessian calculation . . . . .	59
2.6	Calculation of onset temperature . . . . .	61
2.6.1	$T_{onset}$ calculation from Inherent structure energy . . . . .	61
2.6.2	$T_{onset}$ calculation from excess energy . . . . .	61
<b>3</b>	<b>Effective structure of a system with continuous polydispersity</b>	<b>63</b>
3.1	Introduction . . . . .	63
3.2	Simulation details . . . . .	65
3.3	Result . . . . .	65
3.3.1	Effective one-component description . . . . .	65
3.3.2	Pseudo species and its dependence on degree of polydispersity . . . . .	67
3.3.3	Effect of the type of distribution on $M_0$ and $\Delta\sigma_0$ . . . . .	71
3.3.4	Effect of interaction potential on $M_0$ . . . . .	73
3.3.5	System size dependence . . . . .	74
3.3.6	Mutual information and radial distribution function . . . . .	76
3.3.7	Comparison with earlier predictions . . . . .	77
3.4	Conclusion . . . . .	78
<b>4</b>	<b>Dynamic heterogeneity in polydisperse systems: A comparative study of the role of local structural order parameter and particle size</b>	<b>80</b>
4.1	Introduction . . . . .	80
4.2	Simulation Details . . . . .	82
4.3	Computing local caging potential . . . . .	83
4.4	Species dependence of the caging potential . . . . .	84
4.5	Species dependence of the correlation of caging potential with particle dynamics . . . . .	86
4.6	Analysis of dynamics of soft and hard particles . . . . .	88
4.7	Comparative study of the role of particle size and local structure on the dynamics . . . . .	90
4.8	Conclusion . . . . .	94
<b>5</b>	<b>Thermodynamics and its correlation with dynamics in a pinned systems: A comparative study using two different methods of entropy calculation</b>	<b>100</b>
5.1	Introduction . . . . .	100
5.2	Simulation Details . . . . .	102

5.3	Characteristic temperatures of the pinned systems . . . . .	102
5.4	Result . . . . .	104
5.4.1	Binary system entropy . . . . .	104
5.4.2	Pinned system entropy . . . . .	105
5.5	Analysis of the origin of increasing saturation point in pinned system . . . . .	110
5.6	Conclusion . . . . .	113
<b>6</b>	<b>Effect of the presence of pinned particles on the structural parameters of a liquid and correlation between structure and dynamics at the local level</b>	<b>122</b>
6.1	Introduction . . . . .	122
6.2	Simulation Details . . . . .	124
6.3	Entropy and mean field caging potential at macroscopic level . .	125
6.3.1	Macroscopic excess entropy . . . . .	125
6.3.2	Macroscopic pair excess entropy . . . . .	127
6.3.3	Macroscopic mean field caging potential . . . . .	129
6.3.4	Numerical results for the macroscopic pair excess entropy and mean field caging potential . . . . .	130
6.4	Pair excess entropy and mean field caging potential at the microscopic level . . . . .	133
6.4.1	Microscopic pair excess entropy . . . . .	134
6.4.2	Microscopic mean field caging potential . . . . .	134
6.4.3	Numerical results for the microscopic pair excess entropy and mean field caging potential . . . . .	135
6.5	Correlation between structure and dynamics at microscopic level	136
6.5.1	Correlation between structure and dynamics using isoconfiguration runs . . . . .	137
6.5.2	Analysis of dynamics of particles belonging to the softest and hardest regions . . . . .	138
6.5.3	Correlation between structure and dynamics and prediction of onset temperature . . . . .	139
6.6	Conclusion . . . . .	139
<b>7</b>	<b>Summary and future work</b>	<b>150</b>
7.1	Summary . . . . .	150
7.2	Future work . . . . .	153



# Chapter 1

## Introduction of glassy dynamics and existing theories

“Research is to see what everybody else has seen  
and to think what nobody else has thought”  
-Albert Szent-Györgyi

### 1.1 Introduction

Glass is a material that is widely used and has a big impact on our daily life. Although silicate glasses are frequently referred to as “*glass*” and are used in windows, bottles, optics, and other applications, they’re only one type of glass. Broadly speaking, glass is an amorphous solid that exhibits a definite glass transition but lacks the long-range structural order present in crystalline materials. Glasses are different from crystals in that their atomic arrangements are not clearly defined, giving them special characteristics and behaviors. Glass’ amorphous nature gives it transparency, flexibility, and thermal insulation qualities, which make it perfect for a variety of uses in construction, packaging, optics, and technology. For improvements in materials engineering, product development, and scientific research, it is essential to understand the science of glass development and its characteristics.

According to the classical nucleation theory (CNT), if a liquid cools slowly, it typically undergoes a first-order phase transition to the most favorable thermodynamical form, which is a crystalline state, below the melting point. Usually, the specific volume decreases as a result of this first-order phase transition. Due to the nucleation process, crystals form. First, a tiny crystalline phase develops, and if its volume exceeds a certain threshold, it expands until it covers the entire system. By accelerating the cooling process, this nucleation process

can be stopped. If the liquid is cooled rapidly enough to prevent the first-order phase transition of crystallization, or, to put it another way, if the rate of cooling is quick enough to prevent the system from getting enough time to rearrange and form crystals, then the system is in a liquid state below the melting point with a high viscosity and long relaxation time. This state is referred to as the supercooled state, and the temperature at which the transition from a liquid to a supercooled state occurs is referred to as the onset temperature ( $T_{onset}$ ) [1, 2, 3]. After further cooling, the supercooled state turns into glass. The glass transition temperature  $T_g$  is the temperature at which supercooled liquid transitions to glass. Technically, the temperature at which viscosity increases from  $10^{12}$  to  $10^{13}$  poise or relaxation time is equal to 100 seconds known as  $T_g$ . The temperature  $T_g$  is not constant; instead, it changes with the rate of cooling. The volume-temperature (V-T) diagram described in Fig.1.1 can be used to understand the relationship between liquid, supercooled liquid, and glass. With decreasing the T, the supercooled liquid undergoes a process called “vitrification” or “glass transition”. This transition happens when the liquid’s viscosity increases dramatically, and it converts into an amorphous solid known as glass.

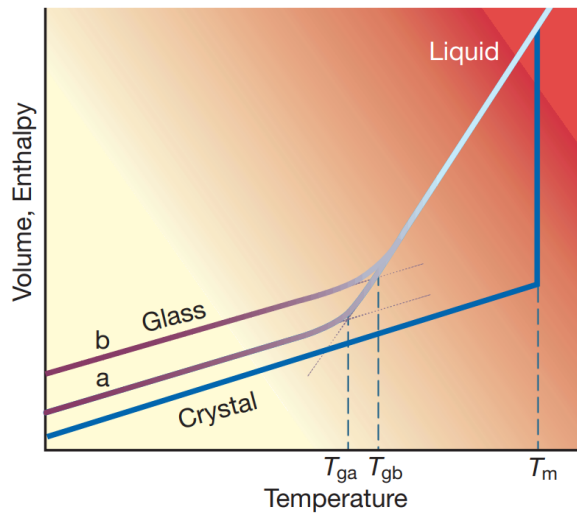


Figure 1.1: *Schematic representation of glass transition phenomena.  $T_g$  depends on the rate of cooling. Reprinted from ref. [4]. The slow and fast cooling rates are denoted by a and b, respectively.  $T_g$  and  $T_m$  represent the glass transition and melting temperatures, respectively.*

Gases and crystals have perfectly disordered and ordered structures. The liquid state of matter is intermediate in nature and has complex structures and dynamics, which is a key research area in condensed matter physics. The relationship between structure and behavior in supercooled states is significantly more complicated. In 1995 P. W. Anderson wrote: “The deepest and most

interesting unsolved problem in solid state theory is probably the theory of the nature of glass and the glass transition. This could be the next breakthrough in the coming decade” [5]. According to the thermodynamical point of view, the supercooled liquid is a metastable state, so the dynamics and thermodynamic properties of the glass are predicted by the study of the equilibrium supercooled liquid state. Below  $T_g$  liquid falls out of equilibrium. Note that  $T_g$  is dependent on the cooling rate. Slow cooling rates result in a longer T range of equilibrium, which means lower  $T_g$  (shown in Fig.1.1).

In a supercooled state, the dynamics of a liquid decrease with a small change in structure. The link between dynamics and thermodynamics in supercooled liquid has been a research area of interest for many years. The fundamental characteristics of the dynamical and thermodynamic properties of supercooled liquids and glasses will be discussed in the section that follows.

## 1.2 Dynamical properties

The fundamental characteristics of the dynamics of supercooled liquids and glasses will be discussed in this section. The correlation function between general quantities, such as the density-density correlation function, which can be estimated from the light scattering function and simulation studies, can be used to calculate the dynamics of the system. The definition of the dynamics correlation function is

$$\phi(t) = \frac{1}{N} \sum_{k=1}^N \langle \psi_k(t) \psi_k(0) \rangle \quad (1.1)$$

where  $k$  is a particle identity and  $\phi$  is a correlation function between generic quantities  $\psi$  with time difference  $t$ .

At high temperatures - the relaxation dynamics in a system are characterized by different regimes. At short timescales, the motion of particles is primarily governed by their free motion, where they move independently without strong interactions. As time progresses, the particles start to interact with each other, leading to an intermediate state where the relaxation is influenced by the interactions between particles. Finally, at longer timescales, the relaxation follows an exponential decay pattern known as Debye relaxation [6, 7]. This behavior can be described by the Arrhenius equation, which states that the correlation function decays exponentially with time. The Arrhenius equation provides a simplified representation of the relaxation dynamics in the high-temperature regime, highlighting the importance of temperature in determining the relaxation behavior of a system. Arrhenius equation is represented as,

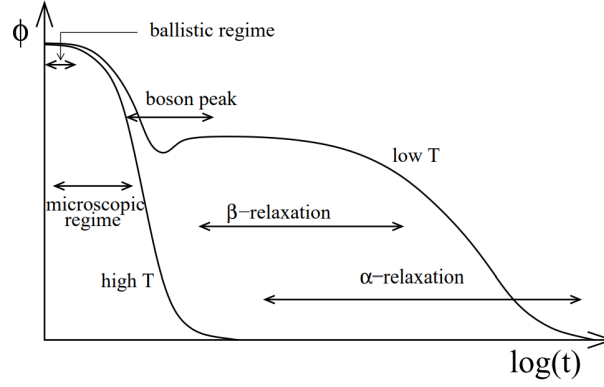


Figure 1.2: *Schematic plot of the two-step relaxation of the correlators. Two curves describe the high and the low-temperature relaxation. Adapted from ref. [6].*

$$\phi(t) = \phi_0 \exp(-t/\tau) \quad (1.2)$$

where  $\tau$  is a relaxation time and  $\phi_0$  is a constant.

However, at low temperatures, the correlation function exhibits a characteristic plateau, indicating that the particles are trapped in their positions and unable to freely move. The short-time dynamics in this region resemble the ballistic regime observed at high temperatures, where particles exhibit unrestricted motion. The  $\beta$  relaxation refers to a time window during which the correlation function remains close to the plateau value, indicating a slow relaxation process. This is a regime that propagates over many decades in time, note the logarithmic scale in Fig.1.2. This  $\beta$  relaxation regime can span a wide range of timescales, often spanning several decades when plotted on a logarithmic scale. The subsequent  $\alpha$  relaxation occurs when the correlation function departs from the plateau and decays towards zero, representing the gradual relaxation of the system towards its equilibrium state. At low temperatures and in the late stages of relaxation, the dynamics exhibit non-exponential behavior. This late relaxation can be well-described by the Kohlrausch-Williams-Watts (KWW) stretched exponential form [8, 9, 10], which captures the gradual decay of correlations. Understanding the non-exponential relaxation and the influence of temperature on the dynamics of supercooled liquids is essential for comprehending the glass transition phenomenon. Form of Kohlrausch-Williams-Watts (KWW) stretched exponential is;

$$\phi(t) = \exp(-t/\tau_0)^\beta \quad 0 < \beta \leq 1 \quad (1.3)$$

where  $\beta$  is the KWW stretch exponent.  $\beta = 1$  at high T and low time win-

dow at low  $T$ , where the system shows ballistic motion, and at low  $T$  large time window,  $\beta < 1$ . The value of  $\beta$  decreases with decreasing the  $T$ . The detailed predictions of basic accuracy of  $\beta$  have been verified experimentally and in computer simulations [11, 12, 13]. Equilibrium relaxation time  $\tau_\alpha$  is define as  $\phi(t = \tau_\alpha) = \exp(-1) = 0.367$

### 1.2.1 Dynamical heterogeneity

This two-step structural relaxation is a hallmark feature of supercooled liquids and glasses that characterizes the dynamics of disordered packing in supercooled liquid and glassy system [14, 15]. The first step, which is called  $\beta$  relaxation, is associated with the ballistic motion of particle motion within cages formed by their neighbors. The second step, which is called  $\alpha$  relaxation, is associated with rearrangements of cage and cage escape by the particle.

The physical origin of the stretched exponential decay of correlation function in supercooled liquids is unclear. Two extreme scenarios are discussed in the literature [6] :

- Homogeneous dynamics - Due to the complicated dynamics system shows a non-exponential relaxation.
- Heterogeneous dynamics - The system does not have enough time to rearrange itself, resulting in each particle in the supercooled liquid having a distinctive surrounding. In the supercooled liquid multiple domains form. This leads to heterogeneous dynamics where different domains or “fast” and “slow” regions evolve at different decay rates of the correlation function. Due to the contributions of many regions with different relaxation times, the overall relaxation time becomes stretched exponentially. This spontaneous decomposition is referred to as dynamical heterogeneity.

### 1.2.2 Fragility

After discussing the heterogeneity of supercooled liquids, it is important to delve into another significant aspect of their behavior: fragility. Fragility provides valuable insights into the temperature-dependent dynamics and viscosity of these materials as they approach the glass transition. Understanding fragility is essential for comprehending the structural relaxation and overall behavior of supercooled liquids. In this section, we will explore the concept of fragility and its implications in the context of supercooled liquids.

Here we discuss the  $T$  dependence of relaxation time ( $\tau_\alpha$ ) or viscosity  $\eta$  in the supercooled liquid. It is known that in liquid state  $\tau_\alpha$  or  $\eta$  increases with

decreasing  $T$  and follows well known Arrhenius equation, that is;

$$\tau_\alpha = \tau_0 \exp(\Delta E/T) \quad \text{or} \quad \eta = \eta_0 \exp(\Delta E/T) \quad (1.4)$$

where  $\tau_0$  and  $\eta_0$  are fitting parameter,  $\Delta E$  is the activation energy. For normal liquid this  $\Delta E$  is independent of temperature. Arrhenius's law can be explained by the phenomenology proposed by Eyring [16]. Here we briefly discuss Eyring's argument on the Arrhenius law. In a liquid state, a particle is surrounded by the cage, which is formed by the neighboring particles. The relaxation process of the liquid is assumed to be breaking the cage and escaping the particle from the cage.

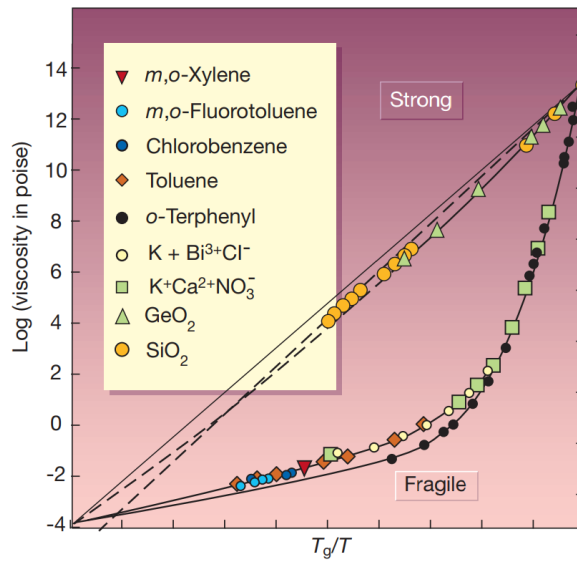


Figure 1.3: Scaled via  $T_g$ , Arrhenius representation of liquid viscosities showing Angell's strong-fragile pattern. Strong liquids exhibit approximate linearity (Arrhenius behavior), indicative of a temperature-independent activation energy  $E \approx \text{constant}$ . Fragile liquids exhibit super-Arrhenius behavior, their effective activation energy increasing as temperature decreases. Adapted from refs [17, 4].

In the liquid state system follow the Arrhenius equation. Now the question arises is it true also for supercooled liquid or not? To answer this question Angell plotted the inverse of  $T$  dependence on  $\log(\tau)$  or  $\log(\eta)$  for different systems [17] (shown in Fig.1.3).  $1/T$  is scaled by respective system  $T_g$  [17]. Open network liquids like  $SiO_2$  and  $GeO_2$  give a straight light fit between viscosity (or structural relaxation time) and  $T_g/T$ , throughout the  $T$  range (from high  $T$  to  $T_g$ ) in Angell plot, which means this liquid obeys Arrhenius law and provide the "strong" liquid extreme of the pattern. On the other hand subgroup of liquid that has van der Waals interaction or non-directional coulomb attractions follows Arrhenius law at high  $T$  but at low  $T$ , viscosity or relaxation time increases drastically with

small changes in T. This type of liquid system is known as “*fragile*” liquids [17]. Most fragile liquids are polymeric in nature. This non-Arrhenius behavior is also called super Arrhenius behavior. This strong/fragile liquid pattern is used for the classification of liquids. This non-Arrhenius behavior can be empirically well fitted by the Vogel-Fulcher-Tammann (VFT) equation[18, 19, 20, 21],

$$\tau_{\alpha} = \tau_0 \exp \frac{1}{K_{VFT}(\frac{T}{T_{VFT}} - 1)} \quad \text{or} \quad \eta = \eta_0 \exp \frac{1}{K_{VFT}(\frac{T}{T_{VFT}} - 1)} \quad (1.5)$$

where  $\tau_0$  and  $\eta_0$  are high T relaxation time and viscosity respectively, and obtained from fitting.  $K_{VFT}$  is a fragility constant.  $T_{VFT}$  is a divergence T of relaxation time or viscosity. At  $T = T_{VFT}$ ,  $\tau, \eta$  goes to infinity. During a dramatic change in dynamics (Dynamical slow down), there is no dramatic structural changes occur, and there are no obvious structure-based explanations for dynamical slow down. Although there is no experimentally accessible, the divergence temperature  $T_{VFT}$  raises the possibility of a true singularity associated with a putative phase transition, either dynamic or thermodynamic. Kauzaman suggested that this transition may be thermodynamic in nature [22].

## 1.3 Thermodynamical properties

The rigidity of solids, which specified them macroscopically, conversely, has been usually traced to their qualitatively different periodic ordered structure[23], a concept that had already occurred to Kepler[24]. For crystals, this concept is accurate. However, the existence of structural glasses (amorphous substances that are rigid) questions this understanding. Here we briefly discuss the structural and thermodynamic signatures of the slowdown of dynamics. In supercooled liquid small changes in structure give a drastic change in dynamics. The correlation between structure and dynamics in supercooled liquid is a hot topic of research. Thermodynamics provides a framework for understanding the energetics, stability, and phase behavior of supercooled liquids. It helps elucidate the complex interplay between temperature (T), energy (E), entropy (S), and molecular interactions (U), ultimately contributing to our understanding of these metastable states and their transitions.

### 1.3.1 Structural arrest in supercooled liquid

In a supercooled liquid, the molecules are not arranged in a regular pattern like a solid. Rather, they maintain a disordered or amorphous structure. The arrested

structure in a supercooled liquid refers to the arrangement of molecules when they become trapped, or arrested, in a metastable state during the vitrification process. The highly organized lattice structure that distinguishes a crystalline solid cannot be formed by these molecules. Depending on the composition, a supercooled liquid's precise structure can change. Generally speaking, the arrangement of molecules in a supercooled liquid is less disordered than a real liquid but more disordered than a crystalline solid.

The molecule's mobility significantly decreases during the glass transition, which causes a solid-like behavior. Several properties like specific heat capacity, thermal expansion coefficient, viscosity, etc. behave differently when the liquid cools towards  $T_g$ . A few properties (entropy ( $S$ ), specific heat ( $C_P$ )) -  $T$  behavior at different states of the system are shown in Fig.1.4. As  $T_g$  approaches, the rate of change for these properties accelerates. The shift in the slope of the property-temperature curve is one of the most important signs that the glass transition is about to occur. Because of the lengthening of the structural relaxation time and the decreased molecular mobility, the slope gets steeper. In several experimental observations, this shift in slope can be seen, and it is frequently connected to the beginning of the glassy state.

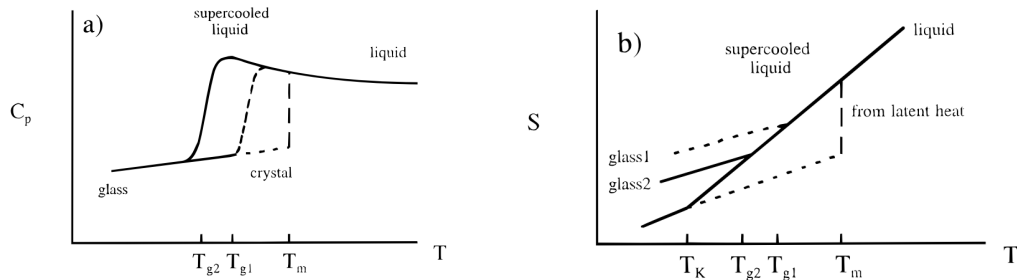


Figure 1.4: A schematic diagram of the temperature dependence of (a) the specific heat,  $C_P$ , and (b) the specific entropy,  $s$ , of a crystal, liquid, supercooled liquid, and glass. Glasses 1 and 2 are obtained with different cooling rates and have different apparent glass transition temperatures  $T_g$ . Glass 1, shown by the dashed curve, represents the result of a faster cooling rate than that used to produce glass 2, the solid curve.  $T_g$ ,  $T_m$ , and  $T_K$  represent the glass transition temperature, melting temperature, and Kauzmann temperature, respectively. Adapted from ref. [25].

It is significant to remember that the precise characteristics of the slope change can alter based on the particular material and cooling circumstances. The ultimate volume at a temperature below  $T_g$  is lower with a slower cooling rate, as seen in Fig.1.5. In addition, a slower cooling rate results in a lower glass transition temperature, which is determined by the temperature at which the slope changes. The history of preparation determines the glass that is produced.



The glass resulting from a particular cooling rate is shown in Fig.1.5 as another example of how, for  $T$  near  $T_g$ , the heating curve differs from the cooling curve if the heating rate is different. As a result, the system's characteristics close to  $T_g$  also depend on the path. The laboratory glass transition happens when the liquid loses equilibrium and is kinetic, as seen by its dependence on the cooling rate and path. Near the glass transition temperature, different materials can behave in various ways, and the rate of cooling can also affect how much and how abruptly the slope changes. Understanding the behavior of supercooled liquids and the creation of glasses depends on the study of these changes in slope and other properties close to the glass transition. It has consequences for several industries, including materials research, polymer physics, and medicines, where managing the glass transition is crucial for the performance and stability of a given product.

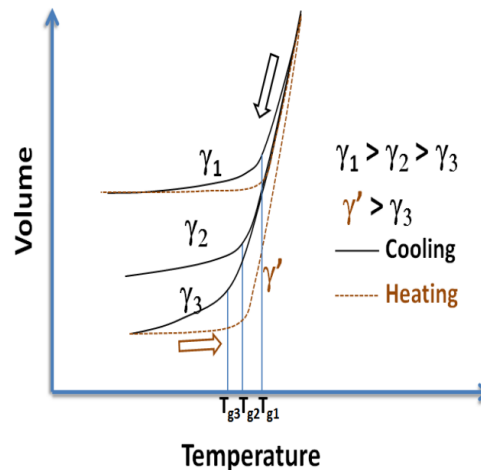


Figure 1.5: Schematic temperature dependence of the volume of a supercooled liquid as it approaches the glass transition temperature,  $T_g$ .  $\gamma_1, \gamma_2, \gamma_3$  are cooling rates and  $\gamma'$  is the heating rate. See also text. Adapted from ref. [26].

### 1.3.2 Entropy in supercooled liquid

Entropy is a fundamental concept in thermodynamics that measures the degree of disorder or randomness in a system. In the context of supercooled liquids, entropy plays a significant role in understanding the behavior and properties of these materials. In supercooled liquid, molecules have limited mobility and are kinetically trapped in a disordered arrangement. The dependence of entropy on the cooling rate at different  $T$  is shown in Fig.1.4 (b).

The entropy ( $S$ ) of a supercooled liquid is primarily composed of two components: configurational entropy  $S_c$  and vibrational entropy  $S_{vib}$ .  $S = S_c + S_{vib}$ .

Both entropy is defined below,

- **Configurational Entropy ( $S_c$ ):** The term configurational entropy describes the variety of arrangements that the system's atoms and molecules can take in while still retaining the same energy. The configurational entropy falls as the system gets more structurally arrested in a supercooled liquid. As the temperature drops, molecules lose mobility and get locked in local energy minima, which limits the number of available configurations and lowers configurational entropy.
- **Vibrational Entropy ( $S_{vib}$ ):** Vibrational entropy accounts for the contributions of molecular vibrations to the overall entropy of the system. Although molecule's movement in a supercooled liquid is limited, they still have vibrational motion. Although vibrational entropy normally decreases as temperature drops, its contribution to total entropy is relatively smaller compared to configurational entropy.

In supercooled liquids, as the temperature approaches the glass transition temperature ( $T_g$ ), the system undergoes a rapid increase in viscosity and loss of mobility, which results in the production of a glassy state. At the same time, the drop in configurational entropy becomes more significant. Understanding supercooled liquids' thermal behavior, phase transitions, and glass formation depends heavily on the study of entropy in these systems. It offers an understanding of the underlying chemical configurations, dynamics, and particular characteristics displayed by these metastable states.

### 1.3.3 Entropy crisis

The specific heat  $C_p(T)$  is largest in the supercooled liquid and decreases to a smaller value, close to the crystal phase, around  $T_g$  [27, 25]. In Fig.1.4 it is shown that the rate at which the liquid cools significantly affects the temperature at which the specific heat rapidly decreases. The two distinct curves in Fig.1.4 represent the outcome of cooling at two various rates. The curve would shift even farther to lower temperatures with a slower cooling. Entropy at temperature  $T$  has the following thermodynamic relationship:

$$S(T) = S(T_{ref}) + \int_{T_{ref}}^T \frac{C_p}{T'} dT' \quad (1.6)$$

where  $T_{ref}$  is a reference temperature. The difference between the liquid and the crystal entropy is  $\Delta S$ .

$$\Delta S(T) = S_{liq}(T) - S_{cry}(T) \quad (1.7)$$

where  $S_{liq}(T)$  is the liquid entropy and  $S_{cry}(T)$  is the entropy of the crystal at temperature  $T$ .  $\Delta S$  decreases with decreasing the  $T$  [25]. When extrapolating the entropy-temperature curve from higher temperatures, the rate of entropy loss frequently deviates from the predicted behavior. It is found that extrapolated excess entropy goes to zero at finite temperature, and that temperature is defined as the Kauzmann temperature  $T_K$ . The Kauzmann temperature  $T_K$  is very close to the VFT divergence temperature  $T_{VFT}$  [28].

The liquid explores a smaller and smaller region of the configurational space as it cools. The liquid is kinetically confined at  $T_g$ , and the length of the relaxation time causes the configurational entropy to collapse. It's important to note that the entropy crisis is a simplified concept to describe the behavior of supercooled liquids near the glass transition, and the underlying mechanisms and dynamics are still the subject of ongoing research and investigation.

### 1.3.4 Kauzmann paradox or entropy in crisis

To answer this puzzling observation regarding the thermodynamics of supercooled liquids and the glass transition, in 1948 Walter Kauzmann proposed Kauzmann's paradox [22]. According to the third law of thermodynamics, as the temperature approaches absolute zero, the entropy of a pure crystalline substance should also approach zero. However, in the case of supercooled liquids, the extrapolated entropy-temperature curve suggests that the entropy would reach zero at a temperature above absolute zero. According to this law, a liquid would have more entropy than a crystalline solid, which contradicts the third law. Now if we believe that the extrapolation is possible and go to an even lower temperature, then the entropy of the liquid state becomes smaller than that of the crystal state at that temperature, this is known as the entropy crisis or Kauzmann's Paradox. Even though there is no statistical theory that forbids this phenomenon, it will be a little strange if it does because the liquid is disordered and the crystal is organized. Therefore the dotted lines in Fig.1.6 show that it is evident that the curve  $\Delta S$  vs.  $T$  must become flat after some temperature below  $T_g$ . The fact that there is no experimental support for this extrapolation should put an end to any worries about  $T_K$ . However,  $T_g$  is not a fixed temperature, it depends on the cooling rate. Thus, in principle, one can reach below  $T_K$  by sufficiently slow cooling or by giving the system enough time to relax. But in this process, the system crystallizes. So, the glass transition saves the entropy crisis.

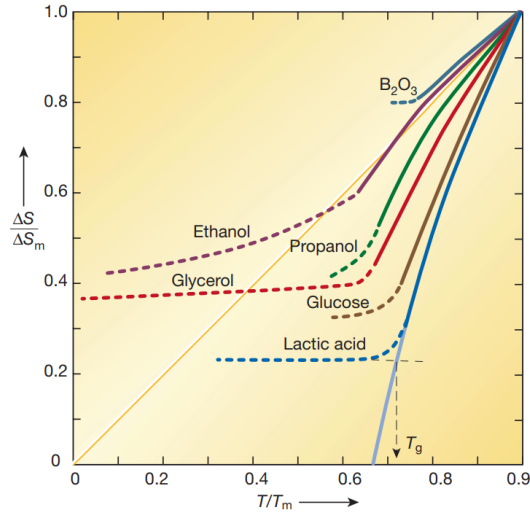


Figure 1.6: *The temperature dependence of the excess entropy. Figure adapted from ref. [22, 4].  $\Delta S_m$  is the entropy of a system at melting  $T$  ( $T_m$ ).*

The resolution to Kauzmann’s paradox is still an active area of research and is not fully understood. Various theories and explanations have been proposed, including the idea that the extrapolated entropy curve may not accurately represent the true behavior of the system. Additionally, the role of thermodynamic and kinetic factors, such as the existence of multiple energy minima and complex relaxation dynamics, can contribute to the paradox. The understanding of Kauzmann’s paradox has implications for our comprehension of the glass transition, the nature of supercooled liquids, and the relationship between thermodynamics and kinetics in these systems. Continued research in this area aims to resolve the paradox and provide a comprehensive understanding of the behavior of supercooled liquids and the glass transition phenomenon.

## 1.4 A summary of theories of the glass transition

The glass transition is a fascinating phenomenon in materials science, and several theories have been proposed to explain the underlying processes and mechanisms. Here is a summary of some prominent theories of the glass transition:

### 1.4.1 Adam-Gibbs theory

In the above section, we have explained the thermodynamics and dynamics of supercooled liquid separately. In this section, we will connect the dynamics and thermodynamics of supercooled liquid using the Adam-Gibbs relation. The Adam-Gibbs relation is a phenomenological equation that describes the relationship between the relaxation time ( $\tau_\alpha$ ) which is a dynamical quantity of a

supercooled liquid and its configurational entropy ( $S_c$ ) which is a thermodynamical quantity. In other words, the Adam-Gibbs (AG) relation is a bridge between dynamics and thermodynamics. It is named after John Adam and James Gibbs, who proposed this relationship [29, 30].

The Adam-Gibbs connection takes cooperative rearrangement regions (CRRs) in supercooled liquids into account. CRRs are areas or clusters of molecules that experience simultaneous cooperative motion during relaxation processes. The Adam-Gibbs relation connects the size of these CRRs to how long it takes a supercooled liquid to relax. The derivation is summarised in the following manner:

- Size of the cooperative rearrangement region ( $\xi$ ): The CRR's size is a defining length scale that symbolizes the geographic area in which cooperative motion takes place. It can be compared to the size of a group of molecules that reorganize all at once as a result of relaxation processes. The probability of a rearrangement of particles at temperature T ( $P(T)$ ) is assumed to depend exponentially on this size of CRR:

$$P(T) = A \exp(-\beta\xi\delta\mu) \quad (1.8)$$

where  $\beta = 1/k_B T$ ,  $k_B$  is a Boltzmann constant.  $\delta\mu$  is associated by Adam and Gibbs with a restricted partition function over configurations that allow rearrangements, at temperature T.

- Correlation between relaxation time with CRR: The probability of rearrangement is higher, which means the dynamics of the liquid become faster and relaxation time decreases. The probability of rearrangement is inversely proportional to the relaxation time  $\tau_\alpha$ .  $\tau \propto P(T)^{-1}$ , substitute the value of  $P(T)$  from above equation,

$$\tau_\alpha = A \exp(-\beta\xi\delta\mu)^{-1} \quad (1.9)$$

- Connect the configurational entropy  $S_c$  to the CRR's size: The amount of different configurations or arrangements of the molecules in the supercooled liquid is represented by the configurational entropy. It has to do with the logarithm of the liquid volume that the CRRs have access to. If N is the total number of particles in the system,  $\xi$  is the size of the CRR,  $N/\xi$  gives the number of CRRs, and  $s_c$  is the configurational entropy per CRR, which is assumed to be roughly constant, then the total configurational entropy of the system can be expressed in terms of the size of the CRR as

$S_c = (N/\xi)s_c$ . The Adam-Gibbs relation is obtained by rearranging the previous equation and substituting the expression for  $\xi$  in terms of  $S_c$ :

$$\tau_\alpha = A \exp\left(\frac{N\beta\delta\mu s_c}{S_c}\right) = A \exp\left(\frac{C}{TS_c}\right) \quad (1.10)$$

where  $C = N\beta s_c \delta\mu$  is a constant.

The assumption of cooperative motion and the idea of CRRs within the supercooled liquid are key components in the formulation of the Adam-Gibbs relation. It gives a phenomenological explanation of the connection between configurational entropy and relaxation time, providing insight into the dynamics of supercooled liquids and how they behave close to the glass transition.

### 1.4.2 Free volume theory

The Free Volume Theory is a theoretical framework used to explain the glass transition in terms of changes in the free volume, or available space, between molecules in a supercooled liquid. According to this theory, the glass transition occurs when the free volume decreases to a critical value, hindering molecular motion and resulting in an increase in viscosity.

The Free Volume Theory places a strong emphasis on how packing and molecular arrangement affect the behavior of the glass transition. It implies that the amount of space available for a molecule's mobility determines the dynamic features of a supercooled liquid, including viscosity, relaxation time, and diffusivity. The molecules experience more intermolecular interactions while coming across more barriers when the free volume becomes limited, resulting in the glassy behavior often seen.

One of the earliest hypothesis to explain the glass transition phenomenon is the free volume theory in the glassy system. Cohen and Turnbull introduced it initially, and Cohen and Grest later expanded on it. A few presumptions are necessary for the free volume theory in glass to work.

- Each molecule has a definite volume on a molecular scale.
- When  $v_f = v - v_c$ , there is an excess volume above the critical value  $v_c$  of  $v$ . This extra volume might be considered free.
- There is no correlation between the redistribution of the free volume,  $v_f = v - v_c$ , and free energy.
- A molecule can only move when its specific  $v_f$  value rises above a particular threshold,  $v_f^*$ .

$$D = \int_{v_f^*}^{\infty} D(v)P(v)dv \quad (1.11)$$

where  $P(v)$  is the probability density of finding a cell with a free volume between  $v$  and  $v+dv$  and  $D(v)$  is the diffusion coefficient for a molecule possessing free volume  $v$ . We now need to determine  $P(v)$  for a system in which a redistribution of the free volume is not accompanied by an energy exchange.  $V_f$  is the total free volume and  $N$  is the number of molecules, the average free volume is given by the formula

$$v_f = V_f/N \quad (1.12)$$

Let's partition the whole range of a molecule's free volume values into separate sections, each with an average value of  $v_i$ . If  $N_i$  is the quantity of molecules in the  $i^{th}$  region with free volume, we obtain

$$\gamma \sum_i N_i v_i = V_f \quad (1.13)$$

where  $\gamma$  is a geometric factor that corrects the overlap of the free volume. For the total free volume, and the total number of molecules is given by

$$\sum_i N_i = N \quad (1.14)$$

The number of ways of redistributing the free volume without changing the  $N_i$  is

$$W = N_i / \Pi_i N_i! \quad (1.15)$$

Now to maximize  $W$  for a given  $N$  and  $V_f$ , use the Lagrange multiplier method and get

$$N_i = \exp[-(\gamma + \beta v_i)] \quad (1.16)$$

where  $\lambda$  and  $\beta$  are the Lagrangian multipliers. By obtaining  $\lambda$  and  $\beta$  from Eq.1.13 and 1.16, and passing to the continuum limit for  $v_i$ , we find

$$P(v) = (\gamma/v_f) \exp[-\gamma v/v_f] \quad (1.17)$$

Considering that  $D(v)$  is now a slowly varying function, we set it equal to  $D_{v_f^*}$  in Eq. 1.11 and obtain

$$D = \text{const.} \exp[-\gamma v_f^*/v_f] \quad (1.18)$$

When there is no more free volume left in the liquid for random redistribution (i.e.,  $v_f = 0$ ), the free-volume equation predicts that  $D$  will disappear. Since it is reasonable to suppose that the free volume exhibits a linear temperature dependency, at least over small temperature ranges (i.e.,  $v_f \propto \alpha_p(T, T_0)$ , where  $\alpha_p$  is the coefficient of thermal expansivity), Eq. 1.18 can be expressed as,

$$\eta(T) = A \exp[B/(T - T_{VFT})] \quad (1.19)$$

Which is in the form of Vogel-Fulcher-Tamann (VFT) [21, 18, 20, 19], where  $T_{VFT}$  is known as VFT temperature, the temperature at which the free volume vanishes (and thus viscosity diverges).

It's critical to keep in mind that the Free Volume Theory simplifies rather than fully explains the glass transition. Other components, including molecular interactions, energy landscapes, and dynamic heterogeneities, also play significant roles. However, the conceptual framework provided by the Free Volume Theory can be used to understand the connection between free volume, molecular mobility, and the glass transition in supercooled liquids.

### 1.4.3 Random first-order transition theory.

When a phase transition takes place in an amorphous or disordered system without any long-range order, it is referred to as a random first-order transition. Random first-order transitions happen in systems with a high degree of disorder, like glasses or amorphous materials, compared to conventional first-order transitions, which often call for crystalline or organized phases. A theoretical framework called random first-order transition theory in glasses uses the idea of random first-order transitions to try and explain how glasses behave and their transitions. Based on the existence of numerous metastable states and a complicated energy landscape, it offers a perspective on the development and characteristics of glasses. This hypothesis states that glasses are disordered systems with amorphous structure and long-range order.

This RFOT theory was proposed by Kirkpatrick, Thirumalai, and Wolynes to investigate the behavior of supercooled liquid and glass transition [31, 32, 33, 34, 35]. It was inspired by the theory of spin-glasses. It is feasible to find multiple physical components of a thermodynamic system to be in different configurational states if the system has several states. Since all of the states have an amorphous order, a border or interface between them can be used to tell two states apart. Due to the mismatch of states at the boundary, the existence of an interface will result in energy loss. The relationship between that energy cost and surface area and surface tension will be proportional.



$$\Delta F_{cost} = Y R^\theta \quad (1.20)$$

$\theta \leq d - 1$ , where  $d$  is the physical dimension.  $R$  is the domain's size, and  $Y$  is the generalized surface tension. The RFOT states that a given region has an exponentially high number of potential states and that free energy can be reduced by traveling to different states. Therefore, the existence of various states in a given location has an entropic origin. By traveling to various configurations, the system can obtain free energy, which will contribute as follows:

$$\Delta F_{gain} = -T S_c R^d \quad (1.21)$$

If the configurational entropy ( $S_c$ ) and temperature ( $T$ ) are both given. The system's overall free energy can then be expressed as,

$$F_{total} = \Delta F_{cost} + \Delta F_{gain} = Y R^\theta - T S_c R^d \quad (1.22)$$

A new state will form according to the classical nucleation theory, when the two opposing forces balance, or when  $\frac{dF_{tot}}{dR} = 0$ . From this, we may derive a length scale, and that length scale is

$$\xi = \left( \frac{Y(T)}{T S_c} \right)^{\frac{1}{d-\theta}} \quad (1.23)$$

The AG theory can be recovered via RFOT theory, but with a different exponent,  $d/(d - \theta)$ .

#### 1.4.4 Mode coupling theory

A theoretical framework known as mode-coupling theory (MCT) describes the dynamics and relaxation procedures in supercooled liquids and glasses. In 1984, Bengtzelius, Götze and Sjölander and Leutheusser [36, 37, 38, 39] introduced mode-coupling theory (MCT), a microscopic theory for glassy dynamics. It was initially created to understand the glass transition phenomenon and how molecular motion slows down as a liquid cools down to become glassy. The basic idea of MCT is the assumption that the dynamics of a supercooled liquid may be modeled as the time development of density fluctuations, or "modes" of the system. It takes into account how different modes interact with one another and how that affects how the material behaves during relaxation. In supercooled liquids, MCT predicts a two-step relaxing process[11]. MCT makes quantitative predictions about how the correlation function will reach and exit the plateau. Thus, MCT can account for both the relaxation  $\alpha$  and  $\beta$ . As of now, MCT accu-

rately predicts the approach and exit from the plateau in addition to the short- and long-term relaxation. It demonstrates good agreement with the experimental results. The behavior of dynamic quantities like the self-correlation function and the intermediate scattering function can also be predicted using MCT. As the temperature approaches the glass transition temperature, “dynamic arrest” occurs when the relaxation time diverges and the system is stuck in a metastable condition. MCT predict many other features of the complex dynamics of glass-forming liquids, and one of the most prominent one is the dynamic transition from an ideal liquid to a nonergodic glassy state at some particular temperature  $T_c$  or particle density,  $\rho_c$ .

In MCT obtain an equation of motion for the time-dependent density correlation function. There are many ways to derive the MCT equation, including the projection operator formalism [40, 41], field-theoretic method [42, 43], fluctuating hydrodynamics [44, 45], microscopic approach beginning with Newton’s equations of motion, etc. Indeed, the Mode-Coupling Theory’s (MCT) prediction of the plateau’s length and the divergence in the relaxation time at a finite temperature  $T_c$ , also known as the MCT singularity, is one of the theory’s drawbacks. This behavior makes it difficult to sufficiently explain the dynamics of relaxation close to the glass transition. The assumption of idealized conditions, such as ignoring dynamic heterogeneity and structural rearrangements that occur in actual glass-forming systems, leads to the MCT singularity. These simplified ways may cause the plateau length to be overestimated and the complex nature of the relaxation processes to be overlooked. MCT predicts the power-law divergence as,

$$\tau_\alpha \approx (T - T_c)^{-\gamma} \quad (1.24)$$

where  $T_c$  is the divergence temperature and  $\gamma$  is the fitting parameter. Although the dynamics do not diverge at  $T_c$ , the MCT power law behavior is found to be present for most experimental and theoretical data. It can therefore be considered an artifact of the theory. Despite significant failures, the theory has made a lot of contributions to our understanding of the dynamics of the liquids that create glass, despite significant disadvantages.

## 1.5 Conclusion

The significance of structural relaxation, nucleation, and crystallization in supercooled liquids has also been mentioned in the introduction. Whether a supercooled liquid crystallizes or enters a glassy state, these processes play a role

in deciding the liquid's outcome.

Key ideas about supercooled liquid have been addressed throughout the introduction, including the glass transition, which denotes the change from a supercooled liquid to an amorphous solid. The glass transition has been examined from a thermodynamic and kinetic perspective, providing an understanding of the underlying mechanisms and elements that control this interesting phenomenon.

# Chapter 2

## Definitions, methods and models

“Knowledge is a treasure hidden in the depths of curiosity; the true quest is in the unearthing, not the complexity of comprehension.”

- Marie Curie

After explaining the fundamental concepts and theories related to glass-forming liquids and glass transition in chapter 1, it is important to establish the definitions and procedures used to calculate the various quantities of interest. These definitions give support for the analysis and interpretation of the current thesis findings. It is also necessary to take into account the multiple glass-forming liquid models that have been looked at. In this section, we'll go through the key terms and procedures for examining liquids that create glass. This includes the definitions of words like configurational entropy, overlap function, and radial distribution function, etc. These values give details about the structural and dynamic properties of the system and are frequently utilized to explain glassy behavior.

### 2.1 Models details

The discovery of a more effective glass-forming mechanism depends significantly on the addition of frustration during crystallization. Trying to build a perfectly ordered crystalline structure in a system with different-sized particles is difficult. In a polydisperse system, where the particles have a distribution in sizes, this frustration can be easily introduced. Due to high frustration, the polydisperse system is seen as better glass forming.

Another effective technique for creating a good glass former is pinning the positions of a few particles in the system to prevent them from taking part in crystal formation. This pinning technique introduces local structural restric-

tions, which prevent crystallization. By increasing the concentration of pinned particles in the fluid, the glassy behavior as a whole is improved.

### 2.1.1 Polydisperse system

The study involves two different kinds of systems with respect to size polydispersity, constant volume fraction (CVF) and Gaussian (as shown in Fig.2.1) and three different kinds of interaction potentials (as shown in Fig.2.2).

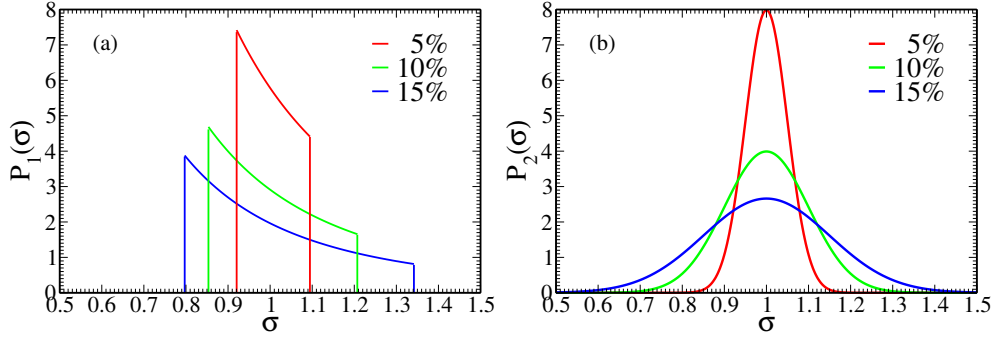


Figure 2.1: *Different kinds of distributions (a) Constant volume fraction distribution,  $P_1(\sigma)$  (b) Gaussian distribution,  $P_2(\sigma)$ . For the same degree of polydispersity, compared to  $P_1(\sigma)$  the distribution is wider for  $P_2(\sigma)$ .*

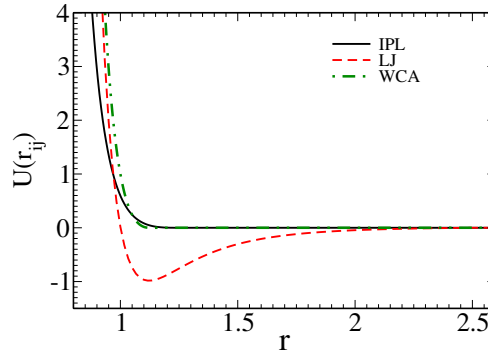


Figure 2.2: *Graphical representation of the inverse power law potential (IPL), Lennard-Jones potential (LJ), Weeks-Chandler-Andersen (WCA) potential energy functions*

The distributions of the particle sizes are continuous. This means each of the  $N$  particles has a different radius. The form of the constant volume fraction distribution is given by [46],

$$P_1(\sigma) = \frac{A}{\sigma^3}, \quad \sigma \in [\sigma_{max}, \sigma_{min}] \quad (2.1)$$

where  $A$  is the normalization constant and  $\sigma_{max}$  and  $\sigma_{min}$  are the maximum and minimum values of particle diameter.  $\sigma_{max}$  and  $\sigma_{min}$  values are given in

Table.2.1. The degree of polydispersity is quantified by [46] the normalized root mean square deviation

$$\text{PDI} = \frac{\sqrt{\langle \sigma^2 \rangle - \langle \sigma \rangle^2}}{\langle \sigma \rangle}$$

where  $\langle \dots \rangle$  defines the average of the particle size distribution.

The Gaussian distribution is given by

$$P_2(\sigma) = \frac{1}{\sqrt{2\pi}\delta^2} \exp\left(-\frac{(\sigma - \langle \sigma \rangle)^2}{2\delta^2}\right) \quad (2.2)$$

where  $\delta$  is the standard deviation. In this distribution we consider  $\sigma_{max/min} = \langle \sigma \rangle \pm 3\delta$ . The degree of polydispersity is quantified by,

$$\text{PDI} = \frac{\sqrt{\langle \sigma^2 \rangle - \langle \sigma \rangle^2}}{\langle \sigma \rangle} = \frac{\delta}{\langle \sigma \rangle}$$

For all the polydisperse systems the particle sizes are chosen such that  $\langle \sigma \rangle = \int P(\sigma)\sigma d\sigma = 1$  and is kept as the unit of length for all the systems studied here.

Table 2.1: *Details of the size distributions, constant volume fraction and Gaussian, for different degrees of polydispersity  $\text{PDI} = \frac{\sqrt{\langle \sigma^2 \rangle - \langle \sigma \rangle^2}}{\langle \sigma \rangle}$ . The maximum,  $\sigma_{max}$ , and minimum  $\sigma_{min}$ , values of the diameter of the particles. The volume fraction  $\eta$  is also given showing an increase in  $\eta$  with degree of polydispersity.*

Distribution	PDI %	$\sigma_{max}$	$\sigma_{min}$	$\Delta\sigma$	$\eta$
$P_1(\sigma)$	5%	1.1	0.92	0.18	0.53
	10%	1.21	0.85	0.36	0.54
	15%	1.34	0.8	0.54	0.56
$P_2(\sigma)$	5%	1.15	0.85	0.3	0.53
	10%	1.3	0.7	0.6	0.54
	15%	1.45	0.55	0.9	0.56

The three different interaction potentials studied here are the inverse power law (IPL) potential, Lennard-Jones (LJ) potential and its repulsive counterpart, the Weeks-Chandler-Andersen (WCA) potential. Fig.2.2 illustrates the graphical representation of the three potential energy functions.

The inverse power law potential (IPL) between two particles  $i$  and  $j$  is given by, [46, 47].

$$U(r_{ij}) = \begin{cases} \epsilon_{ij} \left(\frac{\sigma_{ij}}{r_{ij}}\right)^{12} + \sum_{l=0}^2 c_{2l} \left(\frac{r_{ij}}{\sigma_{ij}}\right)^{2l}, & \left(\frac{r_{ij}}{\sigma_{ij}}\right) \leq x_c \\ 0, & \left(\frac{r_{ij}}{\sigma_{ij}}\right) > x_c \end{cases} \quad (2.3)$$

The constants  $c_0, c_2$  and  $c_4$  are selected such that the potential becomes continuous up to its second derivative at the cutoff  $x_c = 1.25\sigma_{ij}$ .

The LJ potential between the two particles  $i$  and  $j$  is described using truncated and shifted LJ potential;

$$U(r_{ij}) = \begin{cases} U^{(LJ)}(r_{ij}; \sigma_{ij}, \epsilon_{ij}) - U^{(LJ)}(r_{ij}^{(c)}; \sigma_{ij}, \epsilon_{ij}), & r_{ij} \leq r_{ij}^{(c)} \\ 0, & r_{ij} > r_{ij}^{(c)} \end{cases} \quad (2.4)$$

where  $U^{(LJ)}(r_{ij}; \sigma_{ij}, \epsilon_{ij}) = 4\epsilon_{ij}[(\frac{\sigma_{ij}}{r_{ij}})^{12} - (\frac{\sigma_{ij}}{r_{ij}})^6]$ . The cutoff for the LJ system is  $r_{ij}^{(c)} = 2.5\sigma_{ij}$  and for the WCA system is  $r_{ij}^{(c)} = 2^{1/6}\sigma_{ij}$ . The interaction strength between two particles  $i$  and  $j$  is  $\epsilon_{ij} = 1.0$ .  $\sigma_{ij} = \frac{(\sigma_i + \sigma_j)}{2}$ , where  $\sigma_i$  is the diameter of particle ‘ $i$ ’ and it varies according to the system. Length, temperature, and times are given in units of  $\langle \sigma \rangle$ ,  $\epsilon_{ij}$  and  $(\frac{m\langle \sigma \rangle^2}{\epsilon_{ij}})^{\frac{1}{2}}$  respectively.

## 2.1.2 Pinned system

We have used atomistic models that are simulated with two-component mixtures of classical particles (larger ‘‘A’’ and smaller ‘‘B’’ type). Particles of type  $i$  interact with those of type  $j$  with pair potential,  $u(r_{ij})$ , where  $r$  is the distance between the pair. The shifted and truncated Lennard-Jones (LJ) potential form is described in Eq. 2.4.

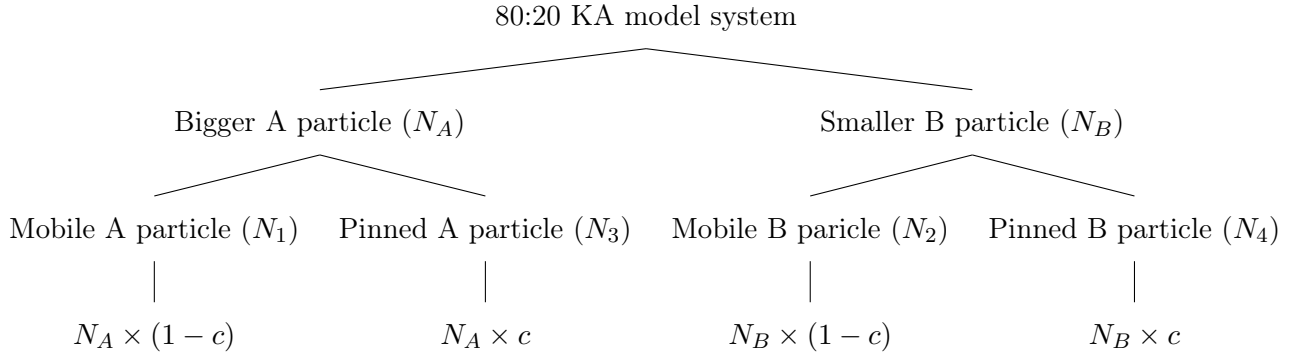
We have used the Kob-Andersen model[13] and performed constant volume and constant temperature (Nosé-Hoover thermostat and velocity rescaling) molecular dynamics simulation (NVTMD). We use  $\sigma_{AA}$  and  $\epsilon_{AA}$  as the units of length and energy, respectively, setting the Boltzmann constant  $k_B = 1$ . We have used reduced time unit in terms of  $\sqrt{\frac{m_A \sigma_{AA}^2}{\epsilon_{AA}}}$  and masses of both types of particles are taken to be the same ( $m_A = m_B$ , set equal to unity). We have used 80% of A particles and 20% of B particles with the diameter  $\sigma_{AA}=1.0$ ,  $\sigma_{AB}=0.8$  and  $\sigma_{BB}=0.88$ . The interaction strengths between the particles are  $\epsilon_{AA}=1.0$ ,  $\epsilon_{AB}=1.5$  and  $\epsilon_{BB}=0.5$ .

In a pinned system, a fraction of particles are artificially pinned at their positions in an equilibrated liquid. For the study of the pinned system, we use the Kob-Andersen 80:20 binary Lennard-Jones mixture[13]. The following pinning procedure is applied to create the pinned system. The pinned particles are chosen randomly from an equilibrium configuration of the KA system at the target temperature[48, 49]. In this process, the ratio of the two types of particles in the pinned state remains the same as the origin system (80:20). This has been checked after the pinning process. Note that the two pin particles can’t be close to each other. The Nosé-Hoover thermostat is used to simulate NVT molecular dynamics in a cubic box with  $N$  number of particle.

We have also worked on a system known as a high-mass system for this thesis. In this case, instead of directly pinning the positions of the particles in this system, we increased the fraction of particle mass to the level where high-mass particles are unable to move during a short period. It acts like a pinned system as a result. This was achieved by applying a significant amount of mass to these particles, limiting their motion, and thus immobilizing them. At a long time interval, the high-mass particles eventually overcame their limitations, resumed their normal motion, and exhibited

regular Kob-Anderson (KA) system behavior.

A simple tree of system details



where,

Number of mobile particle =  $M = N_1 + N_2 = (1-c)N$

Number of pinned particle =  $P = N_3 + N_4 = cN$

Total number of particle =  $N = M+P = N_1 + N_2 + N_3 + N_4$ .

After providing an overview of the simulation model, it is important to know the essential terminologies and their corresponding calculation methods. These terminologies play a crucial role in understanding and analyzing the simulated system.

## 2.2 Calculation of dynamic properties

The dynamics of supercooled liquids are calculated using a variety of techniques. These techniques offer insightful information about the behavior and motion of particles within the liquid. In this section, we'll look at some of the popular techniques for analyzing the dynamics of supercooled liquids.

### 2.2.1 Relaxation time calculation from overlap function

The overlap function ( $q(t)$ ), a two-point time ( $t$ ) correlation function of local density,  $\rho(r, t)$ , is used in the current thesis to study dynamics.

$$\begin{aligned}
 q(t) &\equiv \left\langle \int \int \delta \vec{r} \rho(\vec{r}, t_0) \rho(\vec{r}, t + t_0) \right\rangle \\
 &= \left\langle \sum_{i=1}^N \sum_{j=1}^N \delta(\vec{r}_j(t_0) - \vec{r}_i(t + t_0)) \right\rangle
 \end{aligned} \tag{2.5}$$

Separating the overlap function into “self” and “collective” terms:

$$q(t) = \left\langle \sum_{i=1}^N \delta(\vec{r}_i(t_0) - \vec{r}_i(t + t_0)) \right\rangle + \left\langle \sum_{i=1}^N \sum_{j \neq i}^N \delta(\vec{r}_j(t_0) - \vec{r}_i(t + t_0)) \right\rangle \tag{2.6}$$



The self-part of the total overlap function ignores the terms in the double summation with the value  $i \neq j$ . It has been shown in the past that it is a good approximation of the full overlap function. Consequently, the overlap function's self-component can be expressed as[2],

$$q(t) \approx \left\langle \sum_{i=1}^N \delta(\vec{r}_i(t_0) - \vec{r}_i(t + t_0)) \right\rangle \quad (2.7)$$

Furthermore,  $\omega(x)$ , a window function that defines the condition of ‘‘overlap’’ between two particle positions separated by a period  $t$ , approximates the  $\delta$  function for numerical computation.

$$q(t) = \frac{1}{N} \sum_{i=1}^N \langle \omega(|\mathbf{r}_i(t) - \mathbf{r}_i(0)|) \rangle \quad , \quad (2.8)$$

The function  $\omega(x) = 1$  if  $0 \leq x \leq a$  otherwise  $\omega(x)$  is 0. Based on Eq. 2.8, the selection of the cutoff parameter changes the overlap function's value in simulation. This parameter has been selected to treat particle positions that are separated by small amplitude vibrational motion as identical. The parameter ‘‘ $a$ ’’ (cutoff radius) is usually specified as 0.3 or 0.5, a value that is somewhat greater than the cage's dimensions. The overlap function  $q(t)$  is illustrated in Fig.2.3.

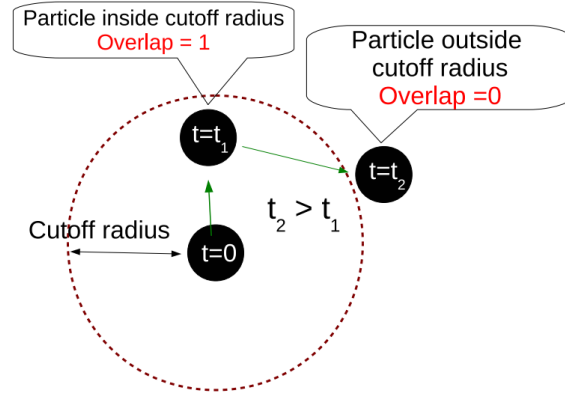


Figure 2.3: *Illustrating the definition of the ‘‘overlap’’ function  $q(t)$ . Adapted from ref. [26].*

We have calculated the relaxation times obtained from the decay of the overlap function  $q(t)$ , where  $q(t = \tau_\alpha, T)/N = 1/e$ . Here,  $N$  is the number of particles in the system, and  $\tau_\alpha$  denotes the time it takes to relax at a particular temperature  $T$ . For each temperature under consideration, we calculate the relaxation time  $\tau_\alpha$  by examining the overlap function's decay behavior. The typical timescale at which the system experiences significant relaxation and achieves a new equilibrium state is represented by this relaxation time. Regarding the dynamics and relaxation procedures in the supercooled liquid, it offers useful information.

### 2.2.2 Mean square displacement (MSD)

The MSD is an important tool for investigating the dynamics and motion of particles in a supercooled liquid. It provides a numerical analysis of the displacements of the particles and can reveal important details regarding the diffusion behavior and relaxation processes of the system. The MSD is defined as the average of the squared displacements of particles from their initial positions. Its mathematical formula is as follows:

$$MSD = \langle (\Delta r)^2 \rangle = \langle (r(t) - r(0))^2 \rangle = \frac{1}{N} \sum_{i=1}^N (r_i(t) - r_i(0))^2 \quad (2.9)$$

where  $N$  represents the total number of particles,  $r(t)$  represents the position of a particle at time  $t$ , and  $r(0)$  represents the position of a particle during the initialization process.

The particle velocity can be used to directly determine the mean-square displacement.

$$(\Delta r)^2 = (v(t)dt)^2 = v(t)^2 dt^2 \quad (2.10)$$

where  $v(t)$  is the particle's velocity at time  $t$ . The MSD for the particle will be,

$$MSD = \langle (\Delta r)^2 \rangle = \int_0^t dt' \int_0^t dt'' \langle v(t')v(t'') \rangle \quad (2.11)$$

where the particle's velocities at times  $t'$  and  $t''$  are denoted by  $v(t')$  and  $v(t'')$ , respectively.

### 2.2.3 Non Gaussian parameter

The first approximation self-part of the Van-Hove correlation function ( $G_s(r, t) = \frac{1}{N} \rho \sum_i \langle \delta(r - [r_i(t) - r_i(0)]) \rangle$ , where  $r_i(t)$  is the position of particle  $i$  at time  $t$ ,  $N$  is the total number of particles,  $\rho$  is the particle number density, and  $\langle \dots \rangle$  denotes an ensemble average over various particle trajectories) has a Gaussian form in the context of supercooled liquids, but deviations from this form at intermediate times have been seen in simulations of liquids that form glass and are believed to reflect the presence of dynamical heterogeneity [50, 51](Shown in Fig.2.4). The non-Gaussian parameter  $\alpha_2$  can be used to describe such discrepancies; in other-words  $\alpha_2$  is a measure of the particle displacement distribution's divergence from Gaussian behavior (Shown in Fig.2.4). It is frequently used to describe the dynamic characteristics of liquids that undergoes supercooled close to the glass transition.

$$\alpha_2(t) = \frac{3\langle r^4(t) \rangle}{5\langle r^2(t) \rangle^2} - 1 \quad (2.12)$$

where  $\langle \Delta r^2 \rangle$  is the second moment (mean square displacement) of the distribution, while  $\langle \Delta r^4 \rangle$  is the fourth moment of the particle displacement distribution.

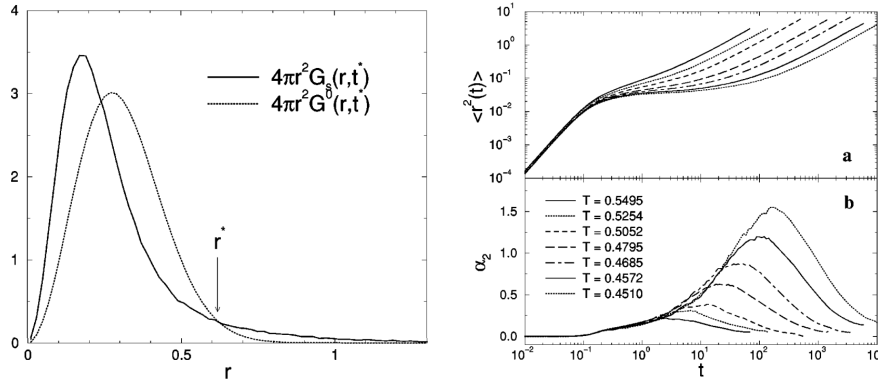


Figure 2.4: **Left side Figure** - Solid line:  $4\pi r^2 G_s(r,t)$  of the A particles at  $t = 155.5$  at  $T = 0.4510$ . Dashed line: Gaussian approximation calculated using the measured  $\langle r^2(t) \rangle$  for the same time. **Right side Figure** - (a) Mean square displacement  $\langle r^2(t) \rangle$  of the A particles vs time for several values of  $T$ . (b) Non-Gaussian parameter  $\alpha_2(t)$  vs time for the same values of  $T$  as in (a). Figures are adapted from ref. [52].

The relaxation dynamics in supercooled liquids slow down as the temperature approaches the glass transition temperature. As a result, the particle displacement distribution deviates more and more from Gaussian behavior. This non-Gaussian behavior is captured by the  $\alpha_2$  parameter, which also provides information about the system's structural and dynamic heterogeneities.

A positive value of  $\alpha_2$  suggests that the particle displacement distribution is more dispersed than a Gaussian distribution and has heavy tails. This indicates the presence of dynamic heterogeneities, where some liquid regions show slower relaxation dynamics than others. A negative  $\alpha_2$  value, on the other hand, predicts a more peaked distribution and a higher level of cooperativity in the dynamics.

For the time scale at which a particle's velocity is ballistic,  $\alpha_2 = 0$ . After entering the time scale of the  $\beta$  relaxation,  $\alpha_2$  starts to rise. At a long time limit, the relaxation time scale of  $\alpha$ ,  $\alpha_2$  begins to decrease from  $\alpha_{max}$  to zero. Cage breakage starts at the point in time that  $\alpha_{max}$  is reached [53].

The non-Gaussian parameter in supercooled liquids can be measured and analyzed to help scientists better understand the complex behavior and structural properties of supercooled liquid close to the glass transition.

## 2.3 Calculation of static properties: Radial distribution function

In statistical mechanics and molecular dynamics simulations, the radial distribution function (RDF), also known as the pair correlation function, is an important concept.

It is used to describe how the particles in a system are distributed geographically. The RDF calculates the probability of discovering a particle at a particular distance “ $r$ ” from a reference particle [10, 54]. Understanding a system’s structure and interactions requires knowing the local density and configuration of particles surrounding a central particle. Radial distribution function is the average number density of particles at a distance  $r$  from a reference particle, normalized by the bulk density of the system. It is denoted as  $g(r)$  and express as;

$$g(r) = [\rho(r)]/[\rho_{bulk}] \quad (2.13)$$

where  $\rho(r)$  denotes the number density of particles that are  $r$  away from the reference particle and  $\rho_{bulk}$  denotes the system’s overall number density. Often, computer models or experimental measurements are used to derive the RDF. In simulations, it is computed by accumulating the particle-particle distances in the system and dividing them into radial shells. To produce a smooth RDF curve, the number of particles in each shell is then averaged over a large number of configurations. A schematic of how the radial distribution function is calculated from particle position and the radial distribution function at different temperatures is shown in Fig.2.5.

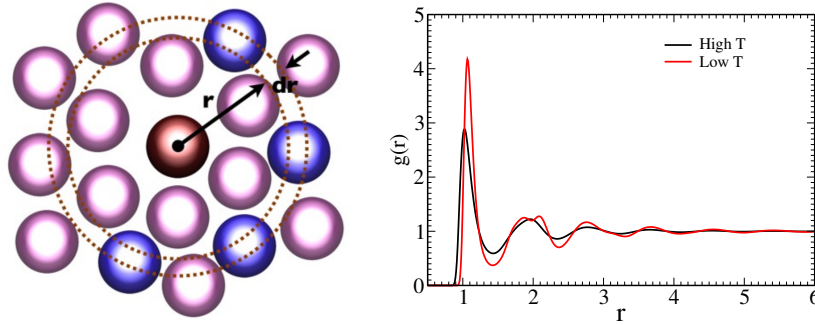


Figure 2.5: (Left) A schematic of how the radial distribution function is calculated from particle position. Picture taken from Wikipedia. (Right) Radial distribution function at 2 different temperatures. As the temperature decreases, the peak height of  $g(r)$  increases.

Consider a system of  $N$  particles that are in thermal equilibrium with a heat bath at temperature  $T$  (let us define  $\beta = \frac{1}{k_B T}$ , where  $k_B$  is a Boltzmann constant) and are contained in volume  $V$  (for an average number density  $\rho = N/V$ ). The canonical ensemble, which describes the statistical distribution of particles in equilibrium with the heat bath, provides the probability of a specific configuration of the particles. The probability of a configuration, according to the canonical ensemble ( $N, V, T$ ), is inversely proportional to the corresponding energy’s ( $U(r_1, r_2, \dots, r_N)$ ) Boltzmann factor [54]:

$$P(\mathbf{r}_1, \mathbf{r}_2, \dots, \mathbf{r}_N) = \frac{e^{-\beta U(\mathbf{r}_1, \mathbf{r}_2, \dots, \mathbf{r}_N)}}{Z_N} \quad (2.14)$$

where configurational integral  $Z_N$  can be written as,

$$\begin{aligned}
Z_N &= \int e^{-\beta U(\mathbf{r}_1, \mathbf{r}_2, \dots, \mathbf{r}_N)} d\mathbf{r}_1, d\mathbf{r}_2, \dots, d\mathbf{r}_N \\
&= \int \dots \int d\mathbf{r}_2, \dots, d\mathbf{r}_N = V^N \quad (\text{If } V_N = 0)
\end{aligned} \tag{2.15}$$

Here,  $\mathbf{r}_1, \mathbf{r}_2, \dots, \mathbf{r}_N$  is a particle coordinate. We can write the probability that particle 1 is in the volume  $dr_1$  about  $r_1$  and particle 2 is in  $dr_2$  about  $r_2$  as

$$P_2 d\mathbf{r}_1 d\mathbf{r}_2 = \frac{e^{-\beta U} d\mathbf{r}_3, \dots, \mathbf{r}_N}{Z_N} d\mathbf{r}_1 d\mathbf{r}_2 \tag{2.16}$$

The probability of finding  $n$  particles in the system with coordinates in the volume element  $dr^n$  is given by the amount  $\rho_N^{(n)}(r^n) dr^n$ , irrespective of the positions of the remaining particles and irrespective of any momenta.

$$\rho_N^{(n)}(\mathbf{r}^n) = \frac{N!}{(N-n)!} \int \frac{e^{-\beta U_N} d\mathbf{r}^{(N-n)}}{Z_N} \tag{2.17}$$

While the low-order particle distribution functions, in particular, the pair density  $\rho_N^{(2)}(r_1, r_2)$ , are frequently sufficient to calculate the equation of state and other thermodynamic properties of the system, the particle densities and the closely related equilibrium particle distribution functions, defined below, provide a complete description of the structure of a fluid. The  $n$ -particle density is defined as follows:

$$\int \rho_N^{(n)}(\mathbf{r}^n) d\mathbf{r}^n = \frac{N!}{(N-n)!} \tag{2.18}$$

Thus,

$$\int \rho_N^{(1)}(\mathbf{r}) d\mathbf{r} = N \tag{2.19}$$

A uniform fluid's single-particle density is therefore the same as its total number density:

$$\rho_N^{(1)}(\mathbf{r}) = \frac{N}{V} = \rho \quad (\text{uniform fluid}) \tag{2.20}$$

We are aware from Eq. 2.15 that in the exceptional situation of an ideal, uniform gas,  $Z_N = V^N$ . The pair density is as a result

$$\rho_N^{(2)} = \rho \left(1 - \frac{1}{N}\right) \quad (\text{ideal gas}) \tag{2.21}$$

The word  $1/N$  appears in Eq. 2.21 related the fact that in a system with a fixed number of particles, the probability of finding a particle in the volume element  $dr_1$ , provided that another particle is in the element  $dr_2$ , is proportional to  $(N-1)/V$  rather than  $\rho$ . In terms of the associated particle densities,  $g_N^{(n)}(r^n)$  defines the  $n$ -particle distribution function.

$$g_N^{(n)}(\mathbf{r}^n) = \frac{\rho_N^{(n)}(\mathbf{r}_1, \dots, \mathbf{r}_n)}{\prod_{i=1}^n \rho_N^{(1)}(\mathbf{r}_i)} \quad (2.22)$$

For a homogeneous system which reduces as,

$$\rho^n g_N^{(n)}(\mathbf{r}^n) = \rho_N^{(n)}(\mathbf{r}^n) \quad (2.23)$$

The degree to which a fluid's structure deviates from pure randomness can be determined by its particle distribution functions. If the system is also isotropic, the pair distribution function  $g_N^{(2)}(r_1, r_2)$  is a function of the separation  $r_{12} = |r_2 - r_1|$  and is, therefore, more commonly referred to as the radial distribution function and represented as  $g(r)$ . The ideal-gas limit, which can be calculated from Eq. 2.21 as  $(1 - 1/N) \approx 1$ , is reached when  $r$  is significantly larger than the interparticle potential's range. In a way that is particularly useful for future uses, the particle densities defined by Eq. 2.17 are also expressible in terms of  $\delta$ -functions of position. According to the definition of a  $\delta$  function,

$$\begin{aligned} \langle \delta(\mathbf{r} - \mathbf{r}_1) \rangle &= \frac{1}{Z_N} \int \delta(r - r_1) \exp[-\beta U_N(\mathbf{r}_1, \mathbf{r}_2, \dots, \mathbf{r}_N)] d\mathbf{r}^N \\ &= \frac{1}{Z_N} \int \dots \int \exp[-\beta U_N(\mathbf{r}_1, \mathbf{r}_2, \dots, \mathbf{r}_N)] d\mathbf{r}_2 \dots d\mathbf{r}_N \end{aligned} \quad (2.24)$$

The particle label (here taken to be 1) does not affect the ensemble average in Eq. 2.24, which is independent of the coordinate  $r$ . As a result, the contribution from each particle is equal to  $N$  times the sum of the labels for all the particles. Then, it is demonstrated by comparison with the definition Eq. 2.17

$$\rho_N^{(1)}(\mathbf{r}) = \left\langle \sum_{i=1}^N \delta(\mathbf{r} - \mathbf{r}_i) \right\rangle \quad (2.25)$$

This indicates the ensemble average of the particle density  $\rho(r)$  at the microscopic scale. The average of the result of two  $\delta$ - functions is similar.

$$\begin{aligned} \langle \delta(\mathbf{r} - \mathbf{r}_1) \delta(\mathbf{r}' - \mathbf{r}_2) \rangle &= \frac{1}{Z_N} \int \delta(\mathbf{r} - \mathbf{r}_1) \delta(\mathbf{r}' - \mathbf{r}_2) \exp[-\beta V_N(\mathbf{r}_1, \mathbf{r}_2, \dots, \mathbf{r}_N)] d\mathbf{r}^N \\ &= \frac{1}{Z_N} \int \dots \int \exp[-\beta V_N(\mathbf{r}, \mathbf{r}', \mathbf{r}_3, \dots, \mathbf{r}_N)] d\mathbf{r}_3 \dots d\mathbf{r}_N \end{aligned} \quad (2.26)$$

which implies that

$$\rho_N^{(2)}(\mathbf{r}, \mathbf{r}') = \left\langle \sum_{i=1}^N \sum_{j=1}^N \delta(\mathbf{r} - \mathbf{r}_i) \delta(\mathbf{r}' - \mathbf{r}_j) \right\rangle \quad (2.27)$$

Terms for which  $i = j$  must be removed are indicated by the prime on the summation sign. Finally, the radial distribution function can be represented by a useful  $\delta$ -

function. It is obvious from this that

$$\begin{aligned} \left\langle \sum_{i=1}^N \sum_{j=1}^N \delta(\mathbf{r} - \mathbf{r}_j + \mathbf{r}_i) \right\rangle &= \left\langle \frac{1}{N} \int \sum_{i=1}^N \sum_{j=1}^N \delta(\mathbf{r}' + \mathbf{r} - \mathbf{r}_j) \delta(\mathbf{r}' - \mathbf{r}_i) d\mathbf{r}' \right\rangle \\ &= \frac{1}{N} \int \rho_N^{(2)}(\mathbf{r}' + \mathbf{r}, \mathbf{r}') d\mathbf{r}' \end{aligned} \quad (2.28)$$

The system is homogeneous and isotropic if both properties are present.

$$\left\langle \frac{1}{N} \sum_{i=1}^N \sum_{j=1}^N \delta(\mathbf{r} - \mathbf{r}_j + \mathbf{r}_i) \right\rangle = \frac{\rho^2}{N} \int g_N^{(2)}(\mathbf{r}, \mathbf{r}') d\mathbf{r}' = \rho g(r) \quad (2.29)$$

The pair correlation function for a binary system  $g_{\alpha\beta}(r)$  is given by,

$$g_{\alpha\beta}(r) = \frac{V}{N_\alpha N_\beta} \left\langle \sum_{i=1}^{N_\alpha} \sum_{j=1, j \neq i}^{N_\beta} \delta(r - r_i + r_j) \right\rangle \quad (2.30)$$

where  $V$  is the system's volume,  $N_\alpha$ ,  $N_\beta$  are the number of particles of the  $\alpha$  and  $\beta$  types, respectively, and  $r_i$  is the  $i^{\text{th}}$  particle's position in the system.

In terms of partial rdf of  $M$  species, the effective one-component radial distribution function,  $g(r)$ , can be stated as follows.

$$g(r) = \sum_{\alpha, \beta=1}^M \chi_\alpha \chi_\beta g_{\alpha\beta}(r) \quad (2.31)$$

where the mole fractions of the particles  $\alpha$  and  $\beta$  are denoted by  $\chi_\alpha$  and  $\chi_\beta$ , respectively. This represents the global radial distribution or macroscopic radial distribution function.

**Particle wise radial distribution function (prdf) or microscopic radial distribution function** - One can learn more about the underlying particle interactions, clustering behavior, and local structure of the system by representing the prdf as a sum of Gaussians. To analyze and understand the system's microscopic features, it gives a quantitative description of the probability distribution of particles surrounding the reference particle. The single particle radial distribution function in a single frame can be expressed as a sum of Gaussians[55]. Mathematically, it can be represented as;

$$g_{\alpha\beta}^i(r) = \frac{1}{4\pi\rho r^2} \sum_j \frac{1}{\sqrt{2\pi\delta^2}} \exp^{-\frac{(r-r_{ij})^2}{2\delta^2}} \quad (2.32)$$

where the variance of the Gaussian distribution is  $\delta = 0.09$ . The discontinuous function is transformed into a continuous one using the variance.

### 2.3.1 Different parameter calculated from macroscopic radial distribution function, $g(r)$

We can learn important information about the structure of the system by examining the RDF, and we can use this knowledge to calculate several thermodynamic quantities. In this section, we use RDF as a tool to calculate a few thermodynamics parameters which are shown below[10],

#### 1. Energy calculation in the form of $g(r)$

First, a formula for the energy  $E$  in term  $g(r)$  is derived [10, 56], utilizing the formula  $Q_N = Z_N/N!\Lambda^{3N}$ . Kinetic energy and potential energy combine to make up the system's total energy.  $\bar{U}$ . It is written as,

$$\begin{aligned} E &= \frac{3}{2}NkT + kT^2 \left( \frac{\delta \ln Z_N}{\delta T} \right)_{N,V} \\ &= \frac{3}{2}NkT + \bar{U} \end{aligned} \quad (2.33)$$

where,

$$\bar{U} = \frac{\int \dots \int U e^{-\beta U} dr_1 \dots dr_N}{Z_N} \quad (2.34)$$

Let's assume that the N-body system's total potential energy is pair-wise additive, as in,

$$U_N(r_1, r_2, \dots, r_N) = \sum_{i < j} u(r_{ij}) \quad (2.35)$$

where all molecular pair pairs are included in the summation, all thermodynamic functions of the system can be expressed in terms of  $g(r)$ . Under this assumption,  $U$  is the product of  $N(N-1)/2$  terms, each of which, when integrated with respect to  $r_1$  through  $r_N$ , produces the same result. As an example of these  $N(N-1)/2$  terms in  $U$  using  $u(r_{12})$ , we have

$$\begin{aligned} \bar{U} &= \frac{N(N-1)}{2Z_N} \int \dots \int e^{-\beta U(r_{12})} dr_1 \dots dr_N \\ &= \frac{N(N-1)}{2} \int \int u(r_{12}) \left\{ \frac{\int \dots \int e^{-\beta U} dr_3 \dots dr_N}{Z_N} \right\} dr_1 dr_2 \\ &= \frac{1}{2} \int \int u(r_{12}) \rho^{(2)}(r_1, r_2) dr_1 dr_2 \\ &= \frac{N^2}{2V} \int_0^\infty u(r) g(r, \rho, T) 4\pi r^2 dr \end{aligned} \quad (2.36)$$

Next comes to the entire energy  $E$



$$\frac{E}{NkT} = \frac{3}{2} + \frac{\rho}{2kT} \int_0^\infty u(r)g(r, \rho, T)4\pi r^2 dr \quad (2.37)$$

The system's per-particle potential energy can be precisely estimated using the simulation  $E_{sim}$ . The same thing can also be expressed using  $E_2$ , the partial radial distribution function.

$$E_2 = \frac{\rho}{2} \sum_{\alpha, \beta=1}^M \chi_\alpha \chi_\beta \int_0^\infty 4\pi r^2 U_{\alpha\beta}(r) g_{\alpha\beta}(r) dr \quad (2.38)$$

The energy in the efficient one-component treatment can be expressed as  $E_2^{eff}$ .

$$E_2^{eff} = \frac{\rho}{2} \int_0^\infty 4\pi r^2 U(r) g(r) dr \quad (2.39)$$

This equation is called the Energy equation.

## 2. Pressure calculation in the form of $g(r)$

The pressure (P) is given by,

$$P = kT \left( \frac{\delta \ln Q}{\delta V} \right)_{N,T} = kT \left( \frac{\delta \ln Z_N}{\delta V} \right)_{N,T} \quad (2.40)$$

where,

$$Z_N = \int_0^{V^{1/3}} \dots \int e^{-\beta U} dx_1 dy_1 dz_1 \dots dx_N dy_N dz_N \quad (2.41)$$

We alter the integration variables such that the limits become constants and U becomes an explicit function of V before differentiating  $Z_N$  with respect to V. The new variables should be  $x'_1, y'_1$ , etc.

$$x_k = V^{1/3} x'_k, \quad etc. \quad (2.42)$$

Then

$$Z_N = V_N \int_0^1 \dots \int_0^1 e^{-\beta U} dx'_1 \dots dz'_N \quad (2.43)$$

$$U = \sum_{1 \leq i < j \leq N} u(r_{ij}) \quad (2.44)$$

and

$$\begin{aligned} r_{ij} &= [(x_i - x_j)^2 + (y_i - y_j)^2 + (z_i - z_j)^2]^{1/2} \\ &= V^{1/3} [(x'_i - x'_j)^2 + (y'_i - y'_j)^2 + (z'_i - z'_j)^2]^{1/2} \end{aligned} \quad (2.45)$$

Therefore,

$$\begin{aligned} \left(\frac{\delta Z_N}{\delta V}\right)_{N,T} &= NV^{N-1} \int_0^\infty \dots \int_0^\infty e^{-\beta U} dx'_1 \dots dz'_N \\ &\quad - \frac{V^N}{kT} \int_0^\infty \dots \int_0^\infty e^{-\beta U} \left(\frac{\delta U}{\delta V}\right) dx'_1 \dots dz'_N \end{aligned} \quad (2.46)$$

where,

$$\left(\frac{\delta U}{\delta V}\right) = \sum_{1 \leq i < j \leq N} \frac{du(r_{ij})}{dr_{ij}} \frac{dr_{ij}}{dV} = \sum_{1 \leq i < j \leq N} \frac{r_{ij}}{3V} \frac{du(r_{ij})}{dr_{ij}} \quad (2.47)$$

We now transform back to the original variables  $x_1, \dots, z_N$  after performing the differentiation with respect to  $V$ . Also take note of the  $N(N-1)/2$  identical term that results from integrating over the sum. As a result, we eventually get

$$\left(\frac{\delta \ln Z_N}{\delta V}\right)_{N,T} = \frac{N}{V} - \frac{1}{6VkT} \int \int_v r_{12} \frac{du(r_{12})}{dr_{12}} \rho^{(2)}(r_1, r_2) dr_1 dr_2 \quad (2.48)$$

This, when entered into the Eq. 2.40 produces

$$\frac{P}{kT} = \rho - \frac{\rho^2}{6kT} \int_0^\infty r u'(r) g(r) 4\pi r^2 dr \quad (2.49)$$

This equation is called the pressure equation.

### 3. Pair excess entropy ( $S_2$ ) in the form of $g(\mathbf{r})$

The pair excess entropy can be estimated using the radial distribution function by employing methods such as the Kirkwood-Buff theory [57] or the Ornstein-Zernike equation [58], which relate the structural information provided by the RDF to the thermodynamic properties of the system.

The Kirkwood-Buff [57] theory relates the excess entropy of mixing to the partial correlation functions, which can be derived from the RDF. By integrating the partial correlation functions over all distances, the pair excess entropy contribution can be obtained.

The Ornstein-Zernike equation [58], in combination with the radial distribution function, provides a framework for calculating the direct correlation function. From the direct correlation function, the excess entropy can be determined through an integration procedure.

Following Kirkwood expansion the per particle excess entropy of a liquid can be written in terms of two body and higher order correlations as[57],

$$S_{ex} = S_2 + S_3 + \dots \quad (2.50)$$

where  $S_n$  is the entropy due to  $n$ -body correlation.  $S_{ex}$  can also be calculated via thermodynamic integration as,

$$S_{ex}(\beta') = \beta' \langle U \rangle - \int_0^{\beta'} d\beta \langle U \rangle \quad (2.51)$$

where  $\langle U \rangle$  is the per particle potential energy. The potential energy in terms of  $g(r)$  is given Eq. 2.36. Let us now assume that the system is such that there are only two-body correlations. This will imply that  $g(r) = \exp(-\beta u(r))$ . The average potential energy per particle level can now be written as,

$$\langle U \rangle = 2\pi\rho \int_0^\infty u(r) \exp(-\beta u(r)) r^2 dr \quad (2.52)$$

Using Eq.2.52, we will go from Eq.2.51 to Eq.2.50. First we will put the value of  $\langle U \rangle$  from Eq.2.52 into Eq.2.51. Energy is in 2 - body correlation so now  $S_{ex}$  due to 2-body correlation will be

$$S_2 = 2\pi\rho \left[ \int_0^\infty \beta^* u(r) \exp(-\beta^* u(r)) r^2 dr - \int_0^{\beta^*} d\beta \int_0^\infty u(r) \exp(-\beta u(r)) r^2 dr \right] \quad (2.53)$$

First term of Eq.2.53 can be written as

$$\begin{aligned} & \int_0^\infty \beta^* u(r) \exp(-\beta^* u(r)) r^2 dr \\ &= \int_0^\infty (-) \ln[\exp(-\beta^* u(r))] \exp(-\beta^* u(r)) r^2 dr \\ &= - \int_0^\infty \ln[g(r)] g(r) r^2 dr \\ &= - \int_0^\infty g(r) \ln[g(r)] r^2 dr \end{aligned} \quad (2.54)$$

as  $\exp(-\beta^* u(r)) = g(r)$

If we integrate the second term of Eq.2.53 for the  $\beta$  variable then we get as

$$\begin{aligned} & - \int_0^{\beta^*} d\beta \int_0^\infty u(r) \exp(-\beta u(r)) r^2 dr \\ &= - \int_0^\infty \left[ u(r) \frac{-1}{u(r)} \exp(-\beta u(r)) \right]_0^{\beta^*} r^2 dr \\ &= \int_0^\infty [\exp(-\beta u(r))]_0^{\beta^*} r^2 dr \\ &= \int_0^\infty [\exp(-\beta^* u(r)) - 1] r^2 dr \\ &= \int_0^\infty [g(r) - 1] r^2 dr \end{aligned} \quad (2.55)$$

Now Eq.2.53 can be rewritten using Eq.2.54 and Eq.2.55 as

$$\begin{aligned}
S_2 &= 2\pi\rho \left[ - \int_0^\infty g(r) \ln[g(r)] r^2 dr + \int_0^\infty [g(r) - 1] r^2 dr \right] \\
&= -2\pi\rho \left[ \int_0^\infty g(r) \ln[g(r)] r^2 dr - \int_0^\infty [g(r) - 1] r^2 dr \right] \quad (2.56) \\
&= -2\pi\rho \int_0^\infty [g(r) \ln g(r) - (g(r) - 1)] r^2 dr
\end{aligned}$$

The above Eq. represents the effective one component excess entropy, also denoted as  $S_2^{eff}$ . The two-body excess is also known as the pair excess entropy.

The expression of two body excess entropy of the system for a binary system,  $S_2$ ,

$$S_2 = -2\pi\rho \sum_{\alpha} x_{\alpha} \sum_{\beta} x_{\beta} \int_0^\infty r^2 dr \{g_{\alpha\beta}(r) \ln g_{\alpha\beta}(r) - (g_{\alpha\beta}(r) - 1)\} \quad (2.57)$$

This equation is called the pair excess entropy equation.

## 2.4 Thermodynamic Properties

Here, we go over the process for examining the thermodynamic characteristics of supercooled liquids.

### 2.4.1 Ideal gas entropy

We can apply statistical mechanics to determine the entropy of an ideal gas. The microstates of an ideal gas, which represent many possible configurations of the gas particles, are closely related to its entropy. Free energy can be related to volume and temperature using the Maxwell equation of thermodynamics as;

$$dF = PdV - SdT \quad (2.58)$$

If an NVT ensemble is used, the volume will not change ( $dV = 0$ ). Now that the above equation has been reduced,

$$\begin{aligned}
dF &= -SdT \\
S &= -dF/dT
\end{aligned} \quad (2.59)$$

Microstates that represent free energy are stated as;

$$F = -k_B T \ln Z \quad (2.60)$$

where  $Z$  is the number of microstates corresponding to the macroscopic state of the gas and  $k_B$  is the Boltzmann constant. Using Eq. 2.59, 2.60, the entropy of an ideal gas may now be directly related to its microstates.

$$S = k_B \ln(Z) \quad (2.61)$$

The positions and momenta  $p_i$  of each particle determine the microstates in an ideal gas. In the limit of an ideal gas, particles only have momentum and do not interact with each other with any kind of potential. The ideal gas system's total Hamiltonian is written as;

$$H(p_i) = \sum_i \frac{p_i^2}{2m_i} \quad (2.62)$$

It is possible to write the partition function for the monodisperse ideal gas in a d-dimensional system at temperature T ( $\beta = 1/k_B T$ ) as;

$$\begin{aligned} Z(\beta) &= \prod_{i=1}^N \frac{1}{h^d} \int d^d q_i d^d p_i \exp[-\beta \frac{p_i^2}{2m_i}] \\ &= \frac{V^N}{h^{dN}} \left\{ \int d^d p_i \exp[-\beta] \frac{p^2}{2m} \right\}^N \\ &= \frac{V^N}{\Lambda^{dN}} \end{aligned} \quad (2.63)$$

where  $\Lambda = \sqrt{\frac{\beta h^2}{2\pi m}}$  is the de Broglie thermal wavelength and h is the Planck constant. The partition function is now expressed for the indistinguishable particles as;

$$Z = \frac{1}{N!} \frac{V^N}{\Lambda^{dN}} \quad (2.64)$$

If d=3 (3-dimensional), then  $S_{id}$ , from Eq. 2.61 and 2.64 can be represented as follows:

$$S_{id} = \ln V + \frac{3}{2} \ln \frac{2\pi m T}{h^2} - \ln N + \frac{5}{2} \quad (2.65)$$

The binary system (which contains particles of types A and B) is given to a similar analysis.

$$Z(\beta) = \frac{1}{N_A! N_B!} \frac{V^{N_A + N_B}}{\Lambda_A^{dN_A} \Lambda_B^{dN_B}} \quad (2.66)$$

For the binary system in three dimensions, the ideal gas entropy is expressed as;

$$\frac{S_{id}}{k_B} = N \ln(V) - N_A \ln N_A - N_B \ln N_B - 3N_A \ln \Lambda_A - 3N_B \ln \Lambda_B + \frac{5}{2} N \quad (2.67)$$

If the particles are separated into " $M_0$ " distinct species such that  $N = \sum_{i=1}^{M_0} N_i$ , then the ideal gas entropy per particle can be expressed as follows;

$$S_{id} = \frac{5}{2} - \ln(\rho) + \frac{3}{2} \ln \left( \frac{2\pi T}{h^2} \right) + \frac{1}{N} \ln \frac{N!}{\prod_{i=1}^{M_0} N_i!} \quad (2.68)$$

This thesis includes work on pinned systems (details of pinned systems are provided in the section 2.1.2). If the system partition function is pinned, it is written as;

$$\begin{aligned} Z &= \frac{V^{N_1}}{N_1! \Lambda_1^{3N_1}} \frac{V^{N_2}}{N_2! \Lambda_2^{3N_2}} \\ &= Z_1 Z_2 \end{aligned} \quad (2.69)$$

where  $N_1, N_2$  represent the number of moving particles of type A and B, respectively, and  $N_3, N_4$  represent the number of pinned particles of type A and B, respectively. Total mobile particle  $M = N_1 + N_2$ . In 3D, the ideal gas ( $S_{id}$ ) can be expressed as,

$$MS_{id} = \frac{d}{dT} T [M \ln(V) - N_1 \ln \Lambda_1^3 - N_2 \ln \Lambda_2^3 - \ln(N_1!) - \ln(N_2!)] \quad (2.70)$$

Since  $m_3 = m_4$  for the pin system is so huge,  $\Lambda_3 = \Lambda_4 \simeq 0$ .

$$\begin{aligned} MS_{id} &= [M \ln(V) - 3M \ln \Lambda - \sum_{i=1}^2 \ln(N_i!)] + \frac{3M}{2} \\ &= M \ln(V) - 3M \ln \Lambda - \sum_{i=1}^2 (N_i \ln(N_i) - N_i) + \frac{3M}{2} \\ &= \frac{3M}{2} - 3M \ln \Lambda + M(1 - \ln \frac{M}{V}) - \sum_{i=1}^2 N_i \ln \frac{N_i}{M} \end{aligned} \quad (2.71)$$

The ideal gas entropy for the pinned system is determined using the equation mentioned above.

## 2.4.2 Excess entropy

The difference between total entropy and ideal gas entropy is known as excess entropy. It stands for the extra entropy produced due to variations in the system's behavior that go beyond what an idealized model would predict. There are numerous ways to calculate excess entropy; in this thesis, we have worked with three alternative methods.

1. **Temperature-density integration** - One way for calculating excess entropy is the temperature-density integration method [59]. With respect to temperature and density, this approach integrates a thermodynamic quantity (internal energy). These integrations can be used to calculate the excess entropy. The entropy of an ideal gas is what is observed at high temperatures and low densities. This  $S_{id}$  serves as a comparative benchmark for all subsequent state point entropy calculations. When calculating alternative state point entropy, it is possible to combine isothermal (Eq. 2.73) and isochoric (Eq. 2.74) pathways while making sure that there are no phase transitions along the chosen path

[59]. Temperature-density landscape is shown in Fig.2.6. The relations between the thermodynamic quantities, internal energy (U), entropy (S), volume (V), temperature (T), and pressure (P), are governed by fundamental principles and equations in thermodynamics,

$$\begin{aligned} dU &= TdS - PdV \\ dS &= \frac{(dU + PdV)}{T} \\ \int dS &= \int \frac{dU}{T} + \int \frac{PdV}{T} \end{aligned} \quad (2.72)$$

We fix the temperature (T) and adjust the density ( $\rho$ ) during the density integration procedure. During this integration, the system's volume (V) shifts from the beginning volume (V), which corresponds to a high temperature and low density, to the target volume (V'). Another name for this procedure is energy integration;

$$\begin{aligned} \int_{T,V}^{T,V'} dS &= \int_{T,V}^{T,V'} \frac{dU}{T} + \int_V^{V'} \frac{PdV}{T} \\ S_{ex}(T, V') - S_{ex}(T, V) &= \frac{U(T, V') - U(T, V)}{T} + \int_V^{V'} \frac{P(V)}{T} dV \end{aligned} \quad (2.73)$$

We fix the density ( $\rho$ ) and alter the temperature (T) while performing the temperature integration. The system's temperature (T) shifts from an initial temperature (T) that corresponds to a high temperature and low density to a target temperature (T') during this integration. U is a function of T and V. Change in volume ( $dV$ ) = 0 at fixed density ( $\rho$ ). Another name for this procedure is pressure integration;

$$\begin{aligned} \int_{T',V'}^{T,V'} dS &= \int_T^{T'} \frac{dU}{T} + 0 \\ \int_{T',V'}^{T,V'} dS &= \int_T^{T'} \frac{1}{T} \left[ \left( \frac{\delta U}{\delta V'} \right)_T dV + \left( \frac{\delta U}{\delta T} \right)_{V'} dT \right] \\ S_{ex}(T', V') - S_{ex}(T, V') &= \int_T^{T'} \frac{1}{T} \left( \frac{\delta U}{\delta T} \right)_{V'} dT \end{aligned} \quad (2.74)$$

By addition of Eq. 2.73 and Eq. 2.74, we can obtain the excess entropy ( $S_{ex}$ ) as a function of temperature and density, which provides insights into the additional entropy beyond the ideal reference system caused by intermolecular interactions and other deviations.

- 2. Temperature integration method** - We investigate how excess entropy changes as the system moves from infinite temperature (a very disordered state) to the target temperature (a particular thermal state of interest) by doing the temperature integration. The key benefit of this approach lies in its ability to capture

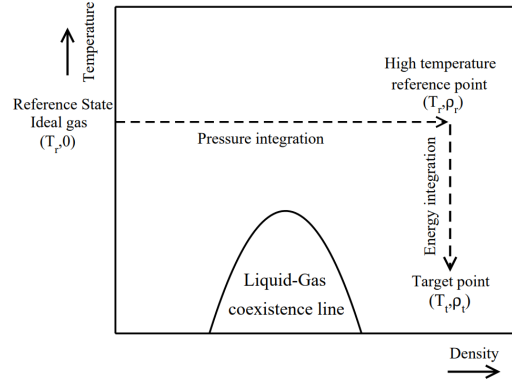


Figure 2.6: *Schematic diagram for thermodynamic (temperature - density) integration. Adapted from ref. [60].*

the thermodynamic effects connected with the system's transition from highly energetic, random configurations to a more defined and structured state at the target temperature. It gives us insights into the system's behavior and the function that temperature performs in controlling its entropy as well as the ability to quantify the change in excess entropy associated with this shift. The target temperature ( $T'$ ) is integrated thermodynamically from infinite temperature and ends up at the following expression, which represents the calculation of excess entropy:

$$S_{ex}(\beta') = \beta' \langle U \rangle - \int_0^{\beta'} d\beta \langle U \rangle \quad (2.75)$$

where  $\langle U \rangle$  is the average per-particle potential energy of the system at the desired temperature and  $\beta' = \frac{1}{k_B T'}$ .

Integrating over-density in a pinned system is neither practical nor useful because the density is fixed or restricted. The system's thermodynamic properties can still be studied by integrating temperature, though. Therefore, temperature integration becomes the proper way to compute the excess entropy in a pinned system when density integration is not relevant. For a pinned system, excess entropy is calculated as;

$$NS_{ex} = S_{ex}(T', V) - S_{ex}(T, V) = \int_{T=\infty}^{T'} \frac{1}{T} \left( \frac{\delta U_N}{\delta T} \right)_V dT \quad (2.76)$$

where the system is integrated from  $\infty$  temperature ( $T$ ) to target temperature ( $T'$ ).  $U_N$  is the total system energy and can be expressed as;

$$U_N = U_{PP} + U_{MP} + U_{PM} + U_{MM}$$

where  $U_{PP}$ ,  $U_{PM}$ ,  $U_{MP}$ ,  $U_{MM}$  represent interaction energy between pin-pin (PP), mobile-pin(MP), pin-mobile(PM), mobile-mobile(MM) particles. In the pinned



system, the pin-pin particle has no interaction, hence  $U_{PP} = 0$ . The only source of energy for a pinned system is a moving particle, hence its new source of energy will be;

$$U_M = U_{MM} + U_{MP} + U_{PM} \quad (2.77)$$

Since  $U_M$  represents the energy for a moving particle, the energy per particle will be  $\frac{U_M}{M}$ . The pinned system's excess entropy is given by the following equation:

$$MS_{ex}(\beta') = \beta' \langle U_M \rangle - \int_0^{\beta'} d\beta \langle U_M \rangle \quad (2.78)$$

The entropy caused by moving particles in a pinned system is given by the above equation.

3. **Two-phase thermodynamics (2PT) method** - The two-phase thermodynamics method for the calculation of excess entropy involves considering a two-phase system, typically consisting of a gas phase and a liquid phase, in equilibrium at a given temperature and pressure. The density of states (DOS) of the liquid phase can be used to calculate the thermodynamic quantities in the two-phase thermodynamics (2PT) technique. The distribution of possible states or configurations in the system is represented by the DOS, which offers important details on the energy levels and associated probability of the system. So we can say that the complicated energy landscape and related thermodynamic behavior are captured by the 2PT technique by utilizing the DOS of the liquid phase.

In the 2PT method, the phonon in the solid-like DOS was taken as a non-interacting harmonic oscillator, just like in the Debye model, to compute the thermodynamic quantities. On the other hand, gas-like DOS was described as a low-density, analytically determined hard-sphere fluid. Lin et al. showed that the LJ fluid's thermodynamic properties can be calculated with high accuracy throughout a wide range of thermodynamic state points with a very short MD trajectory using the 2PT description. Later, Lin et al. used the 2PT approach to calculate the binary fluid's entropy. Here, we give a brief overview of how DOS breaks down in 2PT. Nevertheless, for a thorough discussion of 2PT, we direct the reader to the original articles. The mass-weighted atomic spectral densities, given as, can be used to calculate the density of state function,  $g(\nu)$ .

$$g(\nu) = \frac{2}{k_B T} \sum_{j=1}^N \sum_{k=1}^3 m_j s_j^k(\nu) \quad (2.79)$$

where  $k$  stands for the direction in Cartesian coordinates,  $s_j^k(\nu)$  stands for the atomic spectral densities, and  $m_j$  is the mass of the  $j^{\text{th}}$  atom.

$$s_j^k(\nu) = \lim_{\tau \rightarrow \infty} \frac{|\int_{-\tau}^{\tau} \nu_j^k(t) e^{-i2\pi\nu t} dt|^2}{2\tau} \quad (2.80)$$

where  $\nu_j^k(t)$  stands for the  $j^{\text{th}}$  atom's velocity component in the  $k^{\text{th}}$  direction. The velocity auto-correlation function (VACF)  $c_j^k(t)$  Fourier transform can be used to calculate the atomic spectral density, or  $s_j^k(\nu)$ .

$$s_j^k(\nu) = \lim_{\tau \rightarrow \infty} \int_{-\tau}^{\tau} c_j^k(t) e^{-i2\pi\nu t} dt \quad (2.81)$$

$c_j^k(t)$  is determined by:

$$c_j^k(t) = \lim_{\tau \rightarrow \infty} \frac{1}{2\tau} \int_{-\tau}^{\tau} \nu_j^k(t+t') \nu_j^k(t') dt' \quad (2.82)$$

Eq. 2.79 can be rewritten as follows:

$$g(\nu) = \frac{2}{k_B T} \lim_{\tau \rightarrow \infty} \int_{-\tau}^{\tau} \sum_{j=1}^N \sum_{k=1}^3 m_j c_j^k(t) e^{-i2\pi\nu t} dt \quad (2.83)$$

In 2PT formalism,  $g(\nu)$  can be divided into solid and gas-like components, as we discussed earlier. Lin et al. presented a self-consistent fluidity factor,  $f$ , which determines the degree of freedom shared by the solid and gas components. This factor is based on the diffusivity of the system relative to hard-sphere gas at the same density. It is possible to draw the link between  $f$  and dimensionless diffusivity,

$$2\Delta^{-9/2} f^{15/2} - 6\Delta^{-3} f^5 - \Delta^{-3/2} f^{7/2} + 6\Delta^{-3/2} f^{5/2} + 2f - 2 = 0 \quad (2.84)$$

Dimensionless diffusivity constant  $\Delta$ , based on the characteristics of the material.

$$\Delta(T, \rho, m, g_0) = \frac{2g_0}{9N} \left(\frac{6}{\pi}\right)^{2/3} \left(\frac{\pi k_B T}{m}\right)^{1/2} \rho^{1/3} \quad (2.85)$$

where the DOS of the system at zero frequency is given by  $g_0 = g(0)$ . A hard-sphere diffusive model can be used to calculate the DOS in the gas-like diffusive component using  $f$  from Eq. 2.84 and 2.85

$$g^g(\nu) = \frac{g_0}{1 + \left[\frac{\pi g_0 \nu}{6fN}\right]^2} \quad (2.86)$$

One can use the equation to determine the solid-like DOS,  $g_s(\nu)$ , given the DOS in the gas-like component.

$$g(\nu) = g^g(\nu) + g^s(\nu) \quad (2.87)$$

Any thermodynamic quantity,  $A$ , can be computed using the relevant weight function after DOS has been decomposed.

$$A = \beta^{-1} \left[ \int_0^\infty g^g(\nu) W_A^g d\nu + \int_0^\infty g^s(\nu) W_A^s d\nu \right] \quad (2.88)$$

The definition of the weight function for entropy in the solid,  $W_S^s$ , and gas-like,  $W_S^g$ , component

$$W_S^s(\nu) = W_S^{HO}(\nu) = \frac{\beta \hbar \nu}{\exp(\beta \hbar \nu) - 1} - \ln[1 - \exp(-\beta \hbar \nu)] \quad (2.89)$$

where  $h$  is the Plank constant,  $\hbar = h/(2\pi)$ , and  $\beta = 1/k_B T$ .

$$W_S^g(\nu) = \frac{1}{3} \frac{S^{HS}}{k} \quad (2.90)$$

where  $S^{HS}$  stands for the hard sphere's entropy. The total entropy of the system can be expressed as, using Eqs. 2.87, 2.90

$$S_{total} = S^S + S^g \quad (2.91)$$

### 2.4.3 Vibrational entropy

Vibrational entropy can be calculated by approximating harmonically with respect to a local minimum [2, 61, 62, 63]. To obtain the vibrational density of states (DOS), we diagonalize the Hessian that is computed (see section 2.5). The following calculations are used to calculate  $S_{vib}$  after finding the DOS. The vibrational DOS is made up of a variety of vibrational energies or frequencies. It displays the number of vibrational states that are present for each unit of frequency or energy interval. The DOS is obtained by analyzing the eigenvalues obtained by diagonalizing the Hessian matrix. The eigenvalues are typically transformed into frequencies by using the proper scaling factors. We may determine the relationship between entropy, free energy, and partition function using the equations 2.59 and 2.60.

$$\begin{aligned} S &= \frac{-dF}{dT} = -k_B T \ln Z \\ S_{vib} &= \frac{-dF_{basin}}{dT} = -k_B T \ln Z_{basin} \end{aligned} \quad (2.92)$$

Free energy ( $F$ ) and  $Z$  are expressed in terms of the basin in the case of vibrational entropy. Stillinger and Weber's work on the inherent structure formalism established the idea of a basin in the potential energy surface. A local minimum on the potential energy surface, which reflects a stable configuration of atoms in a system is referred to as the inherent structure. Stillinger and Weber offered a framework for understanding the energy landscape and the idea of basins by describing the possible energy landscape in terms of these inherent structures. A basin is made up of a collection of locations

that, via the sharpest fall, map to the same minimum, which is the inherent structure energy IS.

### Basin partition function and Basin entropy

The canonical partition function of a harmonic oscillator in one dimension with frequency, ' $\omega_i$ ' and mass, ' $m$ ' is provided by;

$$\begin{aligned}
 z_{harm}(\omega, T, V) &= \int \frac{dpdq}{h} \exp\left(-\frac{\beta p^2}{2m} - \frac{\beta m \omega^2 q^2}{2}\right) \\
 &= \frac{1}{h^{3N}} \int d^{3N} p \exp\left(\frac{-\beta p^2}{2m}\right) \times \int d^{3N-3} q \exp\left(\frac{-\beta m \omega_i^2 q^2}{2}\right) \int d^3 q \\
 &= \frac{1}{h^{3N}} \left(\frac{2m\pi}{\beta}\right)^{\frac{3N}{2}} V \prod_{i=1}^{3N-3} \left(\frac{2\pi}{\beta m \omega_i^2}\right)^{\frac{1}{2}} \\
 &= \Lambda^{-3N} V \prod_{i=1}^{3N-3} \left(\frac{2\pi}{\beta m \omega_i^2}\right)^{\frac{1}{2}}
 \end{aligned} \tag{2.93}$$

Therefore, the basin partition function can be expressed as follows using harmonic approximation:

$$\begin{aligned}
 z_{basin}(e_{IS}, N, V, T) &= \exp(-\beta e_{IS}) \left[ \prod_{i=1}^{3N-3} \left(\frac{2\pi}{\beta m \omega_i^2}\right)^{\frac{1}{2}} \right] V \left(\frac{2\pi m}{h^2 \beta}\right)^{\frac{3N}{2}} \\
 &= \exp(-\beta e_{IS}) \exp(-\beta f_{basin})
 \end{aligned} \tag{2.94}$$

The distributions of the inherent structure (IS) energy, ( $P(e_{IS}, T)$ ), for various temperatures, have been demonstrated by Sciortino et al. [64] to fall on a master curve in the low-temperature zone. This suggests that at low temperatures, there is no temperature dependence through  $e_{IS}$ . With the contribution from  $e_{IS}$  ignored, basin-free energy can be expressed as

$$\begin{aligned}
 \beta f_{basin} &= -\ln z_{harmonic} \\
 \beta f_{basin} &= -\frac{3N}{2} \ln\left(\frac{2\pi m}{h^2 \beta}\right) - \ln(V) - \frac{1}{2} \sum_{i=1}^{3N-3} \ln\left(\frac{2\pi}{\beta m \omega_i^2}\right)
 \end{aligned} \tag{2.95}$$

It is possible to write the basin entropy,  $S_{basin}$ , as,

$$\begin{aligned}
 N S_{vib} = S_{basin} &= -\frac{df_{basin}}{dT} \\
 &= -\frac{3N}{2} \ln\left(\frac{2\pi m}{h^2 \beta}\right) + \ln(V) + \frac{1}{2} \sum_{i=1}^{3N-3} \ln\left(\frac{2\pi}{\beta m \omega_i^2}\right) - \frac{3}{2} + 3N
 \end{aligned} \tag{2.96}$$

In case of pinned system we consider of a weakly vibrating system (IS) around an inherent structure. The potential energy can be approximated well by the following formula, if we indicate by  $r_i$  the displacement of the  $i^{th}$  particle from its point in the IS.

$$U \approx U_{IS}(S) + \frac{1}{2} \sum_{i,j}^M \frac{\delta^2 U}{\delta r_i \delta r_j} \delta r_i \delta r_j \quad (2.97)$$

In the pinned system it is crucial to understand that in inherent structure calculation, we minimize the mobile particle only, pinned particle coordinate remain same. It is important to understand that the coordinates of pinned particles should not be considered, just the derivative of the potential energy with respect to the coordinates of mobile particles are considered. However, it stands to reason that  $U$  will be influenced by the positions of pinned and mobile particles. The Hessian matrix is therefore  $3M \times 3M$  in size. The harmonic vibrational entropy of the given inherent structure with the given pinned particle configuration can be represented as by introducing the eigenvalues  $\lambda_1, \lambda_2, \dots, \lambda_{3M}$  of the Hessian. For pin system  $m_3 = m_4$  is so large that  $\Lambda_3 = \Lambda_4 \simeq 0$ , and only  $3M$  frequencies are present. In the pinned system 3 non-zero frequencies are not present.

$$z_{harm}(\omega, T, V) = -\Lambda^{3M} \prod_{i=1}^{3M} \left( \frac{2\pi}{\beta m \omega_i^2} \right)^{\frac{1}{2}} \quad (2.98)$$

where the number of mobile particles  $M = (N_1 + N_2)$ .  $N_1$  and  $N_2$  represent the number of mobile A and mobile B particles, respectively.

$$\begin{aligned} \beta f_{basin} &= -\ln z_{harmonic}, \\ &= \frac{3M}{2} \ln \left( \frac{2\pi}{h^2 \beta} \right) - \frac{1}{2} \sum_{i=1}^{3M} \ln \left( \frac{2\pi}{\beta m \omega_i^2} \right) \end{aligned} \quad (2.99)$$

The basin entropy,  $S_{basin}$  can be written as,

$$\begin{aligned} MS_{vib} = S_{basin} &= -\frac{\delta f_{basin}}{\delta T} \\ &= -\frac{3M}{2} \ln \left( \frac{2\pi}{h^2 \beta} \right) + \frac{1}{2} \sum_{i=1}^{3M} \ln \left( \frac{2\pi}{\beta m \omega_i^2} \right) + 3M \\ &= 3M(1 - \ln \Lambda) + \frac{1}{2} \sum_{i=1}^{3M} \ln \frac{2\pi}{\beta m \omega_i^2} \end{aligned} \quad (2.100)$$

Eq. 2.100 is used to calculate the  $S_{vib}$  entropy for the pinned system.

**Anharmonic vibrational entropy** Anharmonic vibrational entropy is the term used to describe how anharmonic vibrations affect a system's total entropy. Anharmonic vibrations contain deviations from harmonic behavior and higher-order terms in the potential energy function, in contrast to harmonic vibrations, which are modeled by straightforward harmonic oscillators.

In general, the anharmonic potential energy variables affecting the system's Hamiltonian are taken into account, and their effects on the vibrational modes are taken into

account when calculating the anharmonic vibrational entropy. For the bulk system, Refs. [61, 65] discuss this method in detail. The anharmonic vibrational entropy for pinned systems is being determined in this section since it was employed in this thesis to calculate the anharmonic vibrational entropy for pinned systems.

$$U_{anh}(c, T) = U(T) - U_{IS}(c, T) - \frac{3}{2}(1 - c)NT \quad (2.101)$$

where  $U(T)$  and  $U_{IS}(c, T)$  stand for the pinned system's inherent structure energy and equilibrium bulk potential energy, respectively. The energy of the harmonic vibrations of  $(1-c)N$  mobile particles is the last term in Eq. 2.101.  $U_{anh}(c, T)$  when expanded around the value of  $T = 0$  yields

$$U_{anh}(c, T) = \sum_{k=2} C_k(c)T^k \quad (2.102)$$

where  $C_k(c)$  are coefficients independent of  $T$ . Because the system is harmonic in the low-temperature limit, it should be noted that the sum begins at  $k = 2$ . The anharmonic contribution on the vibrational entropy  $S_{anh}(c, T)$  is given by

$$S_{anh}(c, T) = \int_0^T dT' \frac{1}{T'} \frac{\delta U_{anh}(c, T')}{\delta T'} \quad (2.103)$$

We have set  $S_{anh}(c, T = 0)$  to be equal to 0. When Eq. 2.102 is substituted in Eq. 2.103, we get

$$S_{anh}(c, T) = \sum_{k=2} \frac{k}{k-1} C_k(c)T^{k-1} \quad (2.104)$$

A numerical approach is used to assess  $S_{anh}$ , the anharmonic contribution to the entropy. Conducting simulations to determine the anharmonic potential energy,  $U_{anh}(c, T)$ , as a function of the system's configuration,  $c$ , and temperature,  $T$ , is the first stage. To find the coefficients  $C_k(c)$ ,  $U_{anh}(c, T)$  is then fitted using a polynomial function of  $T$ . For this fitting technique, the first two terms,  $C_2(c)$  and  $C_3(c)$ , are often used. The anharmonic contribution to entropy is related by the equation 2.104, which is used to determine  $S_{anh}(c, T)$ . It should be noted that the sign of  $S_{anh}(c, T)$  depends on the signs of the coefficients  $C_k(c)$ .

#### 2.4.4 Configurational entropy

Configurational entropy and vibrational entropy make up the two main components of the total entropy of a system. The number of independent or uncorrelated configurations that a system can sample from the configuration space at a given density and temperature is connected with the configurational entropy, denoted as  $S_c$ . The entropy connected to the small oscillations of the system's particles around their equilibrium positions is accounted for via vibrational entropy. The configurational entropy, on the other hand, accounts for the entropy connected with the numerous arrangements the

particles can make in the configuration space while retaining the same energy.

By deducting the vibrational entropy ( $S_{vib}$ ) from the total entropy ( $S_{total}$ ), as shown in the equation below, one can obtain the configurational entropy ( $S_c$ ):

$$\begin{aligned}
S_c &= S_{total} - S_{vib} \\
&= S_{id} + S_{ex} - S_{vib} \\
&= \ln V + \frac{3}{2} \ln \left( \frac{2\pi m T}{h^2} \right) - \ln N + \frac{5}{2} + S_{ex} - \frac{3}{2} \ln \left( \frac{2\pi m}{h^2 \beta} \right) - \frac{\ln(V)}{N} + \frac{1}{2N} \sum_{i=1}^{3N-3} \ln \left( \frac{2\pi}{\beta m \omega_i^2} \right) + \frac{3}{2N} - 3 \\
&= \ln(V) \left[ 1 - \frac{1}{N} \right] - \frac{\ln(N!)}{N} - \frac{3}{2} \left[ 1 - \frac{1}{N} \right] - \frac{1}{2N} \sum_{i=1}^{3N-3} \ln \left( \frac{2\pi}{\beta m \omega_i^2} \right) + S_{ex}
\end{aligned} \tag{2.105}$$

## 2.5 Hessian calculation

The Hessian matrix is a square matrix that contains the second-order partial derivatives of a function with respect to its variables. The Hessian matrix is frequently used in thermodynamics to examine the curvature and second-order characteristics of the potential energy surface. The second derivatives of the two-body potential  $u_{jk}$  with respect to the coordinates of the particles  $j$  and  $k$  must be determined to build the Hessian matrix. The definition of the Hessian matrix  $H$  is:

$$H_{jk} = \frac{\delta^2 u(r_{jk})}{\delta \mathbf{r}_j \delta \mathbf{r}_k} \tag{2.106}$$

and,

$$\frac{\delta}{\delta \mathbf{r}_j} \equiv \hat{i} \frac{\delta}{\delta x_j} + \hat{j} \frac{\delta}{\delta y_j} + \hat{k} \frac{\delta}{\delta z_j} \tag{2.107}$$

where  $(x_j, y_j, z_j)$  are the particle  $j$ 's three-dimensional cartesian coordinates. The Hessian is a  $3N \times 3N$  matrix in three dimensions for  $N$  particles.

$$\begin{aligned}
r_{jk} &= [(x_j - x_k)^2 + (y_j - y_k)^2 + (z_j - z_k)^2]^{(1/2)} \\
\frac{\delta r_{jk}}{\delta x_j} &= \frac{x_j - x_k}{r_{jk}} \equiv \frac{x_{jk}}{r_{jk}} \\
\frac{\delta r_{kj}}{\delta x_k} &= \frac{x_k - x_j}{r_{jk}} \equiv -\frac{x_{jk}}{r_{jk}}
\end{aligned} \tag{2.108}$$

The first derivative is;

$$\begin{aligned}
\frac{\delta u(r_{jk})}{\delta \mathbf{r}_k} &= \hat{i} \frac{\delta u}{\delta x_k} + \hat{j} \frac{\delta u}{\delta y_k} + \hat{k} \frac{\delta u}{\delta z_k} \\
\hat{i} \frac{\delta u(r_{jk})}{\delta x_k} &= \hat{i} \frac{\delta r_{jk}}{\delta x_k} \frac{\delta u(r_{jk})}{\delta r_{jk}} = \frac{-\hat{i}(x_j - x_k)}{r_{jk}} \frac{\delta u(r_{jk})}{\delta r_{jk}}
\end{aligned} \tag{2.109}$$

By using the chain rule, the first amount in the previous formula was obtained. We also came to the same conclusion for the  $y$  and  $z$  components. We may write by

combining them and expressing them in a vector notation,

$$\frac{\delta}{\delta \mathbf{r}_{\mathbf{k}}} u(r_{jk}) = -\frac{\delta u(r_{jk})}{\delta r_{jk}} \hat{r}_{jk} \quad (2.110)$$

The second derivative is currently,

$$\frac{\delta}{\delta \mathbf{r}_{\mathbf{j}}} \left( -\frac{\delta u(r_{jk})}{\delta r_{jk}} \hat{r}_{jk} \right) = \left( \hat{i} \frac{\delta}{\delta x_k} + \hat{j} \frac{\delta}{\delta y_k} + \hat{k} \frac{\delta}{\delta z_k} \right) \left( -\frac{\delta u(r_{jk})}{\delta r_{jk}} \hat{r}_{jk} \right) \quad (2.111)$$

here, we demonstrate details of the algebra for just the x component:

$$\hat{i} \frac{\delta}{\delta x_j} \left( -\frac{\delta u(r_{jk})}{\delta r_{jk}} \hat{r}_{jk} \right) = \left( \hat{i} \frac{\delta}{\delta x_j} \frac{-\delta u}{\delta r_{jk}} \right) \otimes \hat{r}_{jk} + \frac{-\delta u}{\delta r_{jk}} \left( \hat{i} \frac{-\delta}{\delta x_j} \otimes \hat{r}_{jk} \right) \quad (2.112)$$

where the tensor product of two vectors is represented by  $\otimes$ . The initial term is

$$\begin{aligned} \left( \hat{i} \frac{\delta}{\delta x_j} \frac{-\delta u}{\delta r_{jk}} \right) \otimes \hat{r}_{jk} &= \left( \hat{i} \frac{\delta r_{jk}}{\delta x_j} \frac{\delta}{\delta r_{jk}} \frac{-\delta u(r_{jk})}{\delta r_{jk}} \right) \otimes \hat{r}_{jk} = \left( \frac{\hat{i} x_{jk} - \delta^2 u}{r_{jk} \delta^2 r_{jk}} \right) \otimes \hat{r}_{jk} \\ &= -\frac{\delta^2 u}{\delta^2 r_{jk}} \left( \frac{\mathbf{r}_{\mathbf{jk}}}{r_{jk}} \right)_{x\text{-component}} \otimes \frac{\mathbf{r}_{\mathbf{jk}}}{r_{jk}} \\ &= -\frac{1}{r_{jk}^2} \frac{\delta^2 u}{\delta^2 r_{jk}} (\mathbf{r}_{\mathbf{jk}} \otimes \mathbf{r}_{\mathbf{jk}})_{x\text{-component}} \end{aligned} \quad (2.113)$$

The second expression is:

$$\begin{aligned} \frac{-\delta}{\delta r_{jk}} \left( \hat{i} \frac{\delta}{\delta x_j} \otimes \hat{r}_{jk} \right) &= \frac{-\delta}{\delta r_{jk}} \left( \hat{i} \frac{\delta}{\delta x_j} \otimes \frac{x_{kj} \hat{i} + y_{jk} \hat{j} + z_{jk} \hat{k}}{r_{jk}} \right) \\ &= \frac{-\delta u}{\delta r_{jk}} \left( \frac{1}{r_{jk}} \hat{i} \otimes \hat{i} + \hat{i} \frac{\delta}{\delta x_j} \left( \frac{1}{r_{jk}} \right) \otimes \mathbf{r}_{\mathbf{jk}} \right) \\ &= \frac{-\delta u}{\delta r_{jk}} \left( \frac{1}{r_{jk}} \hat{i} \otimes \hat{i} + \hat{i} \frac{\delta r_{jk}}{\delta x_j} \frac{\delta}{\delta r_{jk}} \left( \frac{1}{r_{jk}} \right) \otimes \mathbf{r}_{\mathbf{jk}} \right) \\ &= \frac{-\delta u}{\delta r_{jk}} \left( \frac{1}{r_{jk}} \hat{i} \otimes \hat{i} + \frac{\hat{i} x_{jk} - 1}{r_{jk} r_{jk}^2} \otimes \mathbf{r}_{\mathbf{jk}} \right) \\ &= -\frac{1}{r_{jk}} \frac{\delta u}{\delta r_{jk}} (\mathbf{I})_{x\text{-component}} + \frac{1}{r_{jk}^3} \frac{\delta u}{\delta r_{jk}} (\mathbf{r}_{\mathbf{jk}} \otimes \mathbf{r}_{\mathbf{jk}})_{x\text{-component}} \end{aligned} \quad (2.114)$$

where, The  $3 \times 3$  identity matrix in a 3D system is defined as  $\mathbf{I} = \hat{i} \otimes \hat{i} + \hat{j} \otimes \hat{j} + \hat{k} \otimes \hat{k}$ .

When the first and second terms are combined, the second derivative is

$$\begin{aligned} H(j, k) &= \frac{\delta}{\delta \mathbf{r}_{\mathbf{j}}} \frac{\delta}{\delta \mathbf{r}_{\mathbf{k}}} u(r_{jk}) \\ &= \left( -\frac{1}{r_{jk}^2} \frac{\delta^2 u}{\delta r_{jk}^2} \frac{1}{r_{jk}^3} \frac{\delta u}{\delta r_{jk}} \right) \mathbf{r}_{\mathbf{jk}} \otimes \mathbf{r}_{\mathbf{jk}} - \frac{1}{r_{\mathbf{jk}}} \frac{\delta \mathbf{u}}{\delta r_{\mathbf{jk}}} \mathbf{I}. \end{aligned} \quad (2.115)$$



## 2.6 Calculation of onset temperature

The onset temperature serves as a reference point for understanding and characterizing the temperature-dependent properties and transformations of a system, providing insights into its thermal behavior and phase transitions.

The system's thermodynamic and dynamic properties depart from its high-temperature behavior when it cools a glass-forming liquid from high temperatures at  $T_{onset}$ . Various dynamical and thermodynamical measurements exist for  $T_{onset}$ . The temperature predicted by each method is not identical but lies in a similar range. In this thesis, we discuss the two estimates method of onset T calculation. one based on inherent structural energy and the other on excess entropy.

### 2.6.1 $T_{onset}$ calculation from Inherent structure energy

The inherent structural energy of a system can be used to calculate the onset temperature. The energy and configuration of a system at a local energy minimum on the potential energy landscape are referred to as the system's inherent structure. It represents the system in a stable or metastable state. Usually, the change in inherent structural energy with temperature is taken into account when calculating the onset temperature[3]. The system explores higher energy levels as the temperature increases and undergoes transitions or transformations. The temperature at which there is a noticeable change or divergence in the inherent structural energy is known as the onset temperature.

The onset temperature is calculated by running simulations or calculations at various temperatures and examining the system's inherent structural energy at each one. One can determine the temperature range at which major changes take place by tracking the inherent structural energy as a function of temperature. The inherent structure energy is the potential energy evaluated at the local minimum of the energy reaching from the configuration via the steepest descent procedure. As suggested earlier, [3] the onset temperature is connected to the inherent structure energy. At high temperatures, as the system is not influenced by the landscape properties, the average inherent structure energy is almost temperature-independent. However, below a certain temperature, where the landscape properties influence the system, the inherent structure energy starts to decrease rapidly (Shown in Fig.2.7). Usually, the two different regimes are fitted to two straight lines, and the point where these lines cross is identified as the onset temperature,  $T_{onset}$ .

### 2.6.2 $T_{onset}$ calculation from excess energy

The onset temperature can be found by plotting the excess energy and pairing excess entropy as functions of temperature. The temperature at which these two curves cross or meet is the onset temperature[1, 66]. The thermodynamic behavior of the system has undergone a significant change or transition at this time. When the excess energy

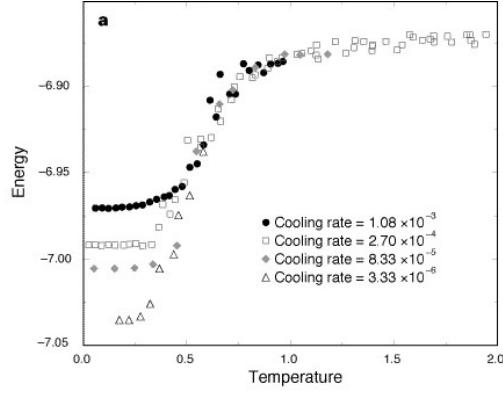


Figure 2.7: *Temperature dependence on inherent structure energy( $e_{IS}$ ). At high  $T$ ,  $e_{IS}$  is almost constant, and below a certain  $T$ ,  $e_{IS}$  start decreases rapidly. Adapted from ref. [3]*

and pair excess entropy curves intersect, the system's thermodynamic behavior has significantly changed.

The pair excess entropy describes the departure from perfect gas behavior in terms of the pairwise interactions between particles, whereas the excess energy represents the difference between the total energy of the system and the energy of the ideal gas state. From the thermodynamics integration,  $S_{ex}$  can be determined (details are provided in section 2.4.2). Additionally, the Kirkwood expansion of the excess entropy per particle of a liquid in terms of two body and higher-order correlations can be used to determine excess entropy. This is shown in Eq. 2.50.

Many body correlation ( $\Delta S$ ) has a negative effect on entropy at high  $T$ , whereas it has a favorable effect when entropy starts to fill the cage at low  $T$ .  $\Delta S = 0$  represented the onset  $T$ .

# Chapter 3

## Effective structure of a system with continuous polydispersity

“Research is creating new knowledge.”

- Neil Armstrong

### 3.1 Introduction

Most systems that can be found in nature are inherently polydisperse. Polydispersity can be of different kinds like in size, in mass, and also in the shape of the particles. Also, the type of polydispersity and the degree of it varies with systems. Polydispersity brings variation in the properties of the material and there are specially designed controlled experiments to create monodisperse particles[67, 68]. However, in some cases polydispersity is a desirable property. The size polydispersity is one of the most common types and it has been found that systems beyond certain value of polydispersity, known as the terminal polydispersity are good glass former [69, 70, 71, 72, 73, 46, 74]. It was shown that in a polydisperse system due to an increase in surface free energy, the crystal nucleation is suppressed promoting glass formation [75]. Thus in study of supercooled liquids, polydisperse systems play an important role.

In recent time, it has been shown that structure plays an important role in the dynamics of glass forming supercooled liquids [76, 77, 78, 79, 80, 81, 82]. Since polydisperse systems are good glass former describing the structure of these systems becomes important. For a continuous polydisperse system, the number of species is the number of particles in the system. In this case, describing the system’s partial structure in terms of independent species becomes an impossible task. Thus it is common practice to treat a polydisperse system in terms of an effective one component system[83, 84, 85, 86, 87] . However, it has been shown that we not only lose a large deal of information of the system by pre averaging the structure, the properties of the liquid thus predicted can also give spurious results[88, 89]. Truskett and coworkers[88] have shown that for moderate polydispersity the thermodynamic quantities like the

pair excess entropy obtained from the effective one component radial distribution function (rdf) predicts that with an increase in interaction the static correlation becomes weaker thus predicting structural anomaly. The study showed that when the system is expressed in terms of 60 pseudo neighbors and the excess entropy is calculated in terms of the partial structure factors (radial distribution functions), this structural anomaly disappears. Weysser *et. al.* while working with Mode coupling theory have shown that for a polydisperse system, we need to provide information about the partial structure factors to obtain the correct dynamics [89]. Ozawa and Berthier have highlighted the fact that for a system with continuous size polydispersity the contribution from the mixing entropy term diverges [90]. This makes the calculation of entropy and any other dependent quantity ill-defined. They showed by calculating the inherent structure properties that when the position of the particles with similar sizes is exchanged, the system stays in a similar basin. This modifies the vibrational entropy, which also has the same mixing entropy term. The process allowed them to group particles into a certain finite number of pseudo species leading to a finite value of the mixing entropy. These studies thus emphasize the importance of describing the structure of a polydisperse system in terms of the partial structure factors of the pseudo species.

The present study attempts to develop a general framework to describe the structure of a system having continuous polydispersity. As discussed before, for a system with continuous polydispersity the number of species is the same as the number of particles which makes it difficult to describe the structure. We also know that describing all the particles in terms of a single species does not work. So the aim of this study is to describe the system in terms of  $M$  pseudo species such that the properties of this system are the same as the original system. The questions that we ask are i) Can we determine the minimum number of pseudo species “ $M_0$ ” required to describe the structure of the system? ii) Is this dependent on the property that we study? iii) Does it depend on the degree and nature of polydispersity? iv) Does it depend on the interaction potential?

To answer these questions we use the route of calculating thermodynamic quantities which can be obtained from the structure of the liquid. Namely the potential energy of the system and the pair excess entropy. Note that the former is a linear function of the structure whereas the latter is a nonlinear function of the structure and thus can have different sensitivities to the effective structure. We find that by studying these above mentioned thermodynamical quantities, we can determine a value of  $M_0$ . It depends on the type of polydispersity, the degree of polydispersity, and the interaction potential. We also provide an estimate of the width of polydispersity that can be treated like a one component system. This width appears to depend primarily on the interaction potential of the system. Systems with longer range and softer interaction potential have a better tolerance towards polydispersity. In these cases, systems with a wider spread of size can be addressed in terms of a one component system.

The organization of the rest of the chapter is the following. Section 3.2 contains

the simulation details. Section 3.3 contains results with discussions, and the paper ends with a brief conclusion in Section 3.4.

## 3.2 Simulation details

With continuous size polydispersity in the canonical ensemble, we simulate molecular dynamics for a three-dimensional polydisperse system in this study. The system has a cubic box with a volume of  $V$ , no. of particle in a system ( $N$ )=1000-4000, a number density of system  $\rho = N/V = 1.0$ . We have used periodic boundary conditions and Nosé-Hoover thermostat with an integration timestep  $0.001\tau$ . The time constants for the Nosé-Hoover thermostat are taken to be 100 timesteps. We have carried out the molecular dynamics simulations using the LAMMPS package [91]. For all state points, the equilibration is performed for  $100\tau_\alpha$ , ( $\tau_\alpha$  is the  $\alpha$ - relaxation time). The study involves two different kinds of systems with respect to size polydispersity, constant volume fraction (CVF) and Gaussian along with three different types of interaction potentials (LJ, WCA, and IPL). Chapter 2, Section 2.1.1, provides the details of polydisperse system.

During the analysis, when the system is described in terms of  $M$  species the particles in the diameter range  $(\sigma_{max} - \sigma_{min})/M$  are treated as single species where  $M = 1, 2, 3, \dots$ . Thus for  $M = 1$ , all particles are assumed to have the average value of the diameter.

## 3.3 Result

### 3.3.1 Effective one-component description

As discussed before, it is a common practice to describe the structure of a polydisperse system in terms of an effective one component system.

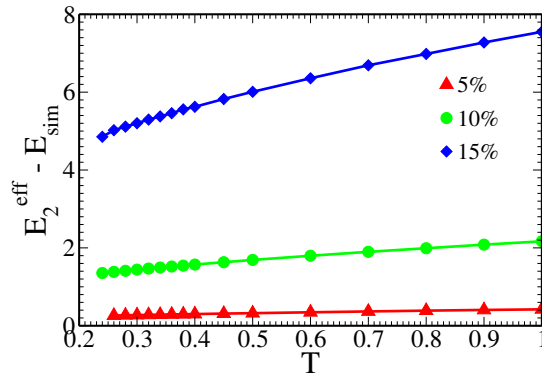


Figure 3.1: The difference in energy obtained from effective one component radial distribution functions,  $E_2^{eff}$  and simulation,  $E_{sim}$  as a function of  $T$  at different PDIs. Here particles are interacting via IPL potential and the particle size distribution is given by  $P_1(\sigma)$  (constant volume fraction distribution).

In Fig.3.1, we plot the difference between the average per particle potential energy of the species agnostic  $E_2^{eff}$  and that obtained from simulation  $E_{sim}$  for systems with different PDI values (5%,10% and 15%). In the simulation study, the particle sizes are obtained from  $P_1(\sigma)$  distribution and they interact via IPL potential. In Fig.3.2 we also plot the  $S_{ex}$  and the species agnostic  $S_2^{eff}$  for the above mentioned systems. Note that if the structure is described properly then  $E_{sim} = E_2$  and  $S_2$  is not exactly equal to  $S_{ex}$  but comprises of 80% of its value [1, 92, 93, 94, 95, 96, 97, 59].

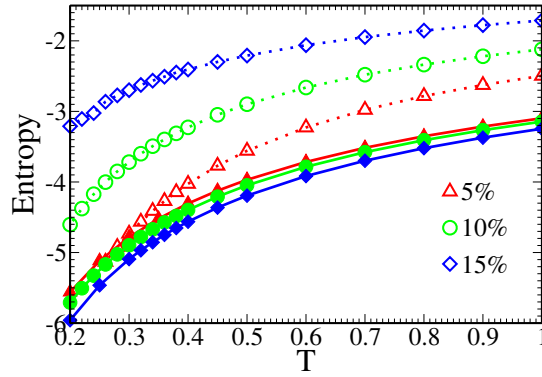


Figure 3.2: *Excess entropy,  $S_{ex}$  and effective one component pair excess entropy,  $S_2^{eff}$  (Eq.2.56) at different PDIs. Solid line with filled symbol represents  $S_{ex}$  and dotted line with open symbol represents  $S_2^{eff}$ . Here particles are interacting via IPL potential and the particle size distribution is given by  $P_1(\sigma)$  (constant volume fraction distribution).*

We find that as the PDI increases the difference between  $E_{sim}$  and  $E_2^{eff}$  (as Eq. 2.39 ) and  $S_{ex}$  and  $S_2^{eff}$  increases. This clearly shows that as expected, with an increase in PDI the effective one component description of the system becomes less accurate. In Fig.3.3 we plot both the dynamics and the effective one component rdf of the systems. We find that within the temperature range studied here although the dynamics remains almost the same, with an increase in polydispersity the structure appears to soften. We have plotted the rdf at two temperatures, ( $T=1.0$  and  $0.5$ ) and it appears that the softening is present in both temperatures. However, the fact that the difference between  $E_2^{eff}$  and  $E_{sim}$  reduces at low temperatures (Fig.3.1) do suggest that the softening also reduces with temperature. This artificial softening of the structure leads to the increase in  $E_2^{eff}$  and  $S_2^{eff}$ . Note that even for 5% polydispersity we find that the effective one component structure of the system fails to provide the correct value of the potential energy and the pair excess entropy. These results presented in Fig.3.1 and Fig.3.2 are not surprising but a confirmation of the observations made earlier [88, 89].

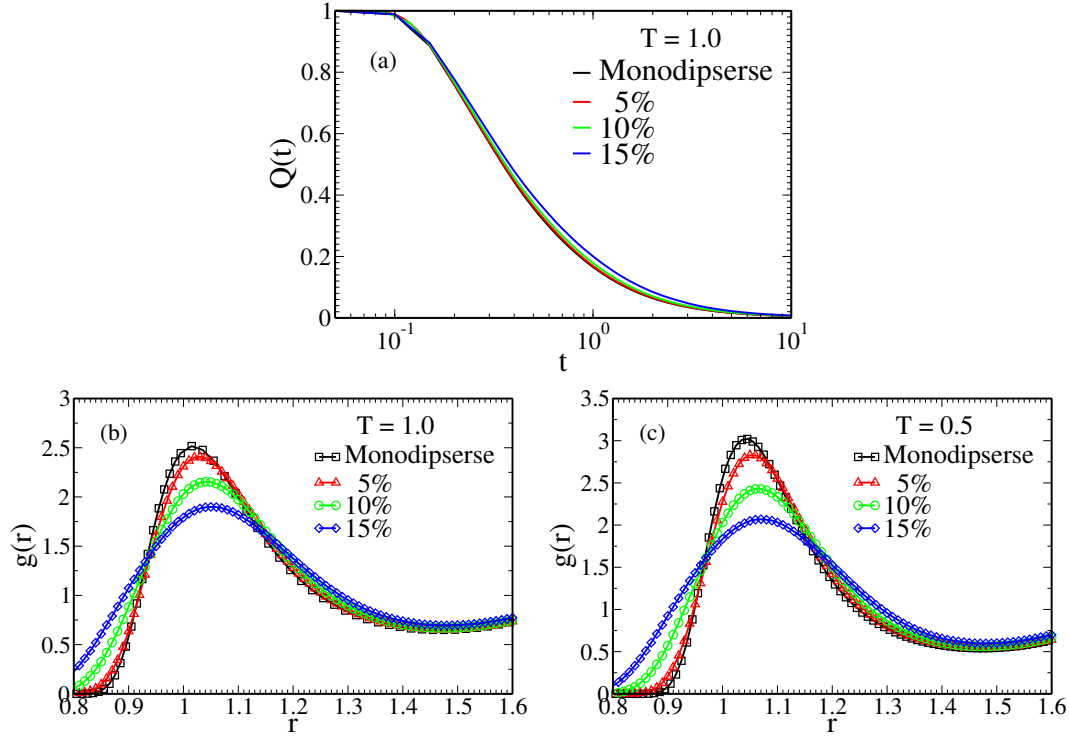


Figure 3.3: (a) Dynamics of systems at different PDIs. The overlap function is plotted against time. (b) Effective one component radial distribution function of the systems at  $T = 1.0$ . (c) Same as Fig.3.3(b) at  $T = 0.5$ . Black square, red triangle, green circle and blue diamond represent a mono disperse system, 5% PDI, 10% PDI and 15% PDI, respectively. With an increase in PDI although the dynamics remains almost the same the structure shows a substantial softening. Here particles are interacting via IPL potential and the particle size distribution is given by  $P_1(\sigma)$  (constant volume fraction distribution).

### 3.3.2 Pseudo species and its dependence on degree of polydispersity

Describing the structure of a continuous polydisperse system can be challenging? Unlike in a discrete polydisperse system where each species has a finite number of particles and all of them have the same size, for a continuous polydisperse system the number of species is the same as the number of particles. However, let us assume that we describe a pseudo system where we divide the particles into  $M$  number of pseudo species (where  $M < N$ ) in terms of the size of the particles. In doing so we bunch particles with similar but different sizes, in a group and assign an average size to them. This introduces disparity in the actual size and the assigned size of the particles and leads to an error in describing the properties of the system. An extreme case of that ( $M = 1$ ) can be seen in Fig.3.1 and Fig.3.2. For a fixed  $M$ , the maximum difference in the actual diameter of a particle and its assigned average diameter is  $\Delta\sigma/2M$ . Thus with an increase in  $M$  this error reduces and at  $M = N$  the pseudo system is exact. So the first question is can we describe the structure of a system in terms of an optimum

number of species  $M_0$ , where  $M_0 \ll N$  such that the structure can provide a correct estimate of the thermodynamic quantities? If we can then how does  $M_0$  depend on the degree of polydispersity?

In Fig.3.4(a) we plot  $\frac{E_2}{E_{sim}}$  as a function of  $M$ , at two different temperatures for the different PDIs. For systems with a fixed value of PDI as we increase the value of  $M$  the  $E_2$  decreases and after a certain value of  $M$ ,  $E_2 \simeq E_{sim}$ . We find that this is weakly temperature dependent. For this work, we consider that at  $T = 1$  the minimum number of pseudo species for which  $\frac{(E_2 - E_{sim})}{E_{sim}} < 0.01$  is  $M_0$ . The value of  $M_0$  is system dependent and as expected increases with the increase in PDI value as can be seen from Fig.3.4(b). Note that while determining  $M_0$  this choice of the relative error (0.01) is arbitrary but practical. In principle, we can choose values much smaller or probably larger than this. However, later, while discussing the value of  $M_0$  as obtained from entropy, we will see that this choice is reasonable.

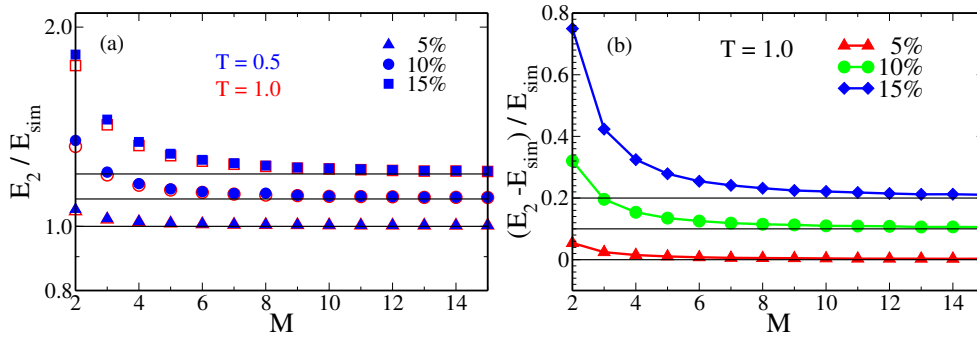


Figure 3.4: Comparison between energy obtain from simulation,  $E_{sim}$ , and energy obtain from partial radial distribution functions,  $E_2$  (Eq. 2.38). (a) Ratio of  $E_2$  and  $E_{sim}$  vs the number of pseudo species  $M$  at  $T = 1.0$  (open red symbols) and  $T = 0.5$  (filled blue symbols) for different PDIs. (b) Relative error calculation between  $E_{sim}$  and  $E_2$ ,  $(E_2 - E_{sim})/E_{sim}$  plotted as a function of  $M$  for different PDIs. For better visualization, we have shifted the y-axis of the 10% PDI plot by 0.1, and 15% PDI plot by 0.2. The horizontal lines signify the corresponding large  $M$  values which are 1.0 for (a) and 0.0 for (b). Here particles are interacting via IPL potential and the particle size distribution is given by  $P_1(\sigma)$  (constant volume fraction distribution).

Is the value of  $M_0$  sensitive to the thermodynamic quantity that we calculate or is it universal? To answer this question we calculate the two body pair entropy for different values of  $M$ . We find that similar to the energy, as  $M$  increases the  $S_2$  comes closer to  $S_{ex}$  (Fig.3.5). However, even for large values of  $M$ ,  $S_2$  is not equal to  $S_{ex}$ . This is because unlike the potential energy which can be exactly calculated in terms of the partial rdf, only a part of the excess entropy can be calculated from the rdf (Eq.2.57) [1, 92, 93, 94, 95, 96, 97, 98]. This makes it difficult to use the same methodology as used for potential energy to make an estimation of  $M_0$  from entropy.

However, from our earlier studies, we know that if the structure of the liquid is described properly then the excess entropy and the two body pair entropy crosses each



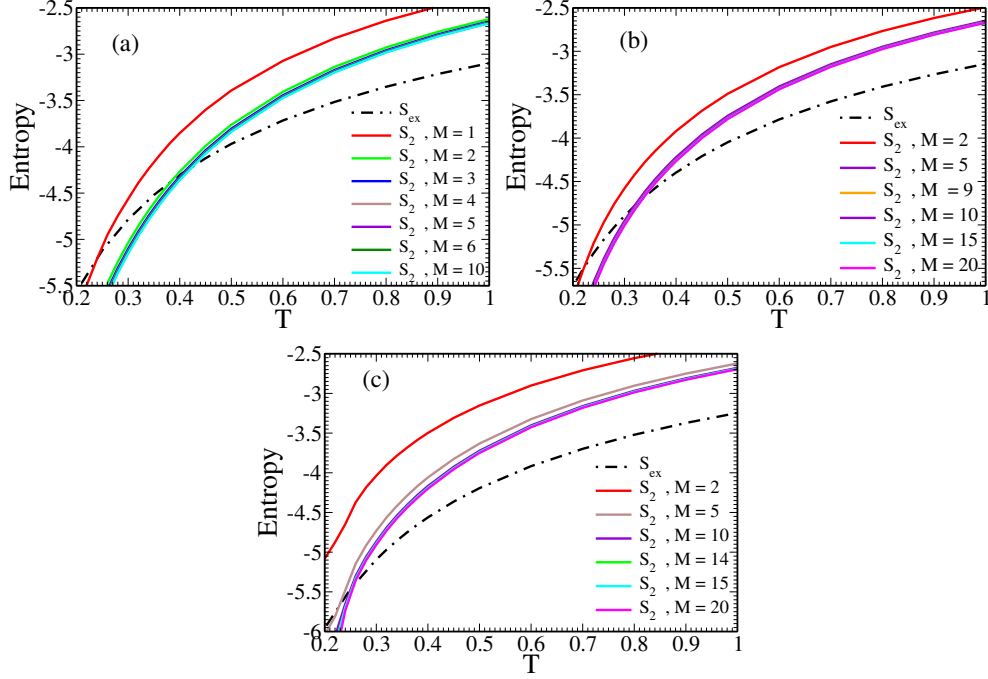


Figure 3.5: *Excess entropy,  $S_{ex}$ , and pair excess entropy  $S_2$ . The latter is calculated at different values of  $M$  (Eq.2.57). Dashed dot line represents  $S_{ex}$  and solid lines represent  $S_2$ . (a) PDI 5% (b) PDI 10% (c) PDI 15%. Here particles are interacting via IPL potential and the particle size distribution is given by  $P_1(\sigma)$  (constant volume fraction distribution).*

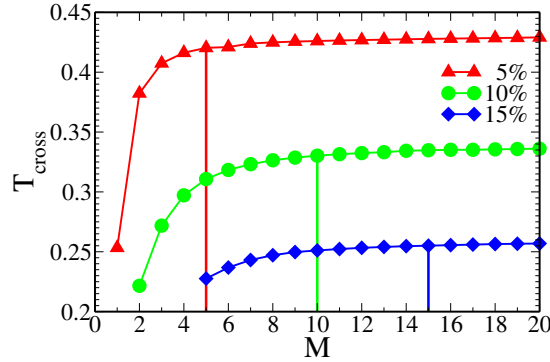


Figure 3.6:  *$T_{cross}$  vs  $M$  plot for different PDIs. Initially,  $T_{cross}$  increases with  $M$  but after certain value of  $M$ , it saturates. For larger PDI the saturation takes place at a higher  $M$  value. The vertical lines give the value of  $M_0$  obtained from energy criteria. Here particles are interacting via IPL potential and the particle size distribution is given by  $P_1(\sigma)$  (constant volume fraction distribution).*

other at a temperature,  $T_{cross}$  which can be considered as the onset temperature of the supercooled liquid dynamics [1]. This onset temperature can also be obtained from the change in the slope of the temperature dependence of the inherent structure energy [3] and also other methods [1]. As shown earlier the values of the onset temperatures obtained using these different methods are not exactly the same but they are in a similar range [1].

In Fig.3.6 we plot the variation of  $T_{cross}$  with  $M$  for the different systems. For higher PDI, at small values of  $M$ , we cannot calculate  $T_{cross}$  which implies that  $S_2$  is far away from  $S_{ex}$  and never crosses it as seen in Fig.3.5. However, from our other estimates of onset temperature, we know that we are in a temperature range where these two forms of entropy should cross. As  $M$  increases the two functions cross at some temperature  $T_{cross}$ . We find that initially  $T_{cross}$  increases with  $M$  and then after a certain value of  $M$  it shows a saturation. As mentioned before  $S_2$  is not the total excess entropy of the system. There is no other method of calculating  $S_2$ . Thus it is not possible to do a similar error estimation of pair excess entropy as done for the potential energy. However, the saturation of  $T_{cross}$  is an indication of the saturation of  $S_2$  w. r. t.  $M$ . We find that this saturation value of  $T_{cross}$  is in a similar range as the estimated onset temperature using the method of inherent structure energy (see Sec III E and Table 3.1). In this plot we also mark the  $M_0$  values as obtained from the potential energy. We find that the  $M$  value for which  $T_{cross}$  saturates falls in the similar range as  $M_0$ . The values of  $T_{cross}$  at  $M = M_0$  and the  $T_{onset}$  are given in Table 3.1. Thus we show that the minimum number of pseudo species required to describe the potential energy of the system can also describe the two body excess entropy of the system. Note that although with  $M_0$  pseudo species we can get a reasonable value of  $S_2$ , this quantity is not the total excess entropy of the system. The residual multi-particle entropy (RMPE) defined as the difference between the total excess entropy and the pair excess entropy,  $S_{ex} - S_2$  although has a small value when compared to  $S_2$ , plays an important role in describing the thermodynamics of the system. For example, it has been observed that if we ignore RMPE then the correlation between dynamics and thermodynamics expressed via the well known Adam-Gibbs relation does not hold [99]. It has also been observed that in the supercooled liquid regime RMPE provides us a measure of the activated dynamics of the system [80, 99]. Thus although the pseudo species description provides us a reasonable estimation of  $S_2$ , care should be taken while using this quantity in describing the full thermodynamics of the system.

The details of the  $M_0$  values for the different systems are given in Table 3.1. We also tabulate a quantity  $\Delta\sigma_0 = \frac{\Delta\sigma}{M_0}$ . We find that although  $M_0$  is dependent on the PDI this quantity  $\Delta\sigma_0$  is not. Note that when  $M = M_0$ , the maximum error in assigning a diameter to a particle is  $\frac{\Delta\sigma_0}{2}$ . Thus our study suggests that the thermodynamic properties of the system studied here are not sensitive to a change in diameter by  $\frac{\Delta\sigma_0}{2}$  and for a constant volume fraction polydisperse system interacting via IPL potential when  $\Delta\sigma \approx 0.036$  we can treat it as a monodisperse system.

Interestingly we find that when we plot the partial rdf for two consecutive pseudo species,  $g_{11}(r)$  and  $g_{22}(r)$  (here these two species 1 and 2 have the largest and the second largest number of particles, respectively) for different values of  $M$  then for  $M = M_0$  the peaks of the two rdfs almost overlap (Fig.3.7). Thus we can say that when the size difference of the two consecutive species are such that there is a large overlap between the radial distribution functions of two consecutive species then they

can be treated as a single species.

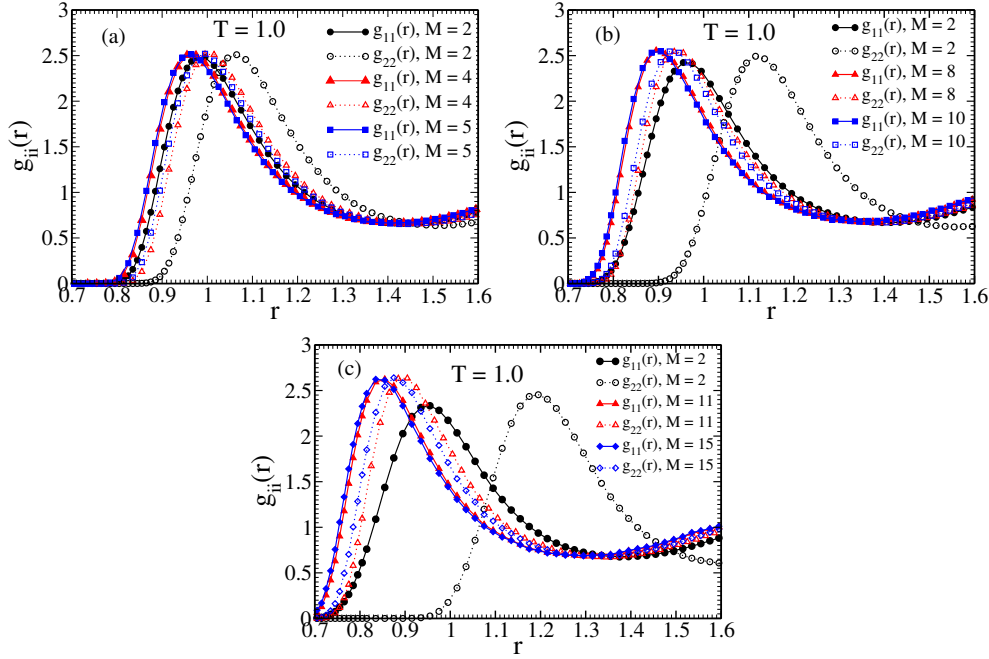


Figure 3.7: The partial radial distribution function for the first two species for different values of  $M$ . (a) PDI 5% (b) PDI 10% (c) PDI 15%. For  $M = M_0$  the rdf peak of the two consecutive species almost overlap. Here particles are interacting via IPL potential and the particle size distribution is given by  $P_1(\sigma)$  (constant volume fraction distribution).

Table 3.1: The values of  $M_0$  and  $\Delta\sigma_0$  for different systems. We also provide the values of  $T_{cross}$  at  $M = M_0$  and for comparison we give the  $T_{onset}$  values obtained from fitting the Inherent structure energy to two straight lines.

Distribution	Potential	PDI %	$M_0$	$\Delta\sigma_0 = \frac{\Delta\sigma}{M_0}$	$T_{cross}(M_0)$	$T_{onset}$
$P_1(\sigma)$	IPL	5%	5	0.036	0.42	0.43
		10%	10	0.036	0.33	0.36
		15%	15	0.036	0.26	0.31
$P_2(\sigma)$	IPL	5%	7	0.043	0.43	0.46
		10%	14	0.043	0.35	0.34
		15%	21	0.043	0.28	0.30
$P_1(\sigma)$	WCA	15%	20	0.027	0.58	0.7
	LJ	15%	12	0.045	0.67	0.81

### 3.3.3 Effect of the type of distribution on $M_0$ and $\Delta\sigma_0$

We next study the effect of the type of distribution on  $M_0$  and  $\Delta\sigma_0$ . In Fig.3.8 we compare the  $M$  dependence of  $T_{cross}$  for systems where polydispersity is described in terms of  $P_1(\sigma)$  (constant volume fraction) and  $P_2(\sigma)$  (Gaussian), for three different

PDI. In the same plot the  $M_0$  values as obtained from the potential energy are also marked.

At the same PDI, the nature of saturation of  $T_{cross}$  and also the value of  $M_0$  are different for the two different distributions. Compared to the constant volume fraction distribution, the values of  $M_0$  are higher for the Gaussian distribution. The reason behind this can be understood by comparing Fig.2.1 and Fig.2.2 (also see Table 2.1). For the same PDI, the Gaussian distribution is wider compared to the constant volume fraction distribution. A closer observation tells us that the saturation of  $T_{cross}$  is better for the CVF distribution when compared to the Gaussian distribution. Note that for the Gaussian distribution  $M_0$  is higher (more number of species), and by nature towards the tail of the distribution the number of particles is less so the partial rdf for the largest and the smallest species are poorly averaged. We have seen that with an increase in system size the saturation improves (not shown here).

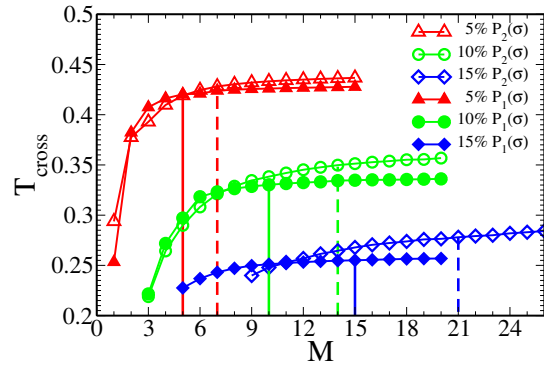


Figure 3.8: *The effect of the type of distribution on  $M_0$ .  $T_{cross}$  vs  $M$  plot for different PDIs for systems where particles are interacting via IPL potential and the particle size distribution are given by  $P_1(\sigma)$  (constant volume fraction distribution) and  $P_2(\sigma)$  (Gaussian distribution). The vertical lines give the value of  $M_0$  obtained from energy criteria (solid lines for  $P_1$  and dashed lines for  $P_2$  distribution). At the same value of PDI for the Gaussian distribution the  $M_0$  is higher and  $T_{cross}$  saturates at a higher  $M$  value.*

We find that when compared to CVF distribution, the  $\Delta\sigma_0$  is marginally higher for the systems with Gaussian distribution (see Table 3.1). Note that we divide a continuous polydisperse system into  $M$  species in a way that the difference in diameter of two consecutive species is always separated by  $\frac{\Delta\sigma}{M}$ . This implies that the percentage error in calculating the size of the smaller particles are higher than that of the larger particles. Also, note that in constant volume fraction distribution the smallest particles are the largest in number thus by construction the error is maximum for the dominant species. On the other hand for the Gaussian distribution, the place where the percentage error is maximum the population of particles are the minimum. Thus compared to the Gaussian distribution for continuous volume fraction we need to go to marginally smaller values of  $\Delta\sigma_0$ . A way to increase  $\Delta\sigma_0$  (decrease  $M_0$ ) in CVF distribution can be to have a size dependent bin width such that the percentage error in describing the size of a smaller particle is the same as that of a larger particle.

### 3.3.4 Effect of interaction potential on $M_0$

Next, we study the role of interaction potential on the value of  $M_0$  (also  $\Delta\sigma_0$ ) and the saturation of  $T_{cross}$ . For this we study  $P_1(\sigma)$  system, with PDI=15% and vary the interaction potential between the particles (IPL, WCA, and LJ). The parameter values are given in Table 3.1. When we compare the IPL, WCA and LJ systems we find that  $M_0$  value is higher for the WCA system and also the  $T_{cross}$  of the WCA system appears to saturate at a higher  $M$  value (see Fig.3.9). This suggests that  $\Delta\sigma_0$  for the WCA potential is smaller than the LJ and the IPL systems (see Table.3.1).

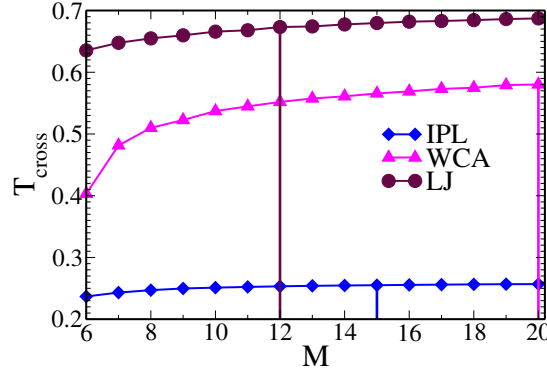


Figure 3.9: Role of interaction potential on  $M_0$ .  $T_{cross}$  vs  $M$  plot for 15% PDIs for systems where particles are interacting via IPL, WCA and LJ potential and the particle size distribution are given by  $P_1(\sigma)$  (constant volume fraction distribution). The vertical lines give the value of  $M_0$  obtained from energy criteria. The value of  $M_0$  is higher for WCA potential and the  $T_{cross}$  also saturates at higher value of  $M$ .

To understand the origin of this lower tolerance of the WCA system in Fig.3.10 we plot for the WCA system the partial rdfs of the first two species for different values of  $M$  and find that compared to the IPL system we need to go to higher values of  $M$  to observe a good overlap between the two rdfs. Similar to that found for the IPL system, at  $M = M_0$  the rdf peaks almost overlap. Note that compared to the WCA potential the IPL potential is softer and has a longer range. Thus compared to the WCA system the IPL system has a flatter rdf and a larger overlap of the rdfs of two consecutive species. This definitely explains why compared to the IPL system the  $M_0$  is higher for the WCA system.

In Fig.3.11 we compare the rdf values for the first two species of the IPL, WCA and LJ systems, for  $M = 15$ . Note that for the IPL and the LJ systems  $M_0 \leq 15$  and for the WCA system  $M_0 > 15$ . However, compared to the WCA and IPL systems, the partial rdfs for the LJ system are more sharply peaked. This does not explain why the  $M_0$  for the LJ system is smaller than the WCA system. Note that the structure along with the interaction potential describes both the potential energy and also the two body entropy. In  $S_2$  the leading term is  $-g(r) \ln g(r) \simeq g(r)U(r)$  where  $U(r) = -\ln g(r)$  can be considered as the effective potential of the system. Thus along with the rdf the interaction potential also plays a role in determining these

thermodynamic quantities. The range of the LJ potential is much larger compared to the IPL and WCA potentials. Moreover, the attractive part of the potential which provides a dominant contribution also varies much more smoothly compared to the WCA and IPL potentials. It appears that this slow variation of the potential increases the tolerance of thermodynamic quantities w.r.t the particle size which leads to a smaller  $M_0$  value.

We will like to mention that in this work while working with the LJ system we only vary the size of the particles while keeping the interaction energy constant. This choice is quite similar to that used in earlier studies of model polydisperse systems [74, 100, 101]. However, this choice of system is not consistent with the van der Waals attraction dependence on particle volume. Thus the system can have some unusual structures like that of clustering of smaller particles observed earlier [101]

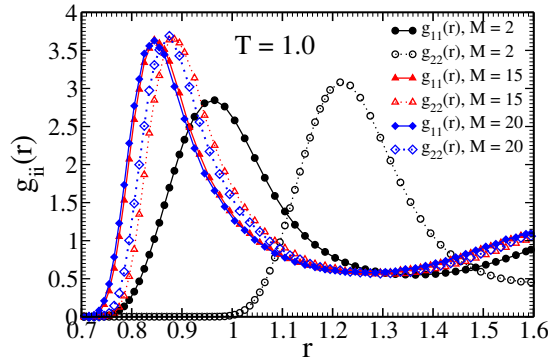


Figure 3.10: The partial radial distribution function for the first two species for different values of  $M$ . The particles are interacting via WCA potential and the polydispersity of the system is described by  $P_1(\sigma)$  with 15% PDI.

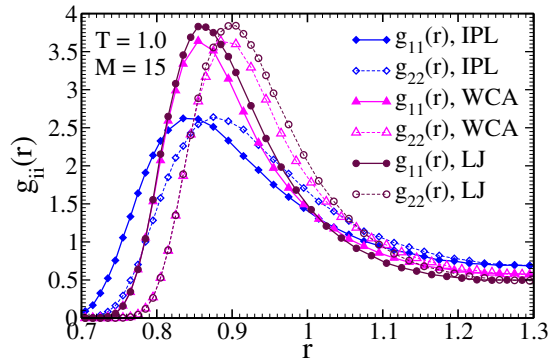


Figure 3.11: The partial radial distribution functions for the first two species for IPL, WCA and LJ potentials for  $M = 15$ . The size distribution of the particles is given by  $P_1(\sigma)$  with 15% polydispersity.

### 3.3.5 System size dependence

Note that for finite number of particles ( $N$ ) in the system, we can still describe the  $N * N$  partial structure factors. However in the thermodynamic limit when  $N \rightarrow \infty$

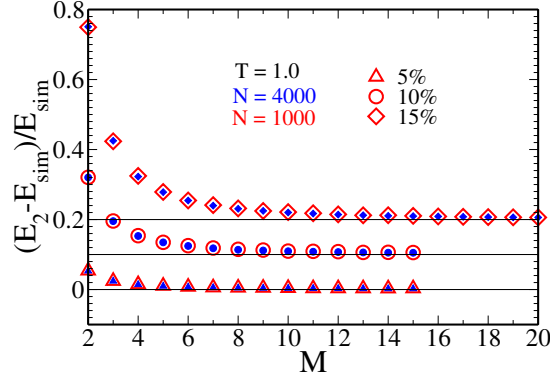


Figure 3.12: System size dependence of relative error calculation between  $E_{sim}$  and  $E_2$ .  $(E_2 - E_{sim})/E_{sim}$  plotted as a function of  $M$  for different PDIs for  $N = 1000$  (red open symbols) and  $N = 4000$  (blue filled symbols). For better visualization, we have shifted the y-axis of the 10% PDI plot by 0.1 and 15% PDI plot by 0.2. The horizontal lines signify the corresponding zero values.

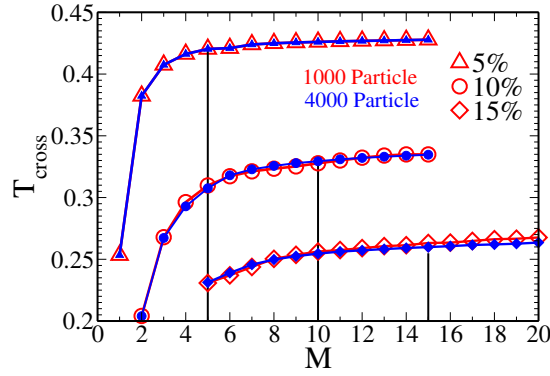


Figure 3.13: The system size dependence of  $M_0$ .  $T_{cross}$  vs  $M$  plot for different PDIs for systems where particles are interacting via IPL potential and the particle size distribution are given by  $P_1(\sigma)$ . The open red symbols are for  $N=1000$  and the filled blue symbols are for  $N=4000$ . The vertical lines give the value of  $M_0$  obtained from energy criteria.  $M_0$  from energy is independent of system size and for systems with higher PDI the  $T_{cross}$  saturates better for higher system size.

this becomes ill-defined. Thus for larger systems describing the system in terms of pseudo species becomes even more important. In this section, we study the system size dependence of  $M_0$ . For this study, we take the system where particle size distribution is given by  $P_1(\sigma)$  and the particles interact via IPL potential. We study three systems at 5%, 10% and 15% PDI. In Fig.3.12 we plot the  $\frac{(E_2 - E_{sim})}{E_{sim}}$  for systems with 1000 and 4000 particles. We find that the relative error in energy is independent of the system size and so is  $M_0$ . In Fig.3.13 we plot the  $T_{cross}$  values for the two different system sizes. We find that for 5% and 10% PDI they overlap and for 15% PDI the bigger system size predicts a better saturation of  $T_{cross}$ . This is because we now have a larger number of particles in each species giving rise to better averaging. Thus we can say that  $M_0$  is independent of system size.

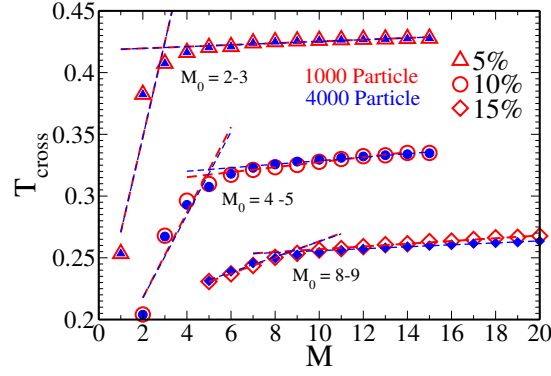


Figure 3.14: *Alternate definition of  $M_0$ .  $T_{cross}$  vs  $M$  has two different regimes, low  $M$  shows growth and high  $M$  shows a near saturation. The two different regimes are fitted to two straight lines and the  $M$  value where these lines cross is identified as  $M_0$ . The open red symbols are for  $N=1000$  and the filled blue symbols are for  $N=4000$ . The  $M_0$  values thus obtained are smaller than that obtained from energy criteria and similar to that obtained by Ozawa and Berthier [90]*

### 3.3.6 Mutual information and radial distribution function

We have used the correlation between the total excess entropy and its two body counterpart to determine the optimum number of species required to describe the system [66]. We will now show that this method is similar in spirit to the calculation of mutual information (MI) between the species and their structure [102].

The temperature dependence of  $S_2$  changes with  $M$ , and this also changes the  $T_{cross}$  value. As shown in Fig.3.15, as a function of the number of species  $M$ ,  $T_{cross}$  first increases and then almost saturates at a value. This saturation value is similar to the onset temperature obtained from other methods [1, 3, 66]. The saturation of  $T_{cross}$  implies that the structure/rdf does not change considerably when an even larger number of species is used to describe the system. Thus this provides us with information on the optimum number of species,  $M = M_0$  required to describe the system.

Interestingly our formalism is similar in spirit to the formalism suggested recently using mutual information (MI) theory, the difference in two body entropy when the system is expressed as a single species and as  $M$  species can be approximately written as [102],

$$\Delta S_2 \simeq \sum_{k=1}^M \int_0^R 4\pi r^2 \rho \chi_k g_k(r) \ln \left( \frac{g_k(r)}{g(r)} \right) dr \quad (3.1)$$

where  $g_k(r)$  is the rdf of the  $k^{th}$  species and the total rdf  $g(r) = \sum_k \chi_k g_k(r)$ . Coslovich *et.al.* beautifully argued that this difference in two body entropy is similar to the MI [102]. From Eq. 3.1, we notice that in this formalism, the probability distribution in the MI is replaced by the radial distribution function, which is the probability of finding a particle at a distance  $r$  from a central particle over and above the ideal gas prediction. Thus this formalism, instead of using the bare probability of finding a particle, is based



on the probability of finding particles at certain interparticle distances.

In Fig.3.15 along with  $T_{cross}$  we also plot  $\Delta S_2$  as a function of  $M$  for systems with 7% and 15% polydispersities. Both quantities are scaled by their respective saturation values at high  $M$ . We find that both show similar  $M$  dependence. Ideally, the peak in the  $\Delta S_2$  vs  $M$  plot should describe the optimum value of  $M$ . However, there is no such peak, but just like  $T_{cross}$ , the  $\Delta S_2$  value increases sharply with  $M$  and then shows saturation. Note that MI is large when the distribution between two species is well segregated. However, the rdf of two consecutive species overlap. This may be the reason the entropy difference does not show a peak. Results shown in Fig.3.15 clearly suggest that for these systems, the structure and any quantity that need structure as an input must be described by dividing the particles into a certain optimum number of species, and this division is going to increase the MI.

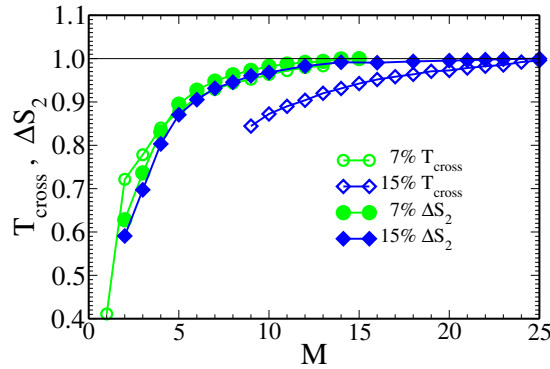


Figure 3.15: Scaled MI of  $\Delta S_2$  and  $T_{cross}$  [66] saturated at same  $M$ . scaling is done by dividing the  $\Delta S_2$  and  $T_{cross}$  value by there respective saturation value at high  $M$ .

### 3.3.7 Comparison with earlier predictions

Next, we compare our results with that of Ozawa and Berthier (OB) [90]. The goal of both studies is to find an effective number of pseudo species that can describe a polydisperse system. However, the methodologies are quite different. We work with the partial rdf of the liquid and use them to calculate the excess entropy and total energy near the onset temperature. Ozawa and Berthier used the information of the vibrational entropy and the inherent structure properties and the study was performed below the MCT transition temperature. They divided the system into  $M$  species and then swapped particles within a species. After  $N$  such swaps, they minimized the system and obtained the mean square displacement (MSD) between the original equilibrium configuration and swapped configuration. The MSD as a function of  $M$  initially decreased with increasing  $M$  and showed saturation at high values of  $M$ . They fitted these two regimes to two different power laws, and the intersection point of the power laws determined the value of  $M_0$ . In their study they have calculated the value of  $M_0$  for an IPL potential system with  $P_1(\sigma)$  distribution at 23% PDI. They then

extrapolated the value of  $M_0$  for smaller PDIs. For 10% PDI they predicted a value of  $M_0 = 4 - 5$  and for 5% PDI,  $M_0 = 2 - 3$ . We can do a similar exercise with  $T_{cross}$ . In Fig.3.14 we show that  $T_{cross}$  also shows two different regimes. We fit the two different regimes to two straight lines and the point where they cross is,  $M_0 = 2 - 3$  for 5% PDI,  $M_0 = 4 - 5$  for 10% PDI, and  $M_0 = 8 - 9$  for 15% PDI. Interestingly these numbers are surprisingly the same as that extrapolated by Ozawa and Berthier [90] although the two methodologies are completely different. However, these values of  $M_0$  are lower than our earlier prediction which was made by looking at the saturation point of  $T_{cross}$ . In the OB study if they define the  $M_0$  at the value where their MSD becomes independent of  $M$  then they too will have a higher value of  $M_0$ .

We next compare our predictions with an earlier work which involved the study of the dynamics [89]. As discussed in the Introduction, Weysser *et al* studied the effect of polydispersity on the dynamics [89]. They studied a system with constant polydispersity where  $\Delta\sigma = 0.2$ . According to their study, the dynamics can be well explained when the system is divided into 5 pseudo species and thus  $\Delta\sigma_0 = 0.04$  falls in a similar range as predicted here and so is  $M_0$ .

At this point, we cannot comment on which will be a better choice of  $M_0$ , the value at which  $T_{cross}$  saturates or the value at which two different regimes intersect. When we compare our result with the study using the dynamics [89] it appears that the former which leads to higher values of  $M_0$  is a better choice whereas if we compare with OB study then the latter seems to be a better choice. It is possible that the dynamics is more sensitive to change in  $M_0$ . This suggests that further studies are required to narrow down the value of  $M_0$ . One such option will be to see how the configurational entropy for different values of  $M_0$  correlates with the dynamics.

### 3.4 Conclusion

In this work we attempt to develop a framework to describe the structure of systems with continuous polydispersity. The study involves systems where the polydispersity is described in terms of different distributions (constant volume fraction and Gaussian) and the degree of polydispersity is varied. We also study the effect of the interaction potential.

We exploit the fact that the potential energy and the pair excess entropy can be described in terms of the partial radial distribution functions. First, we describe the system in terms of pseudo species. In the case of potential energy, we obtain the minimum number of pseudo species,  $M_0$  required to match the energy obtained from the partial rdf with that obtained from the simulation. For the entropy part, since the excess entropy and pair excess entropy are never equal, we calculate the temperature where they cross each other. Our earlier study has shown that this  $T_{cross}$  is an estimate of the onset temperature of supercooled liquids[1]. We show that for a smaller number of species, the  $T_{cross}$  varies with  $M$  and as a function of species this temperature shows

a saturation, suggesting a saturation of the pair excess entropy w.r.t  $M$ . This gives us a second estimation of  $M_0$  which we find is similar to that obtained from the potential energy.

Our study reveals that for a given system, it is possible to define a parameter  $\Delta\sigma_0$  which gives the limiting width of the size distribution that can be treated as a monodisperse system. This limiting value primarily depends on the interaction potential. The softer the interaction potential the larger is the value of  $\Delta\sigma_0$ . Depending on the type of distribution this limiting width  $\Delta\sigma_0$  translates into different values of PDI.

For a 1% PDI system with constant volume fraction distribution,  $\Delta\sigma = 0.036$  and with Gaussian distribution,  $\Delta\sigma = 0.06$ . When we compare these values with  $\Delta\sigma_0$ , we can say that polydispersity greater than 1% when treated as an effective monodisperse system will not provide us with the correct structure of the liquid. This implies that when the effective one component structure is used to study the influence of polydispersity on some property, we have to be careful in decoupling the effect of this artificial softening of the structure from the actual effect of the polydispersity. Note that  $M_0$  and  $\Delta\sigma_0$  are independent of the system size. This makes this pseudo neighbour description of a system more useful for larger systems.

After showing that for a polydisperse system, the correct structural description is obtained only when the system is expressed in terms of multiple species,  $M$ . We show that our method also leads to an increase in the mutual information, thus validating the method further.

# Chapter 4

## Dynamic heterogeneity in polydisperse systems: A comparative study of the role of local structural order parameter and particle size

“In the laboratory of life, wrong turns often lead to the most groundbreaking discoveries”.

- Alexander Fleming

### 4.1 Introduction

When a liquid is cooled fast enough, it enters the supercooled liquid regime, where the properties of the liquid are very different from that of the normal liquid regime. When the supercooled liquid approaches the glass transition, its dynamics increases by orders of magnitude [4, 17], with the structure showing marginal changes. This observation questioned the role of structure in the dynamics and the application of the liquid state theories [103, 104, 10] in the supercooled regime. However, studies have shown that although the structure does not change drastically, static properties which depend on the structure can change enough to affect the dynamics [79, 105, 82]. One of the key signatures of supercooled liquid is the dynamical heterogeneity which increases with a decrease in temperature [25, 106, 53]. There have been a large number of studies attempting to causally connect this dynamical heterogeneity and local order parameter, some of the order parameters being purely structural in origin [107, 108, 109, 110, 111, 102, 112, 113, 82, 114]. In recent studies, we have defined a structural order parameter (SOP) that is connected to the depth of the mean-field

caging potential [82, 114]. Our study has shown that for a large number of systems, the SOP is a good parameter to describe the relaxation process in the systems [82]. We have also shown that this causality persists even at the local level [114]. The distribution of the particle level SOP becomes wider at lower temperatures, thus suggesting an increase in the local structural heterogeneity. The correlation between the SOP and the dynamics at the particle level is observed only below the onset of the glassy dynamics,  $T_{onset}$ , and increases as the temperature is decreased. Thus, according to this study, the structural heterogeneity and the coupling between the SOP and dynamics increase at lower temperatures. [114].

Given the good predictive power of this new structural order parameter, it should be tested for other glass-forming liquids. Amongst systems that are good glass formers, polydisperse systems with size polydispersity come high in the order [101, 69, 115, 116, 117, 118, 119, 120]. Polydisperse systems beyond some degree of polydispersity can be easily supercooled [69, 70, 71, 72, 73, 46, 74] and most experimental colloidal systems are polydisperse [121, 122, 123, 124, 125, 126, 126, 127]. Moreover, the swap Monte Carlo algorithm, which allows the system to be cooled to unprecedentedly low temperatures, is best applied to polydisperse systems with continuous size polydispersity [128, 129, 130, 90, 131, 132, 133].

However, for a system with continuous size polydispersity describing the structure and any parameter which depends on the structure is a challenge. For these systems, the number of species,  $M$  equals the total number of particles. Many a time, these systems are treated like a monodisperse system ( $M = 1$ ), and the average structure/radial distribution function (rdf) shows an artificial softening [66, 100, 74, 134]. Thus any property calculated using the rdf does not show the correct value. Depending on the diameter of the particles, we can always approximately describe the system in terms of a certain number of species. However, what is the optimum number of species,  $M = M_o$  needed to describe the properties of the system is a question often asked [100, 90, 88, 66]. In earlier work, we used the correlation between the total excess entropy of the system, and its two-body counterpart, which needs the information of the rdf, to obtain the optimum number of species,  $M = M_o$  [66]. The method is quite simple and much less computer intensive but provides similar results as obtained from the study of the configurational entropy using diameter permutation [90]. In previous chapter we have also shown that our method of describing the system into multiple species increases the mutual information of the system.

In this chapter we will show that the SOP and its correlation with the dynamics depend on  $M$ . It was earlier shown that the correlation between SOP and dynamics helps us to identify  $T_{onset}$  [114]. Since the SOP and its correlation varies with  $M$ , so does the  $T_{onset}$ . Similar to our earlier study [66], the  $T_{onset}$  first changes with  $M$  and then saturates. This clearly suggests that for a polydisperse system, for the calculation of the SOP, the system needs to be described in terms of multiple species. However, to our surprise, we find that the correlation between the SOP and the dynamics is

maximum for  $M = 1$ . Further study reveals that at low polydispersity, the SOP is a good predictor of the dynamics but at high polydispersity, the size of the particle plays a dominant role in determining the dynamics. Moreover, the SOP and the size are also correlated, and this correlation increases with an increase in polydispersity and decreases with an increase in  $M$ . Thus at high polydispersity and for  $M = 1$  where the SOP and the particle size are strongly correlated, the SOP appears to be strongly correlated with the dynamics. However, this does not depict the true correlation and is mediated by the particle size. We also study Vibrality, another order parameter independent of the system's structure. We find that at high polydispersity, compared to the SOP, the Vibrality has an even stronger correlation with the particle size. Thus it appears to be a better predictor of the dynamics. These results clearly suggest that for systems with high polydispersity, any local order parameter correlated with the particle size might appear to be a good predictor of the dynamics and these results should be cautiously interpreted and not assumed to be a generic result.

The organization of the rest of the chapter is the following. Section 4.2 contains the simulation details. In section 4.3, we present the calculation of the caging potential in a polydisperse system. In section 4.4, we discuss the species dependence of the caging potential. In section 4.5, we discuss the species dependence of the correlation of the SOP and the particle dynamics. In section 4.6, we analyze the dynamics of the particles having soft and hard SOP. In section 4.7, we do a comparative analysis of the role of particle size and SOP in the dynamics. The chapter ends with a brief conclusion in Section 4.8. This chapter contains 3 Appendix sections at the end.

## 4.2 Simulation Details

For this study, we have performed 3-dimensional MD simulations (using LAMMPS package [91]) for polydisperse systems in a canonical (NVT) ensemble.  $N = 4000$  particles are present in a cubic box with volume  $V$  and density  $\rho = \frac{N}{V} = 1.0$ . We have used periodic boundary conditions (pbc) for the simulation. Nosé-Hoover thermostat with integration timestep  $0.001\tau$  and 100 timesteps as time constants are taken in this simulation. The study involves the Gaussian type of size distribution for continuous size polydispersity. This means each of the  $N$  particles has a different radius.

For all the polydisperse systems, the particle sizes are chosen such that  $\langle \sigma \rangle = \int P(\sigma)\sigma d\sigma = 1$ . In this study, particle  $i$  and  $j$  interact via inverse power law potential (IPL). The interaction strength between two particles  $i$  and  $j$  is  $\epsilon_{ij} = 1.0$ .  $\sigma_{ij} = \frac{(\sigma_i + \sigma_j)}{2}$ , where  $\sigma_i$  is the diameter of particle  $i$ . Length, temperature and time are given in units of  $\langle \sigma \rangle$ ,  $\epsilon_{ij}$  and  $\left(\frac{m\langle \sigma \rangle^2}{\epsilon_{ij}}\right)^{\frac{1}{2}}$  respectively. For all state points, the equilibration is performed for  $100\tau_\alpha$  ( $\tau_\alpha$  is the  $\alpha$ -relaxation time, details given in Appendix I)[66]. During the analysis, when the system is described in terms of  $M$  species the particles in the diameter range  $(\sigma_{max} - \sigma_{min})/M$  are treated as single species where  $M = 1, 2, 3, \dots$ . Thus for  $M = 1$ , all particles are assumed to have the average value of the diameter.

Details of polydisperse system is given in Section 2.1.1

Since these systems are not that well known, we provide information on the different characteristic temperatures of the systems in Appendix - I

### 4.3 Computing local caging potential

In a recent study, we have described a structural parameter that describes the local caging potential [82, 114]. We have also shown that for the KA model, the softness of this potential and the short-time dynamics are causal [114]. The computation of the local caging potential requires information on the radial distribution function. As discussed in the previous section, the radial distribution function of a system with continuous polydispersity depends on the number of species we divide the particles of the system into. Extending our earlier work, the average depth of the mean-field caging potential for a system with  $M$  species can be written as [114],

$$\beta\Phi_r^{av}(\Delta r = 0) = -\rho \int dr \sum_{u=1}^M \sum_{v=1}^M C_{uv}(r) \chi_u \chi_v g_{uv}(r) \quad (4.1)$$

where  $\beta = \frac{1}{k_B T}$ ,  $k_B = 1$ ,  $\rho$  is a density, and  $r$  denotes the distance between the central tagged particle and its neighbors.  $\Delta r$  is the distance of the tagged particle from its equilibrium position.  $C_{uv}(r)$  is the direct correlation function and, according to the Hypernetted chain approximation, can be written as [10],

$$C_{uv}(r) = -\beta U_{uv}(r) + [g_{uv}(r) - 1] - \ln[g_{uv}(r)] \quad (4.2)$$

where  $U_{uv}$  is the interaction potential. It was shown that the depth of the potential is inversely proportional to the curvature and thus the softness parameter [82, 114]. Please note that we consider the depth of the caging potential as an energy barrier, and thus we work with the absolute magnitude of the caging potential (given by Eq 4.1).

For the microscopic analysis, we need to calculate  $\beta\Phi_r(\Delta r = 0)$  for every snapshot at a single particle level. This is given by Eq. 4.1 where the rdf and the direct correlation function,  $C_{uv}(r)$  are now obtained at the single particle level. The single particle partial rdf in a single frame can be expressed as a sum of Gaussian, and it is calculated as: [55]

$$g_{uv}^i(r) = \frac{1}{4\pi\rho r^2} \sum_j \frac{1}{\sqrt{2\pi\delta^2}} \exp^{-\frac{(r-r_{ij})^2}{2\delta^2}} \quad (4.3)$$

where  $\delta$  is the variance of the Gaussian distribution used to make the discontinuous function a continuous one. In this work, we assume  $\delta = 0.09 < \sigma >$ . The direct correlation function can also be calculated at the single particle level using Eq. 4.2 but with single particle rdf. At higher PDI, when the system is described by one

species, the rdf shows a large softening and is non-zero at very small values of 'r' compared to the interaction potential. Thus any function that calculates the product of the potential and rdf incurs a large error[66]. This error is higher for repulsive potential and increases with PDI (as shown in Appendix II). In our calculation of the potential depth, such products lead to unphysical large positive values of the caging potential. This implies an unstable potential and negative curvature /softness parameter. Note that this is an artificial effect. To overcome this problem, we have made one approximation. We assume that the potential of mean force is the same as the interaction potential *i.e.*  $-\beta U_{uv}(r) = \ln[g_{uv}(r)]$  and  $C_{uv}^{approx}(r) \approx [g_{uv}(r) - 1]$ . For smaller polydispersity where the error due to softening of the rdf is less and we can compute physically meaningful caging potential by assuming all three terms in the direct correlation function, we have compared our theoretical prediction with total and approximate direct correlation functions. As discussed in Appendix II, although the absolute value of the caging potential is different, the prediction of the correlation of the dynamics and softness parameter remains the same. Thus, in this work, we use the approximate direct correlation function  $C^{approx}(r)$  at the single particle level to avoid unphysical results of the caging potential at higher PDI.

The inverse of the depth of the caging potential is related to the softness, but they are not the same [114]. There are some system dependent but temperature independent constants that are needed for the calculation of the absolute value of softness but not its correlation with the dynamics [135]. In this work, we will seamlessly use the term “inverse” of the depth of the caging potential and the “softness” of the caging potential as they are qualitatively the same.

## 4.4 Species dependence of the caging potential

First, we assume the systems to be monodisperse *i.e.*  $M = 1$  and obtain the per particle depth of the caging potential from the microscopic version of Eq.4.1. As shown in Fig.4.1 for all the systems, with a decrease in temperature, there is a shift of the probability distribution of  $\beta\Phi_r(\Delta r = 0)$  to higher values. This implies that, as expected, the cage structure is more well-defined at lower temperatures, and the particles sit at a deeper potential minimum. In Fig.4.1, we also plot the probability distribution of  $\beta\Phi_r(\Delta r = 0)$  as a function of  $M$ . We find that for all the systems with an increase in  $M$ , the probability distribution of  $\beta\Phi_r(\Delta r = 0)$  moves to higher values of  $\beta\Phi_r(\Delta r = 0)$ . This shift is concurrent with the fact that when a polydisperse system is treated as a monodisperse system, the RDF shows artificial softening [66]. However, when the polydisperse system is divided into  $M$  number of species, the inter and intra-species RDFs become sharper than the RDF obtained assuming single species. Thus the cage is better defined by the multispecies system. This gives rise to the increase in the depth of the minima. This increase in the depth of the caging potential with an increase in  $M$  is similar to the decrease in the two-body pair entropy obtained in



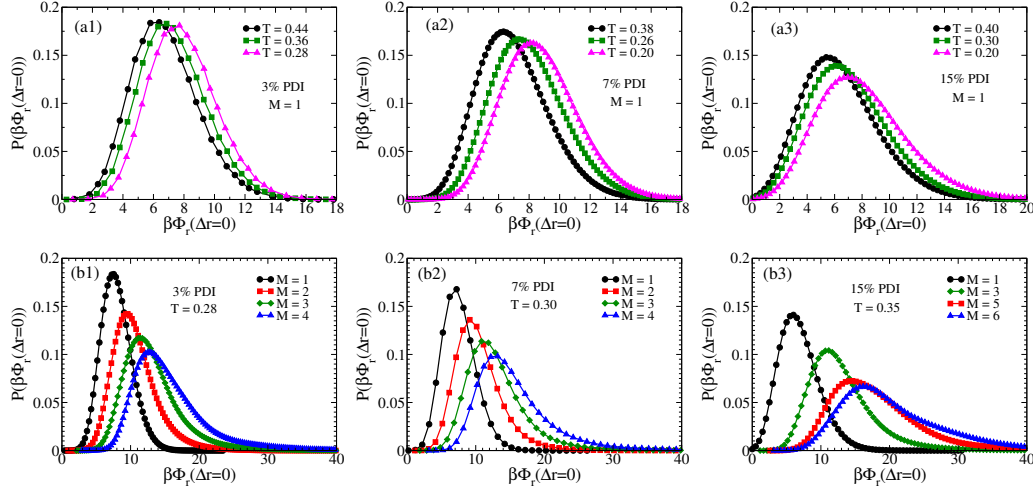


Figure 4.1: *Distribution of caging potential. Top panel:- Different temperatures for a fixed  $M = 1$ . Bottom panel:- Different  $M$  values. a1 and b1 - 3% PDI and  $T=0.28$ , a2 and b2 - 7% PDI and  $T=0.30$ , a3 and b3- 15% PDI and  $T=0.35$ . As expected, the caging potential increases with decreasing  $T$ . The caging potential also increases with increasing  $M$ . The temperatures are chosen such that the relaxation times are similar for all the systems.*

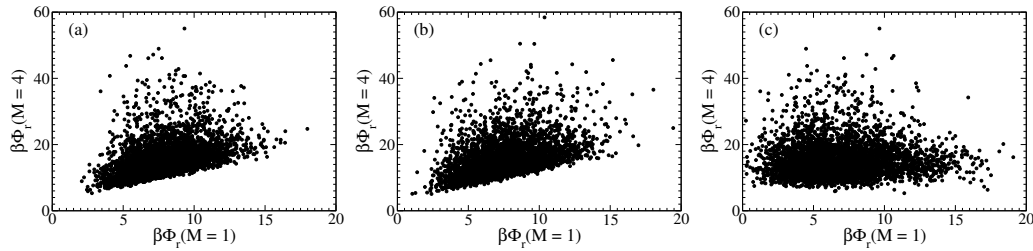


Figure 4.2: *Scatter plot between  $\beta\Phi_r$  at  $M = 1$  and  $M = 4$  at different PDIs (a) 3% PDI, at  $T=0.28$  (b) 7% PDI, at  $T=0.30$  (c) 15% PDI, at  $T=0.35$ . The temperatures are chosen such that the relaxation times are similar for all the systems. It clearly shows that the rank of the structural order parameter of a particle changes with  $M$ . The effect increases with PDI.*

our earlier study [66]. Further, to understand if this shift in the distribution of the caging potential with  $M$  is just an increase in the depth of the particle level caging potential affecting all particles equally, in Fig.4.2 as a representative plot, we show a scatter plot of the particle level caging potential obtained for  $M=1$  and  $M=4$ . This clearly shows that this shift in the distribution is not just a shift in the value of the particle level caging potential and affects each particle differently. As expected, the  $M$  dependence is more at a higher PDI.

## 4.5 Species dependence of the correlation of caging potential with particle dynamics

In the previous section, we have shown that the distribution of the local caging potential varies with  $M$ . Suppose this variation was just a shift in the value of the caging potential of each particle. In that case, we do not expect the correlation between the caging potential and the dynamics to be affected by  $M$ . However, as shown, that is not the case. Thus in this section, we study the correlation of the dynamics and the structure obtained via the local caging potential as a function of  $M$ . To understand the correlation between the dynamics and the structure, we follow the methodology used in earlier works [108, 114]. We identify fast particles using a well-documented method [136, 137, 114] also given in Appendix III. After identifying the fast particles, we correlate them with the local SOP. We calculate the fraction of particles having a specific value of  $1/\beta\Phi_r$  that undergoes rearrangement,  $P_R(1/\beta\Phi_r)$ , and plot it as a function of  $1/\beta\Phi_r$  at different  $T$  and  $M$  values. The plots for the system with 15% PDI where the effect is maximum, are shown here in Fig.4.3. The results are similar for other systems. We find that  $P_R(1/\beta\Phi_r)$  has a dependence on the SOP that becomes stronger at lower temperatures. At lower temperatures, particles with a higher value of softness (sitting in a shallow caging potential) have a higher probability of moving. Apparently, the behavior appears to be  $M$  independent. Following our earlier work, we plot the  $P_R(1/\beta\Phi_r)$  as a function of temperature for different  $1/\beta\Phi_r$  values. We find that for all the cases it can be expressed in an Arrhenius form,  $P_R(1/\beta\Phi_r) = P_0(1/\beta\Phi_r) \exp[\Delta E(1/\beta\Phi_r)/T]$ , where  $\Delta E$  is the activation energy. These plots also appear to be similar for all  $M$  values. It was earlier shown that the temperature where these  $P_R(1/\beta\Phi_r)$  vs  $T$  plots for different softness values intercept marks the onset temperature of glassy dynamics [108, 114]. The origin of this observation was explained by the microscopic mean field theory [114, 82]. Accordingly to the theory, we can correlate softness and dynamics only when the cage around the particles is well-defined. It is well known in the supercooled liquid literature that only below onset temperature where there is a separation between the short and the long time dynamics the particles in the short time feel caged by their neighbors and this cage becomes longer lived at lower temperatures. Thus the crossing of the plots marks the highest temperature where this theory is valid and beyond that due to the absence of any well-defined cage the theoretical formulation breaks down. Also at lower temperatures where the lifetime of the cage increases the structure becomes a better predictor of the dynamics. We extract the onset predicted by the crossing of the  $P_R(1/\beta\Phi_r)$  vs  $T$  plots. They are plotted in Fig.4.4. It clearly shows that the  $T_{onset}$  values have a  $M$  dependence. The value of  $M$  where it saturates increases with the percentage of polydispersity. The saturation temperature is similar to the onset temperature obtained using other methods [66]. This result is similar in spirit to that obtained in our earlier work using two body excess entropy [66].

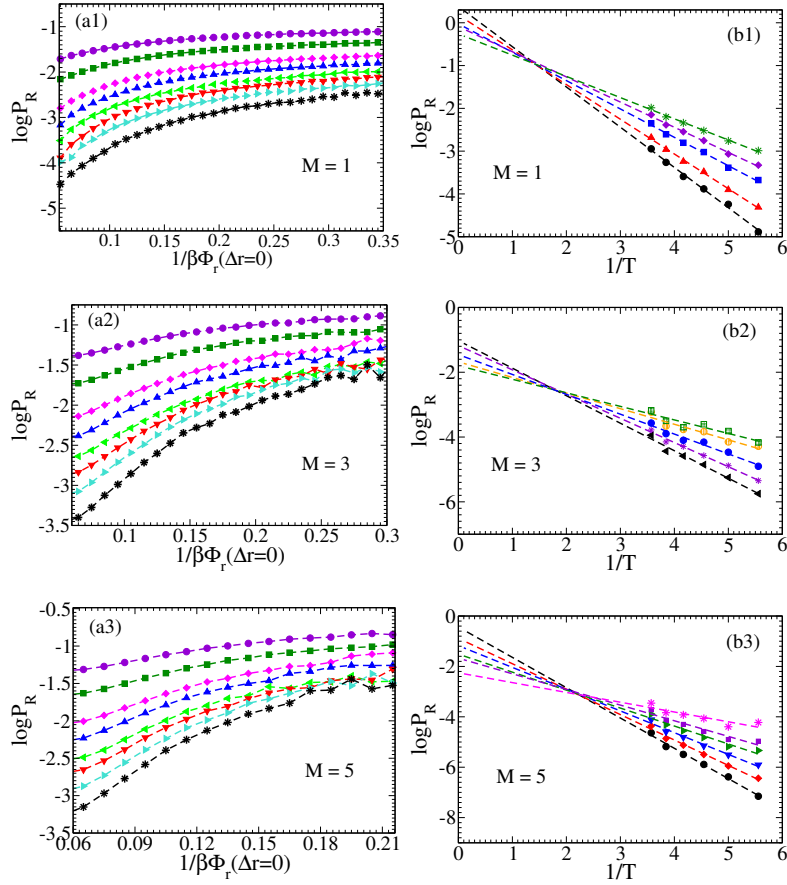


Figure 4.3: *Correlation between structure and dynamics as a function of  $M$ . Left panel- (a1-a3) The fraction of particles that undergo rearrangement  $P_R(1/\beta\Phi_r)$ , vs the depth of the caging potential,  $1/\beta\Phi_r$  at different  $T$  (0.4 (violet circle) - 0.2 (black star)), Right panel- (b1-b3)  $P_R(1/\beta\Phi_r)$  as a function of  $1/T$  at different values of the inverse of caging potential. The results are for 15% PDI*

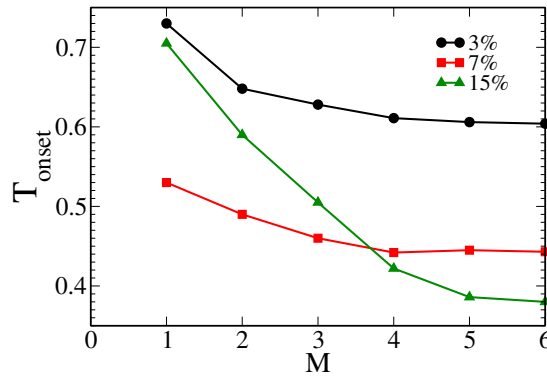


Figure 4.4: (a)  $T_{onset}$  obtained from the crossing of  $P_R(1/\beta\Phi_r)$  vs  $1/T$  plots (Fig.4.3) as a function of  $M$ . The  $T_{onset}$  initially decreases with  $M$  before saturating at higher values of  $M$ . With an increase in polydispersity, the saturation increases to higher  $M$  values.

## 4.6 Analysis of dynamics of soft and hard particles

Since we have established that, on average, the particles with higher softness have a higher probability of moving, we can expect that if we compare the dynamics (via overlap function) of a few hardest and softest particles, then at short times they will show a large difference and eventually due to the evolution of the cage and its softness around the particle they will decay at the same time [114]. Dynamics of particles via overlap function ( $q(t)$ ) can be calculated as:

$$q(t) = \frac{1}{N} \sum_{i=1}^N \omega(|r_i(t) - r_i(0)|) \quad (4.4)$$

where function  $\omega(x) = 1$  when  $0 \leq x \leq a$  and  $\omega(x) = 0$  otherwise. The cutoff of overlap parameter  $a = 0.5$  is chosen such that particle positions separated due to small amplitude vibrational motion are treated as the same[2] Here we restrict our study to one temperature for each system. For the 3% PDI system, we choose  $T=0.28$ , the lowest temperature where we can run the system before it undergoes crystallization. For the other two systems, we study them at temperatures where the relaxation times are similar to that of the 3% PDI system at  $T=0.28$ . We pick a few (around 2) of the hardest and the softest particles where the softness parameter is calculated for the same system at different values of  $M$  (Fig.4.5).

We find that the difference in the overlap of the few hardest and softest particles changes with  $M$ . However, beyond a certain value of  $M$ , the overlap functions of the hardest and the softest particles do not change with  $M$ . This suggests that beyond this  $M$  value the identification of the hardest and softest particles becomes independent of  $M$ . We consider this as the optimum value of the species,  $M_0$ , needed to describe the system. For 3% PDI,  $M_0 = 3$ , for 7% PDI,  $M_0 = 4$  and for 15% PDI,  $M_0 = 6$ . Note that the  $T_{onset}$  values for different PDIs (Fig.4.4) also show saturation at similar values of  $M$ . Thus the results are consistent. The results obtained also agree with our previous study where we showed that parameters which need the structural input are better determined when the system is described in terms of multiple species [66] and the optimum number of species increases with polydispersity. Thus we can say that the structural order parameter of a system should be calculated by describing the system in terms of  $M_0$  species. This structural order parameter will provide a true description of the local caging potential and will correlate with the dynamics.

However, although the structure of a system is not well described for  $M = 1$ , the difference in dynamics between the hardest and softest particles is best determined when we treat the system as monodisperse. This is a contradictory result and it appears that in these systems, apart from the structure, there can be other parameters that drive the dynamic heterogeneity. To understand the result, in Fig.4.6, we plot the distribution of the particle diameters of the hardest and the softest particles for

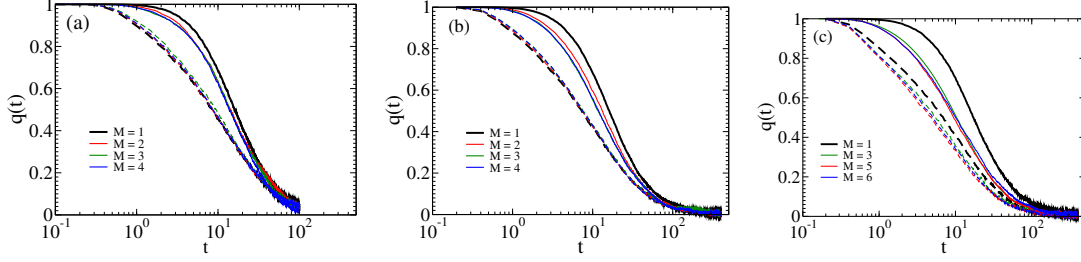


Figure 4.5: Dynamics of a few softest (high  $1/\beta\Phi_r$  value)(Dotted line) and few hardest (low  $1/\beta\Phi_r$  value)(solid line) particles at different  $M$  values. (a) 3% PDI ( $T = 0.28$ ), (b) 7% PDI ( $T = 0.30$ ), (c) 15% PDI ( $T = 0.35$ ).  $T$  is chosen such that the relaxation times of each system are in the same range. The dark lines are for  $M=1$  and with an increase in  $M$  the plots shift.

different values of  $M$  for all three systems. We also plot the particle size distribution of the whole system,  $P(\sigma)$ . When  $M = 1$ , we find that the distribution of the hardest and softest particles are skewed towards the bigger and the smaller-sized particles, respectively. This effect is more prominent at higher polydispersity. With an increase in  $M$  the distribution of the hardest particles moves towards  $P(\sigma)$ . This clearly shows that as we divide particles into species, the cage around smaller particles, which for  $M = 1$ , is loosely defined, gets defined better at higher  $M$ . This leads to an increase in the depth of the caging potential, thus, a decrease in the softness of the potential. The distribution of the diameter of the softer particles also shows some change with  $M$ , but unlike the hard particles, it always remains skewed towards smaller particles which is similar to that observed for granular systems [138]. This implies that the cage around the bigger particles is mostly well-defined, and this effect is again more for higher polydispersity.

Notice that the shift in the size distribution of the hardest/softest particles (Fig.4.6) with  $M$  is also accompanied by a shift in the overlap function of the hardest/softest particles with  $M$  (Fig.4.5) suggesting that these shifts are correlated. In both cases (particle size distribution and overlap), the shift is more for the harder particles and also increases with polydispersity. This implies that the size also plays a role in the dynamics. In Fig.4.7, we plot the dynamics of the two biggest and two smallest particles and compare them with the two hardest and softest particles for  $M=1$ . We find that for the 3% PDI, the difference in dynamics of the biggest and smallest particles are less than the softest and hardest particle. This implies that the heterogeneity in the dynamics is primarily determined by the local structural heterogeneity. With an increase in polydispersity, the scenario reverses. For the 15% PDI system, the difference in the dynamics is better described by the size than the local structural order parameter. We know from our earlier study [114] that at lower temperatures, the structure becomes a better predictor of the dynamics. To understand the role of temperature, we choose the 15% PDI system, where the size appears to be dominant, and plot the different overlap functions at two different temperatures (Fig.4.8). We find that at the lower

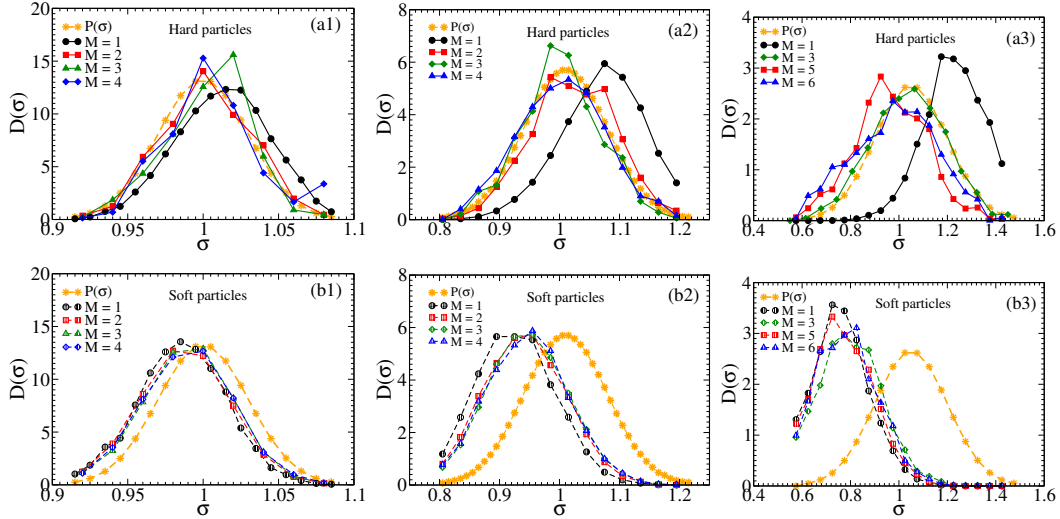


Figure 4.6: Particle size distribution,  $D(\sigma)$ , of the hardest and softest particles as a function of  $M$  (as defined in Fig.4.5). Top panel: (a1-a3) Size distribution of all hard particles. Bottom panel: (b1-b3) Size distribution of all soft particles. a1 and b1 are for 3% PDI, a2 and b2 are for 7% PDI, a3 and b3 are for 15% PDI. For comparison, we also plot the size distribution of all the particles,  $P(\sigma)$ .

temperature, although the structure becomes a better predictor of the dynamics, the size still plays a dominant role in determining the dynamics.

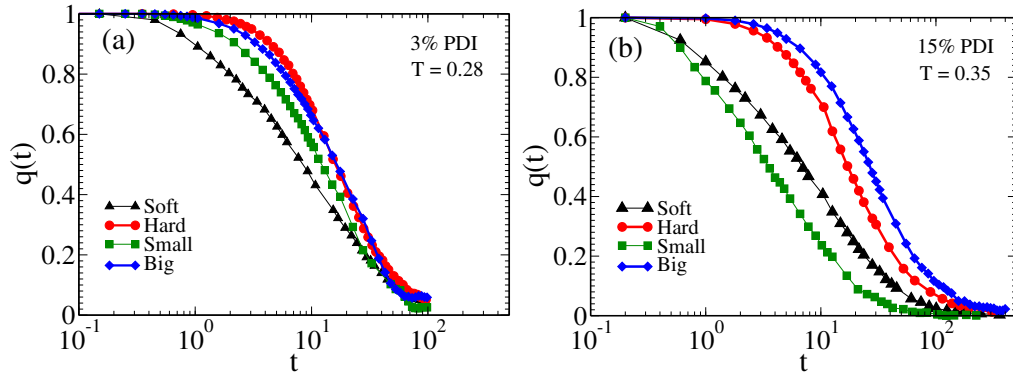


Figure 4.7: Overlap function of 2 hardest particles (Red circle), 2 softest particles (Black triangle), 2 biggest in size particles (Blue diamond), and 2 smallest in size particles (Green square) at different PDIs. The structural order parameter is calculated for  $M=1$  (a) 3% PDI (b) 15% PDI

## 4.7 Comparative study of the role of particle size and local structure on the dynamics

The above analysis suggests that for polydisperse systems, both size and local structure can play a role in the dynamics. To quantify the dependence of the dynamics on the

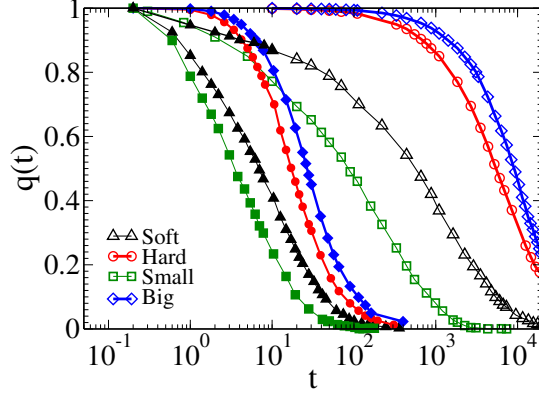


Figure 4.8: *Overlap function for 15% PDI at  $T = 0.35$  (Closed symbol),  $T = 0.22$  (open symbol). Color codes are similar like Fig.4.7.*

structure and particle size, we perform isoconfigurational runs (IC). IC is a powerful technique introduced by Harrowell and co-workers to investigate the role of structure in the dynamical heterogeneity of the particles [139, 140, 107, 141]. Among other factors, a particle's displacement can depend on the structure and also the initial momenta. This technique was proposed to remove the uninteresting variation in the particle displacements arising from the choice of initial momenta and extract the role of initial configuration on the dynamics and its heterogeneity. For each system, five different isoconfigurational runs are carried out for 4000 particles. To ensure that all configurations are different, the configurations are chosen such that the two sets are greater than  $100\tau_\alpha$  apart. We run 100 trajectories for each configuration with different starting velocities randomly assigned from the Maxwell-Boltzmann distribution for the corresponding temperatures. Mobility,  $\mu$  is the average displacement of each particle over these 100 runs and is calculated as,  $\mu^j(t) = \frac{1}{N_{IC}} \sum_{i=1}^{N_{IC}} \sqrt{(r_i^j(t) - r_i^j(0))^2}$ . Here  $\mu^j(t)$  is the mobility of  $j^{th}$  particle at time  $t$  and  $N_{IC}$  is the number of trajectories. We calculate the Spearman rank correlation ( $C_R$ ) between different parameters as a function of time (scaled by the  $\alpha$  relaxation time  $\tau_\alpha$ ). We plot  $C_R(\mu, 1/\beta\Phi_r)$  against time for  $M = 1$  and  $M = M_0$ . We find that  $C_R(\mu, 1/\beta\Phi_r)$  decreases with an increase in  $M$ . This result is similar in spirit to that observed for the difference in the overlap functions of the hardest and softest particles (Fig.4.5). In Fig.4.9 we also plot  $C_R(\mu, \sigma)$ . We find that for all systems, it grows at longer times, and for systems with higher polydispersity, the correlation is large, even at shorter times. This supports our earlier conclusion that at higher PDI, the size of the particles plays a greater role in describing the dynamic heterogeneity.

Note that apart from the softness parameter described in this work, other parameters are often used to describe the local static property of a supercooled liquid [111]. We check if size plays any role in an order parameter that does not include the radial distribution function. Earlier studies have shown that Vibrality, the local Debye-Waller Factor [111, 109, 107], is a good predictor of the dynamics. The analysis is done on the inherent structure. The Fast Inertial Relaxation Engine (FIRE) algorithm is employed

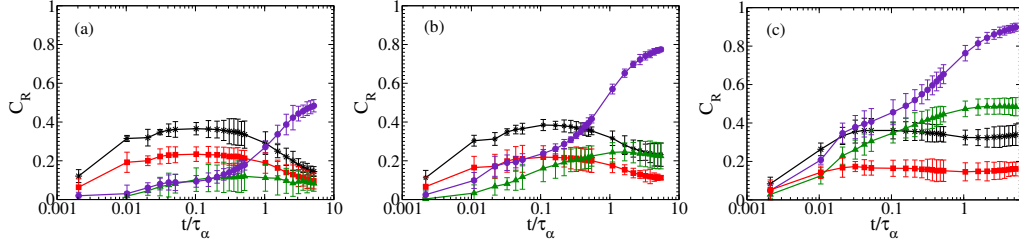


Figure 4.9: Spearman rank correlation  $C_R$  between mobility and different order parameters at different PDIs (a) 3% PDI (b) 7% PDI (c) 15% PDI. (colour code -  $C_R(\mu, 1/\beta\Phi_r)$   $M = 1$  (black star),  $M = M_0$  (red square),  $C_R(\mu, \Psi)$  (green triangle),  $C_R(\mu, \sigma)$  (violet circle).  $M_0 = 3, 4,$  and  $6$  for 3%, 7%, and 15% PDI respectively.

to obtain the inherent structures [142]. Vibrality is written as,  $\Psi(i) = \sum_{k=1}^{3N-3} \frac{|\mathbf{v}_{\mathbf{k}}^i|^2}{\omega_k^2}$  where the sum runs over the entire set of eigenmode with frequency  $\omega_k$ .  $\mathbf{v}_{\mathbf{k}}^i$  is a vector that has the three components of the eigenvector  $\vec{v}_{\mathbf{k}}$  associated with the  $i^{th}$  particle.  $\Psi(i)$  is the mean square vibrational amplitude of  $i^{th}$  particle, assuming the vibrational energy is equally distributed to all modes. In Fig.4.9, we plot  $C_R(\mu, \Psi)$  and find that it increases with polydispersity which is similar to  $C_R(\mu, \sigma)$ . It appears that  $C_R(\mu, \sigma)$  affects  $C_R(\mu, \Psi)$  more compared to  $C_R(\mu, 1/\beta\Phi_r)$ .

To quantify the above observations, we now use multiple linear regression to model mobility in terms of  $\Phi$  and  $\sigma$ . To evaluate the predictive power of the model, we use the standard 5-fold cross-validation approach, where the data is randomly split into five equal sets and a model built on four parts is used to predict mobility on the held-out test set. This is done five times, with each data point tested exactly once. The mean relative error,  $MRE = \frac{1}{N} \sum_{j=1}^N \frac{|\mu_p^j - \mu_t^j|}{\mu_t^j}$  and the root mean square deviation,  $RMSD = \sqrt{\frac{1}{N} \sum_{j=1}^N (\mu_p^j - \mu_t^j)^2}$  are shown along with the error bar computed from the five test sets. Here  $\mu_p^j$  and  $\mu_t^j$  are the predicted mobility and true mobility of  $j^{th}$  particle respectively. The mobility used here is calculated at  $t = 5$ , but the results are independent of  $t$ .

We compare results with simple linear regression, also evaluated in the same manner, but using only one of the parameters i.e either  $\Phi$  or  $\sigma$ . From the analysis of the errors plotted in Fig.4.10, we find that for lower PDI the caging potential is a good parameter to describe the mobility. However, with an increase in PDI, size becomes the dominant variable in prediction. We also do a similar analysis using  $\Psi$  and  $\sigma$  and find that between this pair, size always plays a dominant role for all systems. For smaller PDI where size does not play a strong role, it appears that among the three variables, SOP is the best predictor of the dynamics.

Note that in the above analysis, although we have treated  $\Phi$  and  $\Psi$  as independent variables, both have some dependence on the size. The dependence of  $\Phi$  on size can be seen in Fig.4.6, where we find that soft particles are primarily small and hard particles are primarily big in size. The figure also suggests that this dependence increases with



PDI and decreases as we increase  $M$ . Note that in the figure, we have taken only the hardest and softest particles. To quantify this observation for all particles, in Table 4.1, we report the Spearman rank correlations between the different parameters, and the correlation values do support the inference drawn from Fig.4.6. For all the systems, the correlation between the local structure and size is more for  $M=1$ . Now since dynamics is also correlated with the size of the particles thus, the local structure appears to be better correlated with the dynamics for  $M=1$ . This effect increases with polydispersity. We also find that at higher polydispersity, compared to  $\Phi_r$ ,  $\Psi$  is more correlated with  $\sigma$ . Thus at higher polydispersity, at longer times, the Vibrality appears to be a better predictor of the dynamics, as seen in Fig.4.9. Thus for systems with large PDI, any order parameter which is correlated with the size of the particles will appear to be a good predictor of the dynamics.

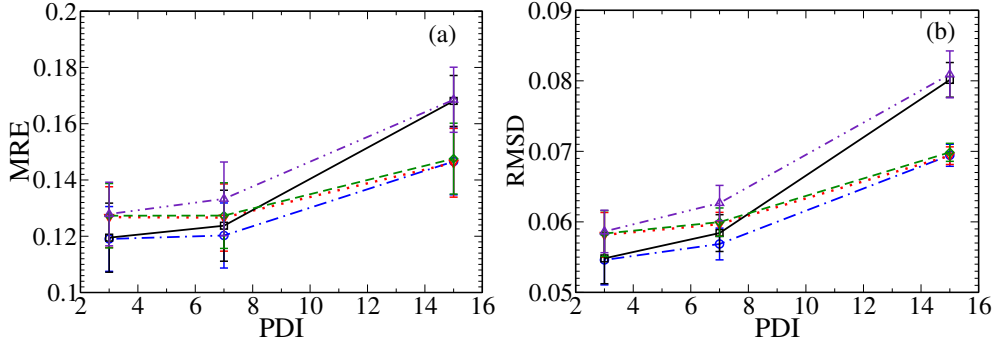


Figure 4.10: Error between predicted and true value of mobility  $\mu$  (a) Mean relative error-  $MRE = \frac{1}{N} \sum_{j=1}^N \frac{|\mu_p^j - \mu_t^j|}{\mu_t^j}$  and (b) Root mean square deviation,  $RMSD = \sqrt{\frac{1}{N} \sum_{j=1}^N (\mu_p^j - \mu_t^j)^2}$ . Color code - Independent variables are  $\Phi_r$  and  $\sigma$  (Blue, dash-dot line), Independent variable is  $\Phi_r$  (Black, solid line), Independent variable is  $\sigma$  (Green, dashed line), Independent variables are  $\Psi$  and  $\sigma$  (Red, dotted line) and Independent variable is  $\Psi$  (Indigo, dash-double dot line).

Table 4.1: Spearman rank correlation,  $C_R$  between particle size,  $\sigma$  and local caging potential,  $\beta\Phi_r$  when the system is assumed to be monodisperse,  $M = 1$  and when the system is described in terms of the optimum number of species,  $M_o$ . We also report the Spearman correlation between  $\sigma$  and Vibrality,  $\Psi$ . The systems are polydisperse with polydispersity index 3% at  $T=0.28$ , 7% at  $T=0.30$ , and 15% at  $T=0.35$ .

PDI	$C_R(\sigma, \beta\Phi_r) M = 1$	$C_R(\sigma, \beta\Phi_r) M = M_o$	$C_R(\sigma, \Psi)$
3%	0.1390155	0.082205	-0.1109721
7%	0.2932547	0.1292865	-0.2533036
15%	0.4645949	0.195008	-0.5164553

## 4.8 Conclusion

In a recent study, we proposed a new structural order parameter that strongly correlates with the dynamics [114]. This SOP is the inverse of the depth of the local mean-field caging potential, described in terms of the local liquid structure. We further showed that this correlation between the SOP and dynamics is valid below the onset temperature of the glassy dynamics. Thus the validity of the theory can be used to determine the onset of glassy dynamics. Since polydisperse systems are good model systems to study supercooled liquid dynamics, in this work, we study the structural order parameter and its correlation with the dynamics for a few polydisperse systems. Note that this SOP needs information on the local structure. It is well known that describing the structure of a polydisperse system is tricky [88, 66]. Treating the system as a monodisperse system leads to artificial softening of the structure.

We find that the distribution of the particle level SOP, changes with  $M$ . We also find that this change does not affect all particles similarly. Thus if we rank particles in terms of the value of the order parameter, then the rank order changes and finally appears to saturate beyond a certain  $M$  value. We also find that the detection of the onset temperature from the correlation of the SOP and the dynamics depends on  $M$ . The onset temperature first changes with  $M$ , and at higher values of  $M$ , it saturates. The saturation of the onset temperature and the rank of the particle order parameter allows us to estimate the optimum number of species needed to describe the system. Like in our earlier study[66], the value of  $M_0$  increases with polydispersity.

However, the most surprising result is that although the structure is not well defined for  $M = 1$ , the correlation between the structure and dynamics is maximum when the system is assumed to be monodisperse. Further analysis using multiple linear regression shows that although at low polydispersity, the local SOP determines the dynamics, at higher polydispersity, the size of the particle plays a dominant role in the dynamics. We also find that for  $M = 1$ , the bigger particles are primarily well-caged, and the smaller particles appear loosely caged. Thus there is a high correlation between the local SOP and the size of the particles. However, with an increase in  $M$  and a better description of the structure, the cage is better defined, especially for smaller particles. This reduces the correlation between the SOP and the particle size. Since size plays a dominant role in determining the dynamics, this reduction in the correlation reduces the apparent predictive power of the SOP at higher  $M$  values. To test if order parameter-size correlation is present for other order parameters where the local structural information is not needed, we calculate the Vibrality, which is the local Debye-Waller factor, known to be a good predictor of the dynamics [111, 109]. We first show that Vibrality also correlates with size, and this correlation increases sharply with an increase in polydispersity. At lower polydispersity, compared to Vibrality, the SOP is a better predictor of the dynamics. However, at higher polydispersity, the Vibrality performs marginally better. This increase in the predictive power of the Vibrality is due to its stronger coupling with the size of the particle.

Thus our study suggests that for a polydisperse system with high PDI, any order parameter with a strong coupling with the particle size will appear to be a good predictor of the dynamics. However, this may not reflect the true predictive power of the order parameter. Thus for a polydisperse system with reasonably high polydispersity, the correlation between dynamics and any static order parameter must be interpreted cautiously, as the size can play a role in this correlation, and the results may not be generic.

In this chapter, we have studied the structure-dynamics correlation at a single particle level which is an acceptable practice [111, 108, 112, 107, 139]. However, the correlation between structure and dynamics is weak when we use single particle information [141, 143, 110, 113, 140]. On the other hand, the correlation improves when we consider collective dynamical property over a certain region [144, 141, 140] or correlate the coarse grained structural property with the longtime dynamics [110, 113, 143, 102]. In a polydisperse system, this coarse graining of the SOP over a static length reduces the coupling between the order parameter and particle size. It thus can be a useful way to study the real correlation between the order parameter and the dynamics.

### Appendix I: DYNAMICS AND EXCESS ENTROPY

To elucidate the temperature range of the system, we first obtain the onset temperature of the glassy dynamics for the systems by analysing the temperature dependence of their inherent structures (IS)[3] (Fig.4.11). The IS is obtained using FIRE algorithm [142]. For PDI 3%, 7%, and 15% the onset temperatures are 0.64, 0.43, and 0.37, respectively. We calculate the relaxation time  $\tau_\alpha$  by examining the overlap function (see Eq. 4.4) decay to  $1/e = 0.367$ . The relaxation time versus temperature below the onset temperature is plotted in Fig.4.12. The temperature dependence of the relaxation time is fitted to the well known Vogel-Fulcher-Tammann (VFT) equation [21], and the resulting VFT temperatures for the different systems are as follows: 3% - 0.073, 7% - 0.117, and 15% - 0.154. However, as mentioned in the main text the system with 3% PDI crystallizes at a reasonably high temperature (below  $T = 0.28$ ) compared to its VFT temperature.

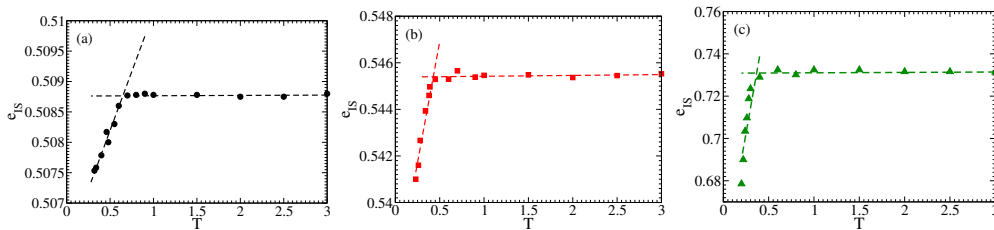


Figure 4.11: *Inherent structure energy ( $e_{IS}$ ) as a function of temperature. (a) 3% PDI (b) 7% PDI (c) 15% PDI. Near the onset temperature the value of IS starts deviating from its high temperature value thus allowing us to predict the onset*

Excess entropy,  $S_{ex}$  is a loss of entropy due to the interaction between particles.

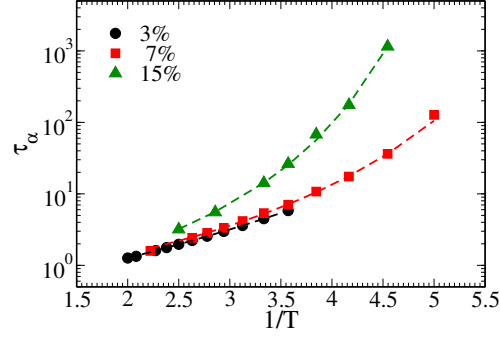


Figure 4.12: The temperature dependence of the  $\alpha$  relaxation time at different PDIs. The dashed lines are the VFT fits.

Excess entropy is calculated via temperature integration (TI) method [54, 145]. As discussed in the main text pair excess entropy,  $S_2$  takes into account the excess entropy due to two-body correlation.  $S_2$  and  $S_{ex}$  crosses each other at a temperature  $T_{cross}$  which is similar to the onset temperature [1]. In Fig.4.13 we plot the temperature dependence of  $S_{ex}$  and  $S_2$  for 7% and 15% PDI where  $S_2$  is calculated at different values of  $M$ . Both  $S_2$  and  $T_{cross}$  change with  $M$ . Initially, they vary strongly, and then the variation is weaker with  $M$ .

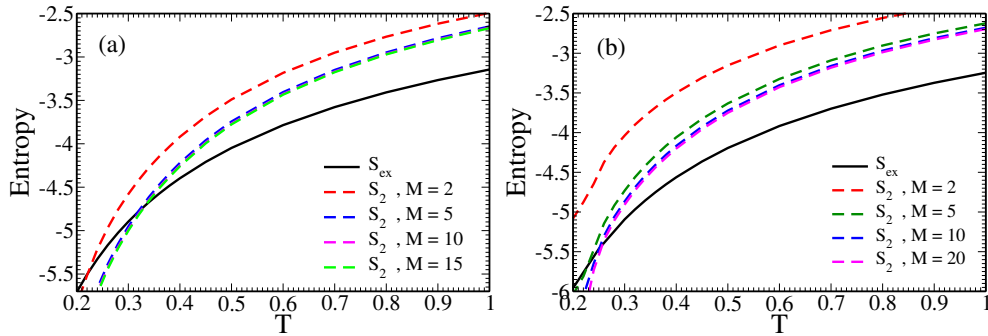


Figure 4.13: Temperature dependence of  $S_2$  changes with  $M$  and this also changes the  $T_{cross}$  values (a) 7% PDI (b) 15% PDI

## Appendix II: CALCULATION OF LOCAL CAGING POTENTIAL USING $C_{uv}$ and $C_{uv}^{approx}$

The potential energy depth calculation using this direct correlation function is given in Eq. 4.1. The expression of  $C_{uv}(r)$  according to the Hypernetted chain approximation (HNC)[10] is given in Eq. 4.2. At higher PDI, when the system is described by one species, the rdf shows a large softening and is non-zero at very small values of 'r' compared to the interaction potential (Shown in Fig.4.14. In experimental systems where the interaction potential is not known, it is often assumed that the potential of mean force is the same as the interaction potential *i.e.*  $-\beta U_{uv}(r) = \ln[g_{uv}(r)]$ . Under this assumption, the expression of the direct correlation function,  $C_{uv}^{approx}(r) \approx [g_{uv}(r) - 1]$ .

Here we present an analysis that shows that using  $C(r)$  and  $C^{approx}(r)$  primarily shifts the distribution of the potential energy depth but does not affect the correlation between the structural order parameter and the dynamics. In Fig.4.15 (a), we show a scatter plot of  $\beta\Phi(r)$  calculated using  $C_{uv}(r)$  vs that using  $C_{uv}^{approx}$  and find that they are strongly correlated. Averaged over 1000 frame, the Spearman rank correlation between  $(C_{uv}, C_{uv}^{approx}) = 0.948$  and Pearson correlation is  $= 0.955$ . This confirms that the use of the approximate direct correlation function primarily shifts the distribution of  $\beta\Phi(r)$  as shown in Fig.4.15 (b). We also plot the distribution of the softness for the fast particles, and it shows that in both cases, more than 80% of the fast particles have a softness value higher than the average softness. In Fig.4.15 (c), we plot the onset temperature obtained when  $\beta\Phi(r)$  is calculated using  $C(r)$  and  $C^{approx}(r)$  (Details of onset temperature calculation is given in Section. 4.5) and interestingly both results are identical. The dynamics of a few hardest and a few softest particles are plotted in Fig.4.15 (d). It clearly shows that using an approximate direct correlation function does not reduce the predictive power of the structural order parameter.

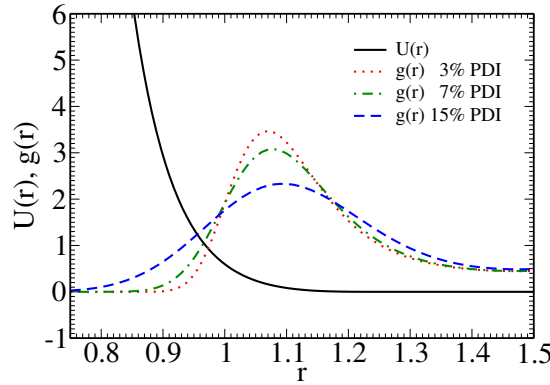


Figure 4.14: Inverse power law potential,  $U$  and radial distribution function,  $g(r)$  for different PDIs at  $M=1$ .

### Appendix III: IDENTIFICATION OF FAST PARTICLES

There are many ways of identifying fast particles [53, 146, 147, 136, 137]. Here we use the method proposed by Candelier et al.[136, 137]. In that method, for each particle in a certain time window  $W = [t_1, t_2]$ , they calculated quantity  $p_{hop}(i, t)$ . When the average position of a particle changes rapidly, a cage jump happens. Expression for  $p_{hop}(i, t)$  is,

$$p_{hop}(i, t) = \sqrt{\langle (r_i - \langle r_i \rangle_U)^2 \rangle_V \langle (r_i - \langle r_i \rangle_V)^2 \rangle_U} \quad (4.5)$$

where  $\Delta t$  timescale over which the particles can rearrange and  $U = [t - \Delta t/2, t]$  and  $V = [t, t + \Delta t/2]$ . For a time window  $W$ , the small value of  $p_{hop}$  means the particle is within the same cage, and large  $p_{hop}$  means that within that time window, the particle has moved between two distinct cages. With the help of  $p_{hop}$ , fast particles are defined in this work. If  $p_{hop}$  is greater than  $p_c$  then we identify that as a fast particle[112, 114].

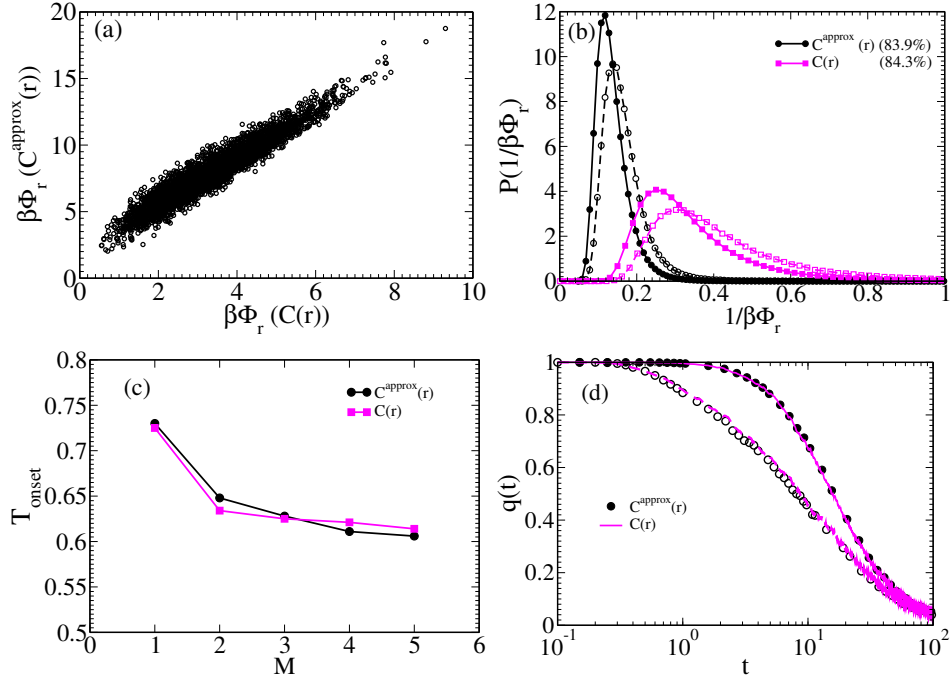


Figure 4.15: *Different parameter for justification of  $1/\beta\Phi_r$  can calculated from  $C_{uv}(r)$  and  $C_{uv}^{approx}(r)$  both. This analysis is done at 3% PDI. (a) Single frame scatter plot from  $C_{uv}(r)$  and  $C_{uv}^{approx}(r)$  at  $T = 0.28$  (b) Distribution of inverse of  $\beta\Phi_r$  of all particles  $P(1/\beta\Phi_r)$  in the system (Solid line with filled symbol) and of those which are about to rearrange (Dotted line with open symbol) at  $T = 0.28$ , from  $C(r)$  (Black) and  $C^{approx}(r)$  (Magenta). (c) Onset temperature obtained from  $C(r)$  (Square) and  $C^{approx}(r)$  (Circle) (d) Overlap function of few particles which has highest  $\beta\Phi_r$  {Solid line ( $C(r)$ ) or closed symbol ( $C^{approx}(r)$ )} and lowest value of  $\beta\Phi_r$  {Dotted line ( $C(r)$ ) or open symbol ( $C^{approx}(r)$ )} at  $T = 0.28$ .*

$p_c$  is the value of the mean square displacement at time  $t_{max}$ , where  $t_{max}$  is a time where the non-Gaussian parameter is maximum. Although we are working with a polydisperse system we have kept the  $p_c$  value fixed for all particles. For more details refer to Reference [114].

# Chapter 5

## Thermodynamics and its correlation with dynamics in a pinned systems: A comparative study using two different methods of entropy calculation

“Don’t raise your voice.  
Improve your argument”.  
- Desmond Tutu

### 5.1 Introduction

The slowing down of the dynamics in supercooled liquids and its correlation with the thermodynamics of the system have been topics of intense research. There are several characteristic temperatures where both thermodynamic and dynamic properties of the system change in a significant manner. At the onset temperature ( $T_{onset}$ ), the relaxation dynamics of the system start to differ from that of a typical liquid because due to the lowering of temperature, the system begins to explore the underlying free energy landscape [3]. This onset temperature can also be identified as the temperature where the pair part of the excess entropy becomes less than the total excess entropy of the system [1, 66]. Below  $T_{onset}$ , the temperature dependence of the dynamics can be described reasonably well by the so-called mode-coupling theory (MCT), which predicts a power-law divergence of the relaxation times at a dynamic transition temperature  $T_c$ . [11] However, experimental and numerical studies found [148, 149, 150, 13, 151, 152] that the relaxation time does not diverge at  $T_c$  as predicted by the MCT, but instead shows a smooth crossover to weaker temperature dependence. This crossover scenario



is consistent with the predictions of the so-called random first-order transition (RFOT) theory [153, 31] and it has been related to the properties of the underlying potential energy landscape [154].

According to the RFOT theory and the phenomenological Adam-Gibbs (AG) theory [29], the low-temperature dynamics of supercooled liquid is controlled by its configurational entropy ( $S_c$ ), which measures the number of possible distinct states accessible to the system. The AG theory predicts the following relationship between the  $\alpha$  relaxation time ( $\tau$ ) and the configurational entropy ( $S_c$ ):  $\tau = \tau_0 \exp(A/TS_c)$  where  $\tau_0$  is a microscopic timescale and  $A$  is a system-dependent constant. Thus, according to the AG theory, the temperature  $T_0$  where the relaxation time diverges is the same as the Kauzmann temperature  $T_K$  where the configurational entropy goes to zero [22]. For a large number of systems the AG relationship is found to hold [29, 155, 156, 157, 158, 159, 160, 161, 162, 163, 164]. There has been a recent study which showed that it is the diffusion coefficient which follows the AG relationship for the widest temperature range [165].

The validity of the AG theory in the form presented above has recently been challenged [155]. It has been argued that according to the RFOT theory, the reduction in the configurational entropy is related to the growth of a static correlation length over which the activation happens, giving rise to the relaxation process. This theory predicts a generalized AG relation given by  $\tau = \tau_0 \exp(-A/TS_c^\alpha)$ , where  $\alpha$  can be different from unity. It was further shown that the generalized AG relation holds [155] both in experiments and in simulations. Note that even according to the generalized AG relationship, the relaxation timescale should diverge below  $T = T_K$  when the configurational entropy vanishes. Also, by definition,  $S_c$  can not be negative.

Walter et al. have shown that with an increase in  $c$ , the Kauzmann temperature becomes higher [166]. However, for larger  $c$  systems, they found that the configurational entropy vanishes at temperatures close to the onset temperature. On the contrary, of self part of the dynamics shows complete relaxation well below the temperature where the configurational entropy vanishes [167, 49]. Thus we can access states with *negative* configurational entropy. This is an unphysical result by definition. Besides, it also violates the RFOT prediction.

The goal of the present work is to understand the thermodynamic properties of the pinned system and its correlation with the dynamics. To do so we employ a completely different method to calculate the entropy of the system, namely the two-phase thermodynamics (2PT) method and compare the results with the entropy obtained via the TI method. The 2PT method is a well-known method [168, 169] that has provided accurate entropy values over a wide range of thermodynamic state points for the LJ fluid and different water models [168, 170]. We first test this method for a standard Kob-Anderson model which is the  $c = 0$ , system in the pinned system. Where  $c$  represents the pinning concentration. We compare the entropy values obtained via the TI

and the 2PT methods and find them close to each other. We then employ the 2PT method for different pinned systems and compare the results with those obtained by the TI method. We find that with increasing pinning concentration ( $c$ ), the difference in entropy obtained by the two methods increases. The entropy calculated using the 2PT method does not produce any negative configurational entropy state points. We also find that it predicts a Kauzmann temperature which is similar to the temperature where the  $\alpha$  relaxation time diverges, thus validating the RFOT prediction. Incidentally, we find that in the range of temperature studied here, the standard AG relation holds. We also show that the thermodynamics transition detected by the TI method of entropy calculation is related to the fractionation of the total accessible volume.

The rest of the chapter is organized as follows: Section 5.2 contains the simulation details. In Section 5.3, we discuss the characteristic temperatures of the pinned systems. In Section 5.4, we discuss about all the finding. The chapter ends with a brief conclusion in Section 5.6. This chapter contains three Appendix sections at the end.

## 5.2 Simulation Details

In this work, we study a pinned system in which a fraction of particles are artificially pinned at their positions in an equilibrated liquid. For the study of the pinned system, we use the Kob-Andersen 80:20 binary Lenard-Jones mixture[13]. Details of this model are given in chapter 2, section 2.1.2. For creating the pinned system, the following pinning protocol is used. The pinned particles are chosen randomly from an equilibrium configuration of the system at the temperature of interest [166, 49]. NVT molecular dynamics simulation is performed in a cubic box using a Nose-Hoover thermostat where  $N=1000$  at  $\rho = 1.2$  ( $L_{box}=9.41036$ ) using a time integration step of  $\Delta t = 0.005$ , at three different pinning concentration ( $c$ ), i.e. 0.05, 0.10 and 0.15. Production runs of pinned configurations are long enough to ensure that within the simulation time, the overlap correlation function  $Q(t)$  decays to zero. Details of the pinned system model are given in Section 2.1.2

## 5.3 Characteristic temperatures of the pinned systems

To calculate the temperature range of the system, we first obtain the onset temperature of the glassy dynamics. In Fig.5.1, we plot the inherent structure energy as a function of  $T$  to calculate the onset temperature ( $T_{onset}$ ) from the inherent structure (IS).  $T_{onset}$  at different pinning concentrations is given in Table 5.1. The IS is obtained using the FIRE algorithm[142]. From this analysis, we observe that the onset temperature increases with increasing pinning concentration, " $c$ " (see Table 5.1).

In this work, to characterize the dynamics, we consider the self part of the overlap

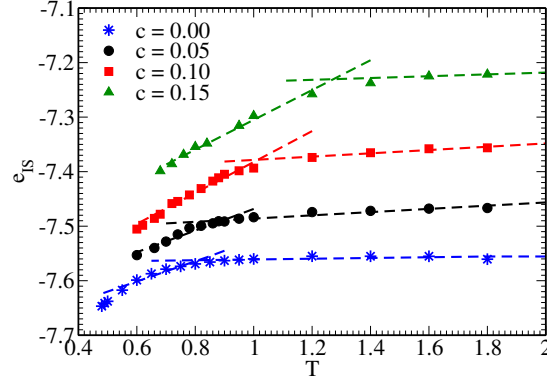


Figure 5.1: *Inherent structure energy ( $e_{IS}$ ) as a function of temperature ( $T$ ). Onset temperature increases as  $c$  increases.*

function,  $q(t)$ , defined as;

$$q(t) = \frac{1}{N} \sum_{i=1}^N \omega(|r_i(t) - r_i(0)|) \quad (5.1)$$

where function  $\omega(x) = 1$  when  $0 \leq x \leq a$  and  $\omega(x) = 0$  otherwise. The overlap parameter cutoff ( $a$ ) = 0.3 is taken such that particle positions separated due to small amplitude vibrational motion are treated as the same [2]. We calculate the relaxation time  $\tau_\alpha$  by examining the overlap function decay to  $1/e = 0.367$ . The relaxation time vs temperature below the  $T_{onset}$  is plotted in Fig.5.2. Dynamics become slower with increasing pinning concentration. The temperature dependence of the relaxation time is fitted to the well-known Vogel–Fulcher–Tammann (VFT) equation[21]:  $\tau_\alpha = \tau_0 \exp(\frac{1}{K_{VFT}(\frac{1}{T} - \frac{1}{T_{VFT}})})$ , where  $\tau_0$  are high T relaxation time,  $T_{VFT}$  and  $K_{VFT}$  is the VFT temperature and fragility constant respectively. The  $T_{VFT}$  and  $K_{VFT}$  for the different pinned systems are shown in Table 5.1. We find that, as reported earlier, the fragility decreases with increasing pinning concentration [49].

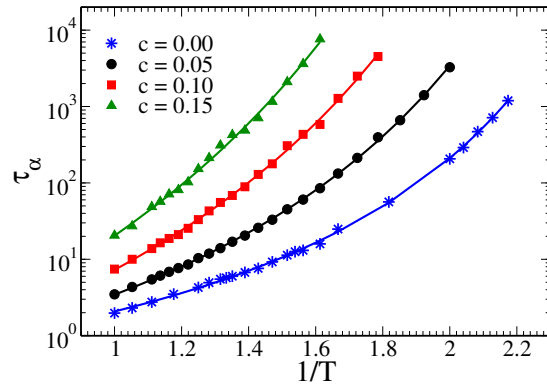


Figure 5.2: *Relaxation time ( $\tau_\alpha$ ) as a function of inverse of temperature ( $1/T$ ) for different concentrations of pinning ( $c$ ). Solid lines represent the VFT fits.*

Table 5.1: *Onset temperature ( $T_{onset}$ ), VFT temperature ( $T_{VFT}$ ) and fragility constant ( $K_{VFT}$ ) at different pinning concentration ( $c$ )*

$c$	$T_{onset}$	$T_{VFT}$	$K_{VFT}$
0.00	0.80	0.314	0.266
0.05	0.89	0.3058	0.1645
0.10	1.01	0.3026	0.1142
0.15	1.27	0.3003	0.0874

## 5.4 Result

### 5.4.1 Binary system entropy

We must first validate the 2PT approach in the well-known KA system before applying it to the pinned system. We will analyze the 2PT approach in the KA system in this section. For a binary system in the 2PT method of entropy calculation, we need to provide the information of the partial volume fraction which can be calculated as [171],

$$\bar{V}_i = \frac{\sigma_i^3}{\sum_j x_j \sigma_j^3} \frac{V}{N} \quad (5.2)$$

where,  $V_i = \bar{V}_i N_i$ .

Partial volume fraction depends on the radii of the particles. In the KA system, the diameter of the  $A$  and  $B$  particles are 1 and 0.88, respectively. However, the potential in the KA model is designed in such a way that it allows interpenetration between the  $A$  and the  $B$  particles ( $\sigma_{AB} < (\sigma_A + \sigma_B)/2$ ). Thus if we assume that the  $B$  particles are surrounded by all  $A$  particles then the effective diameter of a  $B$  particle will be 0.6. To understand the role of partial volume fraction on the entropy we calculated  $S_{tot}$  from the 2PT method, assuming the  $B$  particle diameter to be 0.8 and 0.6, respectively. We find that at high temperatures the 0.6 value provides a better result but at low temperatures, the entropy is almost independent of the small changes in the partial volume fraction. Thus for these systems, we assume the diameter of the  $B$  particles to be 0.6.

We compare the total entropy of the system as estimated from the TI [63] and from the 2PT [168] methods. Fig.5.3 shows that the  $S_{tot}$  obtained from TI and 2PT methods have similar values. The error bar for the 2PT data is estimated from a set of ten runs at each temperature. We find some deviation in the low temperature. At low temperatures as the dynamics become slow, we need longer runs to get a converged DOS. Fig.5.4 shows the effect the time step has on the value of total entropy at lower temperatures. With an increase in time step, the entropy value approaches the value calculated using the TI method. However, at longer times, the slope of the curve decreases.

Configurational entropy,  $S_c$  obtained in the two different methods is plotted in

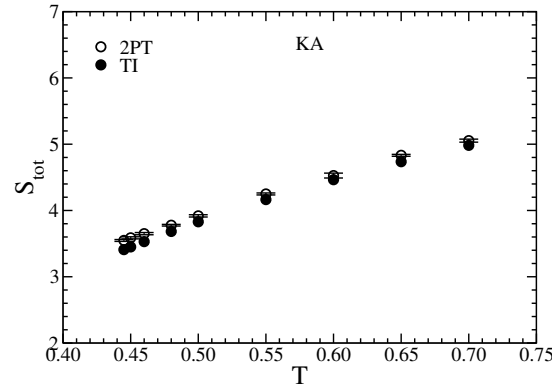


Figure 5.3:  $S_{tot}$  vs.  $T$  for the KA model using the TI and the 2PT method. The two methods agree reasonably well. A small systematic deviation in the low-temperature regime is due to the limited averaging possible for the 2PT method, see Fig.5.4.

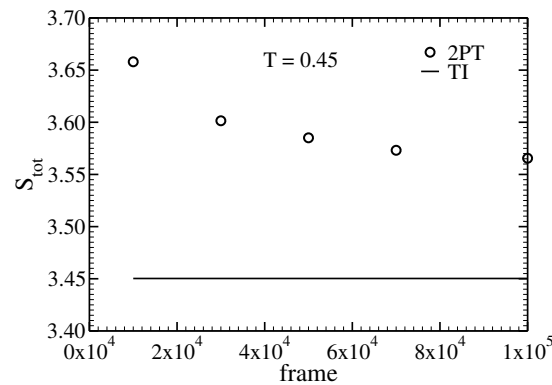


Figure 5.4: The total entropy via the 2PT method as a function of the number of time frames over which the velocity autocorrelation function is integrated to obtain the spectral density at a low temperature  $T = 0.45$ . For comparison, we also plot the entropy value obtained using the TI method. The difference decreases with increasing time intervals, but the rate of convergence becomes slower at longer times.

Fig.5.5. We find that the values of Kauzmann temperature ( $T_K$ ) using two different methods are close which validates the applicability of the 2PT method for the calculation of the configurational entropy.

We have compared the density of states calculated from the calculation of Hessian and the Fourier transform of the velocity autocorrelation function. We find both methods show a similar result in a density of states (Graphical representation is given in Reference [145]).

## 5.4.2 Pinned system entropy

In a pinned system, a fraction  $c$  of the particles is pinned. The details about the pinned system have been discussed in section 2.1.2 Using the TI method the total entropy of

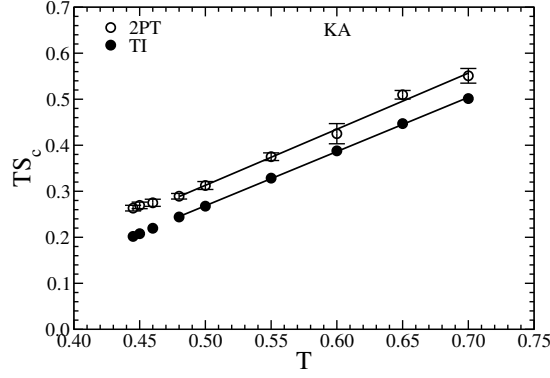


Figure 5.5:  $TS_c$  vs.  $T$  for the KA model using the TI and the 2PT methods. The value of  $T_K$  estimated by the two methods are similar ( $T_K^{TI}=0.27$ ,  $T_K^{2PT}=0.24$ ).

moving particle in the pinned system,  $S_{tot}$  is given by [166],

$$S_{tot} = \frac{3M}{2} - \frac{3M}{2} \ln \left( \frac{2\pi T}{h^2} \right) + M(1 - \ln \frac{N}{V}) - \sum_{i=1}^2 N_i \ln \frac{N_i}{N} + \beta^* \langle U \rangle - \int_0^{\beta^*} d\beta \langle U \rangle \quad (5.3)$$

where  $N_1$  and  $N_2$  are number of moving particles of type  $A$  and  $B$  respectively.  $V$  is the total volume of system,  $M$  is the total number of moving particles. The total potential energy of system  $U = U_{MP} + U_{MM}$ , where  $U_{MM}$  and  $U_{MP}$  denotes the interaction energy between moving- moving particles and moving-pinned particles respectively.

In the pinned system [166, 49, 172, 173, 174], the relaxation time obtained from single-particle dynamics remains finite at temperatures for which the configurational entropy vanishes, and there is some evidence[167] that the relaxation time associated with the collective dynamics also remains finite at such temperatures. It has also been argued that the configurational entropy has a finite value when the vibrational entropy is calculated using an anharmonic approximation [172].

We calculate the total entropy of the pinned system using the TI method used in earlier studies [166] and also mention in Eq. 5.3. We apply the 2PT method in the pinned system and compare it with the TI method. In Fig.5.6 we plot (a) the total entropy obtained using two different methods and in Fig.5.6 (b) their differences, for three different pinning densities and (c) the relative difference. For comparison, we also show the KA system with no pinning which is the same as the KA system. We find a difference between the entropy calculated via the 2PT and the TI methods that increases systematically with pinning. We next calculate the configurational entropy as predicted by the two methods and plot the temperature dependence of  $TS_c$  in Fig.5.7. Both methods predict positive Kauzmann temperatures for each system and similar to the case of mean-field systems[145], the Kauzmann temperature predicted by the 2PT method is lower than that by the TI method, see Table.5.2. In this calculation,

we have used the harmonic approximation for the vibrational entropy.

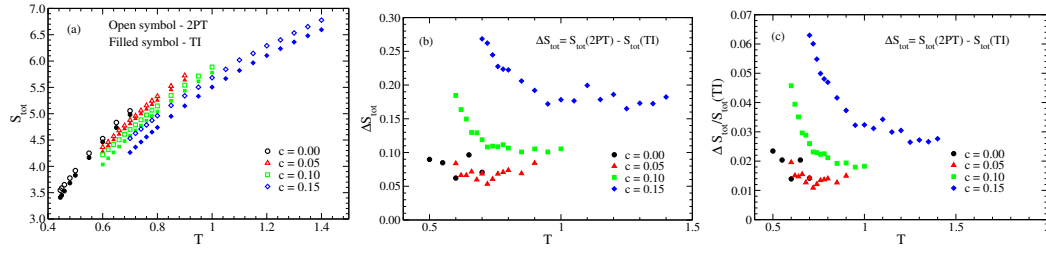


Figure 5.6: Comparison of the TI and 2PT methods of calculation of entropy for a pinned system with different pinning concentrations. (a) The total entropy  $S_{tot}$  vs  $T$ . Filled symbols represent the results of the TI method and open symbols represent those of the 2PT method. (b) The difference in  $S_{tot}$  between 2PT and TI methods increases with increasing pinning concentration  $c$ . (c) The relative difference in the total entropy,  $\frac{\Delta S_{tot}}{S_{tot}(TI)}$ , between 2PT and TI shows similar behavior as Fig.5.6 (b).

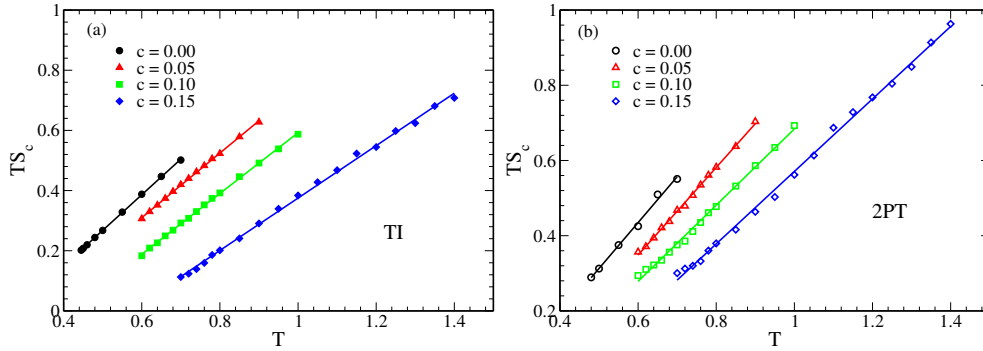


Figure 5.7:  $TS_c$  vs.  $T$  for systems with different pinning concentrations  $c = 0, 0.5, 0.10, 0.15$  using (a) the TI method and (b) the 2PT method. Both the  $T_K^{TI}$  and the  $T_K^{2PT}$  increase with increasing pinning concentration but  $T_K^{2PT} < T_K^{TI}$ , see Table.5.2.

Table 5.2: The values of all characteristic temperatures for pinned systems with different pin concentrations  $c$ .  $T_K^{TI}$  is the Kauzmann temperature estimated from TI.  $T_K^{2PT}$  is the Kauzmann temperature estimated from the 2PT method.

$c$	$T_K^{TI}$	$T_K^{2PT}$
0.00	0.28	0.24
0.05	0.31	0.30
0.10	0.41	0.32
0.15	0.57	0.41

Next, we need to understand if the lowering of the  $T_K$  value in the 2PT method is sufficient to describe the dynamics. In Fig.5.8 we show semi-log plots of  $\tau$  vs.  $\frac{1}{TS_c}$  where the entropy is calculated using the 2PT and the TI methods. The TI method shows a strong breakdown of the AG relation for  $c = 0.1$  and  $c = 0.15$ , whereas the 2PT method follows the AG relation for all  $c$ .

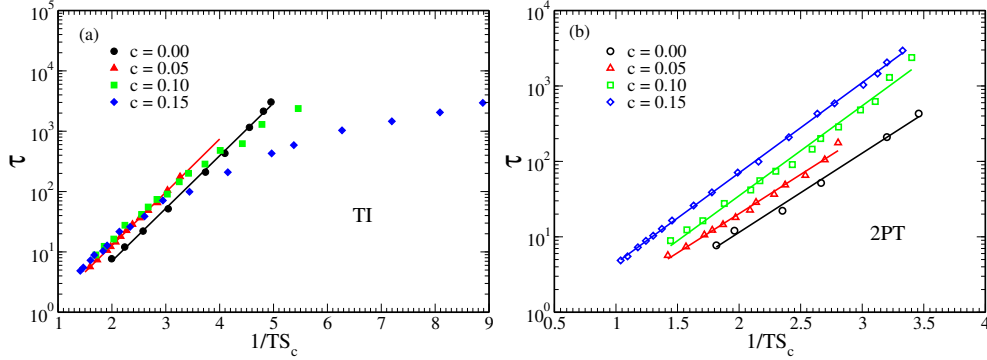


Figure 5.8: *Testing the AG relation between  $\tau$  vs.  $\frac{1}{TS_c}$  for  $c = 0, 0.05, 0.10, 0.15$  systems using (a) the TI method (b) the 2PT method. In the temperature range studied here, the AG relation is violated for  $c = 0.1$  and  $c = 0.15$  when  $S_c$  is calculated using the TI method. However, the AG relation holds for all  $c$  when  $S_c$  is calculated via the 2PT method.*

In their study, Kob et al. highlighted that the vibrational entropy in systems is not solely governed by harmonic contributions but also includes anharmonic contributions [172]. They suggested that incorporating anharmonic configuration entropy leads to a positive contribution. Therefore, to ensure the completeness of our analysis, we have considered the inclusion of anharmonic contributions in the calculation of the vibrational entropy. In our analysis, we observe that the anharmonic approximation will equally affect both the 2PT and TI entropy values. Details of anharmonic entropy calculation are given in chapter 2, Section 2.4.3.

We calculate the configurational entropy by subtracting the vibration entropy from the total entropy by taking into consideration the anharmonic contribution. The temperature dependence of the configurational entropy after taking care of the anharmonic contribution is plotted in Fig.5.9 (a) and the corresponding Adam-Gibbs plot is shown in Fig.5.10 (a). Even after the addition of the anharmonic contribution, the AG relationship is violated. In figure Fig.5.9 (b) we plot the temperature dependence of the configurational entropy where the total entropy is calculated using the 2PT method and the anharmonic contribution is taken into consideration. We show the AG plot of the same data in Fig.5.10 (b). We find that when the total entropy is calculated using the 2PT method the AG relationship holds and also the temperature where the entropy vanishes is lower than that given by the TI method (see Table.5.3).

From Figs. 5.9, 5.10 and Table.5.2 we find that even after taking into consideration the anharmonic term the Kauzmann temperature  $T_K$  appears to be high and the AG



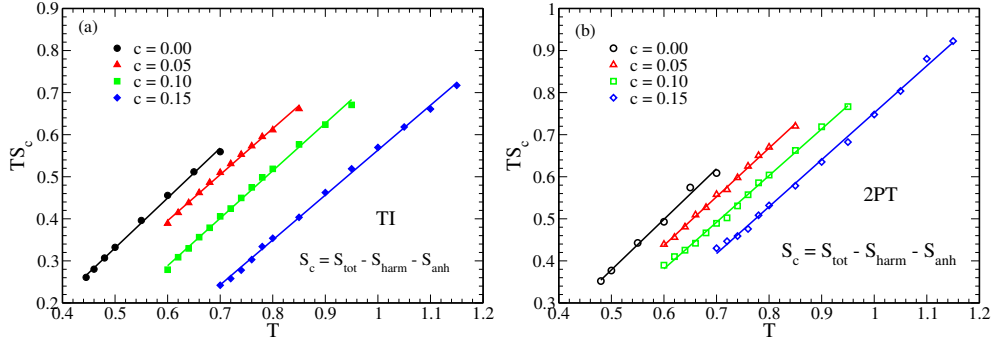


Figure 5.9:  $TS_c$  vs.  $T$  for  $c = 0, 0.5, 0.10, 0.15$  systems using (a) the TI method and (b) the 2PT method.  $S_c$  is computed by including the anharmonic contribution.  $T_K^{TI}$  and  $T_K^{2PT}$  increase with increasing pinning concentration but  $T_K^{2PT} < T_K^{TI}$ , see Table.5.3.

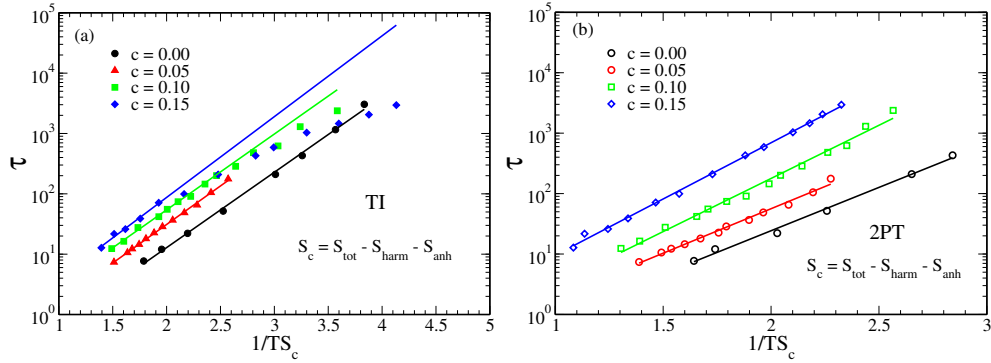


Figure 5.10: Testing the AG relation between  $\tau$  and  $\frac{1}{TS_c}$  for  $c = 0, 0.5, 0.10, 0.15$  systems using (a) the TI method and (b) the 2PT method.  $S_c$  is computed by including the anharmonic contribution. In the temperature range studied here, the AG relation is violated for  $c = 0.10$  and  $c = 0.15$  when entropy is calculated using the TI method. However, the AG relation holds when entropy is calculated via the 2PT method.

Table 5.3: The value of all characteristic temperatures for systems with different 'c' values.  $T_K^{TI}(\text{anh})$ , and  $T_K^{2PT}(\text{anh})$  are Kauzmann temperature estimated from TI and 2PT respectively after the addition of anharmonic contribution.

c	$T_K^{TI}(\text{anh})$	$T_K^{2PT}(\text{anh})$
0.00	0.22	0.18
0.05	0.24	0.22
0.10	0.34	0.26
0.15	0.47	0.33

relationship is violated.

As discussed above, the unphysical feature of negative configurational entropy does not appear in the TI results for the pinned system. Also, the observation that the 2PT results for  $S_c$  lie above the results obtained from the TI method suggests that the 2PT results are less accurate than the TI results because, as mentioned above, there are arguments [172, 133] that suggest that actual configurational entropy is lower than the TI result. However, it should be noted that the expectation that the TI results overestimate the true  $S_c$  has not been verified by any calculation for the pinned system. Also, a difference between the value of the configurational entropy *per particle* obtained from the TI method and its actual value would require the presence of an exponentially large number of energy minima that differ from a particular minimum by the movement of a small number of particles. We are not aware of any study that establishes the presence of such a large number (exponential in the number of particles) of nearby minima.

Available results for the dynamics [49, 173, 167] of the pinned system suggest that the TI results for  $S_c$  may not be consistent with the RFOT theory. There are arguments [174, 172] that suggest that the inconsistency with the RFOT theory may disappear if the relaxation time associated with the collective dynamics (instead of the time scale obtained from single-particle dynamics) is considered. It has also been argued [172] that the disagreement with the RFOT theory may be accounted for by the overestimation of  $S_c$  in the TI method. However, these arguments have not been verified from explicit calculations.

A similar observation of the mismatch between entropy and dynamics for the pinned system has been observed in experimental studies [175]. It was found that although for unpinned systems, the local dynamics correlate with the local pair excess entropy, with an increase in the pinning density, such correlation disappears [175]. Thus, for the pinned system, these traditional methods of entropy calculation cannot explain the dynamics. On the other hand, the 2PT method appears to explain the dynamics quite well. For these reasons, we believe that more studies are necessary to decide the relative merits of the TI and 2PT methods for the pinned system.

## 5.5 Analysis of the origin of increasing saturation point in pinned system

We note that both the 2PT entropy and the dynamics from the self overlap provide us with information on the local behavior. Whereas the entropy calculated via the TI method and the collective overlap provide us with non-local information. So it is important to understand the dynamics and its correlation with the entropy calculated via the TI method.

We show that, in pinned system the intermediate scattering function  $F(q, t \rightarrow \infty)$  and collective overlap  $Q_c(t \rightarrow \infty)$  saturation point increases as increasing the pinning concentration ( $c$ ). We next show that for systems where instead of the pinned particles

we have particles with heavy mass the dynamic correlation functions  $F(q,t)$  and  $Q_c(t)$  show a similar behavior. It's also known as soft pinning. Instead of saturating at a finite value at long time the correlation functions shows a plateau and decays from there. We note that the  $F(q,t)$  and  $Q_c(t)$  saturation points of the pinned system and the heavy mass system are similar at the initial time when the heavy mass particle cannot move; however, once the heavy mass particle begins to move, the heavy mass saturation point decreases and matches with the KA system or the unpinned system (shown in Fig.5.11). This width of the plateau increases with the mass of the heavy particles. This clearly shows that the long time saturation value of the  $F(q, t \rightarrow \infty)$  and  $Q_c(t \rightarrow \infty)$  are related to the immobility of the pinned particles.

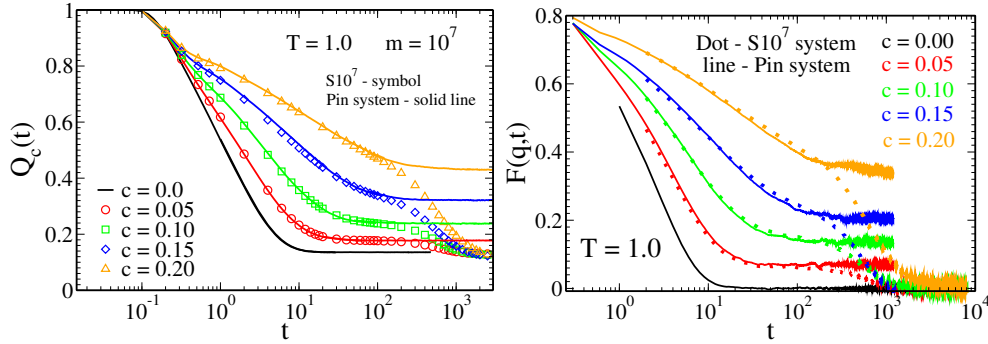


Figure 5.11: (a) Collective overlap at different  $c$  and heavy mass system saturated at the normal system saturation point, once high mass particle start moving. (b) Collective intermediate scattering function at different  $c$  and heavy mass saturated at the normal system saturation point, once high mass particle starts moving.

For a regular glass forming system above the glass transition temperature, the intermediate scattering function  $F(q, t \rightarrow \infty)$  decays to zero, and below the glass transition temperature  $F(q, t \rightarrow \infty)$ , has a finite value. This jump of  $F(q, t \rightarrow \infty)$  from zero to a finite value marks the glass transition of the system. However for the pinned system we find that  $F(q, t \rightarrow \infty)$  does not show such a transition and has a finite value even at very high temperature where the entropy is large (Shown in Fig.5.12). Thus identification of glass transition temperature from the saturation of  $F(q,t)$  is difficult.

As shown by Kob et al. studying the overlap  $q_{\alpha\beta}$  between two configurations  $\alpha$  and  $\beta$  is an alternate strategy for identifying and characterizing the thermodynamic transition:  $q_{\alpha\beta} = N^{-1} \sum_{ij} \theta(a - |r_i^\alpha - r_j^\beta|)$ , where the length scale  $a$  is 0.3, the Heaviside function is  $\theta$ , and  $r_i^\alpha$ , is the position of particle  $i$  in configuration  $\alpha$ . According to RFOT, the average value  $\langle q \rangle$  will quickly rise at the glass transition from a small value in the fluid phase to a large value in the glass phase. Here  $\langle \dots \rangle$  and  $[\dots]$  stand for the thermal and disorder averages, respectively. Kob et al. have computed the overlap distribution  $P(q)$  using replica exchange molecular dynamics[166]. They plotted the  $P(q)$  as a function of  $q$ , which is reproduced in Fig.5.13(a). They observe that at high temperatures,  $[P(q)]$  remains single-peaked for all  $c$ , and as  $c$  rises, the peak position gradually moves towards greater  $q$ . The coexistence of the fluid and

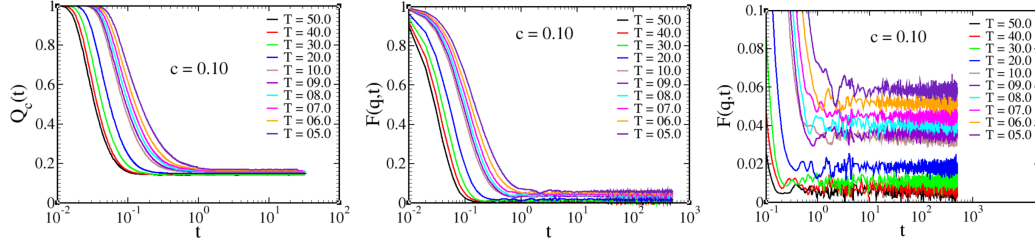


Figure 5.12: *Dynamics analysis at high temperature. (a) Collective overlap  $Q_c(t)$  as a function of time ( $t$ ) (b) Intermediate scattering function as a function of  $t$  (c) Intermediate scattering function at long  $t$ .*

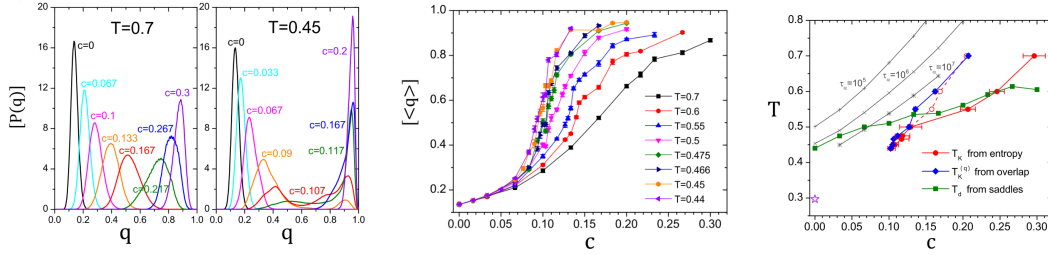


Figure 5.13: *Plot adopted from reference [166]. (a)  $P(q)$  calculated from replica exchange molecular dynamics (b) average overlap  $|\langle q \rangle|$  as a function of  $c$  (c) Kauzmann temperature from different methods.*

glass phases is signaled by the temperature being single-peaked at low and high  $c$ , but having a double-peak structure at intermediate  $c$ , which suggests that the transition from the fluid phase to the glass phase is first-order-like. The average overlap  $|\langle q \rangle|$  as a function of  $c$  was plotted by Kob. et al., and we have reproduced this plot in Fig.5.13(b). The ideal glass transition temperature  $T_K(q)$  can be determined using this overlap approach by determining the temperature at which the skewness of  $[p(q)]$  disappears.  $T_K(q)$  as a function of  $c$  is shown in Fig.5.13(c)[166].

Note that  $Q_c(t \rightarrow \infty) = |\langle q \rangle|$ . For the regular KA system,  $Q_c(t \rightarrow \infty) = \frac{N}{V} \frac{4\pi a^3}{3}$ , where  $a = 0.3$  is employed in the calculation of  $Q_c(t)$  to take into account the particle's vibrational motion within the cage. Due to this finite value of 'a',  $Q_c(t)$  in a regular KA system does not decay to zero and instead saturates at 0.135 in the long time limit. In the pinned system, this expression is no longer the same as a regular KA system. Due to pinned particles, the total volume of the system is not available to the mobile particles. We can write

$$\begin{aligned}
 Q_c(t \rightarrow \infty, c) &= \frac{(N - N_c)}{(V - N_c v_e)} \frac{4}{3} \pi a^3 \\
 &= \frac{N}{V} \frac{(1 - c)}{(1 - \rho c v_e)} \frac{4}{3} \pi a^3 \\
 &= Q_c(t, c = 0) \frac{(1 - c)}{(1 - \rho c v_e)}
 \end{aligned} \tag{5.4}$$

where  $a = 0.3$ ,  $N_c$  is the number of pinned particles,  $v_e$  is the per pinned particle excluded volume, and  $V$  is the system's entire volume. This  $\rho c v_e$  provides the information of the total excluded volume for the pinned particles. Thus, if we have the value of  $Q_c(t \rightarrow \infty, c)$ , then we can calculate the excluded volume due to pinned particles.

Now we reanalyzing the data presented by Kob et al. . We estimated the total excluded volume  $\rho c(v_e)$  using the  $Q_c(t \rightarrow \infty) = \langle q \rangle$  from Fig.5.13. In Fig.5.14,  $\rho c v_e$  as a function of  $T$  is plotted. From this, we observe that as  $c$  grows, we see a dramatic increase in the excluded volume, and after a certain value, the excluded volume no longer increases and saturates to a value ( $\approx 0.83$ ). We demonstrate in Fig.5.14 that the temperature at which the excluded volume achieves a fixed value ( $\approx 0.8$ ) matches with the  $T_K$  value for each system. Thus, we suggest that the thermodynamic transition predicted by the TI method of entropy is related to the excluded volume reaching a finite value. We believe that at this value of the excluded volume, the available volume of the systems undergoes a fractionation; thus, the total available volume is not accessible to all the mobile particles. Here, we also show that not only the distribution of  $q$  but also the average value can provide information of the thermodynamic transition.

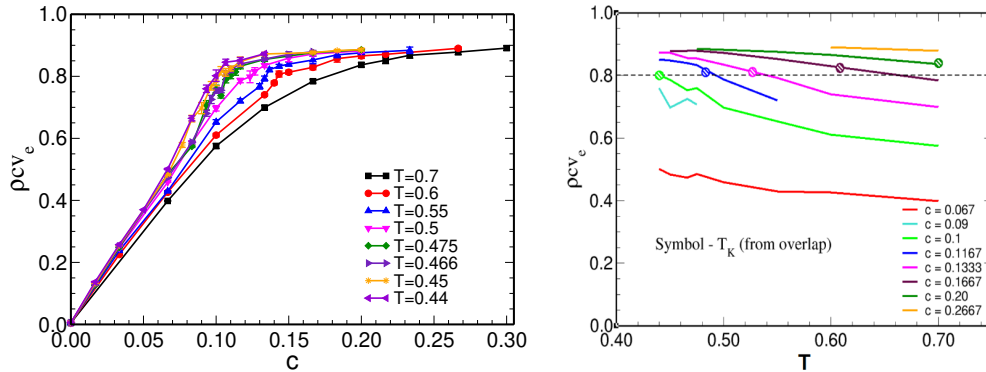


Figure 5.14: Excluded volume calculated from Eq. 5.4. Note that the  $q(t)$  values were adopted from Figure 2(c) of the reference [166] and also shown in Fig.5.13. (b) Excluded volume as a function of  $c$  at different  $T$ . Symbol represent  $T_K$ , which is adapted from reference [166], also shown in Fig.5.13(b).

## 5.6 Conclusion

The present work aims to study the thermodynamics of the system and understand its correlation with the dynamics. To study thermodynamics, we first calculate the entropy using the well-known TI method [78]. We then study the correlation of the entropy with the dynamics. The pinned system shows super-Arrhenius dynamics similar to conventional glassy liquids, suggesting that the RFOT description should apply. However, it is found that configurational entropy vanishes [166] at a temperature that is close to the onset temperature of the system. It is also shown that the relaxation

times calculated from single-particle dynamics remain finite at temperatures where the configurational entropy vanishes[49, 167]. This is different from the prediction of RFOT and the behavior seen in conventional glass-forming liquids for which the (extrapolated) values of  $T_K$  and  $T_0$  are found to be close to each other [29, 155, 176]. This observation also indicates that the system samples state points with negative configurational entropy, which is unphysical by definition.

We thus use another technique, namely the 2PT method, to calculate the entropy. The 2PT method assumes that a liquid can be represented as partially a gas and partially a solid and this fraction is a function of the thermodynamic parameters of the system and also of the size of the particles. The 2PT method has been extensively used to calculate the entropy for many systems, mostly in the high-temperature regime [171, 168]. In recent work, this method was also extended to lower temperatures [170]. We find that for the KA system at  $c = 0$ , both the 2PT method and the TI method provide similar results. We then compare the total entropy calculated by the 2PT method with that by the TI method for different pinned density systems. We find that the difference between the entropy values obtained in the two methods systematically increases with increasing  $c$ . We also find that the entropy calculated via the 2PT method describes the dynamics quite well and confirms the RFOT prediction. We note that both the 2PT entropy and the dynamics from the self overlap provide us with information on the local behavior. In contrast, the entropy calculated via the TI method and the collective overlap provide non-local information. Since the collective overlap at a long time has a finite nonzero value even at high temperatures, just by looking at the value it is difficult to identify the transition temperature. We show here that the collective overlap's long-time value provides us with information on the excluded volume due to the pinned particles. This excluded volume initially increases with the lowering of temperature, and then when the excluded volumes start to overlap, the growth stalls. When the excluded volume overlaps, then the total accessible volume of the system gets fractionated. This fractionation of the volume is what is referred to as thermodynamic phase transition by Kob and co-workers[166]. We also show that the  $T_K$  value for all the systems coincides with the temperature where the excluded volume reaches a fixed value ( $\approx 0.8$ ). Thus, we suggest that the thermodynamic transition predicted by the TI method of entropy is related to the fractionation of the total volume into smaller domains, which can be identified from the estimation of the excluded volume. Thus, it shows that the TI method can identify thermodynamic transition, which has a signature in the dynamics and can be obtained from the long-time saturation value of the collective overlap function for the pinned system. However, the entropy obtained via the 2PT method measures the entropy at the local level and thus correlates well with the self-overlap function. In regular systems, these two entropies and the self and collective dynamics provide similar information. However, for other classes of systems, like the pinned and the meanfield system they are not identical.

## APPENDIX A: Different types of entropy calculation

The various forms of entropy in pinned systems are discussed here.

- Ideal gas entropy : The ideal gas entropy in pinned systems only comes from the moving particle, as discussed in chapter 2. The pinned system's ideal gas entropy is calculated as;

$$MS_{id} = \frac{3M}{2} - 3M \ln \Lambda + M \left(1 - \ln \frac{M}{V}\right) - \sum_{i=1}^2 N_i \ln \frac{N_i}{M} \quad (5.5)$$

where  $M$  is the total number of particles that are moving and,  $\Lambda = \sqrt{\frac{\beta h^2}{2\pi m}}$  is the de Broglie thermal wavelength and  $h$  is the Planck constant. This is explained in more detail in chapter 2, Eq. 2.71. We have plotted the ideal gas entropy of pinned systems at various pinning concentrations in Fig.5.15. As the pinning increases, we see a increase in ideal gas entropy.

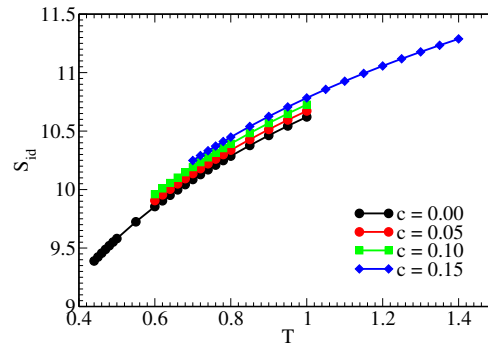


Figure 5.15: *Per mobile particle ideal gas entropy. Ideal gas entropy increases as increasing the pinning concentration.*

- Vibrational entropy : We consider of a weakly vibrating system (IS) around an inherent structure. The potential energy can be approximated well by the following formula, if we indicate by  $r_i$  the displacement of the  $i^{th}$  particle from its point in the IS.

$$U \approx U_{IS}(S) + \frac{1}{2} \sum_{i,j}^M \frac{\delta^2 U}{\delta r_i \delta r_j} \delta r_i \delta r_j \quad (5.6)$$

Note that in inherent structure calculation, we minimize the mobile particle only, pinned particle coordinate remain same. It is important to understand that the coordinates of pinned particles should not be considered, just the derivative of the potential energy with respect to the coordinates of mobile particles. (However, it stands to reason that  $U$  will be influenced by the positions of pinned and mobile particles.) The Hessian matrix is therefore  $3M \times 3M$  in size. The harmonic vibrational entropy of the given inherent structure with the given

pinned particle configuration can be represented as by introducing the eigenvalues  $\lambda_1, \lambda_2, \dots, \lambda_{3M}$  of the Hessian.

$$MS_{vib} = 3M(1 - \ln \Lambda) + \frac{1}{2} \sum_{i=1}^{3M} \ln \frac{2\pi}{\beta m \omega_i^2} \quad (5.7)$$

This is explained in more detail in chapter 2, Eq. 2.100. We have plotted the vibrational entropy of pinned systems at various pinning concentrations in Fig.5.16. As the pinning increases, we see a drop in vibrational entropy.

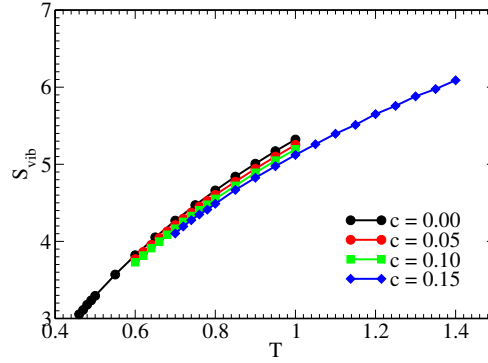


Figure 5.16: *Per mobile particle vibrational entropy. Vibrational entropy drops as increasing the pinning concentration.*

- **Excess entropy :** We employ the thermodynamic integration approach to determine entropy from simulations. The TI technique, which is most frequently used to study Lennard-Jones particles, connects the ideal gas state and the state of interest by combining a compression path (increasing density) and a cooling path (decreasing temperature). Though it is unclear how compression for pinned fluids should be characterised. In order to avoid modifying the density, we only employ the cooling path from the ideal gas limit  $T = \infty$  to the target temperature. Here, we apply the same version of the TI that has been employed for bulk Lennard-Jones particles to pinned systems. Before we start calculating the disorder average over realisations, we first apply the TI to the entropy of a certain pinned particle configuration. At the desired temperature  $\beta'$ , the entropy of the system with the pinned particles  $S$  can be written as;

$$MS_{ex}^M(\beta') = \beta' \langle U_M \rangle - \int_0^{\beta'} d\beta \langle U_M \rangle \quad (5.8)$$

where  $U_M$  is a thermal average of the potential energy. Total system energy can be decomposed as

$$U_N = U_{PP} + U_{MP} + U_{PM} + U_{MM}$$

where  $U_N$  represent total energy of system.  $U_{PP}, U_{PM}, U_{MP}, U_{MM}$  represent interaction energy between pin-pin (PP), mobile-pin(MP), pin-mobile(PM), mobile-



mobile(MM) particles. Note that  $U_{MP} = U_{PM}$ . We should be aware that the pinned system is produced by the KA model, which has two types of particles, large A and small B particles, and in which we pin a fraction of the particle positions. We now have two additional types of particles: pin A particles are designated as C, while pin B types are designated as D. As a result, there are now four different types of particles, including two movable and two pinned types. Energy can now be expressed as an A, B, C, or D kind of particle as follows:

$$U_N = \sum_{i,j=1}^4 U_{ij}$$

Note that  $U_{ij} = U_{ji}$ . In the pinned system, pin-pin particle has no interaction, hence  $U_{PP} = 0$ . The only source of energy for a pinned system is a moving particle, hence its new source of energy will be;

$$U_M = U_{MM} + U_{MP} + U_{PM} \quad (5.9)$$

Because  $U_{PP} = 0$ ,  $U_{CC}$ ,  $U_{DD}$ ,  $U_{CD}$ , and  $U_{DC}$  will be zero. Now, energy is expressed in terms of the particles A, B, C, and D as follows:

$$U_M = \sum_{i,j=1}^2 U_{ij} + 2 \times \sum_{j=1}^2 \sum_{i=3}^4 U_{ij}$$

This is explained in more detail in chapter 2, Eq. 2.78. We have plotted the excess entropy of pinned systems at various pinning concentrations in Fig.5.17. As the pinning increases, we see a drop in excess entropy.

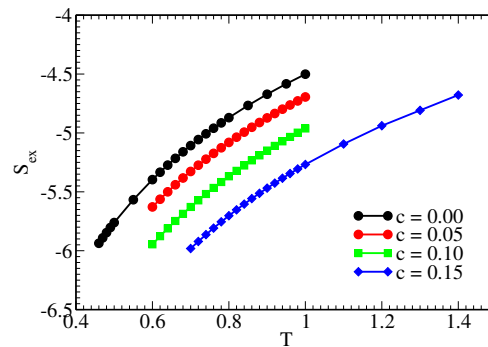


Figure 5.17: *Per mobile particle excess entropy. Excess entropy drops as increasing the pinning concentration.*

## APPENDIX B: Configurations entropy with half interaction potential

As demonstrated in section 5.4.2, employing the TI method system produced a negative entropy and a breakdown of Adam-Gibbs relation. In the pinned system

using the TI method to obtain the excess entropy, we observe that the interaction between a mobile and a pinned particle all together contributes to the loss of entropy of the mobile particle as the pinned particles do not have any entropy (Eq 5.8). In the system where all the particles are mobile, this is not the case. The interaction between the particles contributes to the loss of entropy of both particles. We wanted to test how the entropy behaves if we assume that half of the interaction energy between a pinned and mobile particle contributes to entropy loss (excess entropy). Potential energy for a pinned system is;

$$U_M^I = U_{MM} + \frac{1}{2}U_{MP} + \frac{1}{2}U_{PM} \quad (5.10)$$

In this case, the excess entropy can be written as;

$$S_{ex}^I = \beta' \langle U_M^I \rangle - \int_0^{\beta'} d\beta \langle U_M^I \rangle. \quad (5.11)$$

As shown in Fig.5.18, we find that the excess entropy,  $S_{ex}^I$ , does not decrease with pinning. Rather, it shows a marginal increase. This analysis clearly shows that the decrease in the excess entropy with pinning is due to the higher potential energy contribution of the pinned particles, which leads to a stronger confinement of the mobile particles.

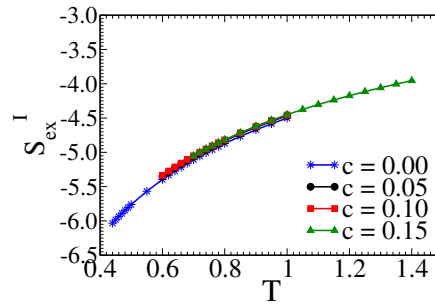


Figure 5.18: *Per mobile particle excess entropy with half interaction,  $S_{ex}^I$ . Excess entropy slightly increases as increasing the pinning concentration.*

The configuration's entropy can now be written as;

$$\begin{aligned} MS_c^I &= MS_{id} + MS_{ex}^I - MS_{vib} \\ &= MS_{id} - MS_{vib} + \beta' \langle U_M^I \rangle - \int_0^{\beta'} d\beta \langle U_M^I \rangle \end{aligned} \quad (5.12)$$

where  $U_M^I$  is the thermal average of the potential energy containing half of the energy generated by the mobile-pin interaction ( $U_M^I$ ). When taking into account full interaction, we find that configurational entropy decreases as the pinning concentration grows (Fig 5.19), but when considering half interaction, surprisingly, we find that the value of  $T_K$  decreases (Fig.5.20) *i.e.* considering half interaction the configurational entropy increases as the pinning concentration increases, as shown in Fig.5.19. This behaviour

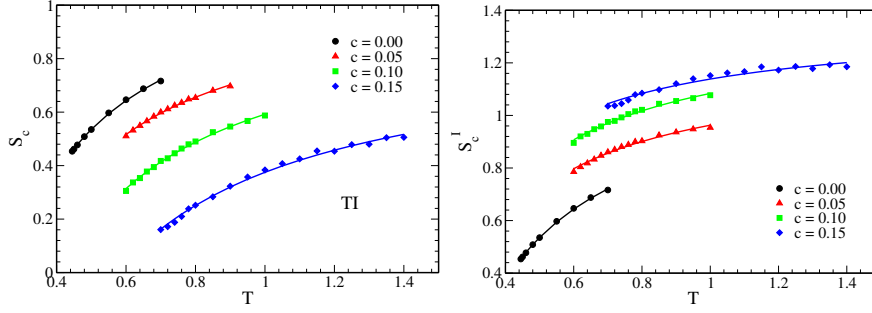


Figure 5.19: *Left side: Per mobile particle configurational entropy,  $TS_c^M = T(S_{id} + S_{ex}^M - S_{vib})$ , as a function of  $T$ . Right side: Per mobile particle configurational entropy with half interaction,  $TS_c^I = T(S_{id} + S_{ex}^I - S_{vib})$ , as a function of  $T$ .*

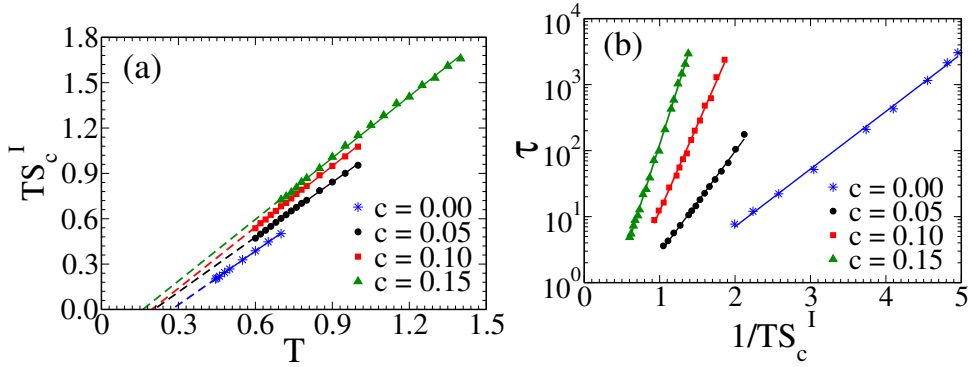


Figure 5.20: (a)  $\tau$  vs.  $1/TS_c^M$  (b)  $\tau$  vs.  $1/TS_c^I$ . The solid lines show the Adam-Gibbs fitting. Adam-Gibbs valid with half interaction.

is similar to that observed for the single particle relaxation dynamics. It was earlier shown that the  $T_{VFT}$  decreases with increasing pinning [49].

In addition, we also find that the Adam-Gibbs relation remains valid when plotted against this entropy (Fig.5.20). The table 5.4 displays the  $T_K$  values for both when we consider total interaction ( $T_K^{TI}$ ) and the partial interaction ( $T_K^{TI(I)}$ ) contributing to the entropy of the mobile particle.  $T_K^{TI}$  rises with rising  $c$ , whereas  $T_K^{TI(I)}$  drops with rising  $c$ .

We do not have a scientific explanation for considering half of the interaction. However, this analysis shows that the reason there is a breakdown of the AG relation in the pinned system is that the interaction between the pinned and mobile particle reduces the entropy of the mobile particle by a significant amount.

### APPENDIX C: Velocity auto correlation function (VACF), density of state (DOS), and fluidity analysis of pinned system

Here, we present some functions used in the calculation of the entropy using 2PT method for the pinned system. The 2PT method is described in chapter 2, section 2.4.2. The first step is to calculate the velocity auto correlation function (VACF). The

Table 5.4: The values of all characteristic temperatures for pinned systems with different pin concentrations  $c$ .  $T_K^{TI}$  is the Kauzmann temperature estimated from TI.  $T_K^{TI(I)}$  is the Kauzmann temperature estimated from the TI method with half interaction potential energy.

$c$	$T_K^{TI}$	$T_K^{TI(I)}$
0.00	0.28	0.28
0.05	0.31	0.21
0.10	0.41	0.19
0.15	0.57	0.16

VACF at various pinning concentrations is shown in Fig. 5.21). Notably, we found that as the pinning concentration increased, the depth of the VACF also increased. This suggests a rise in the caging potential, indicating that the particles become more confined with higher pinning concentrations.

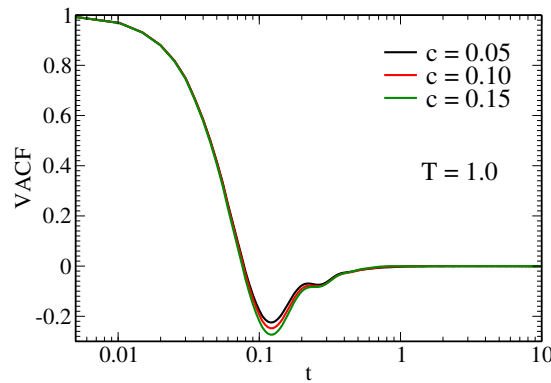


Figure 5.21: *Velocity auto correlation function (VACF) as a function of time.*

We next obtain the Density of States (DOS) from the VACF and plot it against frequency (Fig. 5.22). We then use the 2PT method to separate the gaseous and solid phases. As the pinning concentration increased, we found that the solid contribution to entropy increased, accompanied by a decrease in the gaseous contribution. This DOS analysis is illustrated in Fig. 5.22.

To enhance our understanding, we investigated the fluidity of the system as a function of temperature (Fig. 5.23). Consistent with the DOS findings, the trend indicated a decrease in fluidity with increasing pinning concentration. This aligns with the concept that as the gaseous contribution decreases and the solid contribution increases, the overall fluidity of the system decreases. It also shows that with an increase in pinning, the fluidity of the system decreases.

Our exploration using VACF, DOS, and fluidity provides a clear picture of how increasing pinning concentration affects the system—resulting in heightened caging potential, a shift from gaseous to solid dominance, and a subsequent decrease in fluidity.

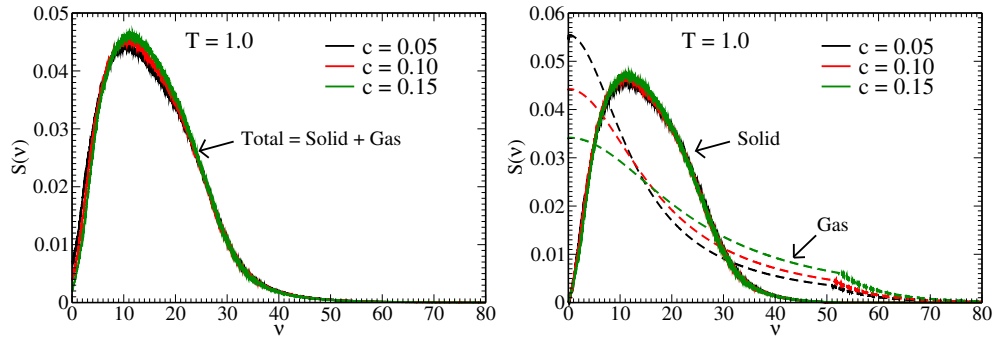


Figure 5.22: (a) Total density of state (DOS) as a function of frequency ( $\nu$ ). (b) Solid and gaseous density of state (DOS) as a function of frequency ( $\nu$ ).

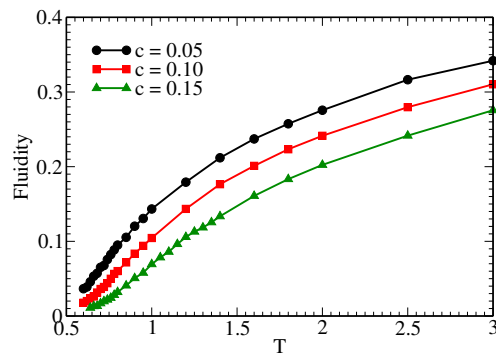


Figure 5.23: Fluidity as a function of temperature ( $T$ ). With increasing pinning concentration ( $c$ ), or decreasing the temperature, mobility decreases because solid contribution increases and gaseous contribution decreases, resulting in fluidity decreasing.

# Chapter 6

## Effect of the presence of pinned particles on the structural parameters of a liquid and correlation between structure and dynamics at the local level

“A goal should scare you a little  
and excite you a lot”.

- Joe Vitale

### 6.1 Introduction

In the previous chapter, we have already introduced the system where a fraction of the particles are pinned. We have shown that the correlation between the dynamics and thermodynamic quantities is not similar to that of a system where all particles are mobile [166, 145]. The entropy calculated via the thermodynamic integration (TI) method [54, 177] deviates from the entropy calculated by the two-phase thermodynamics (2PT) method [168, 169, 171]. The single particle dynamics is controlled by the 2PT entropy, whereas the transition obtained in the collective dynamics due to the overlap of the excluded volume of the pinned particles is predicted by the TI entropy. The entropy calculated via the TI method, which vanishes at a higher temperature, cannot explain the single particle dynamics [166, 49, 173, 174] and is lower than that obtained using 2PT method [145].

The studies mentioned above were all performed at the macroscopic level [166, 49, 173, 174, 145]. However, there have also been microscopic studies of the correlation between entropy and dynamics. The correlation between local pair excess entropy,

which depends on the structure and the local dynamics of the pinned system, was also studied [175]. It was shown that since the pinning process is expected not to affect the structure, the local pair excess entropy remains the same as the unpinned system, whereas the dynamics slows down due to pinning. Thus, there is a decorrelation between pair excess entropy and dynamics even at the microscopic level.

From the above discussion, it appears that both at macroscopic and microscopic levels, the dynamics and the entropy are not correlated. However, at the macroscopic level, pinning decreases the configurational entropy more than slowing down the dynamics [166], whereas, at the microscopic level, the pinning process does not alter the pair excess entropy but slows down the dynamics. Thus, the decorrelation between entropy and dynamics observed at the macroscopic and microscopic levels is just the opposite. Note that for the unpinned system, the macroscopic pair excess entropy,  $S_2$  contributes to 80% of the excess entropy [92]. The configurational entropy  $S_c = S_{id} + S_{ex} - S_{vib}$  has a contribution from three terms: the ideal gas entropy  $S_{id}$ , the excess entropy,  $S_{ex}$  and the vibrational entropy,  $S_{vib}$ . Since pair excess entropy does not change due to pinning, we can expect the excess entropy, which is usually obtained using thermodynamic integration (TI) method [54, 177] also not to change. In that case, we may expect that the other terms are responsible for the observed decrease in the configurational entropy of the pinned systems.

In this chapter, we first revisit the calculation of the configurational entropy. We show that the decrease in the excess entropy is primarily responsible for the decrease in the configurational entropy. We further show that in the calculation of the excess entropy, the pinned particles should be treated as a different species, and the analytical expression shows that compared to the interaction with another mobile particle, the interaction with a pinned particle contributes twice in decreasing the excess entropy of a mobile particle. We next show that when we use a similar methodology in the calculation of the pair excess entropy, both at macroscopic and microscopic levels, it decreases with pinning. The expression of the pair excess entropy shows that this decrease again comes from the stronger interaction between the pinned and mobile particles.

We then extend the recently developed theoretical formulation, where we describe that each particle in a mean field caging potential for the pinned system. Note that, as shown before, this mean field caging potential is obtained from the structure of the liquid [82, 114, 135]. We find that even the mean field potential, both at microscopic and macroscopic levels, shows that the pinned particles have a stronger interaction with the mobile particles, thus increasing the depth of the caging potential and confining the mobile particles. We refer to the inverse depth of the caging potential as the structural order parameter(SOP). Interestingly, a similar confinement effect of the pinned particles was observed in the elastically collective nonlinear equation (ECNLE) theory [178, 179]. In ECNLE theory, the dynamics of the system was obtained using Langevin dynamics on the dynamic free energy surface. The studies showed that with

pinning, the depth of the free energy barrier increases, and the particles are more confined. In the ECNLE theory, while treating the system, the Authors considered that the pinned particles do not change the structure, but the pinned particles are considered to be a different species. Thus, it appears that in any formulation to obtain the stronger confinement effect by the pinned particles, the pinned particles should be treated as a different species.

We next show that contrary to the common belief, the pinning process does change the structure, which can be observed only when the partial radial distribution functions are calculated, assuming the pinned particles are a different species. Our study reveals that with an increase in pinning, it is a combined effect of the change in structure and the stronger contribution of pinned particles in decreasing the potential energy of the mobile particles that reduces both  $S_2$  and SOP, the latter effect playing a more dominant role. Finally, we show that the correlation between the local structural parameters ( $S_2$  and SOP) and local dynamics increases when the above mentioned two effects are taken into consideration in the calculation of  $S_2$  and SOP.

The rest of the chapter is organized as follows: section 6.2 contains the simulation details. The analysis at the macroscopic level is presented in section 6.3 with excess entropy,  $S_{ex}$ , in section 6.3.1, pair excess entropy,  $S_2$ , in section 6.3.2, the depth of local caging potential,  $\beta\Phi_r$ , in section 6.3.3 and the numerical results in section 6.3.4. The analysis at the microscopic level is presented in section 6.4 with microscopic  $S_2$  in section 6.4.1, microscopic  $\beta\Phi_r$  in section 6.4.2 and numerical results in section 6.4.3. In section 6.5, we analyze the structure dynamics correlation at the microscopic level. The chapter ends with a brief conclusion in section 6.6. This chapter contains five Appendix sections at the end.

## 6.2 Simulation Details

In this work, we study a pinned system in which a fraction of particles are artificially pinned at their positions in an equilibrated liquid. For the study of the pinned system, we use the Kob-Andersen 80:20 binary Lennard-Jones mixture[13]. Details of this model are given in chapter 2, section 2.1.2. For creating the pinned system, the following pinning procedure is applied to create the pinned system. The pinned particles are chosen randomly from an equilibrium configuration of the KA system at the target temperature[48, 49]. In this process, the ratio of the two types of particles in the pinned state remains the same as the origin system (80:20). This has been checked after the pinning process. Note that the two pin particles can't be close to each other. The Nosé-Hoover thermostat is used to simulate NVT molecular dynamics in a cubic box with  $N = 4000$ ,  $\rho = 1.2$ , integration time step  $\Delta t = 0.005$ . We have generated three different pinning concentrations “ $c$ ”, i.e., 0.05, 0.10, and 0.15 for this work. Production runs of pinned configurations are long enough to ensure that the overlap correlation function  $q(t)$  (Eq. 2.8) decays to zero during the simulation time. Details



of the pinned system model are given in chapter 2, section 2.1.2.

## 6.3 Entropy and mean field caging potential at macroscopic level

### 6.3.1 Macroscopic excess entropy

The excess entropy of a system is the loss of entropy due to the interaction between particles. The excess entropy of pinned systems has been calculated before, and it was also shown that compared to the unpinned system, the configurational entropy of the system disappears at a higher temperature [166, 145]. As discussed in the Introduction, this disappearance of the configurational entropy at a temperature where the dynamics continues has been a topic of intense research [166, 49, 173, 174, 145]. The configurational entropy,  $S_c = S_{id} + S_{ex} - S_{vib}$  is obtained from the ideal gas entropy,  $S_{id}$ , excess entropy,  $S_{ex}$  and the vibrational entropy,  $S_{vib}$  of the system. All these three terms change due to pinning. Here, we first revisit the configurational entropy calculation and find out which terms are primarily responsible for the vanishing of the configurational entropy of the pinned system at a higher temperature [166, 180]. As shown in chapter 5, we find that as we increase the pinning concentration, the per particle ideal gas entropy increases. However, the per particle excess entropy and per particle vibrational entropy decrease. The decrease in the excess entropy appears to be stronger than the vibrational entropy. We make a comparative analysis of the excess entropy of the pinned and the unpinned systems to understand what leads to this substantial decrease in the excess entropy.

The excess entropy per particle level is expressed as [54, 177];

$$S_{ex}(\beta') = \beta' \langle U \rangle - \int_0^{\beta'} d\beta \langle U \rangle \quad (6.1)$$

where  $\langle U \rangle$  is per partial potential energy.

In the case of a regular binary system, the per particle potential energy in terms of the radial distribution function,  $g(r)$ , can be expressed as [10]:

$$\begin{aligned} \langle U_B \rangle &= 2\pi\rho \int_0^\infty \sum_{i=1}^2 \sum_{j=1}^2 \frac{N_i}{N} \frac{N_j}{N} u_{ij}(r) g_{ij}(r) r^2 dr \\ &= 2\pi\rho \int_0^\infty \sum_{i=1}^2 \sum_{j=1}^2 \chi_i \chi_j u_{ij}(r) g_{ij}(r) r^2 dr \end{aligned} \quad (6.2)$$

where,  $\chi_i = \frac{N_i}{N}$  is the fraction of particles in type  $i$ .  $N$  is the total number of particles in the system.

Note that when we pin particles in a binary system, we actually create a quaternary system of two types of mobile particles and two types of pinned particles. We refer to

the first type of mobile particles as species 1, the second type of mobile particles as species 2, the first type of pinned particles as species 3, and the second type of pinned particles as species 4. The potential energy per particle for a regular quaternary system can be expressed as follows:

$$\begin{aligned}\langle U_Q \rangle &= 2\pi\rho \int_0^\infty \sum_{i=1}^4 \sum_{j=1}^4 \frac{N'_i}{N} \frac{N'_j}{N} u_{ij}(r) g_{ij}(r) r^2 dr \\ &= 2\pi\rho \int_0^\infty \sum_{i=1}^4 \sum_{j=1}^4 \chi'_i \chi'_j u_{ij}(r) g_{ij}(r) r^2 dr\end{aligned}\quad (6.3)$$

Now if we assume that a fraction,  $c$  of particles are pinned then  $N'_1 = (1 - c)N_1$ ,  $N'_2 = (1 - c)N_2$ ,  $N'_3 = cN_1$ ,  $N'_4 = cN_2$ ,  $\chi'_i = \frac{N'_i}{N}$ . The number of mobile particles can be written as  $M = (1 - c)N$ . In our model system, the pinned particles do not interact with each other[166]; thus,  $u_{PP} = u_{33} = u_{34} = u_{43} = u_{44} = 0$ . We also know that the interaction between pinned and mobile particles is symmetric, for example,  $u_{13} = u_{31}$ . These conditions modify the quaternary expression and reduce the first summation in Eq. 6.3 only over types 1 and 2. Moreover, for a system with pinned particles, the excess entropy,  $S_{ex}^M$ , is calculated only for the mobile particles, and the total potential energy is divided only between the  $M$  mobile particles. This further modifies the quaternary expression (Eq. 6.3), and the potential energy at per mobile particle level for the pinned system, which we now also refer to as the modified quaternary system,  $\langle U_M \rangle = \frac{N}{M} \times \langle U_Q(u_{PP} = 0) \rangle$  can be written as;

$$\begin{aligned}\langle U_M \rangle &= 2\pi\rho \int_0^\infty r^2 dr \sum_{i=1}^2 \frac{N'_i}{M} \left[ \sum_{j=1}^2 \frac{N'_j}{N} u_{ij}(r) g_{ij}(r) + 2 \times \sum_{j=3}^4 \frac{N'_j}{N} u_{ij}(r) g_{ij}(r) \right] \\ &= 2\pi\rho \int_0^\infty r^2 dr \sum_{i=1}^2 \frac{(1-c)N_i}{(1-c)N} \left[ \sum_{j=1}^2 \frac{N'_j}{N} u_{ij}(r) g_{ij}(r) + 2 \times \sum_{j=3}^4 \frac{N'_j}{N} u_{ij}(r) g_{ij}(r) \right] \\ &= 2\pi\rho \int_0^\infty r^2 dr \sum_{i=1}^2 \chi_i \left[ \sum_{j=1}^2 \chi'_j u_{ij}(r) g_{ij}(r) + 2 \times \sum_{j=3}^4 \chi'_j u_{ij}(r) g_{ij}(r) \right]\end{aligned}\quad (6.4)$$

The above expression of the potential energy, when replaced in Eq. 6.1, provides us with the excess entropy of the mobile particles in the pinned system,  $S_{ex}^M(\beta')$ . The first and second terms in Eq. 6.4 describe the potential energy of a mobile particle due to the interaction with other mobile particles and pinned particles, respectively. The expression of the first and second term are identical except for the fact that the 2nd term has a factor of 2. This implies that compared to a mobile particle, a pinned particle has a stronger effect in decreasing the potential energy of a mobile particle. In chapter 5, we show that if we neglect this stronger effect of the pinned particles on the mobile particle *i.e.* remove the factor 2 in the second term of  $\langle U_M \rangle$  (Eq. 6.4) then the excess entropy shows a marginal change and the per particle configurational

entropy increases with an increase in pinning density. This is because, with the increase in pinning density, the increase in the ideal gas entropy is more than the decrease in the vibrational entropy. This result is not physical, but it clearly shows that the vanishing of the configurational entropy at higher temperatures is due to the stronger effect of the pinned particles in confining the mobile particles and thus decreasing the excess entropy. We will show in section 6.3.2 and 6.3.3 that this effect of the pinned particles plays an important role in the two body excess entropy and the mean field caging potential.

### 6.3.2 Macroscopic pair excess entropy

The excess entropy,  $S_{ex}$  can be written in terms of an infinite series via the Kirkwood factorization method[57, 181],

$$\begin{aligned} S_{ex} &= S_2 + S_3 + S_4 \dots \\ &= S_2 + \Delta S \end{aligned} \quad (6.5)$$

While  $S_{ex}$  represents the loss of entropy due to total interaction, the pair excess entropy,  $S_2$  describes the loss of entropy due to interaction described by the two-body correlation.  $\Delta S$  is the loss of entropy due to many body correlations (beyond pair correlation). The per particle pair excess entropy, which contributes to 80% of the total excess entropy[92] can be written as[181];

$$\frac{S_2^B}{k_B} = -2\pi\rho \int_0^\infty \sum_{i=1}^2 \sum_{j=1}^2 \chi_i \chi_j \{g_{ij}(r) \ln g_{ij}(r) - (g_{ij}(r) - 1)\} r^2 dr \quad (6.6)$$

Pair excess entropy per particle level for the quaternary system is expressed as;

$$\frac{S_2^Q}{k_B} = -2\pi\rho \int_0^\infty r^2 dr \sum_{i=1}^4 \sum_{j=1}^4 \chi'_i \chi'_j \{g_{ij}(r) \ln g_{ij}(r) - (g_{ij}(r) - 1)\} \quad (6.7)$$

To obtain the pair excess entropy of the pinned system,  $S_2^M$ , we make similar modifications to the pure quaternary system as is done for the calculation of the excess entropy given in the previous system. First, we assume that there is no structure between the pinned particles, *i.e.*  $g_{PP} = g_{33} = g_{44} = g_{34} = g_{44} = 1$ . This assumption is justified as  $u_{33} = u_{34} = u_{43} = u_{44} = 0$ , and we can also neglect any higher order correlation between the pinned particles, thus assuming that the potential of mean force between the pinned particles also vanishes. We also assume that the partial rdf between mobile and pinned particles is symmetric. Thus, the first summation in Eq. 6.7 is only over the mobile particles, types 1 and 2. Next, in the modified system, we calculate the entropy of only the mobile particles. The total pair excess entropy,  $N * S_2^Q(g_{PP} = 1)$  is divided only amongst the mobile particles, and the per particle pair excess entropy of the mobile particles,  $S_2^M = \frac{N}{M} * S_2^Q(g_{PP} = 1)$ . Thus, in the first summation  $\chi'_i$  is replaced by  $\chi_i$  like in Eq. 6.4. The pair excess entropy per particle

level of the mobile particles in the pinned system,  $S_2^M$  can be written as,

$$\begin{aligned} \frac{S_2^M}{k_B} &= -2\pi\rho \int_0^\infty r^2 dr \sum_{i=1}^2 \chi_i \left[ \sum_{j=1}^2 \chi_j' \{g_{ij}(r) \ln g_{ij}(r) - (g_{ij}(r) - 1)\} \right. \\ &\quad \left. + 2 \times \sum_{j=3}^4 \chi_j' \{g_{ij}(r) \ln g_{ij}(r) - (g_{ij}(r) - 1)\} \right] \quad (6.8) \\ &= \frac{S_2^{MM}}{k_B} + \frac{S_2^{MP}}{k_B} \end{aligned}$$

where  $S_2^{MM}$  is the pair excess entropy due to mobile-mobile(MM) interaction and expressed as  $S_2^{MM} = -2\pi\rho \int_0^\infty r^2 dr \sum_{i=1}^2 \sum_{j=1}^2 \chi_i \chi_j \{g_{ij}(r) \ln g_{ij}(r) - (g_{ij}(r) - 1)\}$  and  $S_2^{MP}$  represent the pair excess entropy due to mobile-pin(MP) interaction and expressed as  $S_2^{MP} = -2 \times 2\pi\rho \int_0^\infty r^2 dr \sum_{i=1}^2 \sum_{j=3}^4 \chi_i \chi_j \{g_{ij}(r) \ln g_{ij}(r) - (g_{ij}(r) - 1)\}$ . Note that  $\chi_1 = (1-c)\chi_1'$ ,  $\chi_2 = (1-c)\chi_2'$ ,  $\chi_3 = c\chi_1'$ ,  $\chi_4 = c\chi_2'$ . From Eq. 6.8, we find that similar to that discussed for excess entropy, when we treat the pinned system as this modified quaternary system, the effect of the pinned particles in determining the entropy of the mobile particles is stronger (factor of 2) compared to other mobile particles.

When we pin the particles at their equilibrium position, the structure/rdf of the system is not expected to change. Thus, pinning is believed to keep the equilibrium of the system the same[182, 175, 183]. If the structure/rdf remains the same, then treating the system as quaternary or binary in the calculation of the two body excess entropy gives us identical results,  $S_2^Q = S_2^B$  (see Appendix I). However, note that for the pinned system, the pair excess entropy is not given by  $S_2^Q$  (Eq. 6.7) but by  $S_2^M$  (Eq. 6.8). In the expression of  $S_2^M$ , even if we assume there is no change in structure due to pinning, the pair excess entropy of the system,  $S_2^{M'}$  is different from that of a binary system and can be written as,

$$\begin{aligned} \frac{S_2^{M'}}{k_B} &= -2\pi\rho \int_0^\infty r^2 dr \left[ \chi_1(\chi_1' + 2\chi_3') \{g_{11}(r) \ln g_{11}(r) - (g_{11}(r) - 1)\} \right. \\ &\quad + \chi_1(\chi_2' + 2\chi_4') \{g_{12}(r) \ln g_{12}(r) - (g_{12}(r) - 1)\} \\ &\quad + \chi_2(\chi_1' + 2\chi_3') \{g_{21}(r) \ln g_{21}(r) - (g_{21}(r) - 1)\} \\ &\quad \left. + \chi_2(\chi_2' + 2\chi_4') \{g_{22}(r) \ln g_{22}(r) - (g_{22}(r) - 1)\} \right] \quad (6.9) \\ &= \frac{S_2^B}{k_B} - 2\pi\rho \int_0^\infty r^2 dr \sum_{i=1}^2 \sum_{j=1}^2 \chi_i \chi_{(j+2)}' \{g_{ij}(r) \ln g_{ij}(r) - (g_{ij}(r) - 1)\} \end{aligned}$$

Note that in writing the last equality, we have applied the relation,  $\chi_1 = \chi_1' + \chi_3'$  and  $\chi_2 = \chi_2' + \chi_4'$ . Thus, it shows that even if the pinning process does not change the structure, the pair excess entropy for mobile particles in the pinned system is lower than that in the unpinned system. This implies that the pinned particles have a stronger confinement effect on the mobile particle. In the next section, we will show

that this stronger confining effect of the pinned particles is present not only in entropy but also in other quantities.

### 6.3.3 Macroscopic mean field caging potential

The time evolution of the density, under mean-field approximation, can be written in terms of a Smoluchowski equation in an effective mean field caging potential, which is obtained from the Ramakrishnan-Yussouff free energy functional[76, 82, 114]. Following our earlier studies, the caging potential is calculated by assuming that the cage is static when the particle moves by a distance  $\Delta r$ [82]. The mean field caging potential is expressed in terms of the static structure factor/radial distribution function of the liquid [114]. In this section, we obtain a pinned system's mean field caging potential. Previous work by some of us showed that the depth of caging potential is coupled to the dynamics[82, 114]. Thus, in this study, instead of dealing with the whole potential, we deal with the absolute magnitude of the depth of the caging potential as we view the depth of the caging potential as an energy barrier. We first start with the binary system, where the average depth of mean field caging potential can be expressed as[114];

$$\beta\Phi_r^B(\Delta r = 0) = -4\pi\rho \int r^2 dr \sum_{i=1}^2 \sum_{j=1}^2 \chi_i \chi_j C_{ij}(r) g_{ij}(r) \quad (6.10)$$

Here  $r$  is the separation between the tagged particle and its neighbors and  $\beta = 1/k_B T$ ,  $k_B = 1$ ,  $\rho$  is the density.  $\Delta r$  is the tagged particle's distance from its equilibrium position. According to Hypernetted chain approximation, the direct correlation function,  $C_{ij}(r)$ , can be represented as;

$$C_{ij}(r) = -\beta u_{ij}(r) + [g_{ij}(r) - 1] - \ln[g_{ij}(r)]. \quad (6.11)$$

For a regular quaternary system, the caging potential can be expressed as;

$$\beta\Phi_r^Q(\Delta r = 0) = -4\pi\rho \int r^2 dr \sum_{i=1}^4 \sum_{j=1}^4 \chi'_i \chi'_j C_{ij}(r) g_{ij}(r) \quad (6.12)$$

Next, for the calculation of the mean field caging potential for the pinned system, we apply similar conditions as discussed before for the calculation of the excess and pair excess entropies. Under these conditions the average depth of mean field caging potential of the mobile particles in the pinned system,  $\beta\Phi_r^M$  can be written as;

$$\beta\Phi_r^M(\Delta r = 0) = -4\pi\rho \int r^2 dr \sum_{i=1}^2 \chi_i \left[ \sum_{j=1}^2 \chi'_j C_{ij}(r) g_{ij}(r) + 2 \times \sum_{j=3}^4 \chi'_j C_{ij}(r) g_{ij}(r) \right] \quad (6.13)$$

Note that similar to excess and pair excess entropy, the depth of the mean field caging

potential of mobile particles in this modified quaternary system is affected more by the pinned particles (factor of 2) than by other mobile particles. Also, if the structure does not change due to pinning, the expression of the caging potential for a quaternary and binary system is identical, but that is not the case for the modified quaternary system. The expression for the depth of the mean field caging potential under the assumption that the structure does not change due to pinning can be written as,

$$\begin{aligned}\beta\Phi_r^{M'}(\Delta r = 0) &= -4\pi\rho \int r^2 dr \left[ \chi_1(\chi'_1 + 2\chi'_3)C_{11}(r)g_{11}(r) + \chi_1(\chi'_2 + 2\chi'_4)C_{12}(r)g_{12}(r) \right. \\ &\quad \left. + \chi_2(\chi'_1 + 2\chi'_3)C_{21}(r)g_{21}(r) + \chi_2(\chi'_2 + 2\chi'_4)C_{22}(r)g_{22}(r) \right] \\ &= \beta\Phi_r^B(\Delta r = 0) - 4\pi\rho \int r^2 dr \sum_{i=1}^2 \sum_{j=1}^2 \chi_i \chi'_{(j+2)} C_{ij}(r) g_{ij}(r)\end{aligned}\tag{6.14}$$

In the last equality we have applied the relation that  $\chi_1 = \chi'_1 + \chi'_3$  and  $\chi_2 = \chi'_2 + \chi'_4$ . The above expression suggests that even when we assume that the structure does not change due to pinning, the depth of the caging potential for the pinned system is deeper compared to the unpinned system. This higher confinement effect comes due to the stronger interaction with the pinned particles. Interestingly, a similar effect of the pinned particles has been discussed while studying the nonlinear Langevin equation on a dynamic free energy surface [178, 179]. Note that our mean field caging potential is obtained from the functional derivative of the static version of this dynamic free energy [184, 76]. Similar to the methodology used here, their study, [178, 179] on a monoatomic liquid treats the pinned system as a binary system, thus considering the pinned particle as a different species. They also consider the dynamic free energy of only the mobile particles. Under these conditions, they show that the free energy barrier and confinement of the mobile particles increase with pinning density.

### 6.3.4 Numerical results for the macroscopic pair excess entropy and mean field caging potential

Note that the two body excess entropy and the mean field caging potential are both functions of the radial distribution function (rdf) given by,

$$g_{ij}(r) = \frac{V}{N_i N_j} \left\langle \sum_{\alpha=1}^{N_i} \sum_{\beta=1, \beta \neq \alpha}^{N_j} \delta(r - r_\alpha + r_\beta) \right\rangle\tag{6.15}$$

where  $V$  is the system's volume,  $N_i$ ,  $N_j$  are the number of particles of the  $i$  and  $j$  types, respectively.  $r_\alpha$ ,  $r_\beta$  are the  $\alpha^{th}$  and  $\beta^{th}$  particle's position in the system respectively.

In Fig. 6.1, we plot the partial rdfs of the system where we do not differentiate between the pinned and unpinned particles and we find that, as expected, the rdf

remains the same as the unpinned regular KA model ( $c=0$ ).

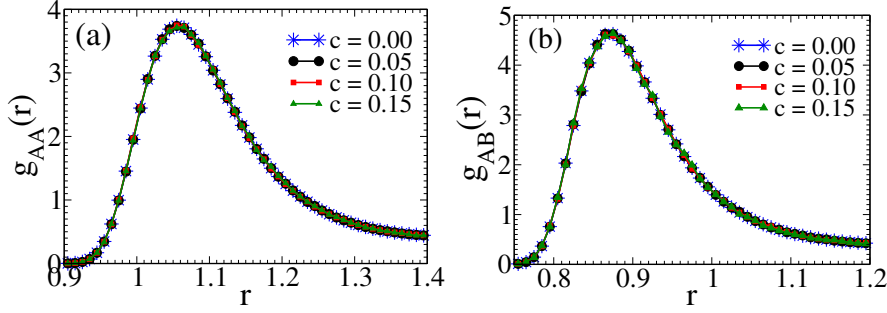


Figure 6.1: *Radial distribution function,  $g(r)$  while treating the pinned system as a binary system, at  $T = 0.68$  (a)  $g_{AA}$  as a function of  $r$  (b)  $g_{AB}$  as a function of  $r$ . Here  $A$  and  $B$  are the bigger and smaller sizes of particles respectively.*

In the rest of the article when we refer to the unpinned binary KA system, following the usual norm, we refer to the particles as  $A$  and  $B$  types. However, as discussed in the previous sections, when we pin particles in a binary system, we actually create a quaternary system. We refer to the mobile  $A$  type of particles as 1, mobile  $B$  type of particles as 2, pinned  $A$  type of particles as 3, and pinned  $B$  type of particles as 4.

We next plot some representative partial rdfs assuming the system to be quaternary at different pinning concentrations (Fig. 6.2). We find that with increased pinning density, the partial rdfs start deviating from the  $c=0$  system. With an increase in “ $c$ ”, there is a drop in the peak value of the rdfs between two mobile particles ( $g_{11}$ ,  $g_{12}$ ). On the other hand, the first peak height of the partial rdfs between mobile and pinned particles ( $g_{13}$ ,  $g_{14}$ ) grows with “ $c$ ”. To ensure that this is not an art effect of choosing the pinned particles as a different species, in the  $c=0$  system, we randomly choose 15% of the particles and treat them as a different species. In Fig. 6.3, we show that in that case,  $g_{11} = g_{13} = g_{AA}$ . A similar result is also observed for other partial rdfs (not shown here). This clearly shows that when we pin a certain fraction of particles, contrary to the common belief, there is a structural change.

We observe that this structural change happens quickly, immediately after the pinning process. We calculate  $g(r)$ , averaged from  $t = 0 - 100$  and  $t = 101 - 200$ , where the pinning is performed at  $t=0$ . We find that both rdfs overlap (Appendix II, Fig. 6.11). In Appendix II, Fig. 6.12, we also show that  $\chi'_1 g_{11} + \chi'_3 g_{13}$  is the same as  $\chi_A g_{AA}$  and  $\chi'_2 g_{12} + \chi'_4 g_{14}$  is the same as  $\chi_B g_{BB}$ . This is precisely why we do not see a change in structure when the pinned particles are not treated as a different species (Fig. 6.1). Note that this change in the partial rdfs is independent of the integration timestep and system size (Fig. 6.14).

Thus, from this analysis, it is clear that the structure of the system does change when particles are pinned. However, this change is significant at higher pinning densities only when we treat the pinned particles as a different species. In Fig. 6.4, we plot the pair excess entropy,  $S_2^{M'}$  (Eq. 6.9) and the caging potential,  $\beta\Phi_r^{M'}$  (Eq. 6.14) of

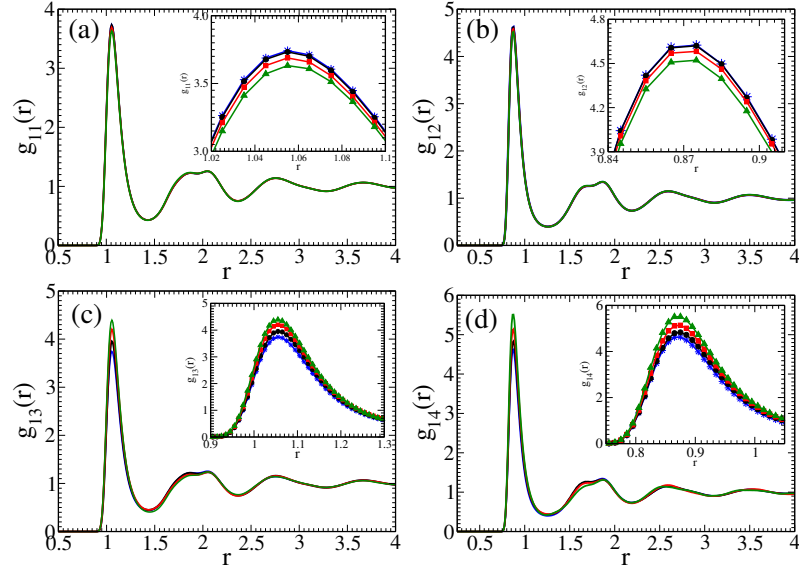


Figure 6.2: Radial distribution function,  $g(r)$  while treating the pinned system as a quaternary system, at  $T = 0.68$ . (a)  $g_{11}$  as a function of  $r$  (b)  $g_{12}$  as a function of  $r$  (c)  $g_{13}$  as a function of  $r$  (d)  $g_{14}$  as a function of  $r$ . Inset: We have zoomed onto the first peak of the respective figures, which clearly shows the difference in the radial distribution functions. Note that color coding is similar to Fig. 6.1. Here, we refer to the mobile A type of particles as 1, mobile B type of particles as 2, pinned A type of particles as 3, and pinned B type of particles as 4.

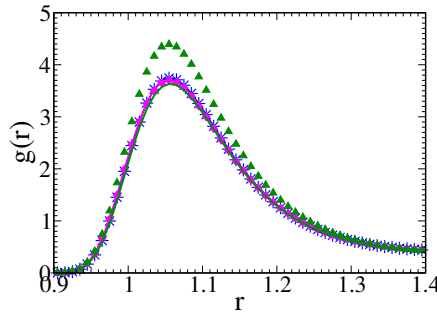


Figure 6.3: Comparison between radial distribution functions,  $g(r)$ s by randomly picking 15% particles in the KA system and treating them as different species (magenta, diamond =  $g_{13}$ , magenta solid line =  $g_{11}$ ) and pinning 15% of particles position during the simulation and treating the pinned particles as different species (green, triangle =  $g_{13}$ , green solid line =  $g_{11}$ ). We also plot the  $g(r)$  for a regular KA ( $c=0$ ) system for comparison (blue, star). The plots are shown only for the big particles.

the pinned systems where we assume that the structure does not change due to pinning. We also plot  $S_2^M$  (Fig. 6.4 (a)) and  $\beta\Phi_r^M$  (Fig. 6.4 (b)), where we consider that the structure changes due to pinning. We find that, even when we consider that the structure does not change, the pair excess entropy of the pinned system differs from that of the binary system and decreases with increasing pinning density. This decrease in entropy is due to the stronger effect of the pinned particles in confining the mobile



particles. When we consider that the structure changes due to pinning, as shown in Fig. 6.2, then the entropy further decreases, and like the structure, this decrease is significant at higher pinning densities. The plot of the mean field caging potential shows a similar effect. The caging potential depth increases with pinning, even if the change in the structure due to pinning is ignored. There is a further increase in the depth when the change in the structure is taken into account.

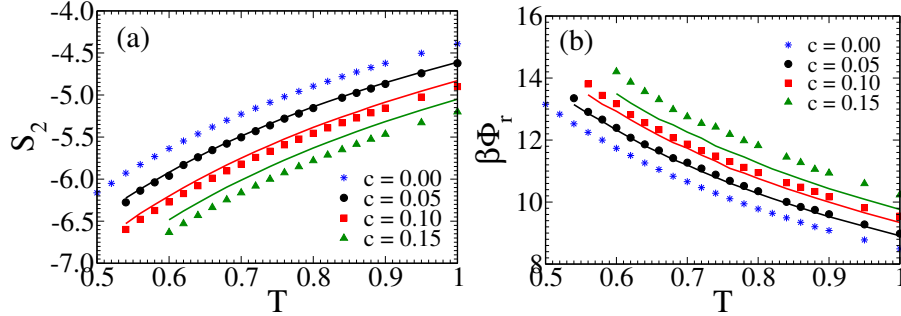


Figure 6.4: (a) Macroscopic  $S_2$  as a function of  $T$ , (b) macroscopic  $\beta\Phi_r$  as a function of  $T$ . Solid line represents  $S_2^{M'}$  (Eq. 6.9) or  $\beta\Phi_r^{M'}$  (Eq. 6.14) and symbol represents  $S_2^M$  (Eq. 6.8) or  $\beta\Phi_r^M$  (Eq. 6.13).

Thus, we find that both the pair excess entropy and the mean field caging potential for the pinned system differ from that of the unpinned system, and this difference comes due to two factors. Firstly, compared to the interaction between two mobile particles, the interaction between a mobile and a pinned particle is stronger, leading to a decrease in entropy and an increase in the caging potential. Secondly, due to pinning, the structure of the liquid changes, and this further decreases the entropy and increases the mean field caging potential. As seen from Fig. 6.4, the first effect is stronger and plays a dominant role.

In Appendix I, we show that the well-known crossover[1] between the excess entropy and the pair excess entropy takes place at a physically meaningful temperature only when we take into consideration these two effects in the calculation of the entropy.

## 6.4 Pair excess entropy and mean field caging potential at the microscopic level

In the previous section, we developed the protocol for calculating the caging potential and pair excess entropy at the macroscopic level for the pinned system. However, our primary goal is to understand how these two order parameters can describe the dynamics at the local level. We clearly demonstrate that the pinned system should be treated as a modified quaternary system. In this section, we make a comparative analysis of these two structural quantities, when the pinned system is treated as a binary system and a modified quaternary system. First, we start with the microscopic expressions, which are obtained from the macroscopic expressions. The bigger "A"

particles, which are larger in number, are the ones for which all microscopic calculations are performed. This is done to make sure that there is no size inhomogeneity, which we know also affects the dynamics[185].

### 6.4.1 Microscopic pair excess entropy

Calculation of the pair excess entropy at the macroscopic level ( $S_2$ ) is given in section 6.3.

In the binary system, the pair excess entropy of each mobile "A" particle, which is type "1" in our notation, can be expressed by removing the first summation in Eq. 6.6;

$$\frac{S_2^B(A)}{k_B} = -2\pi\rho \int_0^\infty r^2 dr \sum_{j=1}^2 \chi_j \{g_{1j}(r) \ln g_{1j}(r) - (g_{1j}(r) - 1)\} \quad (6.16)$$

Similarly, in the modified quaternary system, the pair excess entropy of each mobile "A" particle (type 1) can be expressed by removing the first summation in Eq. 6.8;

$$\begin{aligned} \frac{S_2^M(A)}{k_B} = & -2\pi\rho \int_0^\infty r^2 dr \left[ \sum_{j=1}^2 \chi'_j \{g_{1j}(r) \ln g_{1j}(r) - (g_{1j}(r) - 1)\} \right. \\ & \left. + 2 \times \sum_{j=3}^4 \chi'_j \{g_{1j}(r) \ln g_{1j}(r) - (g_{1j}(r) - 1)\} \right] \end{aligned} \quad (6.17)$$

Note that the differences between the binary and modified quaternary are the following. In the binary expression, when treating the neighbors, we do not differentiate between the mobile and pinned particles; however, in the quaternary expression, we do. Thus, in the binary expression, the effect of the mobile neighbors on the tagged particle is the same as that of the pinned neighbors. However, in the quaternary expression, the effect of the pinned neighbors on the tagged particle is twice that of the mobile neighbors. As shown in the macroscopic calculation (Fig. 6.4), it is this second effect that plays a dominant role in differentiating between the binary and the modified quaternary values of the entropy.

### 6.4.2 Microscopic mean field caging potential

The macroscopic calculation of the depth of the caging potential ( $\beta\Phi_r$ ), the inverse of which we refer to as the structural order parameter (SOP), is given in section 6.3.3. At the microscopic level for a binary system, the caging potential of a mobile "A" type of particle can be written by removing the first summation in Eq. 6.10;

$$\beta\Phi_r^B(A, \Delta r = 0) = -4\pi\rho \int r^2 dr \sum_{j=1}^2 \chi_j C_{1j}(r) g_{1j}(r) \quad (6.18)$$

The mean field caging potential for a mobile "A" type of particle in a modified quaternary system can be written by removing the first summation in Eq. 6.13,

$$\beta\Phi_r^M(A, \Delta r = 0) = -4\pi\rho \int r^2 dr \left[ \sum_{j=1}^2 \chi_j' C_{1j}(r) g_{1j}(r) + 2 \times \sum_{j=3}^4 \chi_j' C_{1j}(r) g_{1j}(r) \right] \quad (6.19)$$

Thus, note that similar to that discussed for the pair excess entropy, in the modified quaternary expression, compared to the mobile neighbors, the pinned neighbors have a stronger effect in confining the tagged particle.

### 6.4.3 Numerical results for the microscopic pair excess entropy and mean field caging potential

To perform the microscopic investigation, we determine  $\beta\Phi_r(\Delta r = 0)$  and  $S_2$  for every snapshot at the single particle level that requires the partial rdfs to be calculated at a single particle level. In this calculation, the sum of Gaussian can be used to express the single particle partial rdf in a single frame, and it is calculated as follows[55];

$$g_{ij}^\alpha(r) = \frac{1}{4\pi\rho r^2} \sum_{\beta} \frac{1}{\sqrt{2\pi\delta^2}} \exp^{-\frac{(r-r_{\alpha\beta})^2}{2\delta^2}} \quad (6.20)$$

where " $\alpha$ " is the particle index,  $\rho$  is the density. The Gaussian distribution's variance ( $\delta$ ) is employed to transform the discontinuous function into a continuous form. We use  $\delta = 0.09\sigma_{AA}$  for this work. Single particle rdf is used to derive the direct correlation function at the single particle level from Eq. 6.11.

We can determine caging potential (Eq. 6.10, 6.12, 6.13) by combining the direct correlation function (Eq. 6.11) and particle level rdf (Eq. 6.20). This leads to a term that is a product of the interaction potential and the rdf. As shown in an earlier work[114], at distances shorter than the average rdf, the particle level rdf generated by the Gaussian approximation has finite values. At small " $r$ " due to this finite value of the rdf, its product with the interaction potential, which diverges at small " $r$ ", leads to a large unphysical contribution from this range. To get around this problem, we use an approximate expression of the direct correlation function,  $C^{approx}(r) = [g_{ij}(r) - 1]$  where we assume that the interaction potential is equal to the potential of mean force  $-\beta u_{ij}(r) = \ln(g_{ij}(r))$ . It has also been shown earlier that using  $C_{ij}^{approx}(r)$  marginally improves the theoretical prediction of structure-dynamics correlation[185, 135]. In the rest of the microscopic calculation, we will use  $C_{ij}^{approx}(r)$  in place of  $C_{ij}(r)$ .

In Fig. 6.5, we plot the distribution of pair excess entropy and local caging potential by describing the pinned system as binary. Note that for all the cases, the quantities are calculated only for the mobile "A" particles. We find that the distribution remains similar to the unpinned system (KA model at  $c=0$ ). This is because the expressions

are identical for pinned and unpinned systems, and even for  $c=0.15$ , there are enough mobile “A” particles to give the correct statistics. However, when we calculate the quantities assuming the pinned system as a modified quaternary system (Eq. 6.13 and 6.8), we observe that as “ $c$ ” increases, the depth of the caging potential increases and the pair excess entropy decreases. Distribution of  $\beta\Phi_r^M$ , and  $S_2^M$  are shown in Fig. 6.5. This analysis clearly shows that the entropy and the SOP (inverse depth of the caging potential) are higher when the system is treated as binary compared to when it is treated as a modified quaternary. In the next section, we will show that the correlation between the dynamics and structural quantities differs when we treat the pinned system as binary or modified quaternary.

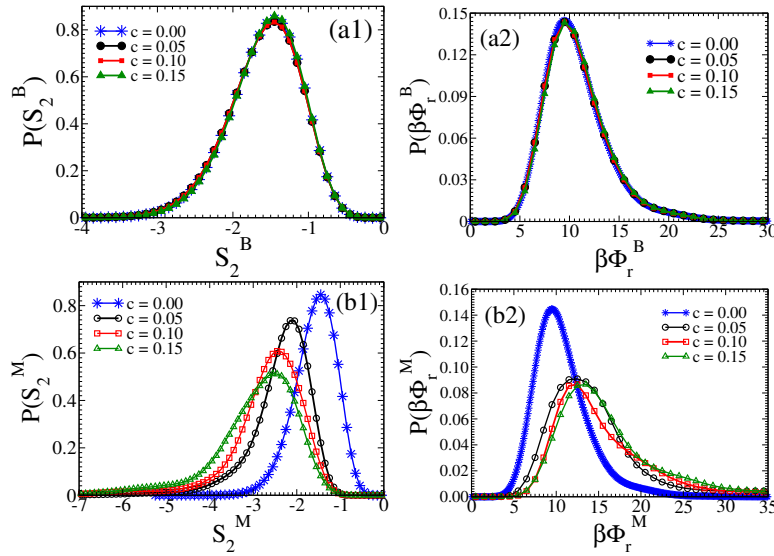


Figure 6.5: *Distribution of pair excess entropy ( $S_2$ ) and depth of mean field caging potential ( $\beta\Phi_r$ ) in different pinned systems at  $T = 0.68$ . (a1) - Distribution of  $S_2$  treating pinned system as binary, (a2) Distribution of  $\beta\Phi_r$  treating pinned system as binary (b1) - Distribution of  $S_2$  treating pinned system as modified quaternary, (b2) Distribution of  $\beta\Phi_r$  treating pinned system as modified quaternary. The distribution remains the same for binary treatment, while for the modified quaternary treatment, the caging potential increases with increasing  $c$ , and pair excess entropy decreases, with increasing  $c$ .*

## 6.5 Correlation between structure and dynamics at microscopic level

In the following section, we study the correlation between two structural order parameters, namely the  $S_2$  and SOP, with the dynamics using different techniques. To make a comparative analysis, while calculating the structural quantities, we treat the pinned system both as binary and modified quaternary systems.

### 6.5.1 Correlation between structure and dynamics using isoconfiguration runs

In this section, we study the correlation between structure and dynamics using isoconfiguration runs (IC). IC is a powerful technique developed by Harrowell et al.[139, 140, 107, 141] to examine the role the structure plays in the dynamics (details are given in Appendix III).

We calculate the Spearman rank correlation,  $C_R(X, Y) = 1 - \frac{6 \sum d_i^2}{m(m^2-1)}$  (where  $d_i^2 = R(X_i) - R(Y_i)$  is the difference between the ranks,  $R(X_i)$  and  $R(Y_i)$  of the raw data  $X_i$  and  $Y_i$  respectively, and  $m$  denotes the number of data), between the mobility,  $\mu$  and the pair excess entropy ( $C_R(\mu, S_2)$ ), and between the mobility,  $\mu$  and the SOP  $C_R(\mu, 1/\beta\Phi_r)$ . In Figs. 6.6(a) and 6.6(b), we plot  $C_R(\mu, S_2)$  and  $C_R(\mu, 1/\beta\Phi_r)$  respectively, for the pinned systems as a function of scaled time. We observe that when considering the system as a binary system, the correlations,  $C_R(\mu, S_2^B)$  and  $C_R(\mu, 1/\beta\Phi_r^B)$  decrease as the pinning concentration increases (Fig. 6.6). This observation is concurrent with the findings of Williams *et al.*[175]. However, when the system is treated as a modified quaternary system, we observe an increase in  $C_R(\mu, S_2^M)$  and  $C_R(\mu, 1/\beta\Phi_r^M)$  compared to when the system is treated as binary. This suggests that treating the system as binary does not capture the full complexity of the structure-dynamics relationship. In the modified quaternary treatment of the system, the pinning decreases the pair excess entropy and the SOP, which is commensurate with the slowing down of the dynamics.

Between the SOP and the pair excess entropy, we find that the SOP can predict the dynamics better and  $C_R(\mu, 1/\beta\Phi_r^M) > C_R(\mu, S_2^M)$ . This is similar to that observed in an earlier study where, for attractive systems compared to entropy, the SOP is a better predictor of the dynamics [135]. Also note that for all values of "c", the peak height of the  $C_R(\mu, 1/\beta\Phi_r^M)$  almost remains constant, whereas the peak height of  $C_R(\mu, S_2^M)$  drops with an increase in "c". Thus the difference between  $C_R(\mu, 1/\beta\Phi_r^M)$  and  $C_R(\mu, S_2^M)$  increases with "c". This drop in the value of  $C_R(\mu, S_2^M)$  with an increase in "c" may be connected to the breakdown of the AG relationship at the macroscopic level. However, we cannot calculate the configurational entropy at the microscopic level, but we do find from Fig. 6.5 that the shift in the distribution of the pair excess entropy with pinning density is stronger than the shift in the distribution of SOP.

We also find that with increasing pinning concentration, the peak height of  $C_R(\mu, 1/\beta\Phi_r^B)$  moves to smaller values of  $t/\tau_\alpha$ . A similar observation was made while comparing the more fragile Lennard-Jones (LJ) and the less fragile Weeks-Chandler-Anderson (WCA) models[135]. Note that in the case of pinned systems, the fragility decreases with increasing "c"[49]. Thus, it appears that for more fragile systems, the correlation between structure and dynamics continues for longer times. However, at this point, this is only a conjecture, and to make more concrete statements, further investigations are needed, which is beyond the scope of the present study.

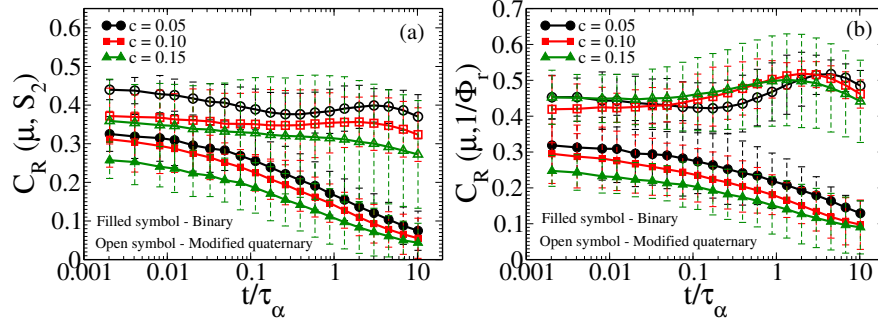


Figure 6.6: Spearman rank correlation,  $C_R$  between different parameters, while treating the pinned system as binary (filled symbol) and modified quaternary (open symbol) (a) Spearman rank correlation ( $C_R$ ) between mobility ( $\mu$ ) and pair excess entropy ( $S_2$ ) (b) Spearman rank correlation ( $C_R$ ) between mobility ( $\mu$ ) and inverse depth of caging potential ( $1/\beta\Phi_r$ ). Working temperature for  $c = 0.05, 0.10$  and  $0.15$  is  $0.52, 0.60,$  and  $0.68$  respectively. Note that  $T$  is chosen such that all the pinned systems have approximately the same  $\tau_\alpha \approx 10^3$ .

## 6.5.2 Analysis of dynamics of particles belonging to the softest and hardest regions

Since we show that the inverse of the mean field caging potential, SOP, is a better predictor of the dynamics, in the next two subsections, we will present the study of the structure-dynamics correlation using only the SOP. At short timescales, we expect to observe a significant difference in the dynamics of the hardest (in a deep cage) and softest (in a shallow cage) particles. The hardest particles, less likely to escape their local cages, will exhibit slower dynamics. On the other hand, the softest particles, with a higher probability of moving, will display faster dynamics. However, over a longer time, as the cage evolves, the separation in dynamics between the hardest and softest particles diminishes [114, 82, 185]. We average over a few (approximately 2-3) hardest and softest particles and compare their dynamics via the overlap function (Eq. 2.8). Note that the identity of the soft and hard particles depends on how the SOP is calculated, *i.e.* assuming the system to be binary or modified quaternary.

The dynamics of the hardest and softest particle for different concentrations of the pinning is shown in Fig. 6.7. When we calculate the SOP treating the system as a modified quaternary system, the difference in dynamics between the hard and the soft particles is wider compared to the case where the system is treated as binary (Fig. 6.7). Note that the difference is greater for the hard particles. This is because our analysis reveals that the identity of the softest particles does not change when we treat the system as binary or modified quaternary. However, the identity of the hardest particles completely changes because, in the binary treatment, we neglect the stronger interaction between the pinned and the mobile particles, which is present in the modified quaternary treatment. Due to this effect in the modified quaternary treatment, the hardest particles are the ones that have pinned particles as their neighbors. As shown in Fig. 6.7, the hardest particles, as identified by the modified quaternary

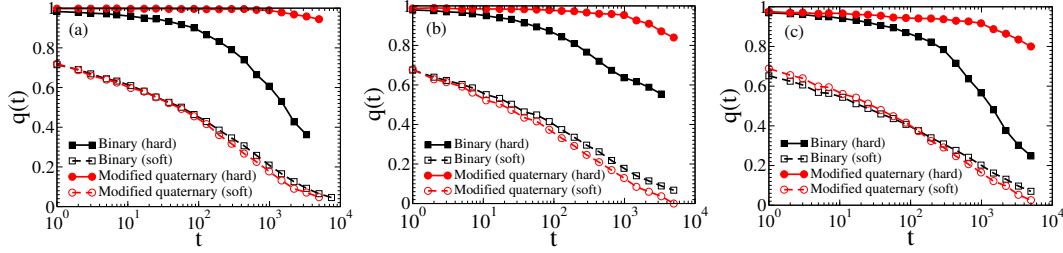


Figure 6.7: Comparison of the dynamics of a few hardest (filled symbol) and a few softest (open symbol) particles at different pinning concentrations while treating the pinned system as binary (Black), and modified quaternary (Red) (a)  $c = 0.05$  (at  $T = 0.52$ ), (b)  $c = 0.10$  (at  $T = 0.60$ ) (c)  $c = 0.15$  (at  $T = 0.68$ ). Note that  $T$  is chosen such that all pinned system has approximately the same  $\tau_\alpha$ .

treatment, are slower than those identified by the binary treatment. This is precisely the reason why the modified quaternary treatment of the system shows higher value of  $C_R(\mu, 1/\beta\Phi_r^M)$  compared to the binary treatment of the system.

### 6.5.3 Correlation between structure and dynamics and prediction of onset temperature

In this section, we use the structure dynamics correlation to identify the onset temperature of the glassy dynamics, a methodology used in earlier studies[108, 114].

We identify fast particles using a well-documented method[136, 137, 114] (details are given in Appendix IV). In Fig. 6.8 we plot  $P_R(1/\beta\Phi_r)$  as a function of temperature for different  $1/\beta\Phi_r$  values and find that it can be expressed in an Arrhenius form,  $P_R(1/\beta\Phi_r) = P_0(1/\beta\Phi_r) \exp(\Delta E(1/\beta\Phi_r)/T)$ , where activation energy,  $\Delta E$  is a function of  $1/\beta\Phi_r$  and is higher for smaller  $1/\beta\Phi_r$  values. The plots cross at a certain temperature, which describes the limiting temperature where the theory is valid[114] and has been identified earlier as the onset temperature of the supercooled liquid[108, 114, 185].

In this analysis, we find that when we treat the system as binary, the onset temperature remains similar for all pinning concentrations. However, when we treat the system as a modified quaternary system, the onset temperature increases with increasing pinning concentration[180]. As we show in chapter 5, this predicted onset temperature is similar to the onset temperature predicted from the well known inherent structure energy method (Fig. 5.1 and Table 5.1)[3].

## 6.6 Conclusion

As discussed in the Introduction, earlier studies on the pinned system have shown that both at macroscopic and microscopic levels, the correlation between the dynamics and entropy breaks down. However, the nature of the breakdown at the microscopic and

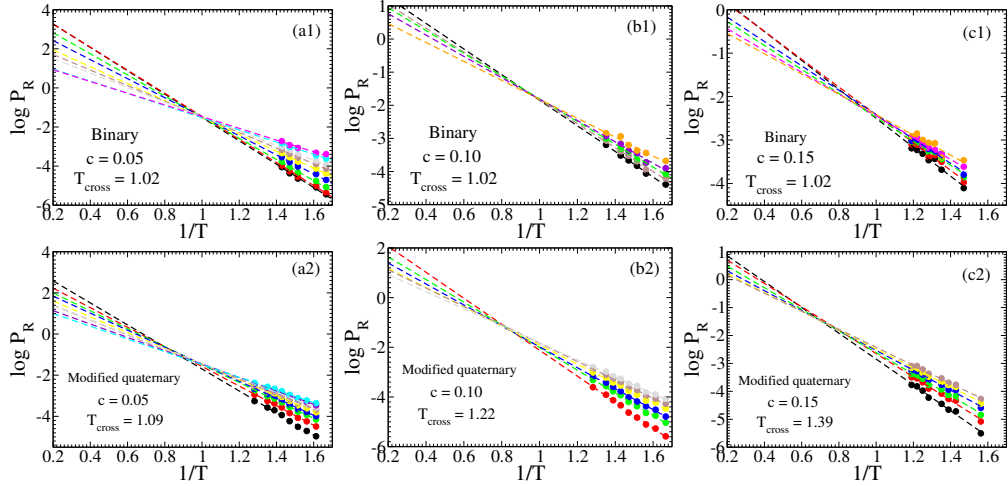


Figure 6.8:  $\log P_R(1/\beta\Phi_r)$  as a function of  $1/T$  at different values of the SOP ( $1/\beta\Phi_r$ ). Top panel - In the calculation of the SOP, the pinned system is treated as a binary system (a1)  $c = 0.05$ , (b1)  $c = 0.10$ , and (c1)  $c = 0.15$ . Bottom panel- In the calculation of the SOP, the pinned system is treated as a modified quaternary system (a2)  $0.05$ , (b2)  $c = 0.10$ , (c2)  $c = 0.15$ .

macroscopic levels is not similar but just the opposite. At the macroscopic level, with pinning, the configurational entropy disappears, whereas the dynamics continues [166, 145, 173]. At the microscopic level, the pair excess entropy remains high and the same as the unpinned system, whereas the dynamics slows down with an increase in pinning density [175]. This is possible only when the macroscopic configurational entropy and the microscopic pair excess entropy are uncorrelated. However, it is well known that for the unpinned systems, the pair excess entropy contributes to about 80% of the excess entropy, which in turn contributes to the configurational entropy [92]. Thus, to understand the different results at the macroscopic and microscopic levels, we revisit the excess entropy calculation of the pinned system.

We show that when we pin particles in a binary system, we should treat this pinned system as a quaternary system under the assumption that there is no interaction between pinned particles (an assumption we use while simulating the system) and the potential energy is only distributed amongst the mobile particles. The excess entropy of this modified quaternary system predicts that the effect of a pinned particle in stabilizing a mobile particle by decreasing the potential energy is a factor of two more than the effect of another mobile particle. We show that this effect leads to the well documented vanishing of configurational entropy at higher temperatures[180] and the breakdown of the Adam-Gibbs relationship in a pinned system[166, 145].

We follow the same methodology to calculate the pair excess entropy and the mean field caging potential at macroscopic and microscopic levels. We first show that the expression of  $S_2$  and SOP (inverse depth of the mean field caging potential) differ when the system is treated as binary and modified quaternary. In the binary treatment, the effect of a pinned particle on the mobile particle is identical to that of another mobile particle. However, in modified quaternary treatment, similar to that



observed in the calculation of the excess entropy, the pinned particles have a stronger effect on the mobile particles than other mobile particles. We next show that contrary to the common belief that if pinned at the equilibrium position, the properties of the system do not change, pinning changes the structure of the liquid, which can be observed only when we treat the pinned particles as a different species. We then show that when we treat the system as a modified quaternary system, the entropy and the SOP are much lower than that obtained by treating the system as a binary system. The analysis reveals that more than the change in structure, the stronger effect of the pinned particles on the mobile particles plays a dominant role in confining the mobile particles by decreasing the entropy and the SOP. Interestingly, a similar confinement effect of the pinned particles was discussed in an earlier study of a monotonic system, where it was shown that the free energy barrier of the mobile particles increases with pinning density [178, 179]. Note that similar to the the present study in these earlier studies [178, 179], the pinned particles were treated as a different species.

We further study the correlation between structure and dynamics using different techniques. In all cases, we show that compared to the case where the pinned system is treated as a binary system, there is an increased correlation between structural order parameters and the dynamics when the pinned system is treated as a modified quaternary system. This is because, unlike in the binary case, in the modified quaternary case, the pinned particles affect not only the dynamics but also the structural properties. We also show that compared to the entropy, the SOP can predict the dynamics better. The correlation between fast particles and the SOP can only predict the correct onset temperature when the SOP is calculated, assuming the pinned system is a modified quaternary system.

In Summary, our study reveals two important points. The pinning affects not only the bulk macroscopic quantities but also the microscopic quantities. The effect of the pinned particles can be expressed by treating the pinned particles as a different species, which then shows that a pinned particle confines the mobile particle more than another mobile particle which then alters the microscopic expression of the quantities that depend on the structure. Thus, pinning not only slows down the dynamics of the mobile particle but also changes the structural parameters. Along with this, the pinning process also affects the structure of the liquid. In future studies, these two effects should be considered when calculating different properties of the pinned system. Also, note that, like local pair excess entropy, the local mean field caging potential depends on the local structure. This allows us to apply it to experimental colloidal systems where, both for quiescent and sheared systems, we find a good structure dynamics correlation [186]. Thus, the mean field caging potential can be applied to study the structure-dynamics correlation even in experimental pinned systems [175, 187].

## Appendix I: Pair excess entropy

In section 6.3.2, we show that the pair excess entropy can have different expressions when the system is treated as binary, quaternary, and modified quaternary. We also show that the rdf is different when the system is treated as binary and quaternary (section 6.3.4).

If the structure (rdf) does not change, then treating the system as quaternary or binary in the calculation of the  $S_2$  gives us identical results. This can be easily seen when comparing Eq. 6.6 and Eq. 6.8. If we assume that in the rdfs we can replace 3 by 1 and 4 by 2 then Eq. 6.7 can be rewritten as,

$$\begin{aligned}
\frac{S_2^Q}{k_B} &= -2\pi\rho \int_0^\infty r^2 dr \left[ (\chi'_1\chi'_1 + 2\chi'_1\chi'_3 + \chi'_3\chi'_3)\{g_{11}(r) \ln g_{11}(r) - (g_{11}(r) - 1)\} \right. \\
&\quad + (\chi'_1\chi'_2 + \chi'_1\chi'_4 + \chi'_3\chi'_2 + \chi'_3\chi'_4)\{g_{12}(r) \ln g_{12}(r) - (g_{12}(r) - 1)\} \\
&\quad + (\chi'_2\chi'_1 + \chi'_2\chi'_3 + \chi'_4\chi'_1 + \chi'_4\chi'_3)\{g_{21}(r) \ln g_{21}(r) - (g_{21}(r) - 1)\} \\
&\quad \left. + (\chi'_2\chi'_2 + 2\chi'_2\chi'_4 + \chi'_4\chi'_4)\{g_{22}(r) \ln g_{22}(r) - (g_{22}(r) - 1)\} \right] \\
&= -2\pi\rho \int_0^\infty r^2 dr \left[ (\chi'_1 + \chi'_3)^2\{g_{11}(r) \ln g_{11}(r) - (g_{11}(r) - 1)\} \right. \\
&\quad + (\chi'_1 + \chi'_3)(\chi'_2 + \chi'_4)\{g_{12}(r) \ln g_{12}(r) - (g_{12}(r) - 1)\} \\
&\quad + (\chi'_2 + \chi'_4)(\chi'_1 + \chi'_3)\{g_{21}(r) \ln g_{21}(r) - (g_{21}(r) - 1)\} \\
&\quad \left. + (\chi'_2 + \chi'_4)^2\{g_{22}(r) \ln g_{22}(r) - (g_{22}(r) - 1)\} \right] \\
&= -2\pi\rho \int_0^\infty r^2 dr \sum_{i,j=1}^2 \chi_i\chi_j\{g_{ij}(r) \ln g_{ij}(r) - (g_{ij}(r) - 1)\}
\end{aligned} \tag{6.21}$$

The last equality can be written because  $\chi_1 = \chi'_1 + \chi'_3$  and  $\chi_2 = \chi'_2 + \chi'_4$ .

In Fig. 6.9 we plot  $S_2^M$  where the change in structure due to the pinned particles is considered. We find that at high temperatures  $S_2^M$  is larger than  $S_{ex}^M$ , and at low temperatures, the scenario is reversed.

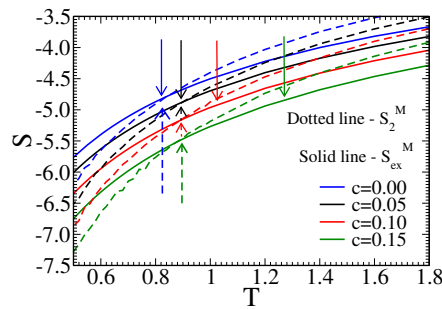


Figure 6.9: The crossing between pair excess entropy  $S_2^M$  (Eq. 6.8) and excess entropy  $S_{ex}^M$  (Eq. 5.8). The  $S_2$  and  $S_{ex}$  crosspoint are indicated by a dotted upward arrow, while the onset temperature from the inherent structure (Fig. 5.1) is shown by a solid downward arrow.

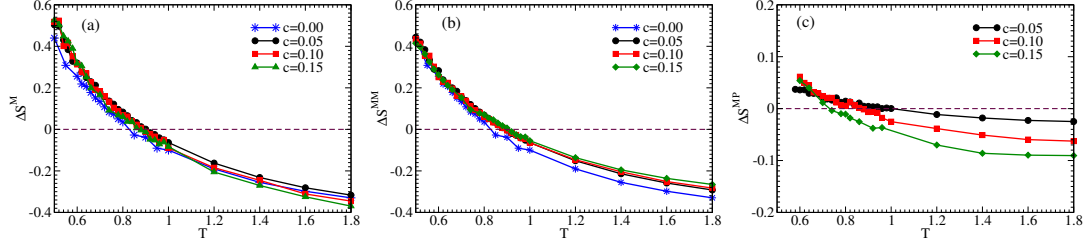


Figure 6.10: *Many body correlation ( $\Delta S$ ), which is a difference between excess entropy ( $S_{ex}^M$ ) and pair excess entropy ( $S_2$ ) while treating the pinned system as modified quaternary (a) Many body correlation due to interaction between mobile-mobile(MM) and mobile-pin(MP) (b) Many body correlation due to interaction between mobile-mobile(MM) (c) Many body correlation due to interaction between mobile-pin(MP).*

The many-body correlations due to MM and MP interaction can be written as;

$$\begin{aligned}
 \Delta S^M &= S_{ex}^M - S_2^M \\
 &= (S_{ex}^{MM} + S_{ex}^{MP}) - (S_2^{MM} + S_2^{MP}) \\
 &= (S_{ex}^{MM} - S_2^{MM}) + (S_{ex}^{MP} - S_2^{MP}) \\
 &= \Delta S^{MM} + \Delta S^{MP}
 \end{aligned} \tag{6.22}$$

The difference between these two entropies is the many body contribution,  $\Delta S$  (Eq. 6.22) which is plotted in Fig.6.10. The temperature where these two entropies cross each other is the  $\Delta S = 0$  (Eq. 6.5) point. For the KA model ( $c=0$ ) and other systems, it was earlier shown that the temperature where these two entropies cross is similar to the onset temperature of glassy dynamics[1, 66]. However, it has also been found that in systems with mean field like characteristics, the temperature where  $\Delta S = 0$  is lower than the onset temperature[80, 188]. The latter scenario is similar to what we find for pinned systems. We find that with the increase in pinning, the difference between the onset temperature and the temperature where the two entropies cross increases. Interestingly, a similar difference between the freezing point and  $\Delta S = 0$  was observed for higher dimensional systems[189] and Gaussian core model (GCM)[190]. Note that if the pair excess entropy is calculated assuming the pinned system to be a binary system, then the cross over between the pair excess entropy and the total entropy will take place at unphysically low temperatures.

To further analyze the origin of this  $\Delta S = 0$  point moving to lower temperatures we separately analyze the contribution from mobile-mobile and mobile-pin interactions (Eq. 6.22). In Fig.6.10 we plot both the contributions to the many-body entropy. We find that the many-body excess entropy due to mobile-mobile interaction does not change with concentration of pinned particles. However, with an increase in “ $c$ ” the  $\Delta S^{MP}$  remains negative till a lower temperature, thus shifting the  $\Delta S^M = 0$  point to a lower temperature. Positive many body excess entropy is connected to activated

motion [1, 80]. Thus, it shows that with an increase in pinning density, there is a suppression of activated motion, and this primarily arises from the mobile-pin interaction.

## Appendix II: Radial distribution function

In Fig. 6.2 (assuming the pinned particles are of a different species) we find that with increased pinning density, the partial rdfs start deviating from the  $c=0$  system. With an increase in “ $c$ ”, there is a drop in the peak value of the rdfs between two mobile particles ( $g_{11}$ ,  $g_{12}$ ). On the other hand, the height of the first peak of the partial rdfs between mobile and pinned particles ( $g_{13}$ ,  $g_{14}$ ) grows with “ $c$ ”.

We observe that this structural change happens quickly, immediately after the pinning process. In Fig. 6.11, we plot  $g(r)$ , averaged from  $t = 0-100$  and  $t = 101-200$ , where the pinning is done at  $t=0$ . We find that both rdfs overlap. This is shown for the  $c=0.15$  system where the difference is maximum.

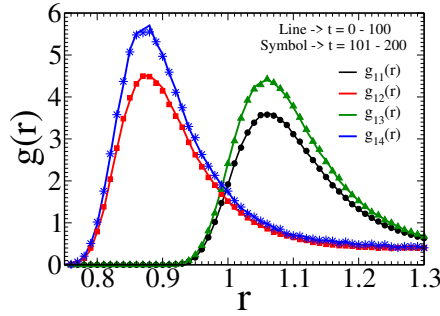


Figure 6.11: Radial distribution function,  $g(r)$  at different time intervals for  $c = 0.15$  system. The solid line and symbol represent the radial distribution function at time  $t = 0 - 100$  and  $t = 100 - 200$ , respectively.

We also show that  $\chi'_1 g_{11} + \chi'_3 g_{13}$  is the same as  $\chi_{AGAA}$  and  $\chi'_2 g_{12} + \chi'_4 g_{14}$  is the same as  $\chi_{BGAB}$  (Fig. 6.12). This is precisely why we do not see a change in structure when the pinned particles are not treated as a different species (Fig. 6.1).

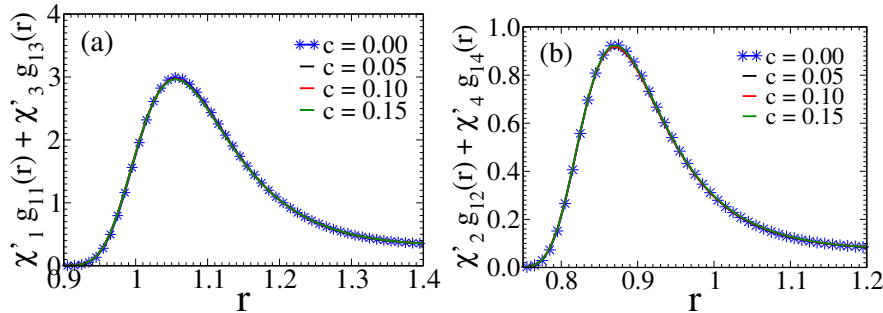


Figure 6.12: (a)  $(\chi'_1 g_{11} + \chi'_3 g_{13})$  of the pinned system and  $\chi_{AGAA}$  of the KA system as a function of  $r$  (b)  $(\chi'_2 g_{12} + \chi'_4 g_{14})$  of the pinned system and  $\chi_{BGAB}$  of the KA system as a function of  $r$ .

To check the system size dependence, in Fig. 6.13, we plot the rdfs for a 4000 particle and 1000 particle system. We find that change in the rdf with pinning is

almost independent of the system size, with the difference between the rdfs of the unpinned and pinned systems increasing marginally for larger system sizes.

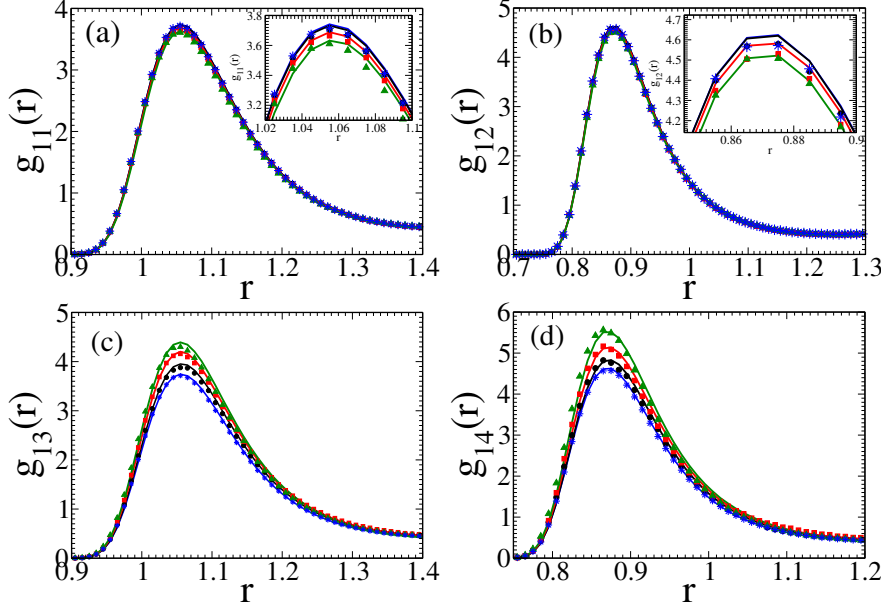


Figure 6.13: *System size dependence in radial distribution function,  $g(r)$  while treating the pinned system as a quaternary system, at  $T = 0.68$  (a)  $g_{11}$  as a function of  $r$  (b)  $g_{12}$  as a function of  $r$  (c)  $g_{13}$  as a function of  $r$  (d)  $g_{14}$  as a function of  $r$ . Inset: We have zoomed onto the first peak of the respective figures, which clearly shows the difference in the radial distribution functions. Note that color coding is similar to Fig. 6.1. Here we refer to the mobile A type of particles as 1, mobile B type of particles as 2, pinned A type of particles as 3, and pinned B type of particles as 4. The solid line represents the 4000 particle system and the symbol represents the 1000 particle system.*

We also check the dependence of the rdf on the integration time  $\Delta t$  (Fig. 6.14). From this plot, we observe that rdf is independent of the integration time step.

### Appendix III: Isoconfiguration run (IC)

To quantify the dependence of the dynamics on the structure and particle size, we perform isoconfigurational runs (IC). IC is a powerful technique introduced by Harrowell and co-workers to investigate the role of structure in the dynamical heterogeneity of the particles [139, 140, 107, 141]. Among other factors, a particle's displacement can depend on its structure and also its initial momenta. This technique was proposed to remove the uninteresting variation in the particle displacements arising from the choice of initial momenta and extract the role of the initial configuration on the dynamics and its heterogeneity. For each system, five different isoconfigurational runs are carried out for 4000 particles. To ensure that all configurations are different, the configurations are chosen such that the two sets are greater than  $100\tau_\alpha$  apart. All these five IC has different structure as well as contain different pin particle position. Note that since we have shown in section 6.3.4 that after pinning, the structure changes; thus after

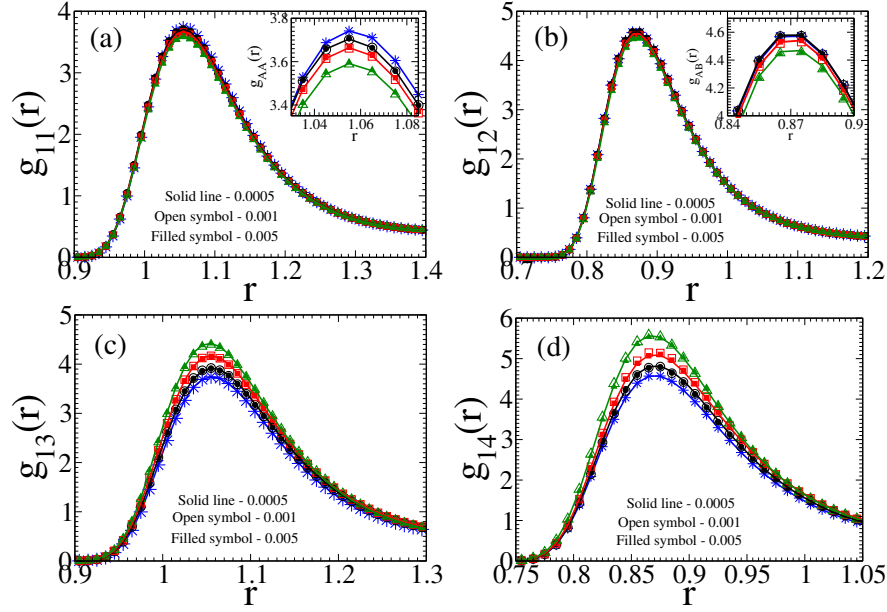


Figure 6.14: *Effect of integration time step,  $\Delta t$  on radial distribution function,  $g(r)$  while treating the pinned system as a quaternary system, at  $T = 0.68$  (a)  $g_{11}$  as a function of  $r$  (b)  $g_{12}$  as a function of  $r$  (c)  $g_{13}$  as a function of  $r$  (d)  $g_{14}$  as a function of  $r$ . Inset: We have zoomed onto the first peak of the respective figures, which clearly shows the difference in the radial distribution functions. Note that color coding is similar to Fig. 6.1. Here we refer to the mobile A type of particles as 1, mobile B type of particles as 2, pinned A type of particles as 3, and pinned B type of particles as 4.*

we pin the equilibrium position of the mobile particles, we run the system for  $t=100$  timestep and then consider that as our initial configuration. We run 100 trajectories for each configuration with different starting velocities randomly assigned from the Maxwell-Boltzmann distribution for the corresponding temperatures.

Mobility,  $\mu$  is the average displacement of each particle over these 100 runs and is calculated as [107],

$$\mu^j(t) = \frac{1}{N_{IC}} \sum_{i=1}^{N_{IC}} \sqrt{(r_i^j(t) - r_i^j(0))^2} \quad (6.23)$$

where  $j^{th}$  particle's mobility at time  $t$  is represented by the term  $\mu^j(t)$ . The position of the  $j^{th}$  particle in the  $i^{th}$  trajectory at time  $t$  is denoted by the term  $r_i^j(t)$ , and its initial position is denoted by the term  $r_i^j(0)$ . The sum of the values is calculated over each of the  $N_{IC}$  trajectories that were carried out during the isoconfiguration runs. We determine the average displacement or mobility for the  $j^{th}$  particle at time  $t$  by averaging these displacements over all trajectories.

#### Appendix IV: Identification of fast particles

There are various methods available for identifying fast particles in the literature [53,

146, 147, 136, 137]. In our study, we employ the approach proposed by Candelier et al.[136, 137]. This method involves the calculation of a quantity called  $p_{hop}(i, t)$  for each particle within a specified time window  $W = [t_1, t_2]$ .

The  $p_{hop}(i, t)$  quantity captures the rate of change in the average position of a particle, indicating the occurrence of a cage jump. The expression for  $p_{hop}(i, t)$  is given as follows[108]:

$$p_{hop}(i, t) = \sqrt{\langle (r_i - \langle r_i \rangle_U)^2 \rangle_V \langle (r_i - \langle r_i \rangle_V)^2 \rangle_U} \quad (6.24)$$

here,  $r_i$  represents the position of particle  $i$ , and  $\langle \cdot \rangle$  denote the averages over the time. The time window  $W$  is divided into two intervals,  $U = [t - \Delta t/2, t]$  and  $V = [t, t + \Delta t/2]$ . By calculating  $p_{hop}(i, t)$  for each particle, we can determine whether a particle experiences a significant change in its average position, indicating its involvement in cage jumps and enhanced dynamics. In our analysis, we compare the calculated  $p_{hop}(i, t)$  values to a threshold value  $p_c$ , which is determined as the mean square displacement,  $\langle \Delta r(t)^2 \rangle$  at a specific time  $t_{max}$  where the non-Gaussian parameter,  $\alpha_2 = \frac{3\langle \Delta r(t)^4 \rangle}{(\langle \Delta r(t)^2 \rangle)^2} - 1$  is maximized. If  $p_{hop}(i, t)$  exceeds  $p_c$ , we identify the particle as a fast particle[114, 112, 66].

It is important to note that in our study, we specifically analyze the structure and dynamics of the mobile A particles. Therefore, we calculate the Mean Square Displacement (MSD) and the non-Gaussian parameter specifically for the mobile A particles. For a more comprehensive understanding of the method and its application in our study, we refer readers to Reference[114, 66, 112, 108].

## Appendix V: Comparison between binary, quaternary, and modified quaternary

From the above analysis, it is clear that considering a pinned system as a modified quaternary system correctly predicts the structural parameters and predicts a stronger structure-dynamics correlation. Note that in the modified quaternary system, the pinned particles have a dual effect. First, it modifies the structure, and then it contributes a factor of two more towards confining the mobile particles /decreasing their entropy. To understand the independent role of these two effects, in Fig.6.15, we plot the different structural parameters at different “ $c$ ” values where we assume the system as binary, quaternary and modified quaternary. In the last two cases, we assume the structure is modified due to pinning. The expressions for the binary and modified quaternary are given in Section 6.4.

In the quaternary system, the pair excess entropy of each mobile “A” particle, which is type “1” in our notation, can be expressed by removing the first summation in Eq. 6.7;

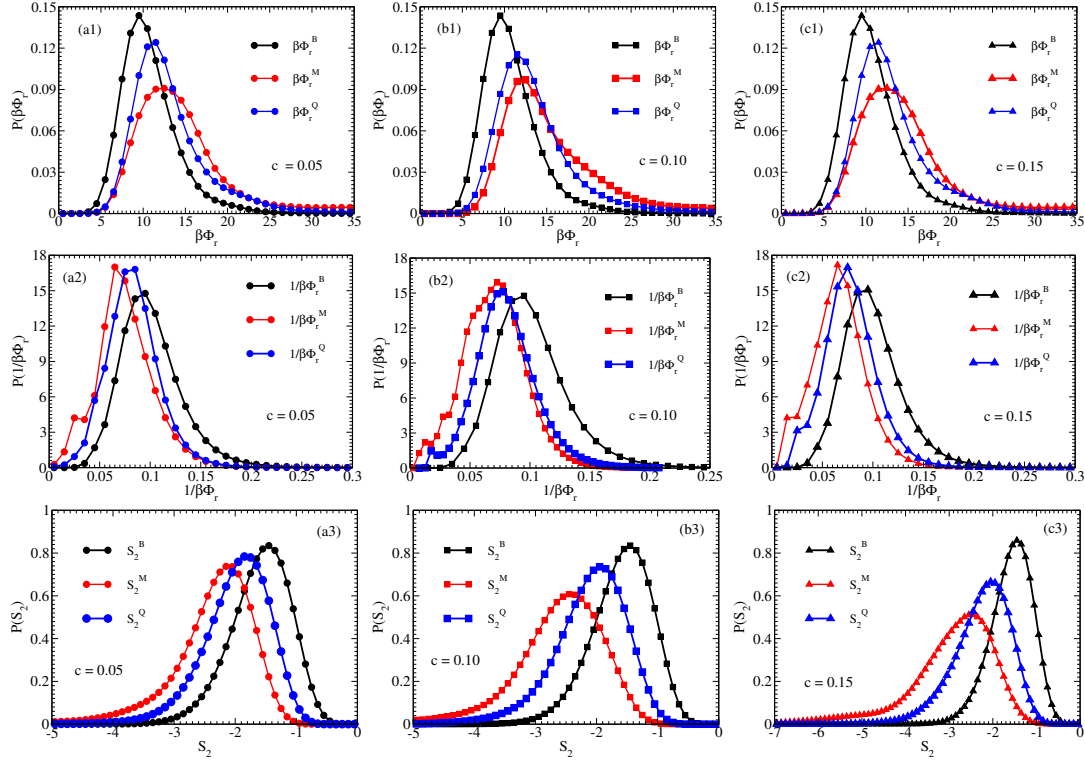


Figure 6.15: *Distribution of caging potential ( $\beta\Phi_r$ ), the inverse of caging potential ( $1/\beta\Phi_r$ ), and pair excess entropy ( $S_2$ ) in different pinned systems treating them as binary (Black), quaternary (Blue), and modified quaternary (Red) at  $T = 0.68$ . (a1-c1) Distribution of depth of local caging potential ( $\beta\Phi_r$ ) for different systems, (a2-c2) Distribution of inverse of depth of local caging potential ( $1/\beta\Phi_r$ ) for different systems, (a3-c3) Distribution of pair excess entropy ( $S_2$ ) for different systems (a1-a3)  $c = 0.05$ , (b1-b3)  $c = 0.10$ , (c1-c3)  $c = 0.15$ .*

$$\frac{S_2^Q(A)}{k_B} = -2\pi\rho \int_0^\infty r^2 dr \sum_{j=1}^4 \chi_j \{g_{1j}(r) \ln g_{1j}(r) - (g_{1j}(r) - 1)\} \quad (6.25)$$

The mean field caging potential for a mobile "A" type of particle in a quaternary system can be written by removing the first summation in Eq. 6.12,

$$\beta\Phi_r^Q(A, \Delta r = 0) = -4\pi\rho \int r^2 dr \sum_{j=1}^4 \chi_j C_{1j}(r) g_{1j}(r) \quad (6.26)$$

We find that even when we go from a binary to a quaternary system due to the change in structure, the caging potential increases and the entropy decreases. However, the caging potential further increases, and the entropy further decreases when we consider the higher effect (factor of 2) of the pinned particles on the mobile particles.

We also plot the Spearman rank correlation,  $C_R$  between mobility ( $\mu$ ) and the inverse depth of caging potential ( $1/\beta\Phi_r$ ) and the pair excess entropy ( $S_2$ ) for different systems in Fig.6.16. When we treat the pinned system as quaternary rather than



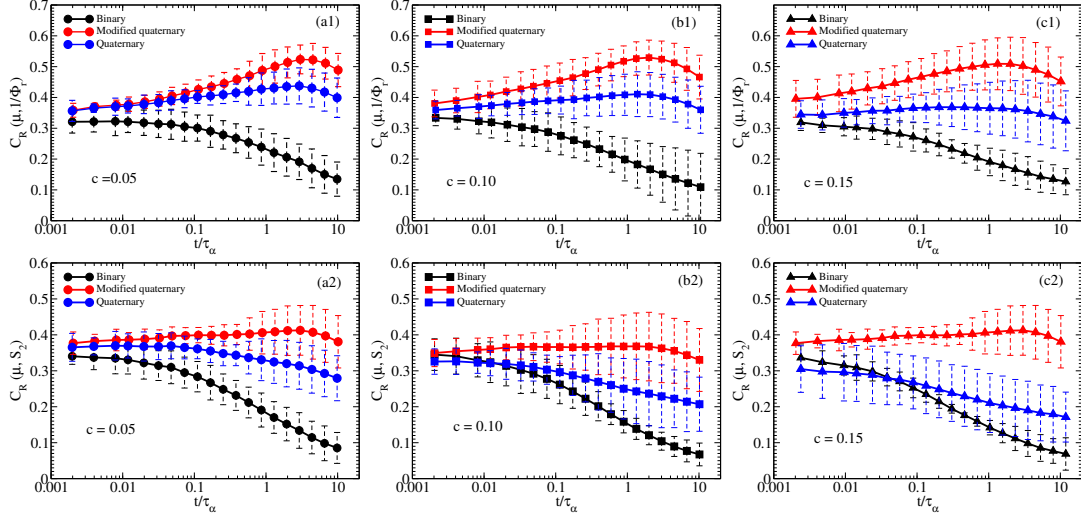


Figure 6.16: Spearman rank correlation between different parameters at different pinning concentrations ( $c$ ), while treating the pinned system as binary (Black), quaternary (Blue), and modified quaternary (Red). (a1-c1) Spearman rank correlation ( $C_R$ ) between mobility ( $\mu$ ) and inverse depth of caging potential ( $1/\beta\Phi_r$ ) for different system, (a2-c2) Spearman rank correlation ( $C_R$ ) between mobility ( $\mu$ ) and pair excess entropy ( $S_2$ ) for different systems, (a1-a2)  $c = 0.05$  (at  $T = 0.52$ ), (b1-b2)  $c = 0.10$  (at  $T = 0.60$ ), (c1-c2)  $c = 0.15$  (at  $T = 0.68$ ).

binary, we see an increase in correlation. This increase in correlation is due to the change in structure. However, we find that the correlation grows further when we treat the system as a modified quaternary system. As expected, with the increase in pinning density, the difference between the quaternary and modified quaternary increases.

# Chapter 7

## Summary and future work

“The end is never the end.  
It is always the the beginning of somethingj.  
— Kate Lord Brown

### 7.1 Summary

The structure, dynamics, and thermodynamics of the glass-forming liquid and the correlation between them are not completely understood and are a topic of intense research. Despite huge efforts through experiments, simulations, and theoretical work, a complete understanding of this system remains challenging. Many studies have clarified the glass transition phenomena and the behavior of materials that create glass, providing valuable details. However, there are still a lot of unanswered questions, which motivates researchers to keep exploring this fascinating field to learn more about the complexities governing glassy behavior and the change from liquid to solid-like states without undergoing crystallization. The work presented in this thesis aims to contribute to ongoing efforts to understand the glass-forming process better.

In Chapter 1, we delved into crucial concepts surrounding the glass transition, exploring its significance and the most widely accepted theories that provide insights into various properties of this phenomenon. Building on this foundation, in chapter 2 we expanded on the understanding of the glass transition by elaborating on its properties and offering detailed explanations of relevant definitions and computational techniques employed in this study.

In Chapter 3, we present the study of polydisperse systems and highlight a significant issue when treating them as monodisperse systems. Polydispersity is ubiquitous in nature as most experimental systems are polydisperse. With the invention of the swap Monte Carlo and the observation that, using this technique, we can equilibrate a polydisperse system till very low temperatures, the polydisperse systems have become a system of choice in studying low-temperature glass-forming liquids. However, doing analytical calculations for systems with continuous-size polydispersity is a challenge.

According to liquid state theories, the structure can describe the thermodynamical properties and dynamics of the system. The exact way to describe the structure of a system with continuous size polydispersity is via  $N(N-1)$  partial structure factors, which present analytic difficulties, and this issue becomes more severe with increasing system size. To avoid this, the systems are typically treated as an effective one-component system, which leads to artificial structural softening and incorrect measures of the thermodynamical quantities. We describe a way to define the system in terms of an optimal number of species,  $M_0$  while keeping  $M_0 \ll N$ . This is done in a way such that we can use the partial structure factors to correctly obtain the thermodynamical quantities of the system. We show that  $M_0$  changes with the type of polydispersity and interaction potential. Notably,  $M_0$  does not depend on the size of the system, highlighting its importance in describing bigger systems where the exact number of species that grows linearly with  $N$  is large. We also employ the information theoretical techniques and show that this definition of  $M_0$  leads to the maximum value of mutual information in the system.

In Chapter 4, we explore the structure dynamics correlation in polydisperse systems using recently developed microscopic mean-field theory [76]. We define the mean field caging potential as an order parameter that describes the local structural order (SOP) [82]. Previous studies have shown that this SOP describes the particle-level dynamics [114]. In polydisperse systems, describing the structure and any structural order parameter (SOP) is not trivial as it varies with the number of species we use to describe the system,  $M$ . As discussed in previous chapter, depending on the degree of polydispersity, there is an optimum value of  $M = M_0$ . However, surprisingly, the analysis reveals that the correlation between a recently proposed SOP and the dynamics is highest for  $M = 1$ , where we know that the structure is not described properly. This effect increases with polydispersity. We find that the SOP at  $M = 1$  is coupled with the particle size,  $\sigma$ , and this coupling increases with polydispersity and decreases with an increase in  $M$ . Careful analysis shows that at lower polydispersities, the SOP is a good predictor of the dynamics. However, at higher polydispersity, the dynamics is strongly dependent on  $\sigma$ . Since the coupling between the SOP and  $\sigma$  is higher for  $M = 1$ , it appears to be a better predictor of the dynamics. We also study the Vibrality an order parameter independent of structural information. Compared to SOP, at high polydispersity we find Vibrality to be a marginally better predictor of the dynamics. However, this high predictive power of Vibrality, which is not there at lower polydispersity, appears to be due to its stronger coupling with  $\sigma$ . Therefore our study suggests that for systems with high polydispersity, the correlation of any order parameter and  $\sigma$  will affect the correlation between the order parameter and dynamics and need not project a generic predictive power of the order parameter.

In Chapter 5, after analysis of polydisperse now we work on another multispecies glass forming system known as the pinned system. In a polydisperse system, due to distribution in sizes, frustration can be easily introduced in the system. Due to high

frustration, the polydisperse system is seen as better glass forming. Another effective technique for creating a good glass former is pinning the positions of a few particles in the system to prevent them from taking part in crystal formation. This pinning technique introduces local structural restrictions, which prevent crystallization. By increasing the concentration of pinned particles in the fluid, the glassy behaviour of the whole system is improved and it is shown that at high pinning concentration, the system undergoes a glass transition at a high temperature where the single particle dynamics still survives. In this chapter, we conduct a thermodynamic analysis of the pinned system. It has been found that the usual thermodynamic integration (TI) approach of estimating entropy predicts that configurational entropy will vanish at a temperature where the system's single-particle dynamics show complete relaxation [166, 49]. To understand the correlation between entropy and dynamics and how dynamics survives when the entropy vanishes, we use a new method to compute entropy, called the two-phase thermodynamics (2PT) approach. We discover that the difference in entropy computed using the two approaches (2PT and TI) grows with an increase in pinning concentration. Additionally, we discover that, for the temperature range under consideration, entropy computed using the 2PT technique satisfies the Adam-Gibbs relationship between the relaxation time and the configurational entropy, whereas entropy calculated using the TI method strongly violates the same. Note that the 2PT entropy is obtained from the velocity autocorrelation function, which is a local property. In the regular KA model, the local and the global entropy are similar. But our study reveals that in the pinned system they deviate from each other, and the local entropy is correlated to the single particle dynamics.

In Chapter 6, we next address the problem of describing the structure and structural order parameter of a system where a fraction of particles are pinned and then study the structure dynamics correlation. These particles are pinned at the equilibrium configuration of the KA system (which is a binary 80:20 system) and it is expected that the equilibrium properties and the structure of the system do not change. First, we show that even after pinning the particles at the equilibrium position of the mobile particle, the structure of the liquid changes and this change is visible only when we treat the pinned particles as a different species. We then derive the expression of the pair excess entropy and the mean-field caging potential for a pinned system by assuming it is a binary and a modified quaternary system. We find that apart from the change in structure, the pinned particles also act towards increasing the caging potential/decreasing the entropy more than other mobile particles. We also show that when the system is treated as binary, the structure dynamics correlation decreases with pinning, whereas it remains similar when the system is treated as a modified quaternary system. Thus, we conclude that structure dynamics correlation at a local level persists with increasing pinning.

## 7.2 Future work

In this thesis, we have conducted a comprehensive investigation into the role of size polydispersity in dynamics and structure. Our findings reveal that particle size significantly influences the system's dynamics in addition to its structure. As a next step, we plan to explore the relationship between interaction energy and dynamics. Dyer et al.[134], have shown that different energy systems can exhibit similar structures and dynamics (Fig. 7.1). We propose to analyze the local caging potential, which is influenced by potential energy, and use it to distinguish between hard and soft regions in the system. We anticipate that increasing the energy polydispersity will enhance the accuracy of this region separation, allowing for a deeper understanding of the interplay between dynamics and energy in complex systems. This investigation holds promise for shedding further light on the complex behaviour of polydisperse systems and their glass-forming properties.

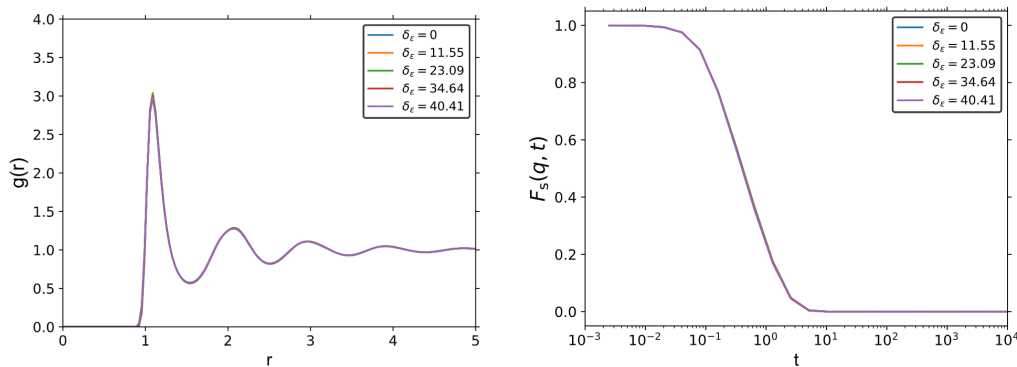


Figure 7.1: Left side: Effect of energy polydispersity on the average rdf at the state point  $(\rho, T) = (0.85, 0.70)$ . Right side: Effect of energy polydispersity on the incoherent intermediate scattering function (ISF)  $F_s(q, t)$  at the state point  $(\rho, T) = (0.85, 0.70)$  for the wave vector corresponding to the first peak of the static structure factor of the monodisperse system. Adopted from Ref. [134].

Once we know how interaction potential affects the analysis of caging potential, we can move on to other types of polydispersity, such as mass, size and mass combinations etc.

# Bibliography

- [1] A. Banerjee, M. K. Nandi, S. Sastry, and S. Maitra Bhattacharyya, *The Journal of Chemical Physics* **147**, 024504 (2017).
- [2] S. Sengupta, F. Vasconcelos, F. Affouard, and S. Sastry, *J. Chem. Phys.* **135**, 194503 (2011).
- [3] S. Sastry, P. G. Debenedetti, and F. H. Stillinger, *Nature* **393**, 554 (1998).
- [4] P. G. Debenedetti and F. H. Stillinger, *Nature* **410**, 259 (2001).
- [5] P. W. Anderson, *Science* **267**, 1615 (1995).
- [6] W. Kob, Course 5: Supercooled liquids, the glass transition, and computer simulations, in *Slow Relaxations and nonequilibrium dynamics in condensed matter*, edited by J.-L. Barrat, M. Feigelman, J. Kurchan, and J. Dalibard, pp. 199–269, Berlin, Heidelberg, 2003, Springer Berlin Heidelberg.
- [7] C. K. Mishra, X. Ma, P. Habdas, K. B. Aptowicz, and A. G. Yodh, *Phys. Rev. E* **100**, 020603 (2019).
- [8] J. Phillips, *Chemical Physics* **212**, 41 (1996).
- [9] M. Cook, D. C. Watts, and G. Williams, *Trans. Faraday Soc.* **66**, 2503 (1970).
- [10] J. P. Hansen and I. R. McDonald, 2nd ed. ,Academic, London (1986).
- [11] W. Götze, *Journal of Physics: Condensed Matter* **11**, A1 (1999).
- [12] W. Kob, *Journal of Physics: Condensed Matter* **11**, R85 (1999).
- [13] W. Kob and H. C. Andersen, *Phys. Rev. E* **51**, 4626 (1995).
- [14] L. Berthier, G. Biroli, J.-P. Bouchaud, L. Cipelletti, and W. van Saarloos, *Dynamical Heterogeneities in Glasses, Colloids, and Granular Media* (Oxford University Press, 2011).
- [15] Y. Takaha, H. Mizuno, and A. Ikeda, arXiv:2303.07817 (2023).
- [16] M. G. Evans and M. Polanyi, *Trans. Faraday Soc.* **31**, 875 (1935).
- [17] C. A. Angell, *Science* **267**, 1924 (1995).

- [18] H. Vogel, *Physikalische Zeitschrift* (in German) **22** (1921).
- [19] G. S. Fulcher, *Journal of the American Ceramic Society* **8**, 339 (1925).
- [20] G. Tammann and W. Hesse, *Zeitschrift für anorganische und allgemeine Chemie* **156**, 245 (1926).
- [21] L. S. Garca-Coln, L. F. del Castillo, and P. Goldstein, *Phys. Rev. B* **40**, 7040 (1989).
- [22] W. Kauzmann, *Chemical Reviews* **43**, 219 (1948).
- [23] G. Brown, *Nuclear Physics* **55**, 350 (1964).
- [24] H. Hoinkes, *Journal of Glaciology* **6**, 757–757 (1967).
- [25] M. D. Ediger, C. A. Angell, and S. R. Nagel, *The Journal of Physical Chemistry* **100**, 13200 (1996).
- [26] S. Sengupta, *Investigations of the role of spatial dimensionality and interparticle interactions in model glass-formers*, Thesis (2013).
- [27] S. R. Nagel, *Susceptibility Studies of Supercooled Liquids and Glasses* (Springer Netherlands, Dordrecht, 1993), pp. 259–283.
- [28] C. Angell, *Journal of Physics and Chemistry of Solids* **49**, 863 (1988).
- [29] G. Adam and J. H. Gibbs, *The Journal of Chemical Physics* **43**, 139 (1965).
- [30] J. H. Gibbs and E. A. DiMarzio, *Journal of Chemical Physics* **28**, 373 (1958).
- [31] T. R. Kirkpatrick and P. G. Wolynes, *Phys. Rev. A* **35**, 3072 (1987).
- [32] T. R. Kirkpatrick and D. Thirumalai, *Phys. Rev. Lett.* **58**, 2091 (1987).
- [33] T. R. Kirkpatrick and D. Thirumalai, *Phys. Rev. B* **36**, 5388 (1987).
- [34] T. R. Kirkpatrick, D. Thirumalai, and P. G. Wolynes, *Phys. Rev. A* **40**, 1045 (1989).
- [35] X. Xia and P. G. Wolynes, *Proceedings of the National Academy of Sciences* **97**, 2990 (2000).
- [36] U. Bengtzelius, W. Gotze, and A. Sjolander, *Journal of Physics C: Solid State Physics* **17**, 5915 (1984).
- [37] W. Götze, *Complex Dynamics of Glass-Forming Liquids: A Mode-Coupling Theory* (Oxford University Press, 2008).
- [38] E. Leutheusser, *Phys. Rev. A* **29**, 2765 (1984).

- [39] W. Kob, *Supercooled liquids, the glass transition, and computer simulations* (arXiv, 2002).
- [40] R. W. Zwanzig, Physics Subject Headings (PhySH) (2001).
- [41] D. R. Reichman and P. Charbonneau, *Journal of Statistical Mechanics: Theory and Experiment* **2005**, P05013 (2005).
- [42] K. Miyazaki and D. R. Reichman, *Journal of Physics A: Mathematical and General* **38**, L343 (2005).
- [43] B. Kim and K. Kawasaki, *Journal of Physics A: Mathematical and Theoretical* **40**, F33 (2006).
- [44] S. P. Das, G. F. Mazenko, S. Ramaswamy, and J. J. Toner, *Physical Review Letters* **54**, 118 (1985).
- [45] S. P. Das and G. F. Mazenko, *Phys. Rev. A* **34**, 2265 (1986).
- [46] A. Ninarello, L. Berthier, and D. Coslovich, *Phys. Rev. X* **7**, 021039 (2017).
- [47] R. Gutiérrez, S. Karmakar, Y. G. Pollack, and I. Procaccia, *EPL* **111**, 56009 (2015).
- [48] W. Kob and L. Berthier, *Phys. Rev. Lett.* **110**, 245702 (2013).
- [49] S. Chakrabarty, S. Karmakar, and C. Dasgupta, *Scientific Reports* **5**, 12577 (2015).
- [50] P. Chaudhuri, L. Berthier, and W. Kob, *Phys. Rev. Lett.* **99**, 060604 (2007).
- [51] M. M. Hurley and P. Harrowell, *The Journal of Chemical Physics* **105**, 10521 (1996).
- [52] C. Donati, S. C. Glotzer, P. H. Poole, W. Kob, and S. J. Plimpton, *Phys. Rev. E* **60**, 3107 (1999).
- [53] W. Kob, C. Donati, S. J. Plimpton, P. H. Poole, and S. C. Glotzer, *Phys. Rev. Lett.* **79**, 2827 (1997).
- [54] D. Frenkel and B. Smit, Appendix k - small research projects, in *Understanding Molecular Simulation (Second Edition)*, pp. 581–585, Academic Press, San Diego, , second edition ed., 2002.
- [55] P. M. Piaggi, O. Valsson, and M. Parrinello, *Physical Review Letter* **119**, 015701 (2017).
- [56] D. A. McQuarrie, *Statistical Mechanics book* (1975).
- [57] J. G. Kirkwood and E. M. Boggs, *J. Chem. Phys.* **10**, 394 (1942).



- [58] V. I. Kalikmanov, *Statistical Physics of Fluids: Basic Concepts and Applications* **1** (2001).
- [59] M. Singh, M. Agarwal, D. Dhabal, and C. Chakravarty, *J. Chem. Phys.* **137**, 024508 (2012).
- [60] M. kumar Nandi, *Role of structure in determining the dynamics using theoretical techniques like mode coupling theory and computer simulations*, Thesis (2017).
- [61] F. Sciortino, *Journal of Statistical Mechanics: Theory and Experiment* **2005**, P05015 (2005).
- [62] B. Doliwa and A. Heuer, *Phys. Rev. Lett.* **80**, 4915 (1998).
- [63] S. Sastry, *Nature* **409**, 164 (2001).
- [64] F. Sciortino, W. Kob, and P. Tartaglia, *Phys. Rev. Lett.* **83**, 3214 (1999).
- [65] S. Mossa *et al.*, *Phys. Rev. E* **65**, 041205 (2002).
- [66] P. Patel, M. K. Nandi, U. K. Nandi, and S. M. Bhattacharyya, *The Journal of Chemical Physics* **154**, 034503 (2021).
- [67] X. Xu, G. Friedman, K. D. Humfeld, S. A. Majetich, and S. A. Asher, *Am. Chem. Soc.* **14**, 1249 (2001).
- [68] V. K. L. Mer, *Am. Chem. Soc.* **44**, 1270 (1952).
- [69] P. G. Bolhuis and D. A. Kofke, *Physical Review E* **54**, 634 (1996).
- [70] D. J. Lacks and J. R. Wienhoff, *J. Chem. Phys.* **111**, 398 (1999).
- [71] S. R. Williams, I. K. Snook, and W. van Megen, *Phys. Rev. E* **64**, 021506 (2001).
- [72] P. Chaudhuri, S. Karmakar, C. Dasgupta, H. R. Krishnamurthy, and A. K. Sood, *Phys. Rev. Lett.* **95**, 248301 (2005).
- [73] S. Sarkar, R. Biswas, M. Santra, and B. Bagchi, *Phys. Rev. E* **88**, 022104 (2013).
- [74] S. E. Abraham, S. M. Bhattacharyya, and B. Bagchi, *Phys. Rev. Lett.* **100**, 167801 (2008).
- [75] S. Auer and D. Frenkel, *Nature* **413**, 711 (2001).
- [76] M. K. Nandi, A. Banerjee, C. Dasgupta, and S. M. Bhattacharyya, *Phys. Rev. Lett.* **119**, 265502 (2017).
- [77] A. Banerjee, M. K. Nandi, S. Sastry, and S. M. Bhattacharyya, *J. Chem. Phys.* **145**, 034502 (2016).
- [78] S. Sastry, *PhysChemComm* **3**, 79 (2000).

- [79] A. Banerjee, S. Sengupta, S. Sastry, and S. M. Bhattacharyya, *Physical Review Letter* **113**, 225701 (2014).
- [80] M. K. Nandi and S. Maitra Bhattacharyya, *The Journal of Chemical Physics* **148**, 034504 (2018).
- [81] I. Saha, M. K. Nandi, C. Dasgupta, and S. M. Bhattacharyya, *J. Stat. Mech.: Theory Exp* **2019**, 084008 (2019).
- [82] M. K. Nandi and S. M. Bhattacharyya, *Phys. Rev. Lett.* **126**, 208001 (2021).
- [83] D. Frydel and S. A. Rice, *Phys. Rev. E* **71**, 041403 (2005).
- [84] C. P. Royall, A. A. Louis, and H. Tanaka, *J. Chem. Phys.* **127**, 044507 (2007).
- [85] P. Salgi and R. Rajagopalan, *Adv. Colloid Interface Sci.* **43**, 169 (1993).
- [86] T. O. Pangburn and M. A. Bevan, *J. Chem. Phys.* **123**, 174904 (2005).
- [87] T. O. Pangburn and M. A. Bevan, *J. Chem. Phys.* **124**, 054712 (2006).
- [88] M. J. Pond, J. R. Errington, and T. M. Truskett, *J. Chem. Phys.* **135**, 124513 (2011).
- [89] F. Weysser, A. M. Puertas, M. Fuchs, and T. Voigtmann, *Phys. Rev. E* **82**, 011504 (2010).
- [90] M. Ozawa and L. Berthier, *The Journal of Chemical Physics* **146**, 014502 (2017).
- [91] D. L. Majure *et al.*, 2008 DoD HPCMP Users Group Conference, IEEE , 201 (2008).
- [92] T. Goel, C. N. Patra, T. Mukherjee, and C. Chakravarty, *The Journal of Chemical Physics* **129**, 164904 (2008).
- [93] P. Giaquinta and G. Giunta, *Physica A: Stat. Mech. and its Appl.* **187**, 145 (1992).
- [94] G. P. V. Prestipino Santi, *J. stat. Phys.* **96**, 135 (1999).
- [95] F. Saija, S. Prestipino, and P. V. Giaquinta, *J. Chem. Phys.* **113**, 2806 (2000).
- [96] F. Saija, S. Prestipino, and P. V. Giaquinta, *J. Chem. Phys.* **124**, 244504 (2006).
- [97] J. Mittal, J. R. Errington, and T. M. Truskett, *J. Chem. Phys.* **125**, 076102 (2006).
- [98] I. H. Bell, J. C. Dyre, and T. S. Ingebrigtsen, *Nature Communications* **11**, 4300 (2020).
- [99] M. K. Nandi, A. Banerjee, S. Sengupta, S. Sastry, and S. M. Bhattacharyya, *The Journal of Chemical Physics* **143**, 174504 (2015).

- [100] N. Kiriushcheva and P. H. Poole, *Physical Review E* **65**, 011402 (2001).
- [101] T. S. Ingebrigtsen and H. Tanaka, *The Journal of Physical Chemistry B* **119**, 11052 (2015).
- [102] J. Paret, R. L. Jack, and D. Coslovich, *The Journal of Chemical Physics* **152**, 144502 (2020).
- [103] W. Gotze and L. Sjogren, *Reports on Progress in Physics* **55**, 241 (1992).
- [104] V. Lubchenko and P. G. Wolynes, *Annual Review of Physical Chemistry* **58**, 235 (2007).
- [105] S. L. Glashow, D. Guadagnoli, and K. Lane, *Physical Review Letter* **114**, 091801 (2015).
- [106] M. M. Hurley and P. Harrowell, *Physical Review E* **52**, 1694 (1995).
- [107] A. W. Cooper, H. Perry, P. Harrowell, and D. R. Reichman, *Nature Physics* **4**, 711 (2008).
- [108] S. S. Schoenholz, E. D. Cubuk, D. M. Sussman, E. Kaxiras, and A. J. Liu, *Nature Physics* **12** (2016).
- [109] R. L. Jack, A. J. Dunleavy, and C. P. Royall, *Physical Review Letter* **113**, 095703 (2014).
- [110] H. Tong and H. Tanaka, *Physical Review Letter* **124**, 225501 (2020).
- [111] D. Richard *et al.*, *Physical Review Materials* **4**, 113609 (2020).
- [112] F. m. c. P. Landes, G. Biroli, O. Dauchot, A. J. Liu, and D. R. Reichman, *Phys. Rev. E* **101**, 010602 (2020).
- [113] T. Hua and T. Hajime, *Nature Communications* **10**, 5596 (2019).
- [114] M. Sharma, M. K. Nandi, and S. M. Bhattacharyya, *Phys. Rev. E* **105**, 044604 (2022).
- [115] T. Kawasaki, T. Araki, and H. Tanaka, *Physical Review Letter* **99**, 215701 (2007).
- [116] M. A. Bates and D. Frenkel, *The Journal of Chemical Physics* **109**, 6193 (1998).
- [117] M. Leocmach, J. Russo, and H. Tanaka, *The Journal of Chemical Physics* **138** (2013).
- [118] J. Russo and H. Tanaka, *Proceedings of the National Academy of Sciences* **112**, 6920 (2015).
- [119] P. Sampedro Ruiz, Q.-l. Lei, and R. Ni, *Communications Physics* **2**, 2399 (2019).

- [120] M. R. Stapleton, D. J. Tildesley, and N. Quirke, *The Journal of Chemical Physics* **92**, 4456 (1990).
- [121] M. Yiannourakou, I. G. Economou, and I. A. Bitsanis, *The Journal of Chemical Physics* **133**, 224901 (2010).
- [122] D. Shaw, *Journal of Dispersion Science and Technology* **15**, 119 (1994).
- [123] R. P. Murphy, K. Hong, and N. J. Wagner, *Journal of Colloid and Interface Science* **501**, 45 (2017).
- [124] J. Roller, J. D. Geiger, M. Voggenreiter, J.-M. Meijer, and A. Zumbusch, *Soft Matter* **16**, 1021 (2020).
- [125] M. Voggenreiter *et al.*, *Langmuir* **36**, 13087 (2020).
- [126] J. Roller, A. Laganapan, J.-M. Meijer, M. Fuchs, and A. Zumbusch, *Proceedings of the National Academy of Sciences* **118** (2021).
- [127] T. Eckert, M. Schmidt, and D. de las Heras, *The Journal of Chemical Physics* **157** (2022).
- [128] T. S. Grigera and G. Parisi, *Physical Review E* **63**, 045102 (2001).
- [129] D. Gazzillo and G. Pastore, *Chemical Physics Letters* **159**, 388 (1989).
- [130] D. Coslovich, M. Ozawa, and L. Berthier, *Journal of Physics: Condensed Matter* **30**, 144004 (2018).
- [131] M. Ozawa, G. Parisi, and L. Berthier, *The Journal of Chemical Physics* **149** (2018).
- [132] L. Berthier, D. Coslovich, A. Ninarello, and M. Ozawa, *Physical Review Letter* **116**, 238002 (2016).
- [133] L. Berthier *et al.*, *Proceedings of the National Academy of Sciences* **114**, 11356 (2017).
- [134] T. S. Ingebrigtsen and J. C. Dyre, *The Journal of Physical Chemistry B* **127**, 2837 (2023).
- [135] M. Sharma, M. K. Nandi, and S. Maitra Bhattacharyya, *The Journal of Chemical Physics* **159**, 104502 (2023).
- [136] R. Candelier *et al.*, *Phys. Rev. Lett.* **105**, 135702 (2010).
- [137] A. Smessaert and J. Rottler, *Phys. Rev. E* **88**, 022314 (2013).
- [138] C. David, A. Emilien, S. Philippe, and R. Farhang, *Physical Review E* **98**, 052910 (2018).

- [139] A. Widmer-Cooper, P. Harrowell, and H. Fynewever, *Phys. Rev. Lett.* **93**, 135701 (2004).
- [140] A. Widmer-Cooper and P. Harrowell, *Phys. Rev. Lett.* **96**, 185701 (2006).
- [141] L. Berthier and R. L. Jack, *Phys. Rev. E* **76**, 041509 (2007).
- [142] J. Gu enol e *et al.*, *Computational Materials Science* **175**, 109584 (2020).
- [143] H. Tong and H. Tanaka, *Physical Review X* **8**, 011041 (2018).
- [144] A. J. Dunleavy, K. Wiesner, R. Yamamoto, and C. P. Royall, *Nature Communications* **6**, 6089 (2015).
- [145] U. K. Nandi *et al.*, *The Journal of Chemical Physics* **156**, 014503 (2022).
- [146] K. Vollmayr-Lee, W. Kob, K. Binder, and A. Zippelius, *The Journal of Chemical Physics* **116**, 5158 (2002).
- [147] A. Widmer-Cooper and P. Harrowell, *Journal of Physics: Condensed Matter* **17**, S4025 (2005).
- [148] W. M. Du *et al.*, *Phys. Rev. E* **49**, 2192 (1994).
- [149] P. Lunkenheimer, A. Pimenov, and A. Loidl, *Phys. Rev. Lett.* **78**, 2995 (1997).
- [150] K. Kim and S. Saito, *The Journal of Chemical Physics* **138**, 12A506 (2013).
- [151] E. Flenner and G. Szamel, *Phys. Rev. E* **72**, 031508 (2005).
- [152] E. Flenner and G. Szamel, *Phys. Rev. E* **72**, 011205 (2005).
- [153] V. Lubchenko and P. G. Wolynes, *The Journal of Chemical Physics* **119**, 9088 (2003).
- [154] A. Cavagna, *Physics Reports* **476**, 51 (2009).
- [155] M. Ozawa, C. Scalliet, A. Ninarello, and L. Berthier, *The Journal of Chemical Physics* **151**, 084504 (2019).
- [156] C. A. Angell, *J Res Natl Inst Stand Technol.* **102**, 171 (1997).
- [157] R. Richert and C. A. Angell, *The Journal of Chemical Physics* **108**, 9016 (1998).
- [158] J. H. Magill, *The Journal of Chemical Physics* **47**, 2802 (1967).
- [159] T. M. Shuichi Takahara, Osamu Yamamuro, *The Journal of Physical Chemistry* **99**, 9589 (1995).
- [160] K. L. Ngai, *The Journal of Physical Chemistry B* **103**, 5895 (1999).
- [161] C. Alba-Simionesco, *Comptes Rendus de l'Acad mie des Sciences - Series IV - Physics-Astrophysics* **2**, 203 (2001).

- [162] C. M. Roland, S. Capaccioli, M. Lucchesi, and R. Casalini, *The Journal of Chemical Physics* **120**, 10640 (2004).
- [163] D. Cangialosi, A. Alegria, and J. Colmenero, *Europhysics Letters (EPL)* **70**, 614 (2005).
- [164] E. Masiewicz *et al.*, *Scientific Reports* **5**, 2045 (2015).
- [165] A. D. S. Parmar, S. Sengupta, and S. Sastry, *Phys. Rev. Lett.* **119**, 056001 (2017).
- [166] M. Ozawa, W. Kob, A. Ikeda, and K. Miyazaki, *Proceedings of the National Academy of Sciences* **112**, 6914 (2015).
- [167] S. Chakrabarty, R. Das, S. Karmakar, and C. Dasgupta, *The Journal of Chemical Physics* **145**, 034507 (2016).
- [168] S.-T. Lin, M. Blanco, and W. A. Goddard, *The Journal of Chemical Physics* **119**, 11792 (2003).
- [169] S.-T. Lin, P. K. Maiti, and W. A. Goddard, *The Journal of Physical Chemistry B* **114**, 8191 (2010).
- [170] M. Moid, S. Sastry, C. Dasgupta, T. A. Pascal, and P. K. Maiti, *The Journal of Chemical Physics* **154**, 164510 (2021).
- [171] P.-K. Lai, C.-M. Hsieh, and S.-T. Lin, *Phys. Chem. Chem. Phys.* **14**, 15206 (2012).
- [172] M. Ozawa, A. Ikeda, K. Miyazaki, and W. Kob, *Phys. Rev. Lett.* **121**, 205501 (2018).
- [173] S. Chakrabarty, S. Karmakar, and C. Dasgupta, *Proceedings of the National Academy of Sciences* **112**, E4819 (2015).
- [174] M. Ozawa, W. Kob, A. Ikeda, and K. Miyazaki, *Proceedings of the National Academy of Sciences* **112**, E4821 (2015).
- [175] I. Williams *et al.*, *Journal of Physics: Condensed Matter* **30**, 094003 (2018).
- [176] L. Berthier, M. Ozawa, and C. Scalliet, *The Journal of Chemical Physics* **150**, 160902 (2019).
- [177] M. Ozawa, *Numerical Study of Glassy Systems: Fragility of Supercooled Liquids, Ideal Glass Transition of Randomly Pinned Fluids, and Jamming Transition of Hard Spheres*, Thesis (2015).
- [178] A. D. Phan and K. S. Schweizer, *The Journal of Chemical Physics* **148**, 054502 (2018).

- [179] A. D. Phan, *Journal of Physics: Condensed Matter* **34**, 435101 (2022).
- [180] C. Cammarota and G. Biroli, *Proceedings of the National Academy of Sciences* **109**, 8850 (2012).
- [181] R. E. Nettleton and M. S. Green, *The Journal of Chemical Physics* **29**, 1365 (1958).
- [182] C. P. Royall, F. Turci, S. Tatsumi, J. Russo, and J. Robinson, *Journal of Physics: Condensed Matter* **30**, 363001 (2018).
- [183] K. B. Peter Scheidler, Walter Kob, *Journal of Physical Chemistry B* **108**, 6673 (2004).
- [184] K. S. Schweizer, *The Journal of Chemical Physics* **123**, 244501 (2005).
- [185] P. Patel, M. Sharma, and S. Maitra Bhattacharyya, *The Journal of Chemical Physics* **159**, 044501 (2023).
- [186] R. Sahu, M. Sharma, P. Schall, S. M. Bhattacharyya, and V. Chikkadi, Under preparation .
- [187] R. Das, B. P. Bhowmik, A. B. Puthirath, T. N. Narayanan, and S. Karmakar, *PNAS Nexus* **2**, pgad277 (2023).
- [188] U. kumar Nandi, *Connecting real glasses to mean-field models: A study of structure, dynamics and thermodynamics*, Thesis (2021).
- [189] W. P. Krekelberg, V. K. Shen, J. R. Errington, and T. M. Truskett, *The Journal of Chemical Physics* **128**, 161101 (2008).
- [190] D. Coslovich, A. Ikeda, and K. Miyazaki, *Phys. Rev. E* **93**, 042602 (2016).

---

---

## ABSTRACT

---

**Name of the Student:** Palak Patel

**Registration No.:** 10CC18A26008

**Faculty of Study:** Chemical Sciences (CS)

**Year of Submission:** 2023

**CSIR Lab:** CSIR-NCL, Pune

**Name of the Supervisor:** Dr. Sarika Maitra Bhattacharyya

**Title of the thesis:** Correlation between structure, entropy, and dynamics in multi-species systems.

---

Intense research is being done to understand the relationship between the glass-forming liquid's structure, dynamics, and thermodynamics. The fact that there are so many unsolved problems encourages researchers to continue studying this interesting topic to understand the complexity driving glassy behavior and the transition from liquid to solid-like states without crystallization. To understand the glassy behavior, we deal with two different multi-species systems known as polydisperse and pinned systems. These systems are known as good glass former.

Polydispersity is ubiquitous in nature as most experimental systems are polydisperse. With the invention of the swap Monte Carlo and the observation that using this technique, we can equilibrate a polydisperse system till very low temperatures, the polydisperse systems have become a system of choice in studying low-temperature glass-forming liquids. However, doing analytical calculations for systems with continuous-size polydispersity is a challenge. According to liquid state theories, the structure can describe the thermodynamical properties and dynamics of the system. The exact way to describe the structure of a system with continuous size polydispersity is via  $N(N-1)$  partial structure factors, which present analytic difficulties, and this issue becomes more severe with increasing system size. To avoid this, the systems are typically treated as an effective one-component system, which leads to artificial structural softening and incorrect measures of the thermodynamical quantities. We describe a way to define the system in terms of an optimal number of species,  $M_0$  while keeping  $M_0 \ll N$ . This is done in a way such that we can use the partial structure factors to correctly obtain the thermodynamical quantities of the system. We also employ the information theoretical techniques and show that this definition of  $M_0$  leads to the maximum value of mutual information in the system. We next explore the structure dynamics correlation in polydisperse systems using recently developed microscopic mean-field theory. We define the mean field caging potential as an order parameter that describes the local structural order (SOP). Previous studies have shown that this SOP describes the particle-level dynamics. Here, we show that for a system with low polydispersity, the SOP is a good parameter to describe the particle-level dynamics. However, with an increase in polydispersity, we find that the dynamics is primarily determined by the size of the particles. We also find that the SOP and the size of the particle are coupled. The study emphasizes the complexities present in polydisperse systems due to the intercoupling of structure, size, and dynamics and the caution we should take in interpreting their roles.

After analysis of polydisperse, we work on another multispecies glass forming system known as the pinned system. By increasing the concentration of pinned particles in the fluid, the glassy behavior of the whole system is improved and it is shown that at high pinning concentration, the system undergoes a glass transition at a high temperature where the single particle dynamics still survives. It has been found that the usual thermodynamic integration (TI) approach to estimating entropy predicts that configurational entropy will vanish at a temperature where the system's single-particle dynamics show complete relaxation. To understand the correlation between entropy and dynamics and how dynamics survive when the entropy vanishes, we use a new method to compute entropy, called the two-phase thermodynamics (2PT) approach. We discover that the difference in entropy computed using the two approaches (2PT and TI) grows with increasing the pinning concentration. Additionally, we discover that, for the temperature range under consideration, entropy computed using the 2PT technique satisfies the Adam-Gibbs relationship between the relaxation time and the configurational entropy, whereas entropy calculated using the TI method strongly violates the same. We also address the problem of describing the structure and structural order parameters in pinned systems. In pinned system particles are pinned at the equilibrium configuration of the KA system (which is a binary 80:20 system) and it is expected that the equilibrium properties and the structure of the system do not change. We show that even after pinning the particles at the equilibrium position of the mobile particle, the structure of the liquid changes, and this change is visible only when we treat the pinned particles as a different species. We then derive the expression of the pair excess entropy and the mean-field caging potential for a pinned system by assuming it is a binary and a modified quaternary system. We find that apart from the change in structure, the pinned particles also act towards increasing the caging potential/decreasing the entropy more than other mobile particles. We also show that when the system is treated as binary, the structure dynamics correlation decreases with pinning, whereas it remains similar when the system is treated as a modified quaternary system. Thus, we conclude that structure dynamics correlation at a local level persists with increasing pinning.



# LIST OF PUBLICATIONS

---

1. **Palak Patel**, Synthesis of tannic acid capped silver nanoparticle for preparation of paper electrode, M.Sc. Thesis (2017).
2. **Palak Patel**, Manoj Kumar Nandi, Ujjwal Kumar Nandi, and Sarika Maitra Bhattacharyya, Effective structure of a system with continuous polydispersity, J. Chem. Phys., 154, 034503 (2021), DOI: 10.1063/5.0038812 .
3. Ujjwal Kumar Nandi, **Palak Patel**, Mohd Moid, Manoj Kumar Nandi, Shiladitya Sengupta, Smarajit Karmakar, Prabal K. Maiti, Chandan Dasgupta, and Sarika Maitra Bhattacharyya, Thermodynamics and its correlation with dynamics in a mean-field model and pinned systems: A comparative study using two different methods of entropy calculation, J. Chem. Phys., 156, 014503 (2022), DOI: 10.1063/5.0065668 .
4. **Palak Patel**, Mohit Sharma and, Sarika Maitra Bhattacharyya, Dynamic heterogeneity in polydisperse systems: A comparative study of the role of local structural order parameter and particle size, J. Chem. Phys., 159, 044501 (2023), DOI: 10.1063/5.0156794 .
5. **Palak Patel**, and, Sarika Maitra Bhattacharyya, Effect of the presence of pinned particles on the structural parameters of a liquid and correlation between structure and dynamics at the local level, Submitted in JCP (Under Review), arXiv:2312.10353.

## Poster Presentation -

1. Science Day 2019 in CSIR - NCL Pune
2. SPSI -Macro 2022 in CSIR - NCL Pune
3. National Chemical Laboratory - Research Foundation (NCL RF) 2022 in CSIR - NCL Pune
4. Compflu 2022 in IIT Kharagpur Research Park, Kolkata
5. Frontiers in active and soft matter in TIFR Hyderabad on February 2023
6. Science Day 2023 in CSIR - NCL Pune

***THESIS RELATED  
PUBLICATIONS***

# Effective structure of a system with continuous polydispersity

Cite as: J. Chem. Phys. **154**, 034503 (2021); <https://doi.org/10.1063/5.0038812>

Submitted: 30 November 2020 • Accepted: 28 December 2020 • Published Online: 21 January 2021

Palak Patel, Manoj Kumar Nandi, Ujjwal Kumar Nandi, et al.

## COLLECTIONS

Paper published as part of the special topic on [Special Collection in Honor of Women in Chemical Physics and Physical Chemistry](#)



View Online



Export Citation



CrossMark

## ARTICLES YOU MAY BE INTERESTED IN

### [Connecting real glasses to mean-field models](#)

The Journal of Chemical Physics **154**, 094506 (2021); <https://doi.org/10.1063/5.0038749>

### [Thermodynamics and its correlation with dynamics in a mean-field model and pinned systems: A comparative study using two different methods of entropy calculation](#)

The Journal of Chemical Physics **156**, 014503 (2022); <https://doi.org/10.1063/5.0065668>

### [When do short-range atomistic machine-learning models fall short?](#)

The Journal of Chemical Physics **154**, 034111 (2021); <https://doi.org/10.1063/5.0031215>

The Journal of Chemical Physics **Special Topics** Open for Submissions

[Learn More](#)

# Effective structure of a system with continuous polydispersity

Cite as: J. Chem. Phys. 154, 034503 (2021); doi: 10.1063/5.0038812

Submitted: 30 November 2020 • Accepted: 28 December 2020 •

Published Online: 21 January 2021



View Online



Export Citation



CrossMark

Palak Patel,<sup>1,2</sup> Manoj Kumar Nandi,<sup>1</sup> Ujjwal Kumar Nandi,<sup>1,2</sup> and Sarika Maitra Bhattacharyya<sup>1,2,a)</sup> 

## AFFILIATIONS

<sup>1</sup>Polymer Science and Engineering Division, CSIR-National Chemical Laboratory, Pune 411008, India

<sup>2</sup>Academy of Scientific and Innovative Research (AcSIR), Ghaziabad 201002, India

**Note:** This paper is part of the JCP Special Collection in Honor of Women in Chemical Physics and Physical Chemistry.

<sup>a)</sup>Author to whom correspondence should be addressed: [mb.sarika@ncl.res.in](mailto:mb.sarika@ncl.res.in)

## ABSTRACT

In a system of  $N$  particles, with continuous size polydispersity, there exists an  $N(N - 1)$  number of partial structure factors, making it analytically less tractable. A common practice is to treat the system as an effective one component system, which is known to exhibit an artificial softening of the structure. The aim of this study is to describe the system in terms of  $M$  pseudospecies such that we can avoid this artificial softening but, at the same time, have a value of  $M \ll N$ . We use potential energy and pair excess entropy to estimate an optimum number of species,  $M_0$ . We then define the maximum width of polydispersity,  $\Delta\sigma_0$ , that can be treated as a monodisperse system. We show that  $M_0$  depends on the degree and type of polydispersity and also on the nature of the interaction potential, whereas  $\Delta\sigma_0$  weakly depends on the type of polydispersity but shows a stronger dependence on the type of interaction potential. Systems with a softer interaction potential have a higher tolerance with respect to polydispersity. Interestingly,  $M_0$  is independent of system size, making this study more relevant for bigger systems. Our study reveals that even 1% polydispersity cannot be treated as an effective monodisperse system. Thus, while studying the role of polydispersity by using the structure of an effective one component system, care must be taken in decoupling the role of polydispersity from that of the artificial softening of the structure.

Published under license by AIP Publishing. <https://doi.org/10.1063/5.0038812>

## I. INTRODUCTION

Most systems that can be found in nature are inherently polydisperse. Polydispersity can be different types such as in size, in mass, and also in the shape of particles. In addition, the type of polydispersity and the degree of it vary with systems. Polydispersity brings a variation in the properties of the material, and there are specially designed controlled experiments to create monodisperse particles.<sup>1,2</sup> However, in some cases, polydispersity is a desirable property. Size polydispersity is one of the most common types, and it has been found that systems beyond a certain value of polydispersity, known as terminal polydispersity, are good glass formers.<sup>3–5</sup> It was shown that in a polydisperse system due to an increase in surface free energy, the crystal nucleation is suppressed, promoting glass formation.<sup>10</sup> Thus, in the study of supercooled liquids, polydisperse systems play an important role.

In recent times it has been shown that the structure plays an important role in the dynamics of glass-forming supercooled

liquids.<sup>11–19</sup> Since polydisperse systems are good glass formers, describing the structure of these systems becomes important. For a continuous polydisperse system, the number of species is the same as the number of particles in the system. In this case, describing the system's partial structure in terms of independent species becomes an impossible task. Thus, it is common practice to treat a polydisperse system in terms of an effective one component system.<sup>20–24</sup> However, it has been shown that we lose a large deal of information of the system by pre-averaging the structure, and the properties of the liquid thus predicted can also give spurious results.<sup>25,26</sup> Truskett and co-workers<sup>25</sup> showed that for moderate polydispersity, the thermodynamic quantities such as the pair excess entropy obtained from the effective one component radial distribution function (rdf) predicts that with an increase in interaction, the static correlation becomes weaker, thus predicting structural anomaly. The study showed that when the system is expressed in terms of 60 pseudoneighbors and the excess entropy is calculated in terms of partial structure factors (radial distribution functions), this structural anomaly disappears.

Weysser *et al.*, while working with mode coupling theory, showed that for a polydisperse system, we need to provide information about the partial structure factors to obtain the correct dynamics.<sup>26</sup> Ozawa and Berthier highlighted the fact that for a system with continuous size polydispersity, the contribution from the mixing entropy term diverges.<sup>27</sup> This makes the calculation of entropy and any other dependent quantity ill-defined. They showed by calculating the inherent structure properties that when the position of particles with similar sizes is exchanged, the system stays in a similar basin. This modifies the vibrational entropy, which also has the same mixing entropy term. The process allowed them to group particles into a certain finite number of pseudospecies, leading to a finite value of mixing entropy. These studies thus emphasize the importance of describing the structure of a polydisperse system in terms of partial structure factors of the pseudospecies.

The present study attempts to develop a general framework to describe the structure of a system having continuous polydispersity. As discussed before, for a system with continuous polydispersity, the number of species is the same as the number of particles, which makes it difficult to describe the structure. We also know that describing all the particles in terms of a single species does not work. Hence, the aim of this study is to describe the system in terms of  $M$  pseudospecies such that the properties of this system are the same as the original system. The questions that we ask are as follows: (i) Can we determine the minimum number of pseudospecies “ $M_0$ ” required to describe the structure of the system? (ii) Is this dependent on the property that we study? (iii) Does it depend on the degree and nature of polydispersity? (iv) Does it depend on the interaction potential?

To answer these questions, we use the method of calculating thermodynamic quantities, which can be obtained from the structure of the liquid, namely, the potential energy of the system and the pair excess entropy. Note that the former is a linear function of the structure, whereas the latter is a nonlinear function of the structure and, thus, can have different sensitivities to the effective structure. We find that by studying these above-mentioned thermodynamical quantities, we can determine a value of  $M_0$ . It depends on the type of polydispersity, the degree of polydispersity, and the interaction potential. We also provide an estimate of the width of polydispersity that can be treated like a one component system. This width appears to depend primarily on the interaction potential of the system. Systems with a longer range and a softer interaction potential have a better tolerance toward polydispersity. In these cases, systems with a wider spread of size can be addressed in terms of a one component system.

The organization of the rest of this paper is as follows. Section II contains the simulation details. In Sec. III, we discuss the methods used for evaluating the various quantities of interest. Section IV contains the results with discussions, and this paper ends with a brief conclusion in Sec. V.

## II. SIMULATION DETAILS

In this study, we perform molecular dynamics simulations for a three-dimensional polydisperse system with continuous size polydispersity in the canonical ensemble. The system contains  $N = 1000$ – $4000$  particles in a cubic box of volume  $V$ . The number density for all

the systems is  $\rho = N/V = 1.0$ . In our simulations, we have used periodic boundary conditions and the Nosé–Hoover thermostat with an integration time step of  $0.001\tau$ . The time constants for the Nosé–Hoover thermostat are taken to be 100 time steps. We have carried out molecular dynamics simulations using the LAMMPS package.<sup>28</sup> This study involves two different kinds of systems with respect to size polydispersity, constant volume fraction (CVF) and Gaussian distributions (as shown in Fig. 1), and three different kinds of interaction potentials. The distributions of the particle size are continuous. This means that each of the  $N$  particles has a different radius. The form of the constant volume fraction distribution is given by<sup>8</sup>

$$P_1(\sigma) = \frac{A}{\sigma^3}, \quad \sigma \in [\sigma_{\max}, \sigma_{\min}], \quad (1)$$

where  $A$  is the normalization constant and  $\sigma_{\max}$  and  $\sigma_{\min}$  are the maximum and minimum values of particle diameter.  $\sigma_{\max}$  and  $\sigma_{\min}$  values are given in Table I. The degree of polydispersity is quantified by<sup>8</sup> the normalized root mean square deviation,

$$\text{PDI} = \frac{\sqrt{\langle \sigma^2 \rangle - \langle \sigma \rangle^2}}{\langle \sigma \rangle},$$

where  $\langle \dots \rangle$  defines the average of the particle size distribution.

The Gaussian distribution is given by

$$P_2(\sigma) = \frac{1}{\sqrt{2\pi\delta^2}} \exp\left(-\frac{(\sigma-\langle\sigma\rangle)^2}{2\delta^2}\right), \quad (2)$$

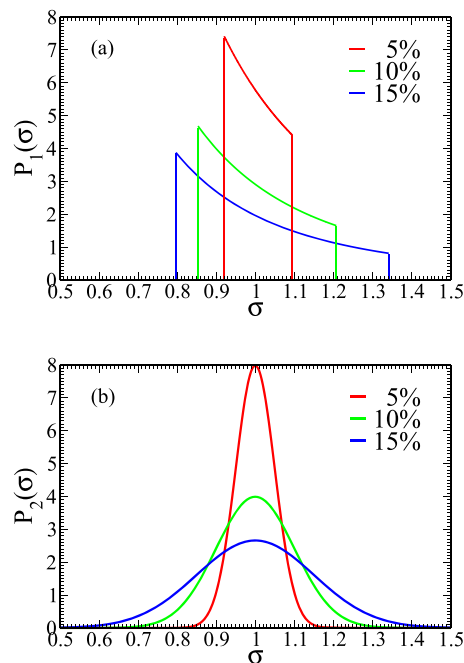


**FIG. 1.** Different kinds of distributions: (a) constant volume fraction distribution,  $P_1(\sigma)$ , and (b) Gaussian distribution,  $P_2(\sigma)$ . For the same degree of polydispersity, compared to  $P_1(\sigma)$ , the distribution is wider for  $P_2(\sigma)$ .

**TABLE I.** Details of size distributions, constant volume fraction and Gaussian, for different degrees of polydispersity  $PDI = \frac{\sqrt{\langle \sigma^2 \rangle - \langle \sigma \rangle^2}}{\langle \sigma \rangle}$ . The maximum,  $\sigma_{\max}$ , and minimum,  $\sigma_{\min}$ , values of the diameter of particles. The volume fraction  $\eta$  is also given, showing an increase in  $\eta$  with a degree of polydispersity.

Distribution	PDI (%)	$\sigma_{\max}$	$\sigma_{\min}$	$\Delta\sigma$	$\eta$
$P_1(\sigma)$	5	1.1	0.92	0.18	0.53
	10	1.21	0.85	0.36	0.54
	15	1.34	0.8	0.54	0.56
$P_2(\sigma)$	5	1.15	0.85	0.3	0.53
	10	1.3	0.7	0.6	0.54
	15	1.45	0.55	0.9	0.56

where  $\delta$  is the standard deviation. In this distribution, we consider  $\sigma_{\max/\min} = \langle \sigma \rangle \pm 3\delta$ . The degree of polydispersity is quantified by

$$PDI = \frac{\sqrt{\langle \sigma^2 \rangle - \langle \sigma \rangle^2}}{\langle \sigma \rangle} = \frac{\delta}{\langle \sigma \rangle}.$$

For all the polydisperse systems, particle sizes are chosen such that  $\langle \sigma \rangle = \int P(\sigma) \sigma d\sigma = 1$  and is kept as the unit of length for all the systems studied here.

The three different interaction potentials studied here are the inverse power law (IPL) potential, the Lennard-Jones (LJ) potential, and its repulsive counterpart the Weeks–Chandler–Andersen (WCA) potential. The inverse power law potential (IPL) between two particles  $i$  and  $j$  is given by<sup>8,29</sup>

$$U(r_{ij}) = \begin{cases} \epsilon_{ij} \left( \frac{\sigma_{ij}}{r_{ij}} \right)^{12} + \sum_{l=0}^2 c_{2l} \left( \frac{r_{ij}}{\sigma_{ij}} \right)^{2l}, & \left( \frac{r_{ij}}{\sigma_{ij}} \right) \leq x_c \\ 0, & \left( \frac{r_{ij}}{\sigma_{ij}} \right) > x_c. \end{cases} \quad (3)$$

Constants  $c_0$ ,  $c_2$ , and  $c_4$  are selected such that the potential becomes continuous up to its second derivative at the cutoff  $x_c = 1.25\sigma_{ij}$ .

The LJ potential between two particles  $i$  and  $j$  is described using the truncated and shifted LJ potential,<sup>30</sup>

$$U(r_{ij}) = \begin{cases} U^{(LJ)}(r_{ij}; \sigma_{ij}, \epsilon_{ij}) - U^{(LJ)}(r_{ij}^{(c)}; \sigma_{ij}, \epsilon_{ij}), & r_{ij} \leq r_{ij}^{(c)} \\ 0, & r_{ij} > r_{ij}^{(c)}, \end{cases} \quad (4)$$

where  $U^{(LJ)}(r_{ij}; \sigma_{ij}, \epsilon_{ij}) = 4\epsilon_{ij} \left[ \left( \frac{\sigma_{ij}}{r_{ij}} \right)^{12} - \left( \frac{\sigma_{ij}}{r_{ij}} \right)^6 \right]$ . The cutoff for the LJ system is  $r_{ij}^{(c)} = 2.5\sigma_{ij}$ , and that for the WCA system is  $r_{ij}^{(c)} = 2^{1/6}\sigma_{ij}$ .<sup>31</sup> The interaction strength between two particles  $i$  and  $j$  is  $\epsilon_{ij} = 1.0$ .  $\sigma_{ij} = \frac{(\sigma_i + \sigma_j)}{2}$ , where  $\sigma_i$  is a diameter of particle  $i$  and it varies according to the system. Length, temperature, and times are given in units of  $\langle \sigma \rangle$ ,  $\epsilon_{ij}$  and  $\left( \frac{m\langle \sigma \rangle^2}{\epsilon_{ij}} \right)^{1/2}$ , respectively. For all state points, the equilibration is performed for  $100\tau_\alpha$  ( $\tau_\alpha$  is the  $\alpha$ -relaxation time), and three to five independent samples are analyzed. As will be discussed later, in this work, both potential energy and pair excess entropy are calculated using the partial structure factors. In a system with continuous polydispersity, each particle has a different diameter. Therefore, there are  $\frac{N \times N}{2}$  partial radial distribution functions. For

$N = 1000$ , there are, thus, 500 000 partial rdfs, and with an increase in  $N$ , this number grows as  $N^2$ . Calculating these many partial rdfs with good precision is an impossible task. However, in this study, we divide the total system into  $M$  species. Particles with a diameter range  $(\sigma_{\max} - \sigma_{\min})/M$  are treated as a single species. Note that this is an approximation because particle sizes in a single species are still different. With an increase in  $M$ , this diameter range becomes narrow and the approximation leads to less error. The maximum value of  $M$  that we have used in this work is 26. Thus, we have calculated at the most 338 partial rdfs. Although the study is performed in the high-temperature regime where the production run length is usually around  $100\tau_\alpha$ , where  $\tau_\alpha$  varies between 5–100, for this study, to get a good precision of the partial rdf, we require longer production run lengths to compensate for the poor particle averaging. For 5% PDI, the production run length is  $10^7$ , and for 15% PDI and 10% PDI, the production run lengths are  $10^7$  for  $T = 5.0$ – $0.38$  and  $6 \times 10^7$  for  $T = 0.36$ – $0.2$ , respectively.

### III. DEFINITION AND BACKGROUND

#### A. Radial distribution function

The partial radial distribution  $g_{\alpha\beta}(r)$  is defined as follows:

$$g_{\alpha\beta}(r) = \frac{V}{N_\alpha N_\beta} \left\langle \sum_{i=1}^{N_\alpha} \sum_{j=1, j \neq i}^{N_\beta} \delta(r - r_i + r_j) \right\rangle, \quad (5)$$

where  $V$  is the volume of the system and  $N_\alpha$ ,  $N_\beta$  are the number of  $\alpha$ - and  $\beta$ -type of particles, respectively.

The effective one component radial distribution function,  $g(r)$ , can be written in terms of partial rdf of  $M$  species as<sup>32</sup>

$$g(r) = \sum_{\alpha, \beta=1}^M \chi_\alpha \chi_\beta g_{\alpha\beta}(r), \quad (6)$$

where  $\chi_\alpha$  and  $\chi_\beta$  are the mole fraction of  $\alpha$  and  $\beta$  particles, respectively.

#### B. Potential energy

The per particle potential energy of the system can be exactly calculated from simulation  $E_{sim}$ . The same can also be written in terms of the partial radial distribution function,  $E_2$ , as follows:

$$E_2 = \frac{\rho}{2} \sum_{\alpha, \beta=1}^M \chi_\alpha \chi_\beta \int_0^\infty 4\pi r^2 U_{\alpha\beta}(r) g_{\alpha\beta}(r) dr. \quad (7)$$

In the effective one component treatment, the energy can be written as  $E_2^{eff}$ , which is given as follows:

$$E_2^{eff} = \frac{\rho}{2} \int_0^\infty 4\pi r^2 U(r) g(r) dr. \quad (8)$$

#### C. Excess entropy

Excess entropy  $S_{ex}$  is a loss of entropy due to the interaction between particles, or in other words, excess entropy is a difference between  $S_{total}$  and  $S_{ideal}$  at the same temperature  $T$  and density  $\rho$ . The value of  $S_{ex}$  is always negative.  $S_{ex}$  can be evaluated by thermodynamic integration (temperature density landscape).<sup>33</sup> Entropy at

high temperature and low density is the same as that of an ideal gas entropy. This  $S_{ideal}$  is a relative reference for any other state points' entropy calculation. Other state point entropy can be calculated using a combination of isotherms [Eq. (9)] and isochoric [Eq. (10)] paths, making sure that no phase transitions occur along the selected path,<sup>33</sup>

$$S_{ex}(T, V') - S_{ex}(T, V) = \frac{U(T, V') - U(T, V)}{T} + \int_V^{V'} \frac{P(V)}{T} dV, \quad (9)$$

$$S_{ex}(T', V') - S_{ex}(T, V') = \int_T^{T'} \frac{1}{T} \left( \frac{\delta U}{\delta T} \right)_{V'} dT. \quad (10)$$

Addition of Eqs. (9) and (10) gives the total excess entropy.

#### D. Pair entropy

Using the Kirkwood factorization,<sup>34</sup> the excess entropy can also be expressed in terms of an infinite series,

$$S_{ex} = S_2 + S_3 + S_4 \dots \quad (11)$$

Here  $S_n$  is an entropy contribution due to  $n$  particle spatial correlation. The pair excess entropy  $S_2$  includes 80% of the total excess entropy.<sup>35</sup> We can calculate  $S_2$  from the partial rdf of  $M$  species,<sup>33</sup>

$$\frac{S_2}{k_B} = -2\pi\rho \sum_{\alpha,\beta=1}^M \chi_\alpha \chi_\beta \int_0^\infty r^2 dr \{g_{\alpha\beta}(r) \ln g_{\alpha\beta}(r) - (g_{\alpha\beta}(r) - 1)\}, \quad (12)$$

where  $k_B$  is the Boltzmann constant.

If we do not consider different species, then the entropy for an effective one component system can be written as  $S_2^{eff}$ , which is given as follows:

$$\frac{S_2^{eff}}{k_B} = -2\pi\rho \int_0^\infty r^2 dr \{g(r) \ln g(r) - (g(r) - 1)\}. \quad (13)$$

#### E. Onset temperature calculation from inherent structure energy

While cooling a glass-forming liquid from high temperatures at the onset temperature,  $T_{onset}$ , the system's thermodynamic and dynamic properties deviate from its high-temperature behavior. There are different dynamical and thermodynamical measures of  $T_{onset}$ . The temperature predicted by using each method is not identical but lies in a similar range. A comparison of the different methods is given in Ref. 15. In this work, we will discuss the one calculated from the inherent structure energy and the other from the excess entropy.

The inherent structure energy is the potential energy evaluated at the local minimum of the energy reached from the configuration via the steepest descent procedure. As suggested earlier,<sup>36</sup> the onset temperature is connected to the inherent structure energy. At high temperatures, as the system is not influenced by the landscape properties, the average inherent structure energy is almost temperature independent. However, below a certain temperature, where the landscape properties influence the system, the inherent structure energy starts to decrease rapidly. Usually, the two different regimes are fitted to two straight lines, and the point where these lines cross is identified as the onset temperature,  $T_{onset}$ .

#### F. Dynamics

In this work, to characterize the dynamics, we consider the self-part of the overlap function  $Q(t)$ , defined as<sup>37</sup>

$$Q(t) = \frac{1}{N} \sum_{i=1}^N \langle \omega(|\mathbf{r}_i(t) - \mathbf{r}_i(0)|) \rangle, \quad (14)$$

where the function  $\omega(x)$  is 1 if  $0 \leq x \leq a$  and  $\omega(x) = 0$  otherwise. Parameter  $a$  is chosen to be 0.3, a value that is slightly larger than the size of the cage.

Note that the dynamics can also be obtained from the self-intermediate scattering function  $F_s(q, t)$ , where  $q = 2\pi/r_{max}$ , with  $r_{max}$  being the position of the first peak of the radial distribution function. Since relaxation times from  $Q(t)$  and  $F_s(q, t)$  behave very similarly at the low temperature, we use  $Q(t)$  for the dynamics.

### IV. RESULT

#### A. Effective one component description

As discussed before, it is a common practice to describe the structure of a polydisperse system in terms of an effective one component system.

In Fig. 2, we plot the difference between the average per particle potential energy of the species agnostic  $E_2^{eff}$  and that obtained from simulation  $E_{sim}$  for systems with different PDI values (5%, 10%, and 15%). In the simulation study, the particle sizes are obtained from  $P_1(\sigma)$  distribution, and they interact via the IPL potential. In Fig. 3, we also plot  $S_{ex}$  and the species agnostic  $S_2^{eff}$  for the above-mentioned systems. Note that if the structure is described properly, then  $E_{sim} = E_2$  and  $S_2$  is not exactly equal to  $S_{ex}$  but comprises of 80% of its value.<sup>15,33,35,38-42</sup>

We find that as the PDI increases, the difference between  $E_{sim}$  and  $E_2^{eff}$  and  $S_{ex}$  and  $S_2^{eff}$  increases. This clearly shows that as expected, with an increase in PDI, the effective one component description of the system becomes less accurate. In Fig. 4, we plot both the dynamics and the effective one component rdf of the systems. We find that within the temperature range studied here, although the dynamics remains almost the same, with an increase in polydispersity, the structure appears to soften. We have plotted the

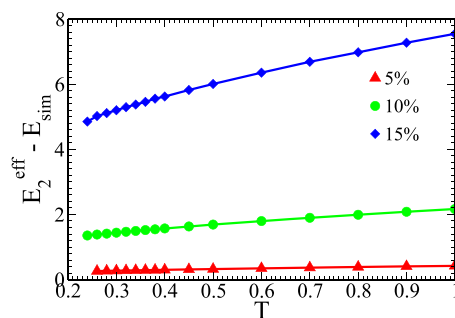
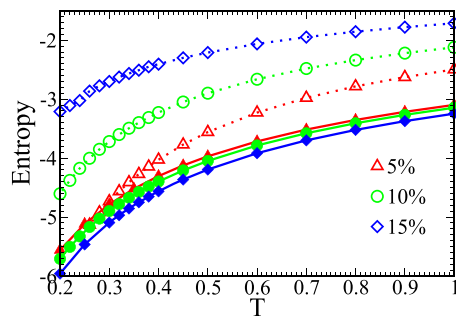


FIG. 2. The difference in energy obtained from effective one component radial distribution functions,  $E_2^{eff}$ , and simulation,  $E_{sim}$ , as a function of  $T$  at different PDIs. Here, particles are interacting via the IPL potential, and the particle size distribution is given by  $P_1(\sigma)$  (constant volume fraction distribution).





**FIG. 3.** Excess entropy,  $S_{ex}$ , and effective one component pair excess entropy,  $S_2^{eff}$  [Eq. (13)], at different PDIs. Solid lines with filled symbols represent  $S_{ex}$ , and dotted lines with open symbols represent  $S_2^{eff}$ . Here, particles are interacting via the IPL potential, and the particle size distribution is given by  $P_1(\sigma)$  (constant volume fraction distribution).

rdf at two temperatures ( $T = 1.0$  and  $0.5$ ), and it appears that the softening is present in both temperatures. However, the fact that the difference between  $E_2^{eff}$  and  $E_{sim}$  reduces at low temperatures (Fig. 2) do suggest that the softening also reduces with temperature. This artificial softening of the structure leads to the increase in  $E_2^{eff}$  and  $S_2^{eff}$ . Note that even for 5% polydispersity, we find that the effective one component structure of the system fails to provide the correct value of the potential energy and the pair excess entropy. These results presented in Figs. 2 and 3 are not surprising, but a confirmation of the observations is made earlier.<sup>25,26</sup>

### B. Pseudosppecies and its dependence on degree of polydispersity

Describing the structure of a continuous polydisperse system can be challenging. Unlike in a discrete polydisperse system where each species has a finite number of particles and all of them have the same size, for a continuous polydisperse system, the number of species is the same as the number of particles. However, let us assume that we describe a pseudosystem where we divide the particles into  $M$  number of pseudosppecies (where  $M < N$ ) in terms of the size of particles. In doing so, we bunch similar particles but with different sizes in a group and assign an average size to them. This introduces disparity in the actual size and in the assigned size of the particles and leads to an error in describing the properties of the system. An extreme case of that ( $M = 1$ ) can be seen in Figs. 2 and 3. For a fixed  $M$ , the maximum difference in the actual diameter of a particle and in its assigned average diameter is  $\Delta\sigma/2M$ . Thus, with an increase in  $M$ , this error reduces, and at  $M = N$ , the pseudosystem is exact. Therefore, the first question is can we describe the structure of a system in terms of an optimum number of species  $M_0$ , where  $M_0 \ll N$  such that the structure can provide a correct estimate of the thermodynamic quantities? If we can, then how does  $M_0$  depend on the degree of polydispersity?

In Fig. 5(a), we plot  $\frac{E_2}{E_{sim}}$  as a function of  $M$ , at two different temperatures for the different PDIs. For systems with a fixed value of PDI, as we increase the value of  $M$ ,  $E_2$  decreases, and after a certain value of  $M$ ,  $E_2 \approx E_{sim}$ . We find that this is weakly temperature dependent. For this work, we consider that at  $T = 1$ , the minimum number

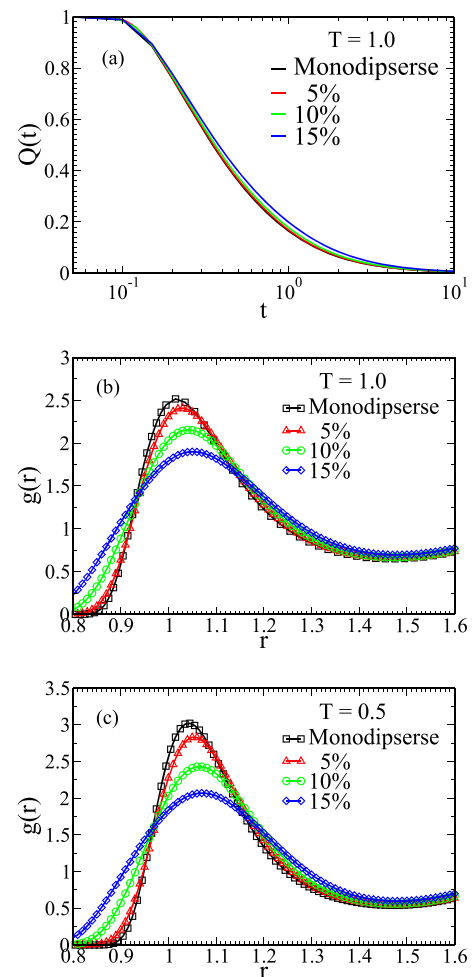


**FIG. 4.** (a) Dynamics of systems at different PDIs. The overlap function is plotted against time. (b) Effective one component radial distribution function of the systems at  $T = 1.0$ . (c) Same as (b) at  $T = 0.5$ . Black square, red triangle, green circle, and blue diamond represent a monodisperse system with 5% PDI, 10% PDI, and 15% PDI, respectively. With an increase in PDI, although the dynamics remains almost the same, the structure shows a substantial softening. Here, particles are interacting via the IPL potential, and the particle size distribution is given by  $P_1(\sigma)$  (constant volume fraction distribution).

of pseudosppecies for which  $\frac{(E_2 - E_{sim})}{E_{sim}} < 0.01$  is  $M_0$ . The value of  $M_0$  is system dependent and as expected increases with the increase in the PDI value, as shown in Fig. 5(b). Note that while determining  $M_0$ , this choice of the relative error (0.01) is arbitrary but practical. In principle, we can choose values much smaller or probably larger than this. However, later, while discussing the value of  $M_0$  as obtained from entropy, we will see that this choice is reasonable.

Is the value of  $M_0$  sensitive to the thermodynamic quantity that we calculate or is it universal? To answer this question, we calculate the two body pair entropy for different values of  $M$ . We find that similar to the energy, as  $M$  increases,  $S_2$  comes closer to  $S_{ex}$  (Fig. 6). However, even for large values of  $M$ ,  $S_2$  is not equal to  $S_{ex}$ . This is because unlike the potential energy that can be exactly calculated in



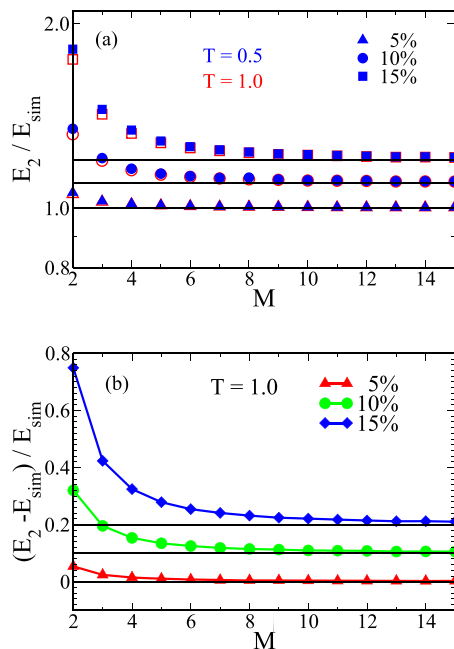


**FIG. 5.** Comparison between the energy obtained from simulation,  $E_{sim}$ , and the energy obtained from partial radial distribution functions,  $E_2$  [Eq. (7)]. (a) Ratio of  $E_2$  and  $E_{sim}$  vs the number of pseudospecies  $M$  at  $T = 1.0$  (open red symbols) and  $T = 0.5$  (filled blue symbols) for different PDIs. (b) Relative error calculation between  $E_{sim}$  and  $E_2$ , with  $(E_2 - E_{sim})/E_{sim}$  plotted as a function of  $M$  for different PDIs. For better visualization, we have shifted the y axis of the 10% and 15% PDI plot by 0.2. The horizontal lines signify the corresponding large  $M$  values, which are 1.0 for (a) and 0.0 for (b). Here, particles are interacting via the IPL potential, and the particle size distribution is given by  $P_1(\sigma)$  (constant volume fraction distribution).

terms of the partial rdf, only a part of the excess entropy can be calculated from the rdf [Eq. (11)].<sup>15,33,35,38–42</sup> This makes it difficult to use the same methodology as used for potential energy to make an estimation of  $M_0$  from entropy.

However, from our earlier studies, we know that if the structure of the liquid is described properly, then the excess entropy and the two body pair entropy cross each other at a temperature,  $T_{cross}$ , which can be considered as the onset temperature of the supercooled liquid dynamics.<sup>15</sup> This onset temperature can also be obtained from the change in the slope of the temperature dependence of the inherent structure energy<sup>36</sup> and also other methods.<sup>15</sup> As shown earlier, the values of the onset temperatures obtained using these different methods are not exactly the same, but they are in a similar range.<sup>15</sup>

In Fig. 7, we plot the variation of  $T_{cross}$  with  $M$  for the different systems. For higher PDI, at small values of  $M$ , we cannot calculate  $T_{cross}$ , which implies that  $S_2$  is far away from  $S_{ex}$  and never crosses it, as shown in Fig. 6. However, from our other estimates of the onset temperature, we know that we are in a temperature range where these two forms of entropy should cross. As  $M$  increases, the two functions cross at some temperature  $T_{cross}$ . We find that initially  $T_{cross}$  increases with  $M$ , and then, after a certain value of  $M$ , it shows a saturation. As mentioned before,  $S_2$  is not the total excess entropy of the system. There is no other method for calculating  $S_2$ . Thus, it

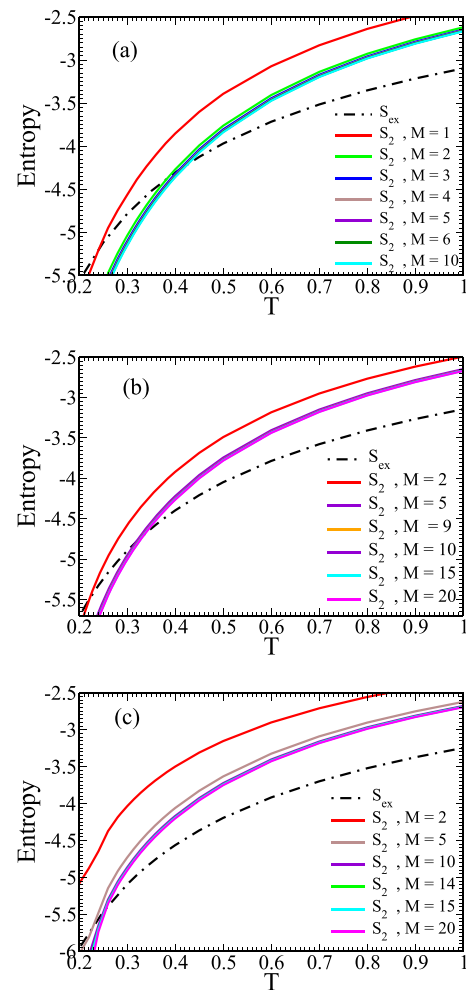


**FIG. 6.** Excess entropy,  $S_{ex}$ , and pair excess entropy  $S_2$ . The latter is calculated at different values of  $M$  [Eq. (12)]. Dashed-dotted lines represent  $S_{ex}$ , and solid lines represent  $S_2$ . (a) PDI 5%, (b) PDI 10%, and (c) PDI 15%. Here, particles are interacting via the IPL potential, and the particle size distribution is given by  $P_1(\sigma)$  (constant volume fraction distribution).

is not possible to do a similar error estimation of pair excess entropy as done for the potential energy. However, the saturation of  $T_{cross}$  is an indication of the saturation of  $S_2$  with respect to  $M$ . We find that this saturation value of  $T_{cross}$  is in the same range as the estimated onset temperature using the method of inherent structure energy (see Sec. III E and Table II). In this plot, we also mark the  $M_0$  values as obtained from the potential energy. We find that the  $M$  value for which  $T_{cross}$  saturates falls in the same range as  $M_0$ . The values of  $T_{cross}$  at  $M = M_0$  and  $T_{onset}$  are given in Table II. Thus, we show that the minimum number of pseudospecies required to describe the potential energy of the system can also describe the two body excess entropy of the system. Note that although with  $M_0$  pseudospecies we can get a reasonable value of  $S_2$ , this quantity is not the total excess entropy of the system. The residual multi-particle entropy (RMPE) defined as the difference between the total excess entropy

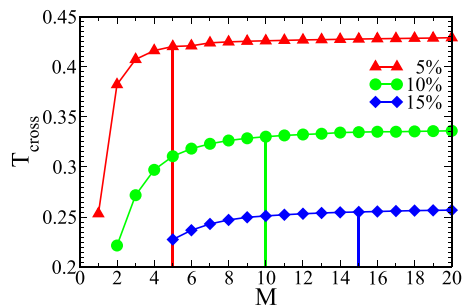


**FIG. 7.**  $T_{cross}$  vs  $M$  plot for different PDIs. Initially,  $T_{cross}$  increases with  $M$ , but after certain value of  $M$ , it saturates. For larger PDI, the saturation takes place at a higher  $M$  value. The vertical lines give the value of  $M_0$  obtained from energy criteria. Here, particles are interacting via the IPL potential, and the particle size distribution is given by  $P_1(\sigma)$  (constant volume fraction distribution).

and the pair excess entropy,  $S_{ex} - S_2$ , although has a small value when compared to  $S_2$ , plays an important role in describing the thermodynamics of the system. For example, it has been observed that if we ignore RMPE, then the correlation between dynamics and thermodynamics expressed via the well-known Adam–Gibbs relation does not hold.<sup>12</sup> It has also been observed that in the supercooled liquid regime, RMPE provides us a measure of the activated dynamics of the system.<sup>12,17</sup> Thus, although the pseudospecies description provides us a reasonable estimation of  $S_2$ , care should be taken while using this quantity in describing the full thermodynamics of the system.

The details of the  $M_0$  values for the different systems are given in Table II. We also tabulate a quantity  $\Delta\sigma_0 = \frac{\Delta\sigma}{M_0}$ . We find that although  $M_0$  is dependent on the PDI, the quantity  $\Delta\sigma_0$  is not. Note that when  $M = M_0$ , the maximum error in assigning a diameter to a particle is  $\frac{\Delta\sigma_0}{2}$ . Thus, our study suggests that the thermodynamic properties of the system studied here are not sensitive to a change in the diameter by  $\frac{\Delta\sigma_0}{2}$ , and for a constant volume fraction, the polydisperse system interacting via the IPL potential when  $\Delta\sigma \approx 0.036$  can be treated as a monodisperse system.

Interestingly, we find that when we plot the partial rdf for two consecutive pseudospecies,  $g_{11}(r)$  and  $g_{22}(r)$  (here, these two species

**TABLE II.** The values of  $M_0$  and  $\Delta\sigma_0$  for different systems. We also provide the values of  $T_{cross}$  at  $M = M_0$ , and for comparison, we give the  $T_{onset}$  values obtained from fitting the inherent structure energy to two straight lines.

Distribution	Potential	PDI (%)	$M_0$	$\Delta\sigma_0 = \frac{\Delta\sigma}{M_0}$	$T_{cross}(M_0)$	$T_{onset}$
$P_1(\sigma)$	IPL	5	5	0.036	0.42	0.43
		10	10	0.036	0.33	0.36
		15	15	0.036	0.26	0.31
$P_2(\sigma)$	IPL	5	7	0.043	0.43	0.46
		10	14	0.043	0.35	0.34
		15	21	0.043	0.28	0.30
$P_1(\sigma)$	WCA	15	20	0.027	0.58	0.7
	LJ	15	12	0.045	0.67	0.81

1 and 2 have the largest and the second largest number of particles, respectively) for different values of  $M$ , then for  $M = M_0$ , the peaks of the two rdfs almost overlap (Fig. 8). Thus, we can say that when the size difference of the two consecutive species is such that there is a large overlap between the radial distribution functions of two consecutive species, they can be treated as a single species.

### C. Effect of the type of distribution on $M_0$ and $\Delta\sigma_0$

We next study the effect of the type of distribution on  $M_0$  and  $\Delta\sigma_0$ . In Fig. 9, we compare the  $M$  dependence of  $T_{cross}$  for systems where polydispersity is described in terms of  $P_1(\sigma)$  (constant volume fraction) and  $P_2(\sigma)$  (Gaussian), for three different PDIs. In the same plot, the  $M_0$  values as obtained from the potential energy are also marked.

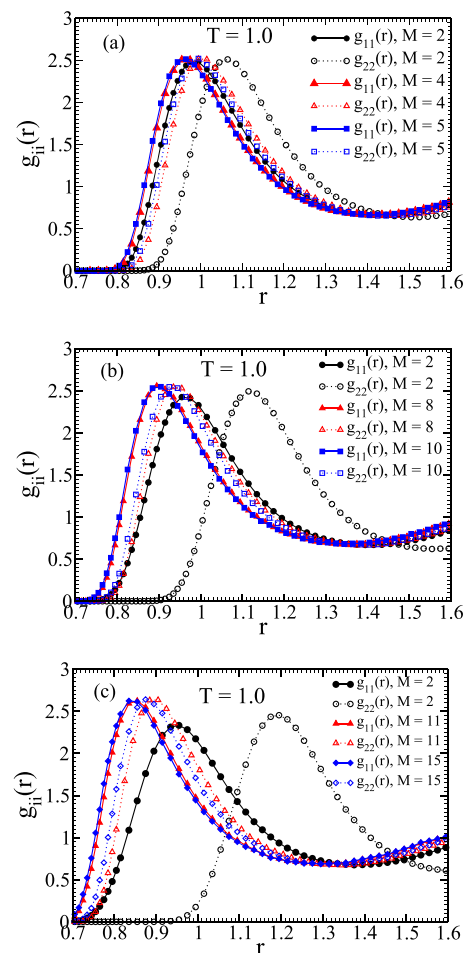


**FIG. 8.** The partial radial distribution function for the first two species for different values of  $M$ . (a) PDI 5%, (b) PDI 10%, and (c) PDI 15%. For  $M = M_0$ , the rdf peak of the two consecutive species almost overlaps. Here, particles are interacting via the IPL potential, and the particle size distribution is given by  $P_1(\sigma)$  (constant volume fraction distribution).

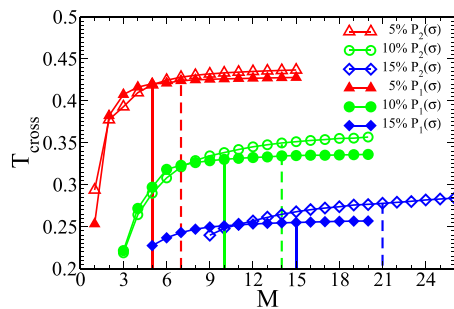


**FIG. 9.** The effect of the type of distribution on  $M_0$ .  $T_{cross}$  vs  $M$  plot for different PDIs for systems where particles are interacting via the IPL potential, and the particle size distribution is given by  $P_1(\sigma)$  (constant volume fraction distribution) and  $P_2(\sigma)$  (Gaussian distribution). The vertical lines give the value of  $M_0$  obtained from energy criteria (solid lines for  $P_1$  distribution and dashed lines for  $P_2$  distribution). At the same value of PDI, for the Gaussian distribution,  $M_0$  is higher and  $T_{cross}$  saturates at a higher  $M$  value.

At the same PDI, the nature of saturation of  $T_{cross}$  and also the value of  $M_0$  are different for the two different distributions. Compared to the constant volume fraction distribution, the values of  $M_0$  are higher for the Gaussian distribution. The reason behind this can be understood by comparing Figs. 1 and 2 (also see Table I). For the same PDI, the Gaussian distribution is wider compared to the constant volume fraction distribution. A closer observation tells us that the saturation of  $T_{cross}$  is better for the CVF distribution when compared to the Gaussian distribution. Note that for the Gaussian distribution,  $M_0$  is higher (more number of species), and by nature, toward the tail of the distribution, the number of particles is less, so the partial rdf for the largest and the smallest species is poorly averaged. We have seen that with an increase in the system size, the saturation improves (not shown here).

We find that when compared to CVF distribution,  $\Delta\sigma_0$  is marginally higher for the systems with Gaussian distribution (see Table II). Note that we divide a continuous polydisperse system into  $M$  species in a way that the difference in the diameter of two consecutive species is always separated by  $\frac{\Delta\sigma}{M}$ . This implies that the percentage error in calculating the size of the smaller particles is higher than that of the larger particles. In addition, note that in constant volume fraction distribution, the smallest particles are the largest in number; thus, by construction, the error is maximum for the dominant species. On the other hand, for the Gaussian distribution, the place where the percentage error is maximum, the population of particles is minimum. Thus, compared to the Gaussian distribution for a continuous volume fraction, we need to go to marginally smaller values of  $\Delta\sigma_0$ . A way to increase  $\Delta\sigma_0$  (decrease  $M_0$ ) in CVF distribution can be to have a size dependent bin width such that the percentage error in describing the size of a smaller particle is the same as that of a larger particle.

#### D. Effect of interaction potential on $M_0$

Next, we study the role of interaction potential on the value of  $M_0$  (also  $\Delta\sigma_0$ ) and the saturation of  $T_{cross}$ . For this, we study the  $P_1(\sigma)$  system, with PDI = 15%, and vary the interaction potential between the particles (IPL, WCA, and LJ). The parameter values are given in

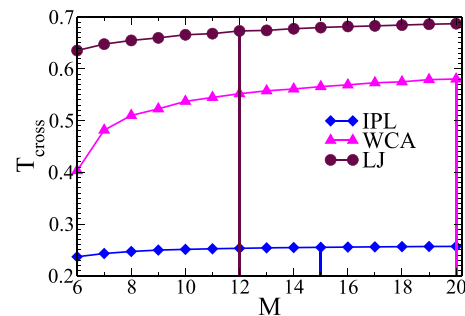


**FIG. 10.** Role of interaction potential on  $M_0$ .  $T_{cross}$  vs  $M$  plot for 15% PDIs for systems where particles are interacting via the IPL, WCA, and LJ potential, and the particle size distribution is given by  $P_1(\sigma)$  (constant volume fraction distribution). The vertical lines give the value of  $M_0$  obtained from energy criteria. The value of  $M_0$  is higher for the WCA potential, and  $T_{cross}$  also saturates at a higher value of  $M$ .

Table II. When we compare the IPL, WCA, and LJ systems, we find that the  $M_0$  value is higher for the WCA system and also find that  $T_{cross}$  of the WCA system appears to saturate at a higher  $M$  value (see Fig. 10). This suggests that  $\Delta\sigma_0$  for the WCA potential is smaller than those for the LJ and the IPL systems (see Table II).

To understand the origin of this lower tolerance of the WCA system in Fig. 11, we plot for the WCA system the partial rdfs of the first two species for different values of  $M$  and find that compared to the IPL system, we need to go to higher values of  $M$  to observe a good overlap between the two rdfs. Similar to that found for the IPL system, at  $M = M_0$ , the rdf peaks almost overlap. Note that compared to the WCA potential, the IPL potential is softer and has a longer range. Thus, compared to the WCA system, the IPL system has a flatter rdf and a larger overlap of the rdfs of two consecutive species. This definitely explains why compared to the IPL system  $M_0$  is higher for the WCA system.

In Fig. 12, we compare the rdf values for the first two species of the IPL, WCA, and LJ systems, for  $M = 15$ . Note that for the IPL and the LJ systems,  $M_0 \leq 15$ , and for the WCA system,  $M_0 > 15$ . However, compared to the WCA and IPL systems, the partial rdfs for the LJ system are more sharply peaked. This does not

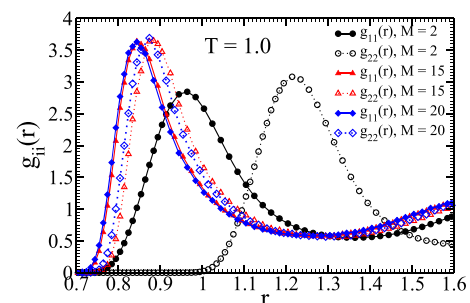


**FIG. 11.** The partial radial distribution function for the first two species for different values of  $M$ . The particles are interacting via the WCA potential, and the polydispersity of the system is described by  $P_1(\sigma)$  with 15% PDI.

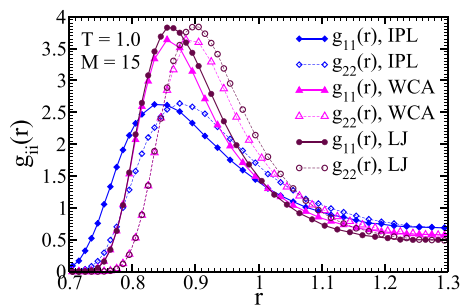


**FIG. 12.** The partial radial distribution functions for the first two species for IPL, WCA, and LJ potentials for  $M = 15$ . The size distribution of the particles is given by  $P_1(\sigma)$  with 15% polydispersity.

explain why  $M_0$  for the LJ system is smaller than the WCA system. Note that the structure along with the interaction potential describes both the potential energy and also the two body entropy. In  $S_2$ , the leading term is  $-g(r) \ln g(r) \simeq g(r)W(r)$ , where  $W(r) = -\ln g(r)$  can be considered as the effective potential of the system. Thus, along with the rdf, the interaction potential also plays a role in determining these thermodynamic quantities. The range of the LJ potential is much larger compared to the IPL and WCA potentials. Moreover, the attractive part of the potential that provides a dominant contribution also varies much more smoothly compared to the WCA and IPL potentials. It appears that this slow variation of the potential increases the tolerance of thermodynamic quantities with respect to the particle size, which leads to a smaller  $M_0$  value.

We would like to mention that in this work while working with the LJ system, we only vary the size of the particles while keeping the interaction energy constant. This choice is quite similar to that used in earlier studies of model polydisperse systems.<sup>9,43,44</sup> However, this choice of system is not consistent with the van der Waals attraction dependence on particle volume. Thus, the system can have some unusual structures like that of clustering of smaller particles observed earlier.<sup>44</sup>

### E. System size dependence

Note that for a finite number of particles ( $N$ ) in the system, we can still describe the  $N \times N$  partial structure factors. However, in the thermodynamic limit when  $N \rightarrow \infty$ , this becomes ill-defined. Thus, for larger systems, describing the system in terms of pseudospices becomes even more important. In this section, we study the system size dependence of  $M_0$ . For this study, we take the system where particle size distribution is given by  $P_1(\sigma)$  and the particles interact via the IPL potential. We study three systems at 5%, 10%, and 15% PDI. In Fig. 13, we plot  $\frac{(E_2 - E_{sim})}{E_{sim}}$  for systems with 1000 and 4000 particles. We find that the relative error in energy is independent of the system size, and so is  $M_0$ . In Fig. 14, we plot the  $T_{cross}$  values for the two different system sizes. We find that for 5% and 10% PDI, they overlap, and for 15% PDI, the bigger system size predicts a better saturation of  $T_{cross}$ . This is because we now have a larger number of particles in each species, giving rise to better averaging. Thus, we can say that  $M_0$  is independent of system size.

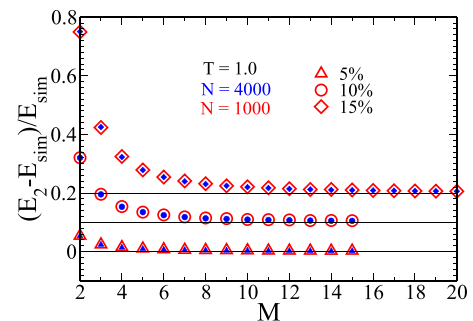


**FIG. 13.** System size dependence of relative error calculation between  $E_{sim}$  and  $E_2$ .  $(E_2 - E_{sim})/E_{sim}$  plotted as a function of  $M$  for different PDIs for  $N = 1000$  (red open symbols) and  $N = 4000$  (blue filled symbols). For better visualization, we have shifted the y axis of the 10% PDI plot by 0.1% and 15% PDI plot by 0.2. The horizontal lines signify the corresponding zero values.

### F. Comparison with earlier predictions

Next, we compare our results with that of Ozawa and Berthier (OB).<sup>27</sup> The goal of both studies is to find an effective number of pseudospices that can describe a polydisperse system. However, the methodologies are quite different. We work with the partial rdf of the liquid and use them to calculate the excess entropy and total energy near the onset temperature. Ozawa and Berthier used the information of the vibrational entropy and the inherent structure properties, and the study was performed below the MCT transition temperature. They divided the system into  $M$  species and then swapped particles within a species. After  $N$  such swaps, they minimized the system and obtained the mean square displacement (MSD) between the original equilibrium configuration and the swapped configuration. The MSD as a function of  $M$  initially decreased with increasing  $M$  and showed saturation at high values of  $M$ . They fitted these two regimes to two different power laws, and the intersection point of the power laws determined the value of  $M_0$ . In their study, they have calculated the value of  $M_0$  for an IPL potential system with the  $P_1(\sigma)$  distribution at 23% PDI. They

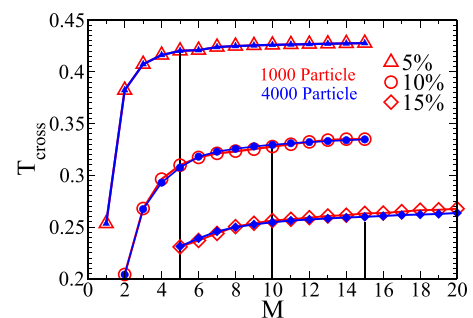


**FIG. 14.** The system size dependence of  $M_0$ .  $T_{cross}$  vs  $M$  plot for different PDIs for systems where particles are interacting via the IPL potential, and the particle size distribution is given by  $P_1(\sigma)$ . The open red symbols are for  $N = 1000$ , and the filled blue symbols are for  $N = 4000$ . The vertical lines give the value of  $M_0$  obtained from energy criteria.  $M_0$  from energy is independent of the system size, and for systems with higher PDI,  $T_{cross}$  saturates better for a higher system size.



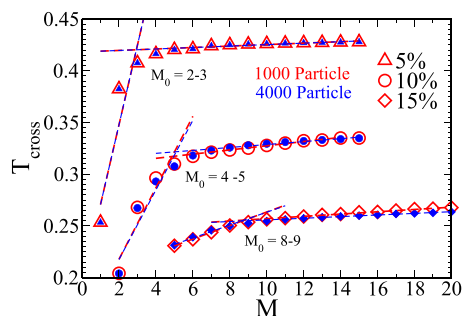


**FIG. 15.** Alternate definition of  $M_0$ .  $T_{cross}$  vs  $M$  has two different regimes, low  $M$  shows growth and high  $M$  shows a near saturation. The two different regimes are fitted to two straight lines, and the  $M$  value where these lines cross is identified as  $M_0$ . The open red symbols are for  $N = 1000$ , and the filled blue symbols are for  $N = 4000$ . The  $M_0$  values thus obtained are smaller than those obtained from energy criteria and similar to those obtained by Ozawa and Berthier.<sup>27</sup>

then extrapolated the value of  $M_0$  for smaller PDIs. For 10% PDI, they predicted a value of  $M_0 = 4-5$ , and for 5% PDI,  $M_0 = 2-3$ . We can do a similar exercise with  $T_{cross}$ . In Fig. 15, we show that  $T_{cross}$  also shows two different regimes. We fit the two different regimes to two straight lines, and the point where they cross is  $M_0 = 2-3$  for 5% PDI,  $M_0 = 4-5$  for 10% PDI, and  $M_0 = 8-9$  for 15% PDI. Interestingly, these numbers are surprisingly the same as that extrapolated by Ozawa and Berthier<sup>27</sup> although the two methodologies are completely different. However, these values of  $M_0$  are lower than our earlier prediction, which was made by looking at the saturation point of  $T_{cross}$ . In the OB study, if they have defined  $M_0$  at the value where their MSD becomes independent of  $M$ , then they too would have got a higher value of  $M_0$ .

We next compare our predictions with an earlier work, which involved the study of dynamics.<sup>26</sup> As discussed in the Introduction, Weysser *et al.* studied the effect of polydispersity on dynamics.<sup>26</sup> They studied a system with constant polydispersity where  $\Delta\sigma = 0.2$ . According to their study, dynamics can be well explained when the system is divided into five pseudospecies, and thus,  $\Delta\sigma_0 = 0.04$  falls in a similar range as predicted here, and so is  $M_0$ .

At this point, we cannot comment on which will be a better choice of  $M_0$ , the value at which  $T_{cross}$  saturates or the value at which two different regimes intersect. When we compare our result with the study using the dynamics,<sup>26</sup> it appears that the former that leads to higher values of  $M_0$  is a better choice, whereas if we compare with the OB study, then the latter seems to be a better choice. It is possible that the dynamics is more sensitive to the change in  $M_0$ . This suggests that further studies are required to narrow down the value of  $M_0$ . One such option will be to see how the configurational entropy for different values of  $M_0$  correlates with the dynamics.

## V. CONCLUSION

In this work, we attempted to develop a framework to describe the structure of systems with continuous polydispersity. This study involved systems where the polydispersity is described in terms of different distributions (constant volume fraction and

Gaussian) and the degree of polydispersity is varied. We also studied the effect of the interaction potential.

We exploited the fact that the potential energy and the pair excess entropy can be described in terms of the partial radial distribution functions. First, we described the system in terms of pseudospecies. In the case of potential energy, we obtained the minimum number of pseudospecies,  $M_0$ , required to match the energy obtained from the partial rdf with that obtained from the simulation. For the entropy part, since the excess entropy and pair excess entropy were never equal, we calculated the temperature where they cross each other. Our earlier study showed that  $T_{cross}$  is an estimate of the onset temperature of supercooled liquids.<sup>15</sup> We show that for a smaller number of species,  $T_{cross}$  varies with  $M$ , and as a function of species, this temperature shows a saturation, suggesting a saturation of the pair excess entropy with respect to  $M$ . This gave us a second estimation of  $M_0$ , which we found is similar to that obtained from the potential energy.

Our study revealed that for a given system, it is possible to define a parameter  $\Delta\sigma_0$ , which gives the limiting width of the size distribution that can be treated as a monodisperse system. This limiting value primarily depends on the interaction potential. The softer the interaction potential, the larger the value of  $\Delta\sigma_0$ . Depending on the type of distribution, this limiting width  $\Delta\sigma_0$  translates into different values of PDI.

For a 1% PDI system with constant volume fraction distribution,  $\Delta\sigma = 0.036$ , and for a 1% PDI system with Gaussian distribution,  $\Delta\sigma = 0.06$ . When we compare these values with  $\Delta\sigma_0$ , we can say that polydispersity greater than 1% when treated as an effective monodisperse system will not provide us with the correct structure of the liquid. This implies that when the effective one component structure is used to study the influence of polydispersity on some property, we have to be careful in decoupling the effect of this artificial softening of the structure from the actual effect of polydispersity. Note that  $M_0$  and  $\Delta\sigma_0$  are independent of the system size. This makes the pseudo-neighbor description of a system more useful for larger systems.

## DEDICATION

This article is dedicated to the memory of Professor Charusita Chakravarty, a mentor and a friend. She not only made a huge contribution in physical chemistry but also was passionate about the upliftment of women scientists. Had she been around, she would have definitely felt very happy about this special issue and contributed to it. Her absence has created a void in the field.

## ACKNOWLEDGMENTS

S.M.B. thanks C. Chakravarty, C. Dasgupta, S. Sastry, and B. Bagchi for discussion. P.P. and U.K.N. thank the CSIR for the research fellowships. M.K.N. thanks the CSIR for funding. S.M.B. thanks the SERB for funding.

## DATA AVAILABILITY

The data that support the findings of this study are available from the corresponding author upon reasonable request.

## REFERENCES

- <sup>1</sup>X. Xu, G. Friedman, K. D. Humfeld, S. A. Majetich, and S. A. Asher, "Synthesis and utilization of monodisperse superparamagnetic colloidal particles for magnetically controllable photonic crystals," *Am. Chem. Soc.* **14**, 1249–1256 (2001).
- <sup>2</sup>V. K. L. Mer, *Am. Chem. Soc.* **44**, 1270 (1952).
- <sup>3</sup>D. A. Kofke and P. G. Bolhuis, *Phys. Rev. E* **59**, 618 (1999).
- <sup>4</sup>D. J. Lacks and J. R. Wienhoff, *J. Chem. Phys.* **111**, 398 (1999).
- <sup>5</sup>S. R. Williams, I. K. Snook, and W. van Megen, *Phys. Rev. E* **64**, 021506 (2001).
- <sup>6</sup>P. Chaudhuri, S. Karmakar, C. Dasgupta, H. R. Krishnamurthy, and A. K. Sood, *Phys. Rev. Lett.* **95**, 248301 (2005).
- <sup>7</sup>S. Sarkar, R. Biswas, M. Santra, and B. Bagchi, *Phys. Rev. E* **88**, 022104 (2013).
- <sup>8</sup>A. Ninarello, L. Berthier, and D. Coslovich, *Phys. Rev. X* **7**, 021039 (2017).
- <sup>9</sup>S. E. Abraham, S. M. Bhattacharyya, and B. Bagchi, *Phys. Rev. Lett.* **100**, 167801 (2008).
- <sup>10</sup>S. Auer and D. Frenkel, *Nature* **413**, 711 (2001).
- <sup>11</sup>A. Banerjee, S. Sengupta, S. Sastry, and S. M. Bhattacharyya, *Phys. Rev. Lett.* **113**, 225701 (2014).
- <sup>12</sup>M. K. Nandi, A. Banerjee, S. Sengupta, S. Sastry, and S. M. Bhattacharyya, *J. Chem. Phys.* **143**, 174504 (2015).
- <sup>13</sup>A. Banerjee, M. K. Nandi, S. Sastry, and S. M. Bhattacharyya, *J. Chem. Phys.* **145**, 034502 (2016).
- <sup>14</sup>A. Banerjee, M. K. Nandi, and S. M. Bhattacharyya, *J. Chem. Sci.* **129**, 793 (2017).
- <sup>15</sup>A. Banerjee, M. K. Nandi, S. Sastry, and S. Maitra Bhattacharyya, *J. Chem. Phys.* **147**, 024504 (2017).
- <sup>16</sup>M. K. Nandi, A. Banerjee, C. Dasgupta, and S. M. Bhattacharyya, *Phys. Rev. Lett.* **119**, 265502 (2017).
- <sup>17</sup>M. K. Nandi and S. Maitra Bhattacharyya, *J. Chem. Phys.* **148**, 034504 (2018).
- <sup>18</sup>I. Saha, M. K. Nandi, C. Dasgupta, and S. M. Bhattacharyya, *J. Stat. Mech.: Theory Exp.* **2019**, 084008.
- <sup>19</sup>M. K. Nandi and S. Maitra Bhattacharyya, [arXiv:2011.02299v1](https://arxiv.org/abs/2011.02299v1) (2020).
- <sup>20</sup>D. Frydel and S. A. Rice, *Phys. Rev. E* **71**, 041403 (2005).
- <sup>21</sup>C. P. Royall, A. A. Louis, and H. Tanaka, *J. Chem. Phys.* **127**, 044507 (2007).
- <sup>22</sup>P. Salgi and R. Rajagopalan, *Adv. Colloid Interface Sci.* **43**, 169 (1993).
- <sup>23</sup>T. O. Pangburn and M. A. Bevan, *J. Chem. Phys.* **123**, 174904 (2005).
- <sup>24</sup>T. O. Pangburn and M. A. Bevan, *J. Chem. Phys.* **124**, 054712 (2006).
- <sup>25</sup>M. J. Pond, J. R. Errington, and T. M. Truskett, *J. Chem. Phys.* **135**, 124513 (2011).
- <sup>26</sup>F. Weysser, A. M. Puertas, M. Fuchs, and T. Voigtmann, *Phys. Rev. E* **82**, 011504 (2010).
- <sup>27</sup>M. Ozawa and L. Berthier, *J. Chem. Phys.* **146**, 014502 (2017).
- <sup>28</sup>D. L. Majure *et al.*, *Large-scale atomic/molecular massively parallel simulator (LAMMPS) simulations of the effects of chirality and diameter on the pullout force in a carbon nanotube bundle* (IEEE, 2008), p. 201.
- <sup>29</sup>R. Gutiérrez, S. Karmakar, Y. G. Pollack, and I. Procaccia, *Europhys. Lett.* **111**, 56009 (2015).
- <sup>30</sup>J. E. Jones and S. Chapman, *Proc. R. Soc. London, Ser. A* **106**, 463 (1924).
- <sup>31</sup>J. D. Weeks, D. Chandler, and H. C. Andersen, *J. Chem. Phys.* **54**, 5237 (1971).
- <sup>32</sup>J. P. Hansen and I. R. McDonald, *The Theory of Simple Liquids*, 2nd ed. (Academic, London, 1986).
- <sup>33</sup>M. Singh, M. Agarwal, D. Dhabal, and C. Chakravarty, *J. Chem. Phys.* **137**, 024508 (2012).
- <sup>34</sup>J. G. Kirkwood and E. M. Boggs, *J. Chem. Phys.* **10**, 394 (1942).
- <sup>35</sup>T. Goel, C. N. Patra, T. Mukherjee, and C. Chakravarty, *J. Chem. Phys.* **129**, 164904 (2008).
- <sup>36</sup>S. Sastry, P. G. Debenedetti, and F. H. Stillinger, *Nature* **393**, 554 (1998).
- <sup>37</sup>S. Sengupta, F. Vasconcelos, F. Affouard, and S. Sastry, *J. Chem. Phys.* **135**, 194503 (2011).
- <sup>38</sup>P. V. Giaquinta and G. Giunta, *Physica A* **187**, 145 (1992).
- <sup>39</sup>S. Prestipino and P. V. Giaquinta, *J. Stat. Phys.* **96**, 135 (1999).
- <sup>40</sup>F. Saija, S. Prestipino, and P. V. Giaquinta, *J. Chem. Phys.* **113**, 2806 (2000).
- <sup>41</sup>F. Saija, S. Prestipino, and P. V. Giaquinta, *J. Chem. Phys.* **124**, 244504 (2006).
- <sup>42</sup>J. Mittal, J. R. Errington, and T. M. Truskett, *J. Chem. Phys.* **125**, 076102 (2006).
- <sup>43</sup>N. Kiriushcheva and P. H. Poole, *Phys. Rev. E* **65**, 011402 (2001).
- <sup>44</sup>T. S. Ingebrigtsen and H. Tanaka, *J. Phys. Chem. B* **119**, 11052 (2015).

# Thermodynamics and its correlation with dynamics in a mean-field model and pinned systems: A comparative study using two different methods of entropy calculation

Cite as: J. Chem. Phys. **156**, 014503 (2022); <https://doi.org/10.1063/5.0065668>

Submitted: 04 August 2021 • Accepted: 14 December 2021 • Accepted Manuscript Online: 15 December 2021 • Published Online: 04 January 2022

 Ujjwal Kumar Nandi,  Palak Patel,  Mohd Moid, et al.

## COLLECTIONS

Paper published as part of the special topic on [Slow Dynamics](#)



[View Online](#)



[Export Citation](#)



[CrossMark](#)

## ARTICLES YOU MAY BE INTERESTED IN

[On the thermodynamics of curved interfaces and the nucleation of hard spheres in a finite system](#)

The Journal of Chemical Physics **156**, 014505 (2022); <https://doi.org/10.1063/5.0072175>

[Perturbation-adapted perturbation theory](#)

The Journal of Chemical Physics **156**, 011101 (2022); <https://doi.org/10.1063/5.0079853>

[Accurate scaling functions of the scaled Schrödinger equation](#)

The Journal of Chemical Physics **156**, 014113 (2022); <https://doi.org/10.1063/5.0077495>

[Learn More](#)

The Journal of Chemical Physics **Special Topics** Open for Submissions

# Thermodynamics and its correlation with dynamics in a mean-field model and pinned systems: A comparative study using two different methods of entropy calculation

Cite as: J. Chem. Phys. 156, 014503 (2022); doi: 10.1063/5.0065668

Submitted: 4 August 2021 • Accepted: 14 December 2021 •

Published Online: 4 January 2022



View Online



Export Citation



CrossMark

Ujjwal Kumar Nandi,<sup>1,2</sup>  Palak Patel,<sup>1,2</sup>  Mohd Moid,<sup>3</sup>  Manoj Kumar Nandi,<sup>4</sup>  Shiladitya Sengupta,<sup>5</sup>  Smarajit Karmakar,<sup>6</sup>  Prabal K. Maiti,<sup>3</sup>  Chandan Dasgupta,<sup>3,7</sup>  and Sarika Maitra Bhattacharyya<sup>1,2,a)</sup> 

## AFFILIATIONS

<sup>1</sup> Polymer Science and Engineering Division, CSIR-National Chemical Laboratory, Pune 411008, India

<sup>2</sup> Academy of Scientific and Innovative Research (AcSIR), Ghaziabad 201002, India

<sup>3</sup> Centre for Condensed Matter Theory, Department of Physics, Indian Institute of Science, Bangalore 560012, India

<sup>4</sup> Department of Engineering, University of Campania "Luigi Vanvitelli", 81031 Aversa (CE), Italy

<sup>5</sup> Department of Physics, Indian Institute of Technology, Roorkee 247667, India

<sup>6</sup> Centre for Interdisciplinary Sciences, Tata Institute of Fundamental Research, 36/P, Gopanpally Village, Serilingampally Mandal, RR District, Hyderabad 500019, India

<sup>7</sup> International Centre for Theoretical Sciences, Tata Institute of Fundamental Research, Bengaluru 560089, India

Note: This paper is part of the JCP Special Topic on Slow Dynamics.

<sup>a)</sup> Author to whom correspondence should be addressed: [mb.sarika@ncl.res.in](mailto:mb.sarika@ncl.res.in)

## ABSTRACT

A recent study introduced a novel mean-field model system where each particle over and above the interaction with its regular neighbors interacts with  $k$  extra pseudo-neighbors. Here, we present an extensive study of thermodynamics and its correlation with the dynamics of this system. We surprisingly find that the well-known thermodynamic integration (TI) method of calculating the entropy provides unphysical results. It predicts vanishing of the configurational entropy at temperatures close to the onset temperature of the system and negative values of the configurational entropy at lower temperatures. Interestingly, well below the temperature at which the configurational entropy vanishes, both the collective and the single-particle dynamics of the system show complete relaxation. Negative values of the configurational entropy are unphysical, and complete relaxation when the configurational entropy is zero violates the prediction of the random first-order transition theory (RFOT). However, the entropy calculated using the two-phase thermodynamics (2PT) method remains positive at all temperatures for which we can equilibrate the system, and its values are consistent with RFOT predictions. We find that with an increase in  $k$ , the difference in the entropy computed using the two methods increases. A similar effect is also observed for a system where a randomly selected fraction of the particles are pinned in their positions in the equilibrated liquid. We show that the difference in entropy calculated via the 2PT and TI methods increases with pinning density.

Published under an exclusive license by AIP Publishing. <https://doi.org/10.1063/5.0065668>

## I. INTRODUCTION

The slowing down of the dynamics in supercooled liquids and its correlation with the thermodynamics of the system have been topics of intense research. There are several characteristic

temperatures where both thermodynamic and dynamic properties of the system change in a significant manner. At the onset temperature ( $T_{onset}$ ), the relaxation dynamics of the system start to differ from those of a typical liquid because, due to the lowering of the temperature, the system begins to explore the underlying free energy



landscape.<sup>1</sup> This onset temperature can also be identified as the temperature where the pair part of the excess entropy becomes less than the total excess entropy of the system.<sup>2,3</sup> Below  $T_{onset}$ , the temperature dependence of the dynamics can be described reasonably well by the so-called mode-coupling theory (MCT), which predicts a power-law divergence of the relaxation times at a dynamic transition temperature  $T_c$ .<sup>4</sup> However, experimental and numerical studies found<sup>5–10</sup> that the relaxation time does not diverge at  $T_c$  as predicted by the MCT but instead shows a smooth crossover to weaker temperature dependence. This crossover scenario is consistent with the predictions of the so-called random first-order transition (RFOT) theory,<sup>11,12</sup> and it has been related to the properties of the underlying potential energy landscape.<sup>13</sup>

According to the RFOT theory and the phenomenological Adam–Gibbs (AG) theory,<sup>14</sup> the low temperature dynamics of a supercooled liquid is controlled by its configurational entropy ( $S_c$ ), which measures the number of possible distinct states accessible to the system. The AG theory predicts the following relationship between the  $\alpha$  relaxation time ( $\tau$ ) and the configurational entropy ( $S_c$ ):  $\tau = \tau_0 \exp(A/TS_c)$ , where  $\tau_0$  is a microscopic timescale and  $A$  is a system-dependent constant. Thus, according to the AG theory, the temperature  $T_0$  where the relaxation time diverges is the same as the Kauzmann temperature  $T_K$  where the configurational entropy goes to zero.<sup>15</sup> For a large number of systems, the AG relationship is found to hold.<sup>14,16–25</sup> There has been a recent study that showed that it is the diffusion coefficient that follows the AG relationship for the widest temperature range.<sup>26</sup>

The validity of the AG theory in the form presented above has recently been challenged.<sup>16</sup> It has been argued that according to the RFOT theory, the reduction in the configurational entropy is related to the growth of a static correlation length over which the activation happens, giving rise to the relaxation process. This theory predicts a generalized AG relation given by  $\tau = \tau_0 \exp(A/TS_c^\alpha)$ , where  $\alpha$  can be different from unity. It was further shown that the generalized AG relation holds<sup>16</sup> both in experiments and in simulations. Note that even according to the generalized AG relationship, the relaxation timescale should diverge below  $T = T_K$  when the configurational entropy vanishes. In addition, by definition,  $S_c$  cannot be negative.

In a recent study, some of us have developed a novel generalization of glass-forming liquids where we can switch between a three-dimensional liquid and a fully connected mean-field system in a continuous manner.<sup>27</sup> The parameter that is introduced to achieve this is  $k$  added pseudoneighbors for each particle. The structure, dynamics, and dynamical heterogeneity of this model have been studied as a function of  $k$ . It was shown that the structure given by the radial distribution function (rdf) of the usual neighbors remains almost unchanged with  $k$ . However, the pseudoneighbors do contribute to the total rdf that shows a weaker modulation with distance, a typical mean-field like behavior.<sup>27,28</sup> With an increase in  $k$ , the dynamics also slows down and the transition temperatures ( $T_0, T_c, T_{onset}$ ) move to higher values. The range over which a system follows the MCT power-law behavior becomes wider with an increase in  $k$ . The heterogeneity decreases with an increase in  $k$ . Thus, it was shown that with an increase in  $k$ , the system becomes more mean-field like.

The goal of the present work is to study the thermodynamic properties of this system and its correlation with the dynamics.

In order to do so, we employ the well-known thermodynamic integration (TI) method to calculate the total entropy and, hence, the configurational entropy of the system.<sup>29</sup> We find that with an increase in  $k$ , the Kauzmann temperature becomes higher, which is similar to that found for  $T_0$ . However, for larger  $k$  systems, we find that the configurational entropy vanishes at temperatures close to the onset temperature. On the contrary, both the self-part and the collective part of the dynamics show complete relaxation well below the temperature where the configurational entropy vanishes. Thus, we can apparently access states with *negative* configurational entropy. This is an unphysical result by definition. In addition, it also violates the RFOT prediction. Thus, in our opinion, this observation implies that the TI method of entropy calculation should be re-examined. We discuss the possible failure points of the TI method. However, at present, we do not know how to incorporate the corrections.

We, thus, employ a completely different method to calculate the entropy of the system, namely, the two-phase thermodynamics (2PT) method. It is a well-known method<sup>30,31</sup> that has provided accurate entropy values over a wide range of thermodynamic state points for the Lennard-Jones (LJ) fluid and different water models.<sup>30,32</sup> We first test this method for a standard Kob–Anderson (KA) model, which is the  $k = 0$  system in the mean-field model. We compare the entropy values obtained via the TI and the 2PT methods and find them close to each other. We then employ the 2PT method for different mean-field systems and compare the results with those obtained by the TI method. We find that with increasing  $k$ , the difference in entropy obtained by the two methods increases. The entropy calculated using the 2PT method does not produce any negative configurational entropy state points. We also find that it predicts a Kauzmann temperature, which is similar to the temperature where the  $\alpha$  relaxation time diverges, thus validating the RFOT prediction. Incidentally, we find that in the range of temperature studied here, the standard AG relation holds.

Similar to the mean-field system, there has been some discussion of the dynamics not following the entropy and the breakdown of the AG relationship when the entropy was calculated using the TI method in another model, namely, randomly pinned systems.<sup>33–36</sup> Given the success of the 2PT method in describing the entropy of the mean-field system, we further employ it to calculate the entropy of the pinned system. We find that with the increase in the pinning density, the difference in entropy computed by the TI and the 2PT methods increases. We also show that in the temperature range studied, the pinned systems follow the AG relationship when the entropy is calculated via the 2PT method.

Although our simulations provide results at relatively high temperatures at which the systems can be equilibrated, they offer an opportunity to critically test theories of the glass transition. The TI method is an important standard method to estimate entropy reliably and easily, both in experiments and in simulations. The unphysical results produced by the TI method for the mean-field model is rather surprising. Given their importance, they should be critically examined. Thus, in the present study, our main focus is on understanding possible issues with entropy calculation in these models.

The rest of this paper is organized as follows: The system and simulation details are described in Sec. II. In Sec. III, we describe different methods for the calculation of entropy. In Secs. IV and V,

we present the results of our analysis for the mean-field and pinned systems, respectively. In Sec. VI, we summarize the results and conclude.

## II. DETAILS OF SYSTEM AND SIMULATIONS

We have studied two different families of models. One is a mean-field system and the other is a pinned system. For both the systems, we have used atomistic models, which are simulated with two-component mixtures of classical particles (larger “A” and smaller “B” type), where particles of type  $i$  interact with those of type  $j$  with pair potential,  $u(r_{ij})$ , where  $r$  is the distance between the pair.  $u(r_{ij})$  is described by a shifted and truncated Lennard-Jones (LJ) potential, given by

$$u(r_{ij}) = \begin{cases} u^{(LJ)}(r_{ij}; \sigma_{ij}, \epsilon_{ij}) - u^{(LJ)}(r_{ij}^{(c)}; \sigma_{ij}, \epsilon_{ij}), & r \leq r_{ij}^{(c)}, \\ 0, & r > r_{ij}^{(c)}, \end{cases} \quad (1)$$

where  $u^{(LJ)}(r_{ij}; \sigma_{ij}, \epsilon_{ij}) = 4\epsilon_{ij}[(\frac{\sigma_{ij}}{r_{ij}})^{12} - (\frac{\sigma_{ij}}{r_{ij}})^6]$  and  $r_{ij}^{(c)} = 2.5\sigma_{ij}$ . We have used the Kob–Andersen model<sup>8</sup> and performed constant volume and constant temperature (Nosé–Hoover thermostat and velocity rescaling) molecular dynamics (NVTMD) simulation. We use  $\sigma_{AA}$  and  $\epsilon_{AA}$  as the units of length and energy, respectively, setting the Boltzmann constant  $k_B = 1$ . We have used reduced time unit in terms of  $\sqrt{\frac{m_A \sigma_{AA}^2}{\epsilon_{AA}}}$ , and masses of both types of particles are taken to be the same ( $m_A = m_B$ , set equal to unity). We have used 80% of A particles and 20% of B particles with the diameter  $\sigma_{AA} = 1.0$ ,  $\sigma_{AB} = 0.8$ , and  $\sigma_{BB} = 0.88$ . The interaction strengths between the particles are  $\epsilon_{AA} = 1.0$ ,  $\epsilon_{AB} = 1.5$ , and  $\epsilon_{BB} = 0.5$ .

### A. Mean-field system

The mean-field system is given by  $N$  particles that interact with each other via a standard short-range potential. In addition, each particle also interacts with “pseudoneighbors,” i.e., particles that are not necessarily close in space. Hence, the total interaction potential of the system is given by

$$U_{\text{tot}}(r_1, \dots, r_N) = \sum_{i=1}^N \sum_{j>i}^N u(r_{ij}) + \frac{1}{2} \sum_{i=1}^N \sum_{j=1}^k u^{\text{pseudo}}(r_{ij}) \quad (2)$$

$$= U + U_k^{\text{pseudo}}. \quad (3)$$

The first term on the right-hand side is the regular interaction between particles, while the second term is the interaction each particle has with its pseudoneighbors. Here, we consider the case in which the regular interaction is described by using Eq. (1).

The interaction potential with the pseudoneighbors is modeled in terms of a modified shifted and truncated LJ potential,

$$u^{\text{pseudo}}(r_{ij}) = u(r_{ij} - L_{ij}) \quad (4)$$

$$= 4\epsilon_{ij} \left[ \left( \frac{\sigma_{ij}}{r_{ij} - L_{ij}} \right)^{12} - \left( \frac{\sigma_{ij}}{r_{ij} - L_{ij}} \right)^6 \right], \quad (5)$$

where  $L_{ij}$  is a random variable defined below. In our simulations, we impose the restriction that any two particles interact either via  $u(r_{ij})$  or via  $u^{\text{pseudo}}(r_{ij})$ . This condition determines how the pseudoneighbors and the values  $L_{ij}$  are chosen for a given configuration equilibrated with the potential  $u$ : for each particle  $i$ , we select  $k$  random numbers  $L_{ij}$  in the range  $r_c \leq L_{ij} \leq L_{\text{max}}$ , where  $L_{\text{max}} \leq L_{\text{box}}/2 - r_c$ , with  $L_{\text{box}}$  being the size of the simulation box. [The distribution of these random variables will be denoted by  $\mathcal{P}(L_{ij})$ , and in the following, we will consider the case that the distribution is uniform.] Subsequently, we choose  $k$  distinct particles  $j$  with  $r_{ij} > r_c$  and use the  $L_{ij}$  to permanently fix the interaction between particles  $i$  and  $j$ . This procedure thus makes sure that each particle  $i$  interacts with not only the particles that are within the cutoff distance but also  $k$  particles that can be far away. Note that once the particle  $j$  is chosen as a pseudoneighbor of particle  $i$ , automatically particle  $i$  becomes a pseudoneighbor of particle  $j$ . The system, as defined here, can then be simulated using standard simulation algorithms.

NVT molecular dynamics (MD) simulation is performed in a cubic box using the velocity rescaling method for  $N = 2744$  particles at  $\rho = 1.2$  ( $L_{\text{box}} = 13.1745$ ) using a time integration step of  $\Delta t = 0.005$ . For  $L_{\text{max}}$ , we have taken 4.0, slightly below the maximum value of 4.09. We have simulated four different systems with the number of pseudoneighbors,  $k = 0, 4, 12$ , and 28.

### B. Pinned system

We also study another conceptually different family of glass-forming models, namely, the pinned system in which a fraction of particles are artificially pinned at their positions in an equilibrated liquid. For the study of the pinned system, we use the Kob–Andersen 80:20 binary Lennard-Jones mixture.<sup>8</sup> Details of this model are given in Sec. II. For creating the pinned system, the following pinning protocol is used. The pinned particles are chosen randomly from an equilibrium configuration of the system at the temperature of interest.<sup>33,35</sup> NVT molecular dynamics simulation is performed in a cubic box using the Nose–Hoover thermostat where  $N = 1000$  at  $\rho = 1.2$  ( $L_{\text{box}} = 9.41036$ ) using a time integration step of  $\Delta t = 0.005$ , at three different pinning concentration ( $c$ ), i.e., 0.05, 0.10, and 0.15. Production runs of pinned configurations are long enough to ensure that within the simulation time, the overlap correlation function  $Q(t)$  (defined in Sec. II C) decays to zero.

### C. Dynamics

To analyze the dynamics, we consider the self-part of the overlap function,

$$Q(t) = \frac{1}{N} \left\langle \sum_{i=1}^N \omega(|\mathbf{r}_i(t) - \mathbf{r}_i(0)|) \right\rangle, \quad (6)$$

where the function  $\omega(x)$  is 1 if  $0 \leq x \leq a$  and  $\omega(x) = 0$  otherwise. The parameter  $a$  is chosen to be 0.3, a value that is slightly larger than the size of the “cage” determined from the height of the plateau in the mean square displacement at intermediate times.<sup>8</sup> Thus, the quantity  $Q(t)$  measures whether or not at time  $t$  a tagged particle is still inside the cage it occupied at  $t = 0$ .

To analyze the collective dynamics of the systems, we have used both the collective overlap function and the collective intermediate scattering function.

The collective overlap function is defined as follows:

$$Q^{tot}(t) = \frac{1}{N} \left\langle \sum_{i=1}^N \sum_{j=1}^N \omega(|\mathbf{r}_i(t) - \mathbf{r}_j(0)|) \right\rangle. \quad (7)$$

The long time saturation value of  $Q^{tot}(t)$  is given by (using  $a = 0.3$ )<sup>37</sup>

$$\lim_{t \rightarrow \infty} Q^{tot}(t) = \frac{N}{V} \frac{4}{3} \pi a^3 = 0.135. \quad (8)$$

We have also calculated the intermediate scattering function  $F(q, t)$ . It is the collective density–density time correlation function in momentum space which provides information about the collective dynamics of the systems,

$$F(q, t) = \frac{1}{NF(q, 0)} \left\langle \sum_{i=1}^N \sum_{j=1}^N \exp[-i\mathbf{q} \cdot (\mathbf{r}_i(t) - \mathbf{r}_j(0))] \right\rangle. \quad (9)$$

The relaxation time ( $\tau$ ) is calculated from the self-part of the overlap function when it decays to  $1/e$ . The rapid increase in relaxation time with decreasing temperature is a signature of glassy dynamics. This is often fitted to the Vogel–Fulcher–Tammann (VFT) equation,

$$\tau(T) = \tau_0 \exp \left[ \frac{1}{K \left( \frac{T}{T_0} - 1 \right)} \right]. \quad (10)$$

Here,  $\tau_0$  is a high-temperature relaxation time and  $T_0$  is the so-called VFT temperature at which the relaxation time of the system is predicted to diverge. The parameter  $K$  describes the curvature of the data in an Arrhenius plot and, hence, can be considered as a measure for the fragility of the glass-former.

### III. ENTROPY

In this work, we have used two different well-known methods for the calculation of the total entropy ( $S_{tot}$ ) of the system. Below, we provide brief sketches of the two methods, namely, the TI method<sup>29</sup> and the 2PT method.<sup>30</sup>

#### A. Thermodynamic integration (TI) method

Below, we describe the different quantities required to calculate the entropy in the TI method.<sup>29</sup>

##### 1. Ideal gas entropy

Ideal gas entropy is the entropy of a set of non-interacting particles. The ideal gas entropy per particle for a binary system at temperature  $T$  is given by

$$S_{ideal} = \frac{5}{2} - \ln(\rho) + \frac{3}{2} \ln \left( \frac{2\pi T}{h^2} \right) + \frac{1}{N} \ln \frac{N!}{N_A! N_B!}, \quad (11)$$

where  $N = N_A + N_B$  is the total number of particles,  $\rho$  is the density of the system, and  $h$  is the Planck constant.  $N_A$  and  $N_B$  are the number of particles of types A and B. The last term contributes to the mixing entropy.

However, if the particles are divided into  $M$  distinguishable species such that  $N = \sum_{i=1}^M N_i$ , then the ideal gas entropy per particle can be written as

$$S_{ideal}^d = \frac{5}{2} - \ln(\rho) + \frac{3}{2} \ln \left( \frac{2\pi T}{h^2} \right) + \frac{1}{N} \ln \frac{N!}{\prod_{i=1}^M N_i!}. \quad (12)$$

#### 2. Excess entropy and total entropy

Excess entropy ( $S_{ex}$ ) estimates the loss of entropy due to interactions among the particles. It is always a negative quantity.  $S_{ex}$  is calculated using the TI method where the integration can be done on the temperature path,<sup>33</sup> in the temperature range  $\infty$  to a target temperature ( $T^*$ ),

$$S_{ex}(\beta^*) = \beta^* \langle U \rangle - \int_0^{\beta^*} d\beta \langle U \rangle. \quad (13)$$

Here,  $\beta = \frac{1}{T}$ . The total entropy of the system at a particular temperature is the sum of the ideal gas entropy and the excess entropy of the system at that particular temperature,

$$S_{tot} = S_{ideal} + S_{ex}. \quad (14)$$

#### B. Two-phase thermodynamics (2PT) method

The 2PT method is another conventional method to compute the entropy of liquids.<sup>30,31</sup> In the 2PT method, the thermodynamics quantities can be computed using the density of states (DOS) of the liquid. One can decompose the DOS of a liquid as a sum of solid-like and gas-like contributions. To compute the thermodynamic quantities, the phonons in the solid-like DOS are treated as non-interacting harmonic oscillators, as in the Debye model.<sup>38</sup> On the other hand, the gas-like DOS is described as a low-density hard-sphere fluid, which can be computed analytically.<sup>38</sup> Using the 2PT description, Lin *et al.*<sup>30,31</sup> demonstrated that the thermodynamics quantities of the LJ fluid can be computed very accurately over a wide range of thermodynamics state points using a very short MD trajectory. In a later work, Lai *et al.*<sup>39</sup> calculated the entropy of a binary fluid using the 2PT method. Here, we provide a brief overview of the decomposition of the DOS in the 2PT method. We refer the reader to the original papers<sup>30,31</sup> for a full description.

The density of state function,  $g(v)$ , can be computed from the mass-weighted atomic spectral densities, defined as<sup>30,31</sup>

$$g(v) = \frac{2}{T} \sum_{j=1}^N \sum_{l=1}^3 m_j s_j^l(v), \quad (15)$$

where  $m_j$  is the mass of the  $j$ th atom,  $l$  denotes the direction in the Cartesian coordinates, and  $s_j^l(v)$  are the atomic spectral densities, defined as

$$s_j^l(v) = \lim_{\tau \rightarrow \infty} \frac{\left| \int_{-\tau}^{\tau} v_j^l(t) e^{-i2\pi vt} dt \right|^2}{2\tau}, \quad (16)$$

where  $v_j^l(t)$  denotes the velocity component of the  $j$ th atom in the  $l$ th direction. The atomic spectral density,  $s_j^l(\nu)$ , can be computed from the Fourier transform of the velocity auto-correlation function (VACF)  $c_j^l(t)$ ,

$$s_j^l(\nu) = \lim_{\tau \rightarrow \infty} \int_{-\tau}^{\tau} c_j^l(t) e^{-i2\pi\nu t} dt, \quad (17)$$

where  $c_j^l(t)$  is given by

$$c_j^l(t) = \lim_{\tau \rightarrow \infty} \frac{1}{2\tau} \int_{-\tau}^{\tau} v_j^l(t+t') v_j^l(t') dt'. \quad (18)$$

Thus, Eq. (15) can be rewritten as

$$g(\nu) = \frac{2}{T} \lim_{\tau \rightarrow \infty} \int_{-\tau}^{\tau} \sum_{j=1}^N \sum_{l=1}^3 m_j c_j^l(t) e^{-i2\pi\nu t} dt. \quad (19)$$

As we mentioned above,  $g(\nu)$  can be decomposed into solid- and gas-like components in the 2PT formalism. Based on the diffusivity of the system compared to hard-sphere gas at the same density, Lin *et al.*<sup>30</sup> proposed a self-consistent fluidity factor,  $f$ , which decides the degrees of freedom shared in solid and gas components. The relationship between  $f$  and dimensionless diffusivity,  $\Delta$ , can be derived (for the details of the derivation, readers are referred to Ref. 30) by

$$2\Delta^{-9/2} f^{15/2} - 6\Delta^{-3} f^5 - \Delta^{-3/2} f^{7/2} + 6\Delta^{-3/2} f^{5/2} + 2f - 2 = 0. \quad (20)$$

The dimensionless diffusivity constant,  $\Delta$ , depends on the material properties,

$$\Delta(T, \rho, m, g_0) = \frac{2g_0}{9N} \left( \frac{6}{\pi} \right)^{2/3} \left( \frac{\pi T}{m} \right)^{1/2} \rho^{1/3}, \quad (21)$$

where  $g_0 = g(0)$  is the DOS of the system at zero-frequency and  $\rho$  is the number density. Using  $f$  obtained from Eqs. (20) and (21), the DOS in the gas-like diffusive component can be obtained using a hard-sphere diffusive model,

$$g^g(\nu) = \frac{g_0}{1 + \left[ \frac{\pi g_0 \nu}{6fN} \right]^2}. \quad (22)$$

Given the DOS in the gas-like component, one can compute the solid-like DOS,  $g^s(\nu)$ , using the following equation:

$$g(\nu) = g^g(\nu) + g^s(\nu). \quad (23)$$

Once the decomposition of the DOS has been done, any thermodynamic quantity,  $A$ , can be computed using the corresponding weight functions,

$$A = \beta^{-1} \left[ \int_0^{\infty} g^g(\nu) W_A^g d\nu + \int_0^{\infty} g^s(\nu) W_A^s d\nu \right]. \quad (24)$$

The weight functions for the entropy in the solid- ( $W_S^s$ ) and the gas-like ( $W_S^g$ ) components are defined as

$$W_S^s(\nu) = W_S^{HO}(\nu) = \frac{\beta \hbar \nu}{\exp(\beta \hbar \nu) - 1} - \ln[1 - \exp(-\beta \hbar \nu)], \quad (25)$$

where  $\beta = \frac{1}{T}$  and  $\hbar = \frac{h}{2\pi}$  and  $h$  is the Planck constant,

$$W_S^g(\nu) = \frac{1}{3} \frac{S^{HS}}{k}, \quad (26)$$

where  $S^{HS}$  denotes the entropy of the hard-sphere system. Using Eqs. (25) and (26), the total entropy of the system can be written as

$$S_{tot} = S^s + S^g. \quad (27)$$

In this work, for the calculation of the entropy using the 2PT method, we have averaged over ten datasets where each dataset starts with a different configuration and velocity distribution. Each dataset contains fifty thousand frames of velocity with an interval of 0.005 time steps.

### C. Configurational entropy

As discussed earlier, we can calculate the total entropy using both the TI and the 2PT methods. Thus, Eqs. (14) and (27) provide us with the same information although the routes of obtaining them are different.

In the supercooled liquid regime, the configurational space can be divided into inherent structure minima and vibrational motion around them. The logarithm of the number of these inherent structure minima gives the configurational entropy ( $S_c$ ) of the system, which can be calculated by subtracting the vibrational entropy,  $S_{vib}$ , from the total entropy of the system,

$$S_c = S_{tot} - S_{vib} = S_{ideal} + S_{ex} - S_{vib}. \quad (28)$$

The vibrational entropy is calculated by making a harmonic approximation about a local minimum.<sup>37,40-42</sup> To obtain the vibrational frequencies, we calculate the Hessian and then diagonalize it. Once we obtain the vibrational frequencies,  $S_{vib}$  is calculated using the following equation:

$$S_{vib} = \frac{3}{2} \ln \left( \frac{2\pi T}{h^2} \right) + \frac{\ln(V)}{N} + \frac{1}{2N} \sum_{i=1}^{3N-3} \ln \left( \frac{2\pi T}{\omega_i^2} \right) - \frac{3}{2N} + 3. \quad (29)$$

## IV. RESULTS FOR MEAN-FIELD SYSTEM

In this section, we will discuss the entropy of the mean-field system and its correlation with the dynamics. We will first discuss the results obtained using the TI method and its shortcomings and then discuss the results obtained from the 2PT method.

## A. Entropy using thermodynamic integration method

In the estimation of the entropy using the TI method, we need to calculate the excess entropy and the vibrational entropy. The configurational entropy is then obtained from Eq. (28).

### 1. Excess entropy

Note that in the calculation of the excess entropy via the TI method, we need the information of the internal energy [Eq. (13)]. For the mean-field systems, the internal energy has two parts, one is the contribution from the regular nearest neighbor (NN) and the other is the contribution from the pseudo-neighbor (PN). A similar decomposition is present for the entropy, where we can write  $S_{ex} = S_{ex}^{NN} + S_{ex}^{PN}$ . The first term on the rhs refers to the contribution from the regular neighbors and the second term refers to that from the pseudoneighbors. These are given by

$$S_{ex}^{NN}(\beta^*, k) = \beta^* \langle U \rangle - \int_0^{\beta^*} d\beta \langle U \rangle \quad (30)$$

and

$$S_{ex}^{PN}(\beta^*, k) = \beta^* \langle U_k^{pseudo} \rangle - \int_0^{\beta^*} d\beta \langle U_k^{pseudo} \rangle. \quad (31)$$

In Fig. 1, we plot the temperature dependence of  $S_{ex}$  from the TI method for different  $k$  systems. In the TI method, we assume the particles to be indistinguishable. We find that the excess entropy decreases with increasing  $k$ . Our earlier study showed that with increasing  $k$ , the structure of the system remains unchanged.<sup>27</sup> Thus, the contribution of the regular neighbors to the entropy does not change with  $k$ . However, with an increase in the number of pseudoneighbors and thus  $U_k^{pseudo}$ , the total excess entropy decreases. Thus, the decrease in excess entropy obtained via the TI method can be attributed to the increase in the pseudoneighbor interactions.

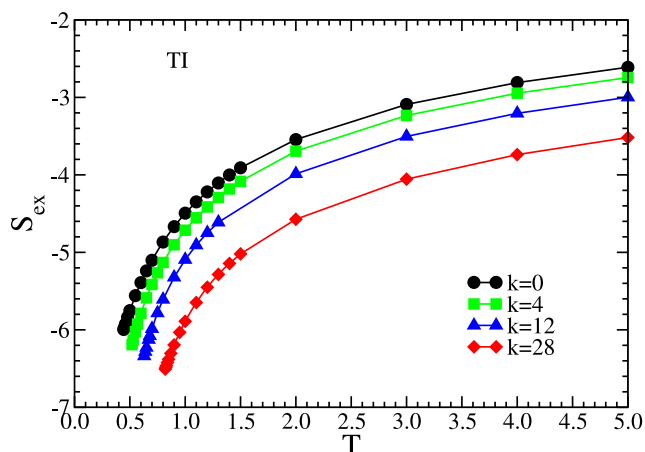


**FIG. 1.** Plot of per particle excess entropy  $S_{ex}$  vs  $T$  for  $k = 0, 4, 12,$  and  $28$  systems.  $S_{ex}$  is estimated using the TI method. With an increase in  $k$ , the excess entropy becomes more negative.

## 2. Vibrational entropy

We next calculate the vibrational density of states (VDOS) for different  $k$  values from the Hessian. This calculation is cross-checked by calculating the VDOS independently from the Fourier transform of the velocity auto-correlation function, which matches the data obtained from the Hessian (see Appendix A).

We find that with an increase in pseudoneighbors, there is a suppression of the low-frequency modes, and the whole spectrum moves to a higher frequency range, as shown in Fig. 2. A similar effect was also seen in the high-temperature dynamics where it was shown that with the increase in the pseudoneighbors, the cage becomes stiffer and the dynamics inside the cage becomes faster.<sup>27</sup>

The temperature dependence of the vibrational entropy  $S_{vib}$  (obtained from the VDOS) is plotted in Fig. 3. We find that with increasing  $k$ , as the vibrational spectrum shifts to higher frequencies, the vibrational entropy decreases.

For a few representative systems ( $k = 0$  and  $k = 28$ ), we also show the vibrational entropy as obtained from the anharmonic approach<sup>43</sup> and the Frenkel and Ladd (FL) method<sup>44</sup> [Figs. 3(b) and 3(c)]. For comparison, we also plot the vibrational entropy as obtained from the harmonic approximation. The details of these methods are given in Appendix A. As expected, the vibrational entropy obtained from these two approaches is slightly lower than that obtained from the harmonic approach.

## 3. Configurational entropy

Next, we study the configurational entropy of the system. For all the systems, the data are plotted below their respective onset temperatures (see Table I).<sup>27</sup> The systems follow the expected linear relationship between  $TS_c$  and  $T$  (Fig. 4). The Kauzmann temperature  $T_K^{TI}$  is obtained by fitting to  $TS_c = K_T(\frac{T}{T_K} - 1)$ . We find that  $T_K^{TI}$  increases with  $k$ . This is expected as in the earlier study, it was found that with an increase in pseudoneighbors, the  $\alpha$  relaxation time of the system appears to diverge at a higher temperature.<sup>27</sup> However, for larger  $k$  systems ( $k = 12$  and  $28$ ), we find negative values of the

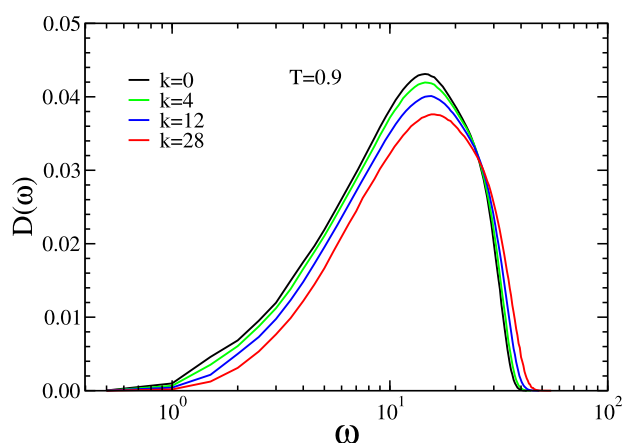


**FIG. 2.** Vibrational density of states (VDOS),  $D(\omega)$  vs  $\omega$ , for  $k = 0, 4, 12,$  and  $28$  systems. With the increase in  $k$ , the low-frequency modes are suppressed and the whole spectrum shifts to higher frequencies.



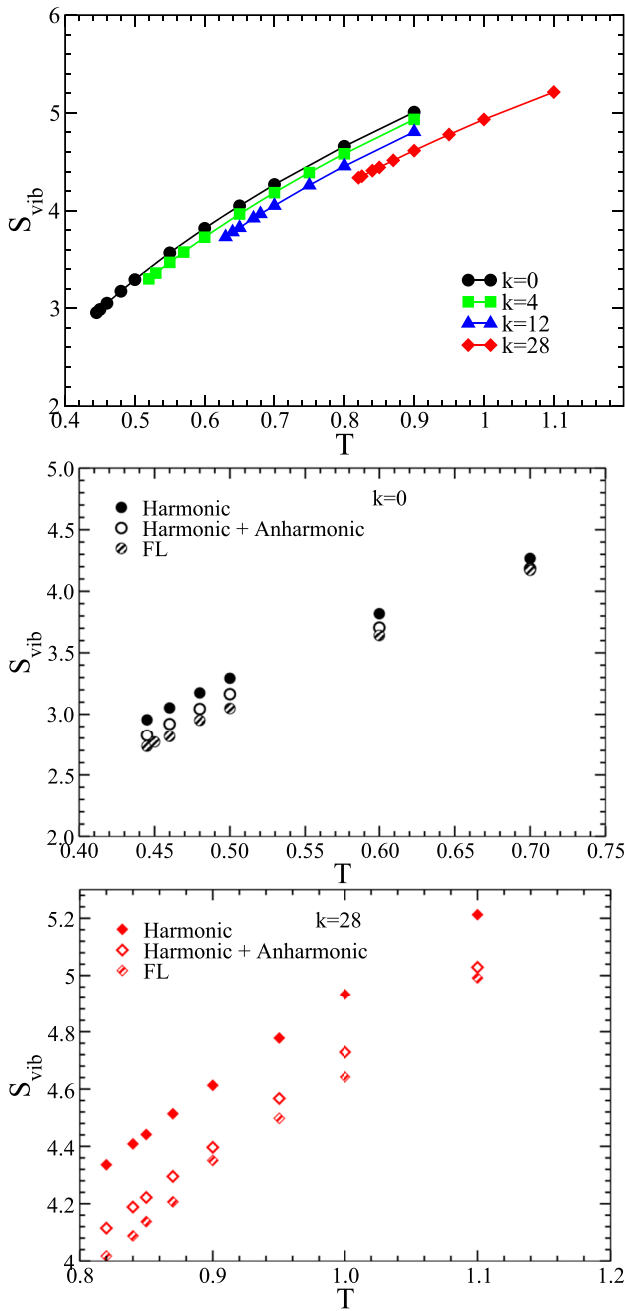


**FIG. 3.** (a) The vibrational entropy  $S_{\text{vib}}$  vs  $T$  for  $k = 0, 4, 12,$  and  $28$  systems. With an increase in  $k$ , the VDOS shifts to higher frequencies, leading to a decrease in the vibrational entropy. The vibrational entropy using the Frenkel–Ladd method and using the anharmonic contribution for (b)  $k = 0$  and (c)  $k = 28$  systems. The estimates by the two methods are closer to each other compared to the harmonic approximation.

configurational entropy at comparatively high temperatures where the liquid can be equilibrated in simulations. Particularly for the  $k = 28$  system, the temperature where the configurational entropy vanishes is close to the onset temperature of glassy dynamics.<sup>27</sup> This

**TABLE I.** Values of all characteristic temperatures for systems with different  $k$  values.  $T_0$  is the VFT temperature where the  $\alpha$  relaxation time diverges according to fits to the VFT equation, Eq. (10).  $T_K^{\text{TI}}$  is the Kauzmann temperature estimated from TI.  $T_K^{2\text{PT}}$  is the Kauzmann temperature estimated from the 2PT method.

$k$	$T_{\text{onset}}$	$T_0$	$T_K^{\text{TI}}$	$T_K^{2\text{PT}}$
0	$0.74 \pm 0.04$	0.28	0.28	0.24
4	$0.83 \pm 0.08$	0.36	0.46	0.31
12	$1.03 \pm 0.07$	0.46	0.68	0.41
28	$1.28 \pm 0.22$	0.61	1.19	0.55

is clearly unphysical. The  $T_K^{\text{TI}}$  values are listed in Table I. In Table I, we also list the respective  $T_0$  values. For many systems, it is found that  $T_K \approx T_0$ , which suggests that the slowing down of the dynamics is driven by thermodynamics.<sup>14</sup> On the contrary, in Table I, we find

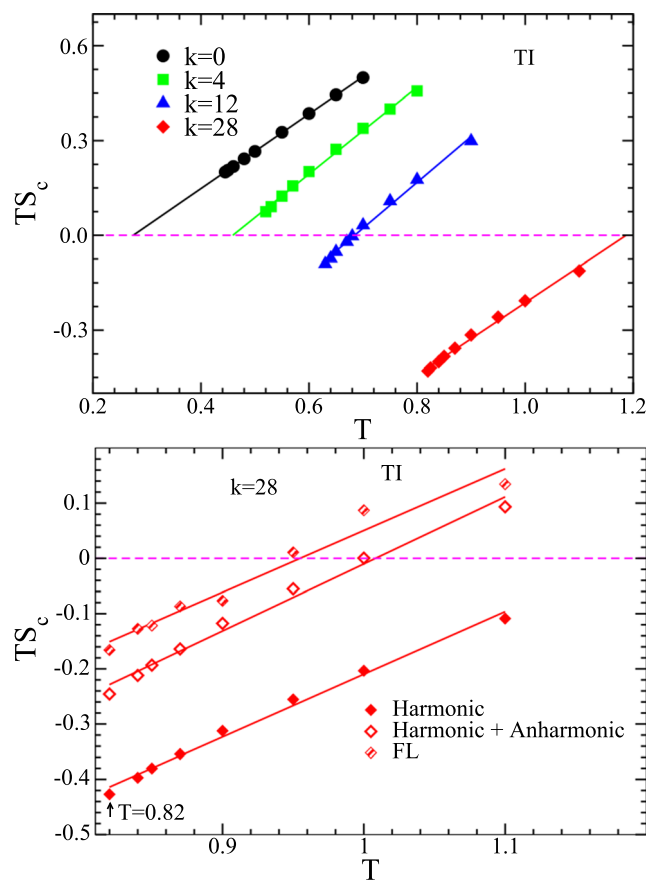


**FIG. 4.** (a)  $TS_c$  vs  $T$  for  $k = 0, 4, 12,$  and  $28$  systems where  $S_c$  is calculated using the TI method. The value of the Kauzmann temperature  $T_K^{\text{TI}}$  increases with increasing  $k$ . The value of  $T_K^{\text{TI}}$  (see Table I) for the  $k = 28$  system is close to its onset temperature. For  $k = 12, 28$  systems,  $T_K^{\text{TI}}$  values are high enough such that temperatures below  $T_K^{\text{TI}}$  are accessible in simulation.  $S_c$  becomes negative for such temperatures. (b)  $TS_c$  vs  $T$  for the  $k = 28$  system. Here, three different vibrational entropies have been estimated using the pure harmonic approximation, including the anharmonic contribution to the harmonic approximation and the Frenkel–Ladd method. All three methods predict negative  $S_c$  below a certain temperature, where the dynamics of the system survives.

that the difference between  $T_K^{TI}$  and  $T_0$  increases with an increase in  $k$  and the former is higher than the latter.

In the TI method, we need information about the ideal gas entropy, the excess entropy, and the vibrational entropy. To improve the estimate of the vibrational entropy, we also incorporate the anharmonic contribution and calculate the vibrational entropy using the Frenkel and Ladd method (Appendix A). In Fig. 4, we plot  $TS_c$  for the  $k = 28$  system where the vibrational entropy is obtained from the anharmonic approximation and the Frenkel and Ladd method. For comparison, we plot the value as obtained from the harmonic approximation. We find that although the configurational entropy now vanishes at a lower temperature, its value is still negative at temperatures where we can equilibrate the system.

We next show in Fig. 5 that for the  $k = 28$  system at  $T = 0.82$ , which is much below  $T_K^{TI} = 1.19$ , both the collective overlap function and the intermediate scattering function decay with time and reach their respective long time values [ $Q^{tot}(t \rightarrow \infty) = 0.135$  and  $F(q, t \rightarrow \infty) = 0$ ]. Note that because of the introduction of the pseudoneighbors at a distance “ $L_{ij}$ ” the system has more than one length scale. Thus, to make sure that the relaxation persists at length scales that are larger and smaller than the nearest neighbor distance, we plot the intermediate scattering function at wave numbers larger and smaller than  $q_{max} = \frac{2\pi}{\sigma_{max}}$ , where  $\sigma_{max}$  is the position of the first peak in the radial distribution function. We find that the intermediate scattering functions relax to zero at all length scales. The fact that the dynamics show full relaxation where the configurational entropy vanishes suggests a strong violation of the RFOT prediction. Note that recent studies have suggested that the TI method overestimates the configurational entropy.<sup>45,46</sup> If we take this into account, i.e., assume that the actual configurational entropy is lower than that obtained via the TI method, then the results obtained here

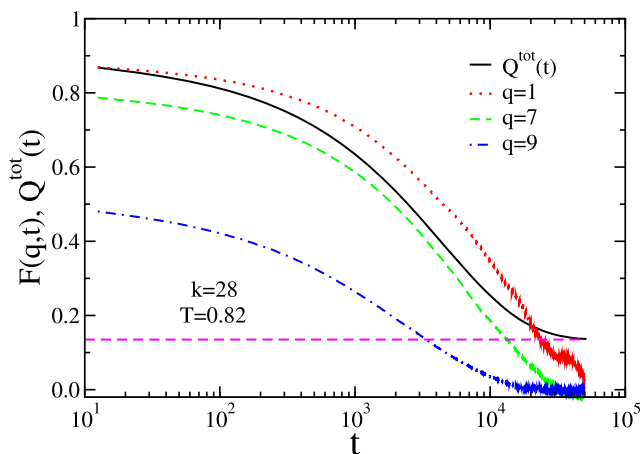


**FIG. 5.** Time dependence of the intermediate scattering function and the collective overlap function for the  $k = 28$  system at a temperature  $T = 0.82$ , which is lower than  $T_K^{TI}$  (see Table I). It shows that the self-dynamics and the collective dynamics relax to their asymptotic values over timescales accessible in simulations at a temperature lower than that at which the configurational entropy vanishes. The magenta horizontal dashed line shows the asymptotic value of the collective overlap function, which is 0.135.

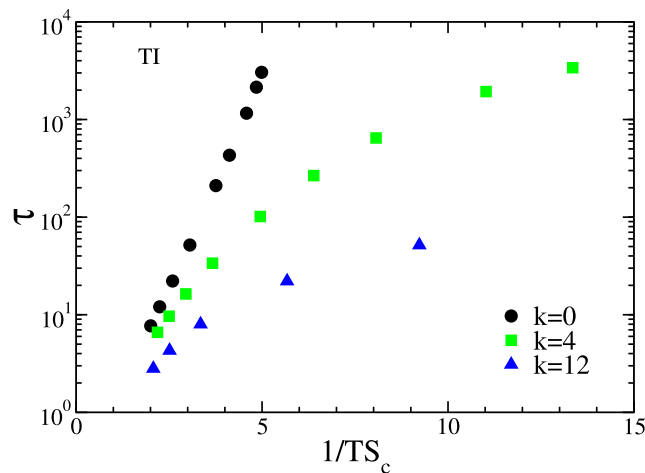


**FIG. 6.** Testing the Adam–Gibbs relation between the relaxation time  $\tau$  and  $1/TS_c$ , for the  $k = 0, 4$ , and  $12$  systems. The AG relation is obeyed for the  $k = 0$  system, but is violated for non-zero  $k$  systems. The relaxation time  $\tau$  is estimated from the self-part of the overlap function.

would be even more flawed. This implies that we need to revisit the TI method of calculating the entropy.

In Fig. 6, we also study the validity of the Adam–Gibbs relationship. We find that with an increase in  $k$ , there is a breakdown of the AG relationship, which in this case is a consequence of the violation of RFOT predictions. The plot also suggests that the relaxation time is smaller than that predicted by the AG relationship.

## B. Possible reasons for the failure of the TI method

Let us first summarize the main observations made here when the entropy is calculated using the TI method: (i) negative values of  $S_c$  at low temperatures for large values of  $k$  and (ii) full relaxation of the dynamical quantities at temperatures lower than the temperature at which  $S_c$  goes to zero. In this section, we discuss the possible failure points of the TI method.

### 1. Ideal gas entropy

In the calculation of the configurational entropy [Eq. (28)], we need the information of the ideal gas entropy. To make the entropy an extensive quantity, we calculate the ideal gas entropy (Sec. III A 1) by assuming the particles to be indistinguishable. However, in the mean-field system, each particle has a different set of pseudoneighbors with different  $L$  values. Thus, one might argue that the particles are distinguishable.

If we assume all particles to be distinguishable, i.e.,  $M = N$ , then the entropy in the thermodynamic limit will diverge [Eq. (12)]. However, for finite  $N$ , we can estimate the entropy, which will increase by a factor that is proportional to  $\log(N)$  but independent of  $k$ . From our analysis, it appears that with an increase in  $k$ , the error in the entropy calculation increases. This implies that the correction term should depend on  $k$ .

Apart from the distinguishability factor, there is one other issue that can affect the ideal gas term. Here, the way the interaction

between a particle and its pseudoneighbor is designed restricts the particle to access a certain part of the total volume. Per pseudoneighbor this volume is a spherical region of radius  $L_{ij}$ . Thus, in the ideal gas limit, the whole volume of the system is not accessible to a particle. The per particle inaccessible volume should increase with  $k$ , which will lower the entropy of the system. Thus, the distinguishability factor will increase the entropy, whereas inaccessible volume will decrease the entropy, the former is independent of  $k$ , but the latter depends on  $k$ . This might appear to solve the  $k$  dependence of the correction term. However, if we combine the distinguishability and inaccessible volume part, then we will find that for systems with small values of  $k$ , the volume correction is really small and the distinguishability factor which is independent of  $k$  increases the entropy by a large amount. Thus, the dynamics for these systems will be similar to the  $k = 0$  system, but the entropy calculated in this way will be much higher.

Another possibility is that the distinguishability is not a binary function but is a function of  $k$ . Having these extra connections with the pseudoneighbors replacing particles with another one while keeping the identity of pseudocontacts the same can increase the energy of the system, and the larger the number of pseudocontacts the higher is the increase in the energy. This appears quite similar to the case of polydisperse systems with continuous polydispersity where depending on the size range of the two particles, the replacement may or may not keep the system in the same minimum.<sup>47</sup> It was argued that after particle swapping if the system remains in the same inherent structure minimum, then the two particles are indistinguishable, and if not, then they belong to different species. Thus, to find the number of species, we need to swap particle positions. Swapping particles while keeping the identity of the pseudoneighbors the same is not straightforward. The swap should make sure that in the new position of the particle, none of the pseudoneighbors are within the interaction range  $r_c$ . With the increase in the number of pseudoneighbors, these swaps will be mostly rejected, thus making it impossible to quantify the number of species and, thus, the entropy.

## 2. Excess entropy scaling

We next test the accuracy of the excess entropy value calculated via the TI method. Apart from the AG relationship which is valid in the low temperature regime and connects the configurational entropy to the dynamics, there is another phenomenological relationship, namely, the Rosenfeld relation between the excess entropy and the dynamics.<sup>48,49</sup> According to the Rosenfeld relation, any dimensionless transport property will follow the excess entropy scaling. For the relaxation time, it can be written as  $\tau^* = R \exp(-KS_{ex})$ , where  $\tau^* = \tau \rho^{-1/3} T^{1/2} m^{-1/2}$ . For simple liquids, it has been found that  $R \approx 0.6$  and  $K \approx 0.8$ , and this relationship is valid in the high-temperature regime, showing a data collapse between scaled diffusion and  $S_{ex}$ <sup>50</sup> and also scaled relaxation time and  $S_{ex}$ .<sup>51,52</sup> A recent study has also shown that scaled viscosity and diffusion coefficient for a large number of systems show a quasi-universal excess entropy scaling, extending over both high and low temperature regimes.<sup>53</sup> In Fig. 7, we plot  $\tau^*$  vs  $S_{ex}$  for the different mean-field systems and do not find any data collapse. Thus, we find a breakdown of the Rosenfeld relation and also of the quasi universal excess entropy scaling.<sup>53</sup> Note that similar to that observed for the

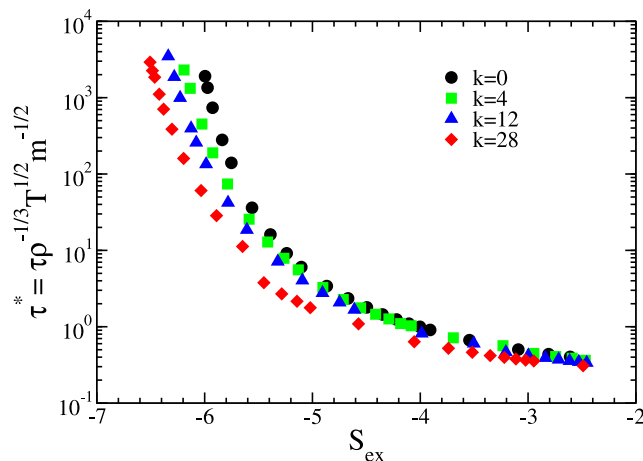


FIG. 7. Scaled relaxation time vs excess entropy. With increasing  $k$ , there is a deviation from the quasi-universal excess entropy scaling.

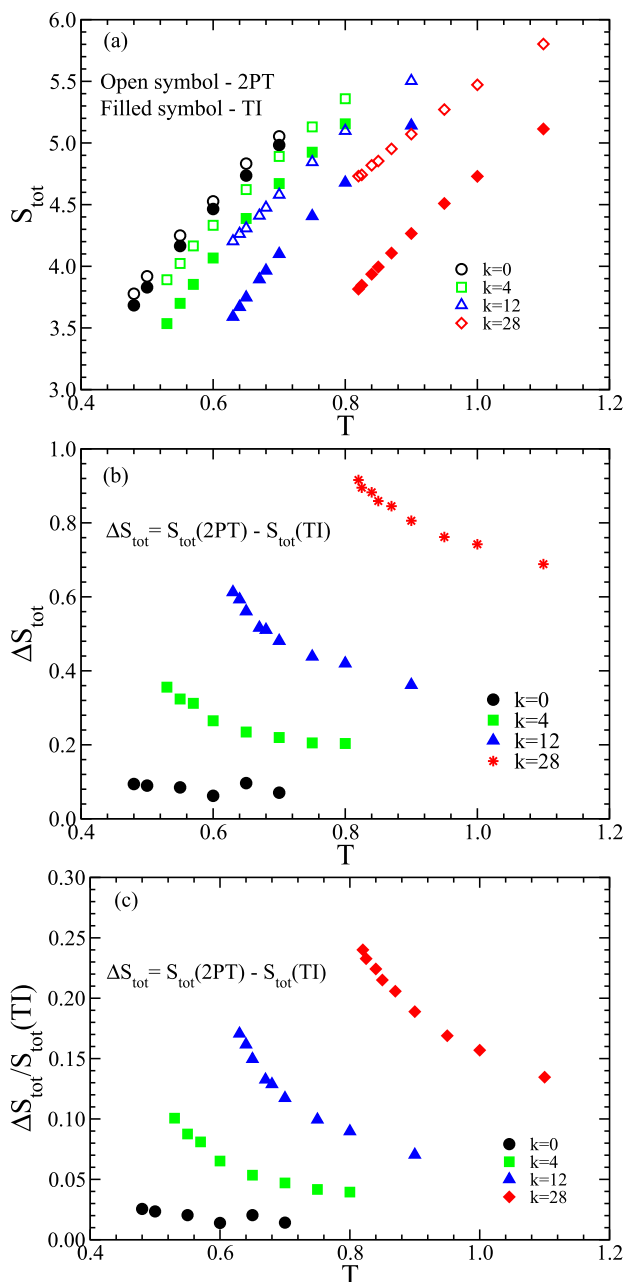
AG relationship, we find that for higher  $k$  systems, the relaxation time is smaller than that predicted by the excess entropy scaling relation.

The deviation from the excess entropy scaling might appear quite weak. However, note that, unlike the AG relationship where we deal with the configurational entropy which has a very small value, here, we deal with the excess entropy, which has a large value. Thus, the excess entropy scaling is less sensitive to small errors in the calculation of the entropy. In the mean-field system, we find that the excess entropy has a strong dependence on the number of pseudoneighbors. On the other hand, the study of the dynamics of the mean-field system showed that the interaction with the pseudoneighbors slows down the overall dynamics of the system but has a weak effect on the structural relaxation.<sup>27</sup> Thus, it appears that the role of the pseudoneighbors is not the same for the TI entropy and the dynamics.

## C. Entropy using the 2PT method

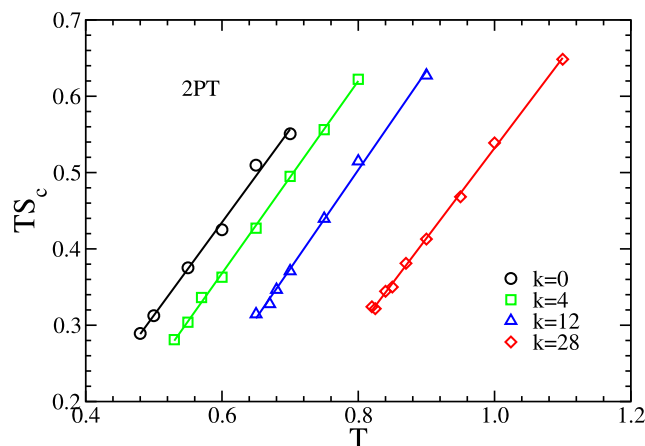
Although we point out the possible sources of error in the TI method, we do not know how to correct them at present. Thus, in this section, we present the results of the calculation of entropy using the 2PT method, which uses an entirely different technique. In the 2PT method, we primarily use information about the dynamics, namely, the velocity autocorrelation function, to determine the entropy. We know that the TI method works well for the regular KA model. Thus, to validate the 2PT method, we compare it with the TI method for a regular KA system ( $k = 0$ ). As shown in Appendix A, the 2PT method works well. At temperatures close to the mode-coupling transition temperature, the 2PT method shows some deviation, which is identified as arising from an averaging issue. Thus, we use the results from the 2PT method in the temperature range where the upper bound is the onset temperature and the lower bound is above the respective mode-coupling theory transition temperature.<sup>27</sup> In this section, we will first compare the total entropy obtained using the 2PT method [Eq. (27)] and the TI [Eq. (14)] method for the different mean-field systems. As shown in





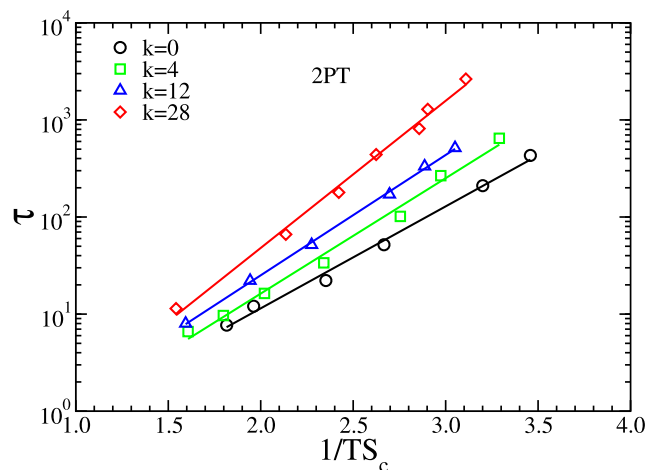
**FIG. 8.** Comparison of the TI and 2PT methods of calculation of the entropy for the mean-field system: (a)  $S_{\text{tot}}$  vs  $T$ . The filled symbols represent the results obtained from the TI method, and the open symbols represent those from the 2PT method.  $S_{\text{tot}}$  computed by the 2PT method is higher than that by the TI method. (b) The difference in total entropy,  $\Delta S_{\text{tot}}$ , between 2PT and TI methods increases with increasing  $k$ . (c) The relative difference in the total entropy,  $\frac{\Delta S_{\text{tot}}}{S_{\text{tot}}(\text{TI})}$ , between 2PT and TI methods shows similar behavior as (b).

Fig. 8, the difference in total entropy between TI and 2PT methods increases systematically with increasing  $k$ . This suggests that for this system, the TI method of calculating the entropy is not correct. We next study the configurational entropy as predicted by the 2PT



**FIG. 9.**  $TS_c$  vs  $T$  for  $k = 0, 4, 12,$  and  $28$  systems using the 2PT method. Values of  $T_K^{2\text{PT}}$ , which are close to  $T_0$ , are given in Table I.

method and its correlation with the dynamics. To calculate the configurational entropy, we need the information of the vibrational entropy, which is the same as that used in the TI method. In Fig. 9, we show the  $TS_c$  vs  $T$  plots. We find that for all the systems,  $T_K^{2\text{PT}}$  is smaller than  $T_K^{\text{TI}}$  and close to  $T_0$  (see Table I). This shows that the entropy calculated via the 2PT method follows the RFOT prediction. As discussed before, recent studies suggested that the TI method overestimates the entropy.<sup>45,46</sup> This might imply that the higher value of entropy estimated by the 2PT method is due to some additional vibrational degrees of freedom. Note that, for the  $k = 0$  system, the entropy estimated by the two methods is close to each other. However, with the increase in  $k$ , as the error in the entropy value calculated by the TI method increases, this difference also increases. For the  $k = 28$  system, when the TI method predicts



**FIG. 10.** Testing the AG relation,  $\tau$  vs  $\frac{1}{TS_c}$ , for  $k = 0, 4, 12,$  and  $28$  systems with  $S_c$  computed by the 2PT method. All the systems follow the AG relation in the range of temperatures studied here.

negative configurational entropy and the 2PT method predicts positive configurational entropy, the self-correlation and the collective correlation functions decay to their respective asymptotic values. This decay of the correlation functions is only possible when the system can explore the configurational space. Vibrational degrees of freedom alone cannot lead to such a decay of the correlation functions. This is consistent with the prediction of the 2PT method.

We next check the validity of the AG relationship. In Fig. 10, we show a semi-log plot of  $\tau$  against  $\frac{1}{TS_c}$ . It clearly shows the validity of the AG relation for all the systems in the temperature range studied. Note that in the 2PT method, there is no adjustable parameter to enforce the validity of the AG relationship.

## V. RESULTS FOR PINNED SYSTEMS

Note that in the mean-field system, the breakdown of the AG relation and also the vanishing of the configurational entropy at a temperature where the dynamics show complete relaxation are similar to what has been observed for another family of models, namely, the pinned system.<sup>33–36,45</sup> In the pinned system, the relaxation time obtained from single-particle dynamics remains finite at temperatures for which the configurational entropy vanishes, and there is some evidence<sup>54</sup> that the relaxation time associated with the collective dynamics also remains finite at such temperatures. It has also been argued that the configurational entropy has a finite value when the vibrational entropy is calculated using an anharmonic approximation.<sup>45</sup>

We calculate the total entropy of the pinned system using the TI method used in earlier studies<sup>33</sup> and also given in Appendix B of the present paper. We then calculate the configurational entropy by subtracting the vibration entropy from the total entropy by taking into consideration the anharmonic contribution. As discussed in Appendix B and shown in Figs. 21 and 22 and Table II, even after taking into consideration the anharmonic term, the Kauzmann temperature  $T_K$  appears to be high and the AG relationship is violated.

Given the success of the 2PT method in determining the entropy for the mean-field system, we apply it for the pinned system and compare it with the TI method. In Fig. 11(a), we plot the total entropy obtained using two different methods, and in Fig. 11(b), we plot their differences for three different pinning densities, and in Fig. 11(c), we plot the relative difference. For comparison, we also show the KA system with no pinning, which is the same as the KA system with  $k = 0$ . Similar to that observed in the mean-field system, we find a difference between the entropy calculated via the

**TABLE II.** The values of all characteristic temperatures for pinned systems with different pin concentration  $c$ .  $T_K^{TI}$  is the Kauzmann temperature estimated from TI.  $T_K^{2PT}$  is the Kauzmann temperature estimated from the 2PT method.

$c$	$T_K^{TI}$	$T_K^{2PT}$
0.00	0.28	0.24
0.05	0.31	0.30
0.10	0.41	0.32
0.15	0.57	0.41

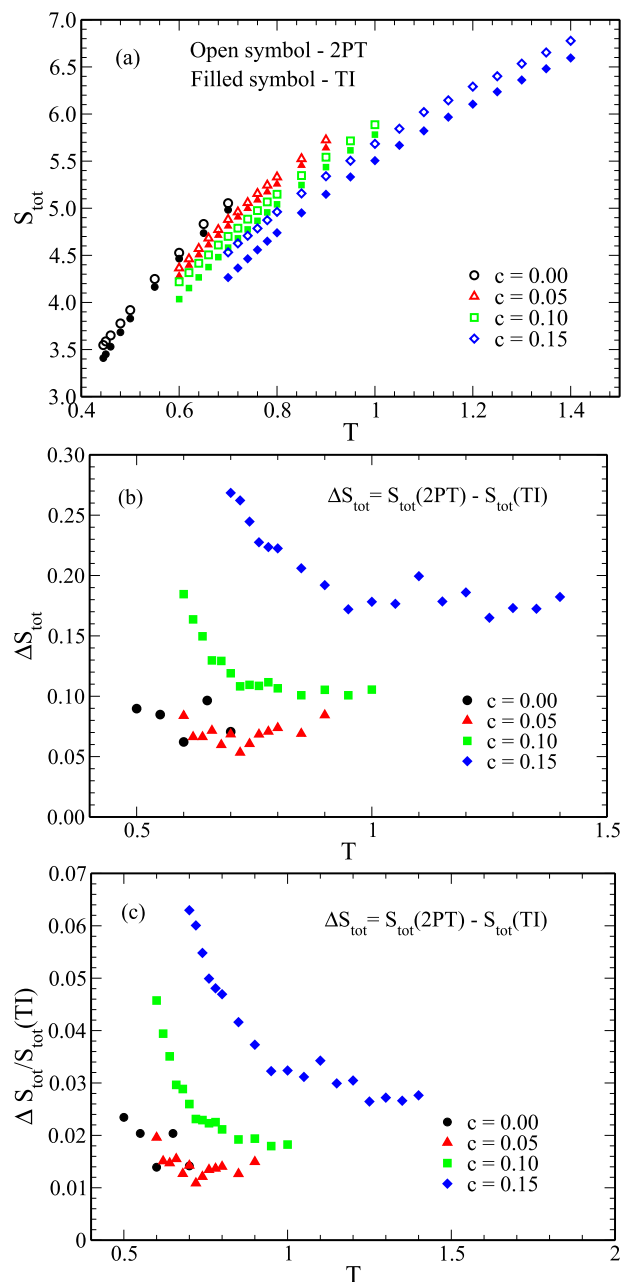


**FIG. 11.** Comparison of the TI and 2PT methods of calculation of entropy for the pinned system with different pinning concentration. (a) The total entropy  $S_{tot}$  vs  $T$ . The filled symbols represent the results of the TI method, and the open symbols represent those of the 2PT method. (b) The difference in  $S_{tot}$  between 2PT and TI methods increases with increasing pinning concentration  $c$ . (c) The relative difference in the total entropy,  $\frac{\Delta S_{tot}}{S_{tot}(TI)}$ , between 2PT and TI shows similar behavior as (b).

2PT and the TI methods that increases systematically with pinning. We next calculate the configurational entropy as predicted by the two methods and plot the temperature dependence of  $TS_c$  in Fig. 12. Both methods predict positive Kauzmann temperatures for

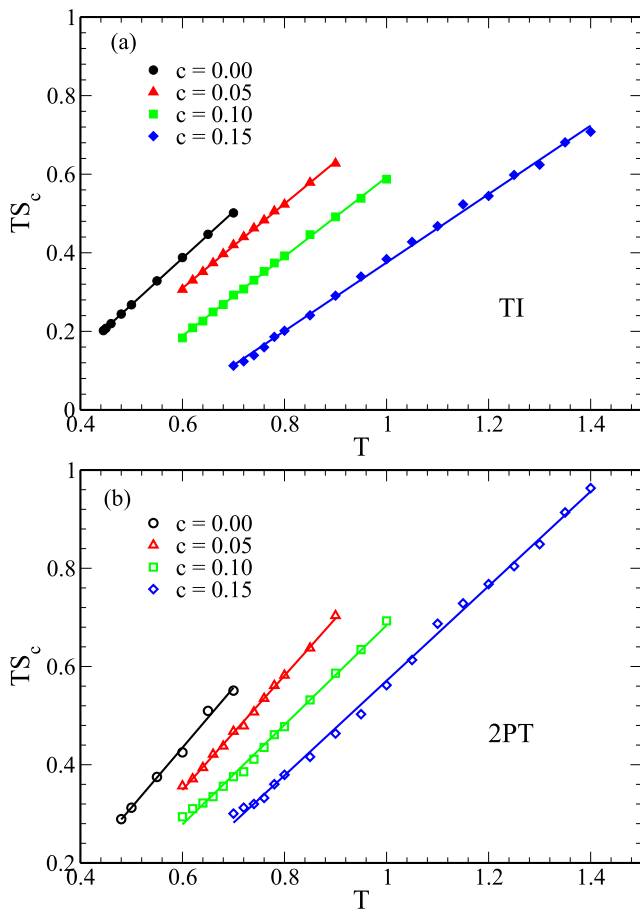


**FIG. 12.**  $TS_c$  vs  $T$  for systems with different pinning concentrations  $c = 0, 0.5, 0.10, 0.15$  using (a) the TI method and (b) the 2PT method. Both  $T_K^{TI}$  and  $T_K^{2PT}$  increase with increasing pinning concentration, but  $T_K^{2PT} < T_K^{TI}$ , see Table II.

each system, and similar to the case of mean-field systems, the Kauzmann temperature predicted by the 2PT method is lower than that by the TI method; see Table II. In this calculation, we have used the harmonic approximation for the vibrational entropy. The anharmonic approximation will equally affect both the 2PT and TI entropy values, and the plots are given in Appendix B.

Next, we need to understand if the lowering of the  $T_K$  value in the 2PT method is sufficient to describe the dynamics. In Fig. 13, we show semi-log plots of  $\tau$  vs  $\frac{1}{TS_c}$  where the entropy is calculated using the 2PT and the TI methods. The TI method shows a strong breakdown of the AG relation for  $c = 0.1$  and  $c = 0.15$ , whereas the 2PT method clearly follows the AG relation for all  $c$ .

As discussed above, the unphysical feature of negative configurational entropy does not appear in the TI results for the pinned system. In addition, the observation that the 2PT results for  $S_c$  lie above the results obtained from the TI method suggests that the 2PT results are less accurate than the TI results because, as mentioned above, there are arguments<sup>45,46</sup> that suggest that actual configurational entropy is lower than the TI result. However, it should be noted that the expectation that the TI results overestimate

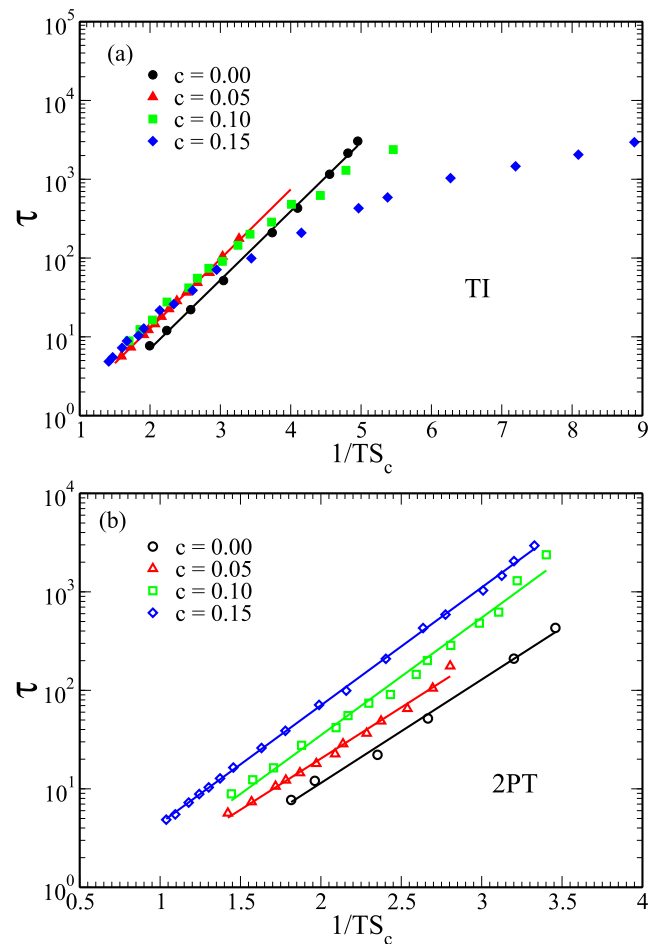


**FIG. 13.** Testing the AG relation between  $\tau$  vs  $\frac{1}{TS_c}$  for  $c = 0, 0.5, 0.10, 0.15$  systems using (a) the TI method (b) the 2PT method. In the temperature range studied here, the AG relation is violated for  $c = 0.1$  and  $c = 0.15$  when  $S_c$  is calculated using the TI method. However, the AG relation holds for all  $c$  when  $S_c$  is calculated via the 2PT method.

the true  $S_c$  has not been verified by any calculation for the pinned system. In addition, a difference between the value of the configurational entropy *per particle* obtained from the TI method and its actual value would require the presence of an exponentially large number of energy minima that differ from a particular minimum by the movement of a small number of particles. We are not aware of any study that establishes the presence of such a large number (exponential in the number of particles) of nearby minima.

Available results for the dynamics<sup>35,36,54</sup> of the pinned system suggest that the TI results for  $S_c$  may not be consistent with the RFOT theory. There are arguments<sup>34,45</sup> that suggest that the inconsistency with the RFOT theory may disappear if the relaxation time associated with the collective dynamics (instead of the timescale obtained from single-particle dynamics) is considered. It has also been argued<sup>45</sup> that the disagreement with the RFOT theory may be accounted for by the overestimation of  $S_c$  in the

TI method. However, these arguments have not been verified from explicit calculations.

A similar observation of the mismatch between entropy and dynamics for the pinned system has been observed in experimental studies.<sup>55</sup> It was found that although for unpinned systems, the local dynamics correlate with the local pair excess entropy, and with an increase in the pinning density, such correlation disappears.<sup>55</sup> Thus, for the pinned system, these traditional methods of entropy calculation cannot explain the dynamics. On the other hand, the 2PT method appears to explain the dynamics quite well. For these reasons, we believe that more studies are necessary for deciding the relative merits of the TI and 2PT methods for the pinned system.

## VI. CONCLUSION

Recently, some of us have developed a model for a glass-forming liquid whereby changing a parameter, the system can continuously switch from a standard three-dimensional liquid to a fully connected mean-field-like system.<sup>27</sup> The parameter is  $k$ , the number of additional particle–particle interactions that are introduced per particle on top of the regular interactions in the system. With increasing  $k$ , the structure and the dynamics were studied, which showed more mean-field-like behavior at higher  $k$  values. The present work aims at studying the thermodynamics of the system and understanding its correlation with the dynamics. To study thermodynamics, we first calculate the entropy using the well-known TI method.<sup>29</sup> We then study the correlation of the entropy with the dynamics. This model shows super-Arrhenius dynamics similar to conventional glassy liquids,<sup>27</sup> suggesting that the RFOT description should apply. However, we find that configurational entropy vanishes at a temperature that is close to the onset temperature of the system. We also find that the relaxation times calculated from both single-particle and collective dynamics remain finite at temperatures where the configurational entropy vanishes. This is different from the prediction of RFOT and the behavior seen in conventional glass-forming liquids for which the (extrapolated) values of  $T_K$  and  $T_0$  are found to be close to each other.<sup>14,16,56</sup> This observation also indicates that the system apparently samples state point with negative configurational entropy, which is unphysical by definition. We discuss the possible source of error in the TI method of calculation of the entropy for the mean-field system. However, at this point, we do not know how to modify the TI method to correctly calculate the entropy of these model systems.

We, thus, use another technique, namely, the 2PT method, to calculate the entropy. The 2PT method assumes that a liquid can be represented as partially a gas and partially a solid, and this fraction is a function of the thermodynamic parameters of the system and also of the size of the particles. The 2PT method has been extensively used to calculate the entropy for many systems, mostly in the high-temperature regime.<sup>30,39</sup> In recent work, this method was also extended to lower temperatures.<sup>32</sup> We find that for the KA system at  $k = 0$ , both the 2PT method and the TI method provide similar results. We then compare the total entropy calculated by the 2PT method with that by the TI method for different mean-field systems. We find that the difference between the entropy values obtained in the two methods systematically increases with increasing  $k$ . We also find that the entropy calculated via the 2PT method describes the dynamics quite well and confirms the RFOT prediction.

The results of the mean-field systems appear quite similar to that of the pinned particle system studied earlier.<sup>33</sup> In the pinned system, the self-part of the density correlation function decays to zero at temperatures where  $S_c$  obtained from the TI method goes to zero.<sup>35</sup> Given the success of the 2PT method in calculating the entropy of the mean-field system, we apply it to calculate the entropy of the pinned system. Interestingly, we find that similar to the mean-field system, the difference between the entropy calculated via 2PT and TI methods systematically increases with pinning. The entropy obtained via the 2PT method seems to explain the temperature dependence of the relaxation time obtained from the self-overlap function well, and the RFOT prediction remains valid. However, due to reasons mentioned in Sec. V, we believe that more work is needed in order to decide whether the 2PT method yields more accurate results for the entropy of the pinned system than the TI method.

## ACKNOWLEDGMENTS

S.M.B. thanks Walter Kob, Misaki Ozawa, Shiang-Tai Lin, Daan Frenkel, Srikanth Sastry, and Anshul D. S. Parmar for discussion and acknowledges funding support from the Science and Engineering Research Board, Department of Science and Technology, Government of India. U.K.N., P.P., and M.M. thank CSIR for the fellowship. C.D. acknowledges support from the Department of Science and Technology, Government of India.

## AUTHOR DECLARATIONS

### Conflict of Interest

We have no conflicts of interest to disclose.

### Author Contributions

U.K.N. and P.P. equally contributed to this work.

## DATA AVAILABILITY

The data that support the findings of this study are available from the corresponding author upon reasonable request.

## APPENDIX A: MEAN-FIELD SYSTEM ENTROPY

For a binary system in the 2PT method of entropy calculation, we need to provide the information of the partial volume fraction, which can be calculated as<sup>39</sup>

$$\bar{V}_i = \frac{\sigma_i^3}{\sum_j x_j \sigma_j^3} \frac{V}{N}, \quad (\text{A1})$$

where  $V_i = \bar{V}_i N_i$ .

The partial volume fraction depends on the radii of the particles. In the KA system, the diameter of the  $A$  and  $B$  particles is 1 and 0.88, respectively. However, the potential in the KA model is designed in such a way that it allows for interpenetration between the  $A$  and the  $B$  particles [ $\sigma_{AB} < (\sigma_A + \sigma_B)/2$ ]. Thus, if we assume that the  $B$  particles are surrounded by all  $A$  particles, then the effective diameter of a  $B$  particle will be 0.6. To understand the role of partial volume fraction on the entropy, we calculated  $S_{tot}$  from

the 2PT method, assuming the  $B$  particle diameter to be 0.8 and 0.6, respectively. We find that at high temperatures, the 0.6 value provides a better result, but at low temperatures, the entropy is almost independent of the small changes in the partial volume fraction. Thus, for these systems, we assume the diameter of the  $B$  particles to be 0.6.

We compare the total entropy of the system as estimated from the TI<sup>40</sup> and from the 2PT<sup>30</sup> methods. Figure 14 shows that  $S_{tot}$  obtained from TI and 2PT methods has similar values. The error bar for the 2PT data is estimated from a set of ten runs at each temperature. We find some deviation in the low temperature. At low temperatures, as the dynamics become slow, we need longer runs to get a converged DOS. Figure 15 shows the effect the time step has on the value of total entropy at lower temperatures. With an increase in the time step, the entropy value approaches the value calculated using the TI method. However, at longer times, the slope of the curve decreases.

Configurational entropy,  $S_c$ , obtained in the two different methods is plotted in Fig. 16. We find that the values of Kauzmann temperature ( $T_K$ ) using two different methods are close, which validates the applicability of the 2PT method for the calculation of the configurational entropy.

We have compared the density of states calculated from the calculation of Hessian and the Fourier transform of the velocity autocorrelation function. We find that both the methods show a similar result in a density of states (see Fig. 17).

To increase the accuracy of the configurational entropy, we incorporate the anharmonic contribution into the vibrational entropy.<sup>43</sup> We estimate the anharmonic contribution of the total potential energy as

$$U_{anh}(T) = U(T) - U_{IS} - \frac{3}{2}NT, \quad (A2)$$

where  $U(T)$  is the total potential energy at temperature  $T$ ,  $U_{IS}$  is the corresponding inherent structure energy, and the last term is the harmonic vibrational energy of all the particles. The anharmonic energy can be expanded around temperature  $T = 0$  as

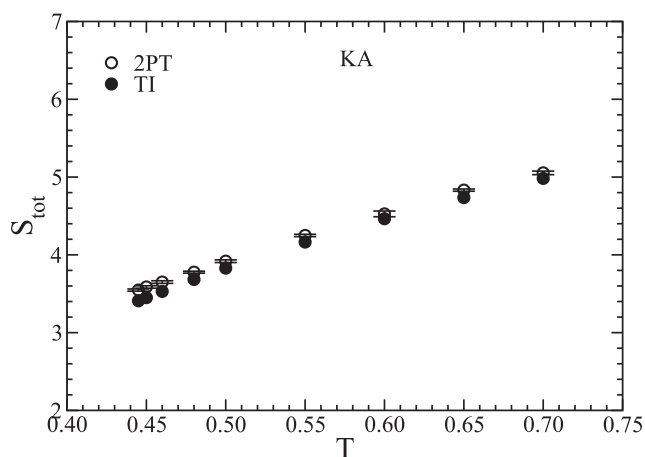


**FIG. 14.**  $S_{tot}$  vs  $T$  for the KA model using the TI and the 2PT method. The two methods agree reasonably well. A small systematic deviation in the low temperature regime is due to limited averaging possible for the 2PT method; see Fig. 15.

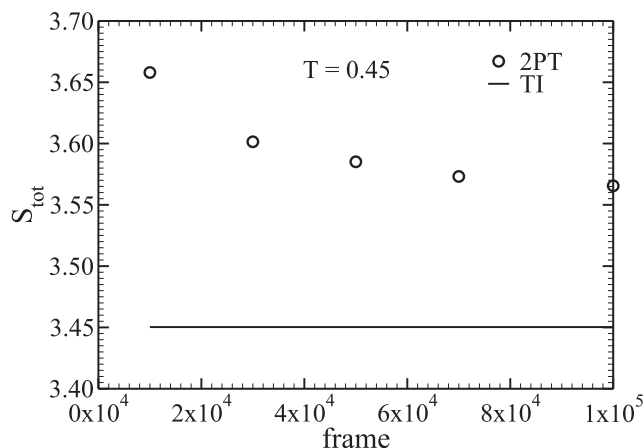


**FIG. 15.** The total entropy via the 2PT method as a function of the number of time frames over which the velocity autocorrelation function is integrated to obtain the spectral density at a low temperature  $T = 0.45$ . For comparison, we also plot the entropy value obtained using the TI method. The difference decreases with the increasing time interval, but the rate of convergence becomes slower at longer times.

$$U_{anh}(T) = \sum_{j=2} C_j T^j. \quad (A3)$$

The coefficients of expansion  $C_j$ s are temperature independent. As the system is completely harmonic in the low temperature limit, the sum starts from  $j = 2$ . The anharmonic contribution for the vibrational entropy ( $S_{anh}$ ) can be written as

$$S_{anh}(T) = \int_0^T dT' \frac{1}{T'} \frac{\partial U_{anh}(T')}{\partial T'}. \quad (A4)$$

If we substitute Eq. (A3) into Eq. (A4), then we get the anharmonic vibrational entropy as

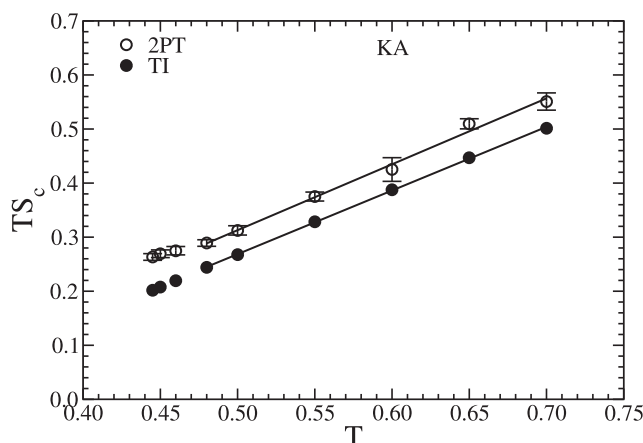


**FIG. 16.**  $TS_c$  vs  $T$  for the KA model using the TI and the 2PT methods. The values of  $T_K$  estimated by the two methods are similar ( $T_K^{TI} = 0.27$  and  $T_K^{2PT} = 0.24$ ).

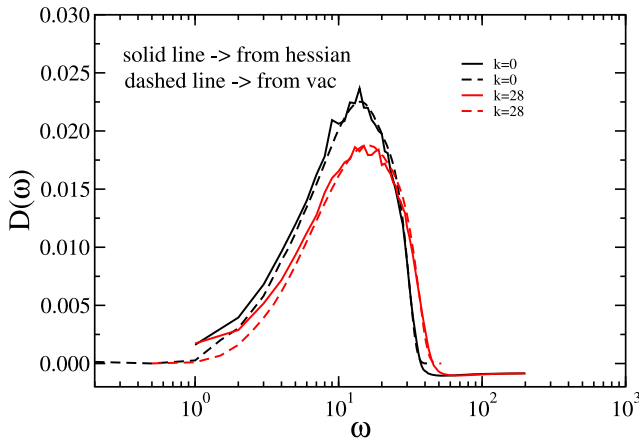


**FIG. 17.** Density of states calculated from the Hessian and the velocity autocorrelation function for  $k = 0$  and  $k = 28$  systems. Both the methods show the similar result.

$$S_{anh}(T) = \sum_{j=2}^j \frac{j}{j-1} C_j T^{j-1}. \quad (\text{A5})$$

In our simulation, we first estimate the anharmonic potential energy, as shown in Fig. 18. We then fit the simulation data to a polynomial function of  $T$  [Eq. (A3)] to obtain the coefficients. We use these coefficients to obtain  $S_{anh}$  using Eq. (A5). We find that for both  $k = 0$  and  $k = 28$  systems,  $S_{anh}$  is negative at all temperatures, thus lowering the vibrational entropy (Fig. 3) and increasing the configurational entropy (Fig. 4).

We also use the Frenkel and Ladd (FL) method to estimate the vibrational entropy of our system.<sup>44</sup> In the FL method, a perturbed Hamiltonian is introduced,

$$\beta H(\alpha) = \beta H(0) + \alpha \sum_{i=1}^N |\mathbf{r} - \mathbf{r}_{0i}|^2, \quad (\text{A6})$$

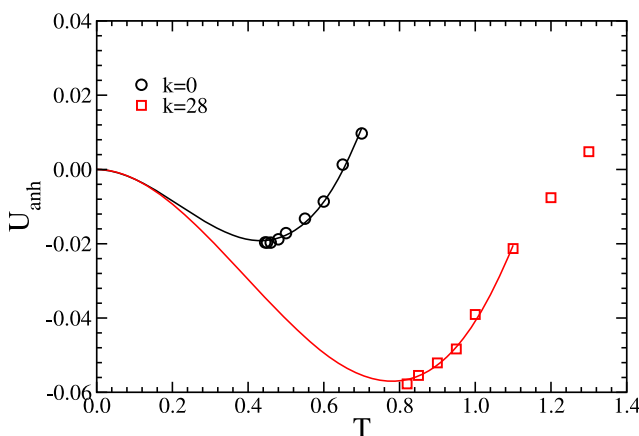


**FIG. 18.** Anharmonic potential energy ( $U_{anh}$ ) vs temperature for  $k = 0$  and  $28$  systems. The solid lines are the fitted line extrapolated to the zero temperature value.

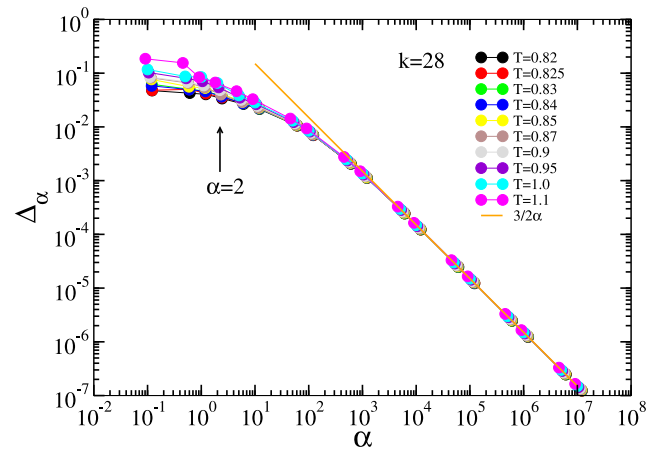


**FIG. 19.** Mean square displacement ( $\Delta_\alpha$ ) vs  $\alpha$  plot for the  $k = 28$  system at different temperatures. The solid line gives the behavior of mean square displacement for the Einstein solid,  $\Delta_\alpha = 3/2\alpha$ .

where  $H(0)$  is the original unperturbed Hamiltonian of the system,  $\beta = \frac{1}{k_B T}$ ,  $\alpha$  is the spring constant which determines the strength of perturbation, and  $\mathbf{r}_{0i}$  is the initial position of the  $i$ -th particle of the unperturbed system. By varying  $\alpha$ , a series of system is obtained, which interpolates between the original system ( $\alpha = 0$ ) and the Einstein crystal (large  $\alpha$  values). For each  $\alpha$  value, we calculate the mean square displacement (MSD) ( $\Delta_\alpha = \sum_{i=1}^N \langle |\mathbf{r} - \mathbf{r}_{0i}|^2 \rangle / N$ ) and the vibrational entropy,

$$S_{FL} = S_E(\alpha_{max}) + \int_0^{\alpha_{max}} d\alpha \Delta_\alpha. \quad (\text{A7})$$

The entropy of Einstein solid is  $S_E(\alpha_{max}) = \frac{3}{2} - 3 \ln \lambda - \frac{3}{2} \ln(\frac{\alpha_{max}}{\pi})$ , where  $\lambda$  is the de Broglie wavelength. Figure 19 shows the mean square displacement at different  $\alpha$  values for different temperatures.

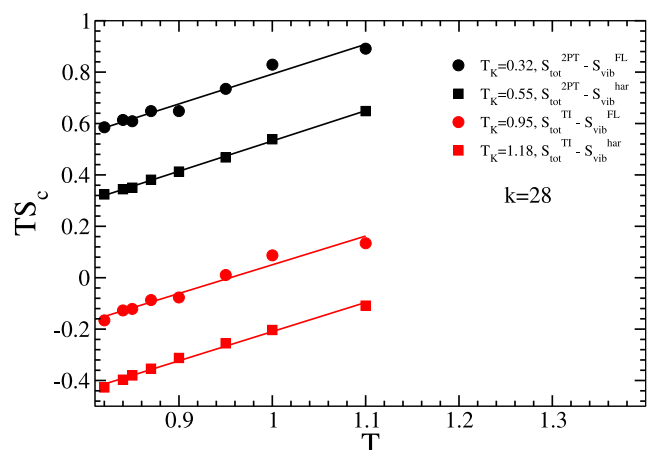


**FIG. 20.**  $TS_c$  vs  $T$  plot for TI and 2PT methods of the  $k = 28$  system. The TI method gives negative  $S_c$  even when the vibrational entropy is calculated from the FL method,  $S_{vib}^{FL}$ . The 2PT method does not give such a unphysical entropy value.



At a high  $\alpha$  value,  $\Delta_\alpha = 3/2\alpha$  follows the behavior of an Einstein solid. At small values of  $\alpha$ , the MSD is not flat, suggesting that eventually, at long time, the particle will escape the cage. Since we are interested in obtaining the vibrational contribution, we choose a lower limit of  $\alpha = \alpha_{\min}$  such that the particle remains inside the cage. Thus, to calculate  $S_{\text{vib}}$ , we integrate Eq. (A7) from  $\alpha_{\min}$  to  $\alpha_{\max}$ . Here, we assume that  $\alpha_{\min} = 2$  and  $\alpha_{\max} = 10^7$ . The contribution from lower values of  $\alpha$  ( $\alpha < \alpha_{\min}$ ) is assumed to be given by  $\Delta_{\alpha_{\min}} \alpha_{\min}$ . The vibrational entropy thus obtained is lower than the harmonic approximation and closer to the entropy obtained, including the anharmonic contribution (Fig. 3). Figure 20 shows the  $TS_c$  vs  $T$  plot for the  $k = 28$  system where we calculate  $S_c$  from both the TI and 2PT methods using vibrational contribution of entropy from the harmonic and FL method. We find that  $S_c$  becomes negative when we calculate total entropy using the TI method and the 2PT method does not give such negative entropy.

## APPENDIX B: PINNED SYSTEM ENTROPY

In a pinned system, a fraction  $c$  of the particles is pinned. The details about the pinned system have been discussed in simulation

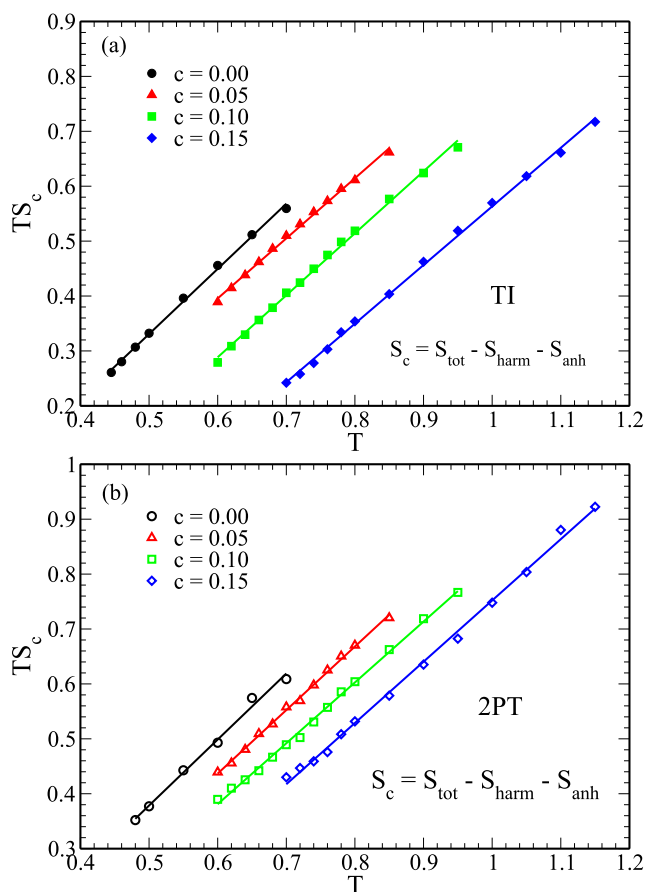


**FIG. 21.**  $TS_c$  vs  $T$  for  $c = 0, 0.5, 0.10,$  and  $0.15$  systems using (a) the TI method and (b) the 2PT method.  $S_c$  is computed by including the anharmonic contribution.  $T_K^{\text{TI}}$  and  $T_K^{\text{2PT}}$  increase with increasing pinning concentration, but  $T_K^{\text{2PT}} < T_K^{\text{TI}}$ ; see Table III.

details (see Sec. II B). Using the TI method, the total entropy of moving particle in the pinned system,  $S_{\text{tot}}$ , is given by<sup>33</sup>

$$S_{\text{tot}} = \frac{3M}{2} - \frac{3M}{2} \ln\left(\frac{2\pi T}{h^2}\right) + M\left(1 - \ln\frac{N}{V}\right) - \sum_{i=1}^2 N_i \ln\frac{N_i}{N} + \beta^* \langle U \rangle - \int_0^{\beta^*} d\beta \langle U \rangle, \quad (\text{B1})$$

where  $N_1$  and  $N_2$  are the number of moving particles of types A and B, respectively.  $V$  is the total volume of the system and  $M$  is the total number of moving particles. The total potential energy of the system is  $U = U_{\text{MP}} + U_{\text{MM}}$ , where  $U_{\text{MM}}$  and  $U_{\text{MP}}$  denote the interaction energy between moving–moving particles and moving–pinned particles, respectively.

The temperature dependence of the configurational entropy after taking care of the anharmonic contribution is plotted in

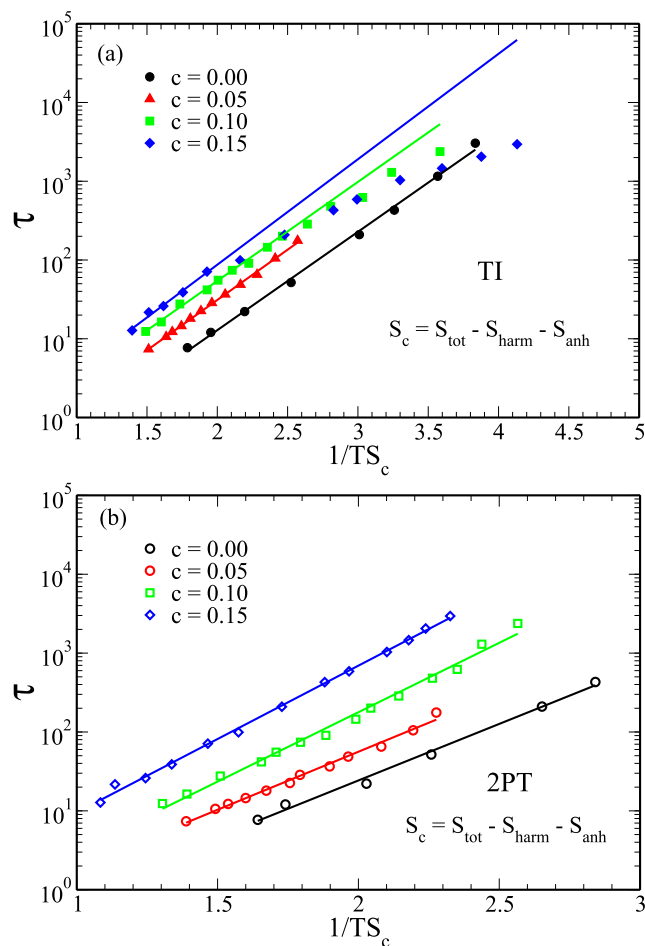


**FIG. 22.** Testing the AG relation between  $\tau$  and  $\frac{1}{TS_c}$  for  $c = 0, 0.5, 0.10,$  and  $0.15$  systems using (a) the TI method and (b) the 2PT method.  $S_c$  is computed by including the anharmonic contribution. In the temperature range studied here, the AG relation is violated for  $c = 0.10$  and  $c = 0.15$  when entropy is calculated using the TI method. However, the AG relation holds when entropy is calculated via the 2PT method.

**TABLE III.** The value of all characteristic temperatures for systems with different “c” values.  $T_K^{TI}$  (anh) and  $T_K^{2PT}$  (anh) are Kauzmann temperature estimated from TI and 2PT, respectively, after the addition of anharmonic contribution.

c	$T_K^{TI}$ (anh)	$T_K^{2PT}$ (anh)
0.00	0.22	0.18
0.05	0.24	0.22
0.10	0.34	0.26
0.15	0.47	0.33

Fig. 21(a), and the corresponding Adam–Gibbs plot is shown in Fig. 22(a). Even after the addition of the anharmonic contribution, the AG relationship is violated. In Fig. 21(b), we plot the temperature dependence of the configurational entropy where the total entropy is calculated using the 2PT method and the anharmonic contribution is taken into consideration. We show the AG plot of the same data in Fig. 22(b). We find that when the total entropy is calculated using the 2PT method, the AG relationship holds, and the temperature where the entropy vanishes is also lower than that given by the TI method (see Table III).

## REFERENCES

- S. Sastry, P. G. Debenedetti, and F. H. Stillinger, *Nature* **393**, 554 (1998).
- A. Banerjee, M. K. Nandi, S. Sastry, and S. Maitra Bhattacharyya, *J. Chem. Phys.* **147**, 024504 (2017).
- P. Patel, M. K. Nandi, U. K. Nandi, and S. Maitra Bhattacharyya, *J. Chem. Phys.* **154**, 034503 (2021).
- W. Götze, *J. Phys.: Condens. Matter* **11**, A1 (1999).
- W. M. Du *et al.*, *Phys. Rev. E* **49**, 2192 (1994).
- P. Lunkenheimer, A. Pimenov, and A. Loidl, *Phys. Rev. Lett.* **78**, 2995 (1997).
- K. Kim and S. Saito, *J. Chem. Phys.* **138**, 12A506 (2013).
- W. Kob and H. C. Andersen, *Phys. Rev. E* **51**, 4626 (1995).
- E. Flenner and G. Szamel, *Phys. Rev. E* **72**, 031508 (2005).
- E. Flenner and G. Szamel, *Phys. Rev. E* **72**, 011205 (2005).
- V. Lubchenko and P. G. Wolynes, *J. Chem. Phys.* **119**, 9088 (2003).
- T. R. Kirkpatrick and P. G. Wolynes, *Phys. Rev. A* **35**, 3072 (1987).
- A. Cavagna, *Phys. Rep.* **476**, 51 (2009).
- G. Adam and J. H. Gibbs, *J. Chem. Phys.* **43**, 139 (1965).
- W. Kauzmann, *Chem. Rev.* **43**, 219 (1948).
- M. Ozawa, C. Scalliet, A. Ninarello, and L. Berthier, *J. Chem. Phys.* **151**, 084504 (2019).
- C. A. Angell, *J. Res. Natl. Inst. Stand. Technol.* **102**, 171 (1997).
- R. Richert and C. A. Angell, *J. Chem. Phys.* **108**, 9016 (1998).
- J. H. Magill, *J. Chem. Phys.* **47**, 2802 (1967).
- S. Takahara, O. Yamamuro, and T. Matsuo, *J. Phys. Chem.* **99**, 9589 (1995).
- K. L. Ngai, *J. Phys. Chem. B* **103**, 5895 (1999).
- C. Alba-Simionesco, *C. R. Acad. Sci., Ser. IV: Phys., Astrophys.* **2**, 203 (2001).
- C. M. Roland, S. Capaccioli, M. Lucchesi, and R. Casalini, *J. Chem. Phys.* **120**, 10640 (2004).
- D. Cangialosi, A. Alegría, and J. Colmenero, *Europhys. Lett.* **70**, 614 (2005).
- E. Masiewicz *et al.*, *Sci. Rep.* **5**, 13998 (2015).
- A. D. S. Parmar, S. Sengupta, and S. Sastry, *Phys. Rev. Lett.* **119**, 056001 (2017).
- U. K. Nandi, W. Kob, and S. Maitra Bhattacharyya, *J. Chem. Phys.* **154**, 094506 (2021).
- R. Mari and J. Kurchan, *J. Chem. Phys.* **135**, 124504 (2011).
- S. Sastry, *PhysChemComm* **3**, 79 (2000).
- S.-T. Lin, M. Blanco, and W. A. Goddard, *J. Chem. Phys.* **119**, 11792 (2003).
- S.-T. Lin, P. K. Maiti, and W. A. Goddard, *J. Phys. Chem. B* **114**, 8191 (2010).
- M. Moid, S. Sastry, C. Dasgupta, T. A. Pascal, and P. K. Maiti, *J. Chem. Phys.* **154**, 164510 (2021).
- M. Ozawa, W. Kob, A. Ikeda, and K. Miyazaki, *Proc. Natl. Acad. Sci. U. S. A.* **112**, 6914 (2015).
- M. Ozawa, W. Kob, A. Ikeda, and K. Miyazaki, *Proc. Natl. Acad. Sci. U. S. A.* **112**, E4821 (2015).
- S. Chakrabarty, S. Karmakar, and C. Dasgupta, *Sci. Rep.* **5**, 12577 (2015).
- S. Chakrabarty, S. Karmakar, and C. Dasgupta, *Proc. Natl. Acad. Sci. U. S. A.* **112**, E4819 (2015).
- S. Sengupta, F. Vasconcelos, F. Affouard, and S. Sastry, *J. Chem. Phys.* **135**, 194503 (2011).
- D. A. McQuarrie, *Statistical Mechanics Book* (University Science Books, 1975).
- P.-K. Lai, C.-M. Hsieh, and S.-T. Lin, *Phys. Chem. Chem. Phys.* **14**, 15206 (2012).
- S. Sastry, *Nature* **409**, 164 (2001).
- S. Sastry, *Phys. Rev. Lett.* **85**, 590 (2000).
- B. Doliwa and A. Heuer, *Phys. Rev. Lett.* **80**, 4915 (1998).
- F. Sciortino, *J. Stat. Mech.: Theory Exp.* **2005**, P05015.
- D. Frenkel and A. J. C. Ladd, *J. Chem. Phys.* **81**, 3188 (1984).
- M. Ozawa, A. Ikeda, K. Miyazaki, and W. Kob, *Phys. Rev. Lett.* **121**, 205501 (2018).
- L. Berthier *et al.*, *Proc. Natl. Acad. Sci. U. S. A.* **114**, 11356 (2017).
- M. Ozawa and L. Berthier, *J. Chem. Phys.* **146**, 014502 (2017).
- Y. Rosenfeld, *Phys. Rev. A* **15**, 2545 (1977).
- Y. Rosenfeld, *J. Phys.: Condens. Matter* **11**, 5415 (1999).
- M. Singh, M. Agarwal, D. Dhabal, and C. Chakravarty, *J. Chem. Phys.* **137**, 024508 (2012).
- A. Banerjee, S. Sengupta, S. Sastry, and S. M. Bhattacharyya, *Phys. Rev. Lett.* **113**, 225701 (2014).
- A. Banerjee, M. K. Nandi, and S. M. Bhattacharyya, *J. Chem. Sci.* **129**, 793 (2017).
- I. H. Bell, J. C. Dyre, and T. S. Ingebrigtsen, *Nat. Commun.* **11**, 4300 (2020).
- S. Chakrabarty, R. Das, S. Karmakar, and C. Dasgupta, *J. Chem. Phys.* **145**, 034507 (2016).
- I. Williams *et al.*, *J. Phys.: Condens. Matter* **30**, 094003 (2018).
- L. Berthier, M. Ozawa, and C. Scalliet, *J. Chem. Phys.* **150**, 160902 (2019).



RESEARCH ARTICLE | JULY 24 2023

## Dynamic heterogeneity in polydisperse systems: A comparative study of the role of local structural order parameter and particle size

Palak Patel ; Mohit Sharma ; Sarika Maitra Bhattacharyya  

 Check for updates

*J. Chem. Phys.* 159, 044501 (2023)

<https://doi.org/10.1063/5.0156794>



View  
Online



Export  
Citation

CrossMark

### Articles You May Be Interested In

Development of distributed POTDR with analyzers of different SOP directions

*AIP Conference Proceedings* (May 2017)

Splitting the sop into general and lab-specific documents

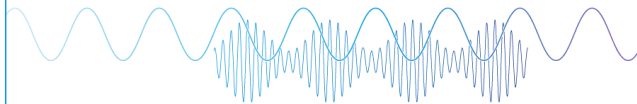
ICALEO

Low-rank sum-of-products finite-basis-representation (SOP-FBR) of potential energy surfaces

*J. Chem. Phys.* (December 2020)

Webinar

Boost Your Signal-to-Noise  
Ratio with Lock-in Detection



Sep. 7th – Register now



Zurich  
Instruments

# Dynamic heterogeneity in polydisperse systems: A comparative study of the role of local structural order parameter and particle size

Cite as: J. Chem. Phys. 159, 044501 (2023); doi: 10.1063/5.0156794

Submitted: 3 May 2023 • Accepted: 3 July 2023 •

Published Online: 24 July 2023



View Online



Export Citation



CrossMark

Palak Patel,<sup>1,2</sup> Mohit Sharma,<sup>1,2</sup> and Sarika Maitra Bhattacharyya<sup>1,2,a)</sup>

## AFFILIATIONS

<sup>1</sup>Polymer Science and Engineering Division, CSIR-National Chemical Laboratory, Pune 411008, India

<sup>2</sup>Academy of Scientific and Innovative Research (AcSIR), Ghaziabad 201002, India

<sup>a)</sup>Author to whom correspondence should be addressed: [mb.sarika@ncl.res.in](mailto:mb.sarika@ncl.res.in)

## ABSTRACT

In polydisperse systems, describing the structure and any structural order parameter (SOP) is not trivial as it varies with the number of species we use to describe the system,  $M$ . Depending on the degree of polydispersity, there is an optimum value of  $M = M_0$  where we show that the mutual information of the system increases. However, surprisingly, the correlation between a recently proposed SOP and the dynamics is highest for  $M = 1$ . This effect increases with polydispersity. We find that the SOP at  $M = 1$  is coupled with the particle size,  $\sigma$ , and this coupling increases with polydispersity and decreases with an increase in  $M$ . Careful analysis shows that at lower polydispersities, the SOP is a good predictor of the dynamics. However, at higher polydispersity, the dynamics is strongly dependent on  $\sigma$ . Since the coupling between the SOP and  $\sigma$  is higher for  $M = 1$ , it appears to be a better predictor of the dynamics. We also study the Vibrality, an order parameter independent of structural information. Compared to SOP, at high polydispersity, we find Vibrality to be a marginally better predictor of the dynamics. However, this high predictive power of Vibrality, which is not there at lower polydispersity, appears to be due to its stronger coupling with  $\sigma$ . Therefore, our study suggests that for systems with high polydispersity, the correlation of any order parameter and  $\sigma$  will affect the correlation between the order parameter and dynamics and need not project a generic predictive power of the order parameter.

Published under an exclusive license by AIP Publishing. <https://doi.org/10.1063/5.0156794>

## I. INTRODUCTION

When a liquid is cooled fast enough, it enters the supercooled liquid regime, where the properties of the liquid are very different from those of the normal liquid regime. When the supercooled liquid approaches the glass transition, its dynamics increase by orders of magnitude,<sup>1,2</sup> with the structure showing marginal changes. This observation questioned the role of structure in dynamics and the application of liquid state theories<sup>3–5</sup> in the supercooled regime. However, studies have shown that although the structure does not change drastically, static properties that depend on the structure can change enough to affect the dynamics.<sup>6–8</sup> One of the key signatures of supercooled liquids is their dynamical heterogeneity, which increases with a decrease in temperature.<sup>9–11</sup> There have been a large number of studies attempting to causally connect this dynamical heterogeneity and local order parameters, some of which are purely structural in origin.<sup>8,12–20</sup> In recent studies, we have defined a structural order parameter (SOP) that is connected to the depth of the

mean-field caging potential.<sup>8,20</sup> Our study has shown that for a large number of systems, the SOP is a good parameter to describe the relaxation process in the systems.<sup>8</sup> We have also shown that this causality persists even at the local level.<sup>20</sup> The distribution of the particle level SOP becomes wider at lower temperatures, thus suggesting an increase in local structural heterogeneity. The correlation between the SOP and the dynamics at the particle level is observed only below the onset of the glassy dynamics,  $T_{onset}$ , and increases as the temperature is decreased. Therefore, according to this study, the structural heterogeneity and the coupling between the SOP and dynamics increase at lower temperatures.<sup>20</sup>

Given the good predictive power of this new structural order parameter, it should be tested for other glass-forming liquids. Among systems that are good glass formers, polydisperse systems with size polydispersity come high in the order.<sup>21–28</sup> Polydisperse systems beyond some degree of polydispersity can be easily supercooled,<sup>22,29–34</sup> and most experimental colloidal systems are polydisperse.<sup>35–41</sup> Moreover, the swap Monte Carlo algorithm,

which allows the system to be cooled to unprecedentedly low temperatures, is best applied to polydisperse systems with continuous size polydispersity.<sup>42–48</sup>

However, for a system with continuous size polydispersity, describing the structure and any parameter that depends on the structure is a challenge. For these systems, the number of species,  $M$ , equals the total number of particles. Many a time, these systems are treated like a monodisperse system ( $M = 1$ ), and the average structure/radial distribution function (rdf) shows an artificial softening.<sup>34,49–51</sup> Therefore, any property calculated using the rdf does not show the correct value. Depending on the diameter of the particles, we can always approximate the system in terms of a certain number of species. However, what is the optimum number of species,  $M = M_o$ , needed to describe the properties of the system? This is a question often asked.<sup>45,49,50,52</sup> In earlier work, we used the correlation between the total excess entropy of the system and its two-body counterpart, which needs the information of the rdf, to obtain the optimum number of species,  $M = M_o$ .<sup>49</sup> The method is quite simple and much less computer intensive, but it provides similar results as those obtained from the study of configurational entropy using diameter permutation.<sup>45</sup>

Here, we first show that our method of describing the system into multiple species increases the mutual information (MI) of the system. We then show that the SOP and its correlation with the dynamics depend on  $M$ . It was earlier shown that the correlation between SOP and dynamics helps us identify  $T_{onset}$ .<sup>20</sup> Since the SOP and its correlation vary with  $M$ , so does the  $T_{onset}$ . Similar to our earlier study,<sup>49</sup> the  $T_{onset}$  first changes with  $M$  and then saturates. This clearly suggests that for a polydisperse system, for the calculation of the SOP, the system needs to be described in terms of multiple species. However, to our surprise, we find that the correlation between the SOP and the dynamics is at its maximum for  $M = 1$ . Furthermore, the study reveals that at low polydispersity, the SOP is a good predictor of the dynamics, but at high polydispersity, the size of the particle plays a dominant role in determining the dynamics. Moreover, the SOP and the size are also correlated, and this correlation increases with an increase in polydispersity and decreases with an increase in  $M$ . Therefore, at high polydispersity and for  $M = 1$ , where the SOP and the particle size are strongly correlated, the SOP appears to be strongly correlated with the dynamics. However, this does not depict the true correlation, which is mediated by particle size. We also study Vibrality, another order parameter independent of the system's structure. We find that at high polydispersity, compared to the SOP, the Vibrality has an even stronger correlation with the particle size. Therefore, it appears to be a better predictor of dynamics. These results clearly suggest that for systems with high polydispersity, any local order parameter correlated with the particle size might appear to be a good predictor of the dynamics, and these results should be cautiously interpreted and not assumed to be a generic result.

The organization of the rest of the paper is as follows: Section II contains the simulation details. In Sec. III, we discuss mutual information as a function of the radial distribution function. In Sec. IV, we present the calculation of the caging potential in a polydisperse system. In Sec. V, we discuss the species' dependence on the caging potential. In Sec. VI, we discuss the species dependence of the correlation between the SOP and the particle dynamics. In Sec. VII,

we analyze the dynamics of the particles with soft and hard SOP. In Sec. VIII, we do a comparative analysis of the role of particle size and SOP in the dynamics. The paper ends with a brief conclusion in Sec. IX. This paper contains three Appendices A–C sections at the end.

## II. SIMULATION DETAILS

For this study, we have performed three-dimensional MD simulations [using the Large-scale Atomic/Molecular Massively Parallel Simulator (LAMMPS) package<sup>53</sup>] for polydisperse systems in a canonical (NVT) ensemble.  $N = 4000$  particles are present in a cubic box with volume  $V$  and density  $\rho = \frac{N}{V} = 1.0$ . We have used periodic boundary conditions for the simulation. In this simulation, a Nosé–Hoover thermostat with an integration timestep  $0.001\tau$  and 100 timesteps as time constants is used. The study involves the Gaussian type of size distribution for continuous size polydispersity. This means each of the  $N$  particles has a different radius. The Gaussian distribution is given by

$$P(\sigma) = \frac{1}{\sqrt{2\pi}\Lambda} \exp\left[-\frac{(\sigma-\langle\sigma\rangle)^2}{2\Lambda^2}\right], \quad (1)$$

where  $\Lambda$  is the standard deviation. In this distribution, we consider  $\sigma_{\max/\min} = \langle\sigma\rangle \pm 3\Lambda$ . The degree of polydispersity is quantified by

$$\text{PDI} = \frac{\sqrt{\langle\sigma^2\rangle - \langle\sigma\rangle^2}}{\langle\sigma\rangle} = \frac{\Lambda}{\langle\sigma\rangle}.$$

For all the polydisperse systems, the particle sizes are chosen such that  $\langle\sigma\rangle = \int P(\sigma)\sigma d\sigma = 1$ .

In this study, particles  $i$  and  $j$  interact via inverse power law (IPL) potential. The form of the potential is given by<sup>33,54</sup>

$$U(r_{ij}) = \begin{cases} \epsilon_{ij} \left(\frac{\sigma_{ij}}{r_{ij}}\right)^{12} + \sum_{l=0}^2 c_{2l} \left(\frac{r_{ij}}{\sigma_{ij}}\right)^{2l}, & \left(\frac{r_{ij}}{\sigma_{ij}}\right) \leq x_c, \\ 0, & \left(\frac{r_{ij}}{\sigma_{ij}}\right) > x_c, \end{cases} \quad (2)$$

where  $c_0$ ,  $c_2$ , and  $c_4$  are constants, and they are selected such that the potential becomes continuous up to its second derivative at the cutoff  $x_c = 1.25\sigma_{ij}$ .

The interaction strength between two particles  $i$  and  $j$  is  $\epsilon_{ij} = 1.0$ .  $\sigma_{ij} = \frac{(\sigma_i + \sigma_j)}{2}$ , where  $\sigma_i$  is the diameter of particle  $i$ . Length, temperature, and time are given in units of  $\langle\sigma\rangle$ ,  $\epsilon_{ij}$ , and  $\left(\frac{m\langle\sigma\rangle^2}{\epsilon_{ij}}\right)^{\frac{1}{2}}$ , respectively. For all state points, the equilibration is performed for  $100\tau_\alpha$  ( $\tau_\alpha$  is the  $\alpha$ -relaxation time; details are given in Appendix A).<sup>49</sup>

During the analysis, when the system is described in terms of  $M$  species, the particles in the diameter range  $(\sigma_{\max} - \sigma_{\min})/M$  are treated as single species, where  $M = 1, 2, 3, \dots$ . Therefore, for  $M = 1$ , all particles are assumed to have the same average diameter.

Since these systems are not that well known, we provide information on the different characteristic temperatures of the systems in Appendix A.

### III. MUTUAL INFORMATION AND RADIAL DISTRIBUTION FUNCTION

As mentioned in Sec. I, in earlier work, we used the correlation between the total excess entropy and its two body counterpart to determine the optimum number of species required to describe the system.<sup>49</sup> We will now show that this method is similar in spirit to the calculation of mutual information (MI) between species and their structures.<sup>17</sup>

The excess entropy  $S_{ex}$  of a system is the loss of entropy due to correlation. This is usually calculated via the thermodynamic integration method.<sup>55,56</sup> It can also be expressed as  $S_{ex} = S_2 + S_3 + \dots$ , where  $S_n$  denotes the entropy due to the  $n$  body correlation.<sup>57</sup> 80% of the total entropy comes from the two body excess entropy and is given by<sup>58,59</sup>

$$S_2 = -2\pi\rho \int_0^\infty \{g(r) \ln g(r) - g(r) + 1\} r^2 dr, \quad (3)$$

where  $g(r)$  is the radial distribution function. For a large number of systems, it was shown that the two body excess entropy calculated using the rdf crosses the total excess entropy, and this crossover temperature  $T_{cross}$  is similar to the onset temperature of the glassy dynamics.<sup>6,60</sup> Above this temperature, the two-body excess entropy is larger than the total excess entropy, and below this temperature, the reverse happens. This concept was then used to describe systems with continuous polydispersity in terms of an optimum number of species,  $M_0$ .<sup>49</sup> The two body entropy for  $M$  species can be written as

$$\frac{S_2}{k_B} = -2\pi\rho \sum_{u,v=1}^M \chi_u \chi_v \int_0^\infty \{g_{uv}(r) \ln g_{uv}(r) - g_{uv}(r) + 1\} r^2 dr, \quad (4)$$

where  $\chi_u$  is the fraction of particles in  $u$  species and  $g_{uv}(r)$  is the partial radial distribution function of species  $u$  and  $v$ , and it is expressed as<sup>5</sup>  $g_{uv}(r) = \frac{V}{N_u N_v} \left( \sum_{i=1}^{N_u} \sum_{j=1, j \neq i}^{N_v} \delta(r - r_i + r_j) \right)$ .

The temperature dependence of  $S_2$  changes with  $M$ , and this also changes the  $T_{cross}$  value (shown in Appendix A). As shown in Fig. 1, as a function of the number of species  $M$ ,  $T_{cross}$  first increases and then almost saturates at a certain value. This saturation value is similar to the onset temperature obtained from other methods.<sup>49,60,61</sup> The saturation of  $T_{cross}$  implies that the structure/rdf does not change considerably when an even larger number of species is used to describe the system. Therefore, this provides us with information on the optimum number of species,  $M = M_0$ , required to describe the system.

Interestingly, our formalism is similar in spirit to the formalism suggested recently using mutual information (MI) theory; the difference in two body entropy when the system is expressed as a single species and as  $M$  species can be approximately written as<sup>17</sup>

$$\Delta S_2 \simeq \sum_{k=1}^M \int_0^R 4\pi r^2 \rho \chi_k g_k(r) \ln \left( \frac{g_k(r)}{g(r)} \right) dr, \quad (5)$$

where  $g_k(r)$  is the rdf of the  $k$ th species and the total rdf  $g(r) = \sum_k \chi_k g_k(r)$ . Coslovich *et al.* beautifully argued that this difference in two body entropy is similar to the MI.<sup>17</sup> From Eq. (5), we notice that in this formalism, the probability distribution in the MI is replaced by the radial distribution function, which is the probability of finding a particle at a distance  $r$  from a central particle

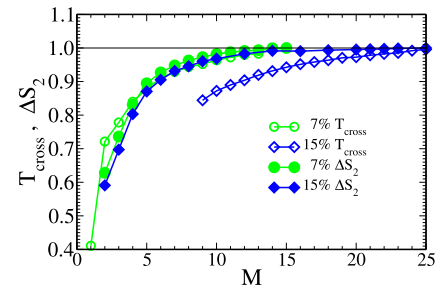


FIG. 1. Scaled MI of  $\Delta S_2$  and  $T_{cross}$ <sup>49</sup> saturated at same  $M$ . Scaling is performed by dividing the  $\Delta S_2$  and  $T_{cross}$  value by their respective saturation values at high  $M$ .

over and above the ideal gas prediction. Therefore, this formalism, instead of using the bare probability of finding a particle, is based on the probability of finding particles at certain interparticle distances.

In Fig. 1, along with  $T_{cross}$ , we also plot  $\Delta S_2$  as a function of  $M$  for systems with 7% and 15% polydispersities. Both quantities are scaled by their respective saturation values at high  $M$ . We find that both show similar  $M$  dependence. Ideally, the peak in the  $\Delta S_2$  vs  $M$  plot should describe the optimum value of  $M$ . However, there is no such peak, but just like  $T_{cross}$ , the  $\Delta S_2$  value increases sharply with  $M$  and then shows saturation. Note that MI is large when the distribution between two species is well segregated. However, the rdf of two consecutive species overlaps. This may be the reason the entropy difference does not show a peak. Results shown in Fig. 1 clearly suggest that for these systems, the structure and any quantity that needs structure as an input must be described by dividing the particles into a certain optimum number of species, and this division is going to increase the MI.

### IV. COMPUTING LOCAL CAGING POTENTIAL

In a recent study, we described a structural parameter that describes the local caging potential.<sup>8,20</sup> We have also shown that for the KA model, the softness of this potential and the short-time dynamics are causal.<sup>20</sup> The computation of the local caging potential requires information on the radial distribution function. As discussed in Sec. III, the radial distribution function of a system with continuous polydispersity depends on the number of species we divide the particles of the system into. Extending our earlier work, the average depth of the mean-field caging potential for a system with  $M$  species can be written as<sup>20</sup>

$$\beta\Phi_r^{av}(\Delta r = 0) = -\rho \int dr \sum_{u=1}^M \sum_{v=1}^M C_{uv}(r) \chi_u \chi_v g_{uv}(r), \quad (6)$$

where  $\beta = \frac{1}{k_B T}$ ,  $k_B = 1$ ,  $\rho$  is a density, and  $r$  denotes the distance between the central tagged particle and its neighbors.  $\Delta r$  is the distance of the tagged particle from its equilibrium position.  $C_{uv}(r)$  is the direct correlation function and, according to the Hypernetted chain (HNC) approximation, can be written as<sup>5</sup>

$$C_{uv}(r) = -\beta U_{uv}(r) + [g_{uv}(r) - 1] - \ln [g_{uv}(r)], \quad (7)$$

where  $U_{uv}$  is the interaction potential. It was shown that the depth of the potential is inversely proportional to the curvature and, therefore, the softness parameter.<sup>8,20</sup> Please note that we consider the depth of the caging potential as an energy barrier and, thus, work with the absolute magnitude of the caging potential [given by Eq. (6)].

For the microscopic analysis, we need to calculate  $\beta\Phi_r(\Delta r = 0)$  for every snapshot at a single particle level. This is given by Eq. (6), where the rdf and the direct correlation function are now obtained at the single particle level. The single particle partial rdf in a single frame can be expressed as a sum of Gaussian, and it is calculated as<sup>62</sup>

$$g_{uv}^i(r) = \frac{1}{4\pi r^2} \sum_j \frac{1}{\sqrt{2\pi\delta^2}} \exp\left[-\frac{(r-r_{ij})^2}{2\delta^2}\right], \quad (8)$$

where  $\delta$  is the variance of the Gaussian distribution used to make the discontinuous function a continuous one. In this work, we assume  $\delta = 0.09\langle\sigma\rangle$ . The direct correlation function can also be calculated at the single particle level using Eq. (7) but with single particle rdf. At higher Polydispersity index (PDI), when the system is described by one species, the rdf shows a large softening and is non-zero at very small values of “ $r$ ” compared to the interaction potential. Therefore, any function that calculates the product of the potential and rdf incurs a large error.<sup>49</sup> This error is higher for repulsive potential and increases with PDI (as shown in Appendix B). In our calculation of the potential depth, such products lead to unphysically large positive values of the caging potential. This implies an unstable potential and a negative curvature/softness parameter. Note that this is an artificial effect. To overcome this problem, we have made one approximation. We assume that the potential of mean force is the same as the interaction potential, i.e.,  $-\beta U_{uv}(r) = \ln[g_{uv}(r)]$  and  $C_{uv}^{approx}(r) \approx [g_{uv}(r) - 1]$ . For smaller polydispersity, where the error due to softening of the rdf is less and we can compute physically meaningful caging potential by assuming all three terms in the direct correlation function, we have compared our theoretical prediction with total and approximate direct correlation functions. As discussed in Appendix B, although the absolute value of the caging potential is different, the prediction of the correlation of the dynamics and softness parameters remains the same. Therefore, in this work, we use the approximate direct correlation function  $C^{approx}(r)$  at the single particle level to avoid the unphysical results of the caging potential at higher PDI.

The inverse of the depth of the caging potential is related to the softness, but they are not the same.<sup>20</sup> There are some system dependent but temperature independent constants that are needed for the calculation of the absolute value of softness but not its correlation with dynamics.<sup>63</sup> In this work, we will seamlessly use the terms “inverse” of the depth of the caging potential and “softness” of the caging potential, as they are qualitatively the same.

## V. SPECIES DEPENDENCE OF THE CAGING POTENTIAL

First, we assume the systems to be monodisperse, i.e.,  $M = 1$ , and obtain the per-particle depth of the caging potential from the microscopic version of Eq. (6). As shown in Fig. 2, for all the systems, with a decrease in temperature, there is a shift of the probability distribution of  $\beta\Phi_r(\Delta r = 0)$  to higher values. This implies that, as

expected, the cage structure is more well-defined at lower temperatures and the particles sit at a deeper potential minimum. In Fig. 2, we also plot the probability distribution of  $\beta\Phi_r(\Delta r = 0)$  as a function of  $M$ . We find that for all the systems with an increase in  $M$ , the probability distribution of  $\beta\Phi_r(\Delta r = 0)$  moves to higher values of  $\beta\Phi_r(\Delta r = 0)$ . This shift is concurrent with the fact that when a polydisperse system is treated as a monodisperse system, the RDF shows artificial softening.<sup>49</sup> However, when the polydisperse system is divided into an  $M$  number of species, the inter- and intra-species RDFs become sharper than the RDF obtained assuming a single species. Therefore, the cage is better defined by the multispecies system. This gives rise to an increase in the depth of the minima. This increase in the depth of the caging potential with an increase in  $M$  is similar to the decrease in the two-body pair entropy obtained in our earlier study.<sup>49</sup> Furthermore, to understand if this shift in the distribution of the caging potential with  $M$  is just an increase in the depth of the particle level caging potential affecting all particles equally, in Fig. 3, as a representative plot, we show a scatter plot of the particle level caging potential obtained for  $M = 1$  and  $M = 4$ . This clearly shows that this shift in the distribution is not just a shift in the value of the particle level caging potential and affects each particle differently. As expected, the  $M$  dependence is more at a higher PDI.

## VI. SPECIES DEPENDENCE OF THE CORRELATION OF CAGING POTENTIAL WITH PARTICLE DYNAMICS

In Sec. V, we have shown that the distribution of the local caging potential varies with  $M$ . Suppose this variation was just a shift in the value of the caging potential of each particle. In that case, we do not expect the correlation between the caging potential and the dynamics to be affected by  $M$ . However, as shown, that is not the case. Therefore, in this section, we study the correlation between the dynamics and the structure obtained via the local caging potential as a function of  $M$ . To understand the correlation between the dynamics and the structure, we follow the methodology used in earlier works.<sup>13,20</sup> We identify fast particles using a well-documented method<sup>20,64,65</sup> also given in Appendix C. After identifying the fast particles, we correlate them with the local SOP. We calculate the fraction of particles having a specific value of  $1/\beta\Phi_r$  that undergo rearrangement,  $P_R(1/\beta\Phi_r)$ , and plot it as a function of  $1/\beta\Phi_r$  at different  $T$  and  $M$  values. The plots for the system with 15% PDI, where the effect is maximal, are shown here in Fig. 4. The results are similar for other systems. We find that  $P_R(1/\beta\Phi_r)$  has a dependence on the SOP that becomes stronger at lower temperatures. At lower temperatures, particles with a higher value of softness (sitting in a shallow caging potential) have a higher probability of moving. Apparently, the behavior appears to be  $M$  independent. Following our earlier work, we plot the  $P_R(1/\beta\Phi_r)$  as a function of temperature for different  $1/\beta\Phi_r$  values. We find that for all the cases, it can be expressed in an Arrhenius form:  $P_R(1/\beta\Phi_r) = P_0(1/\beta\Phi_r) \exp[\Delta E(1/\beta\Phi_r)/T]$ , where  $\Delta E$  is the activation energy. These plots also appear to be similar for all  $M$  values. It was earlier shown that the temperature at which these  $P_R(1/\beta\Phi_r)$  vs  $T$  plots for different softness values intercept marks the onset temperature of glassy dynamics.<sup>13,20</sup> The origin of this observation was explained by the microscopic mean field theory.<sup>8,20</sup> According to the theory, we can correlate softness and dynamics only when the cage around the particles is well-defined. It



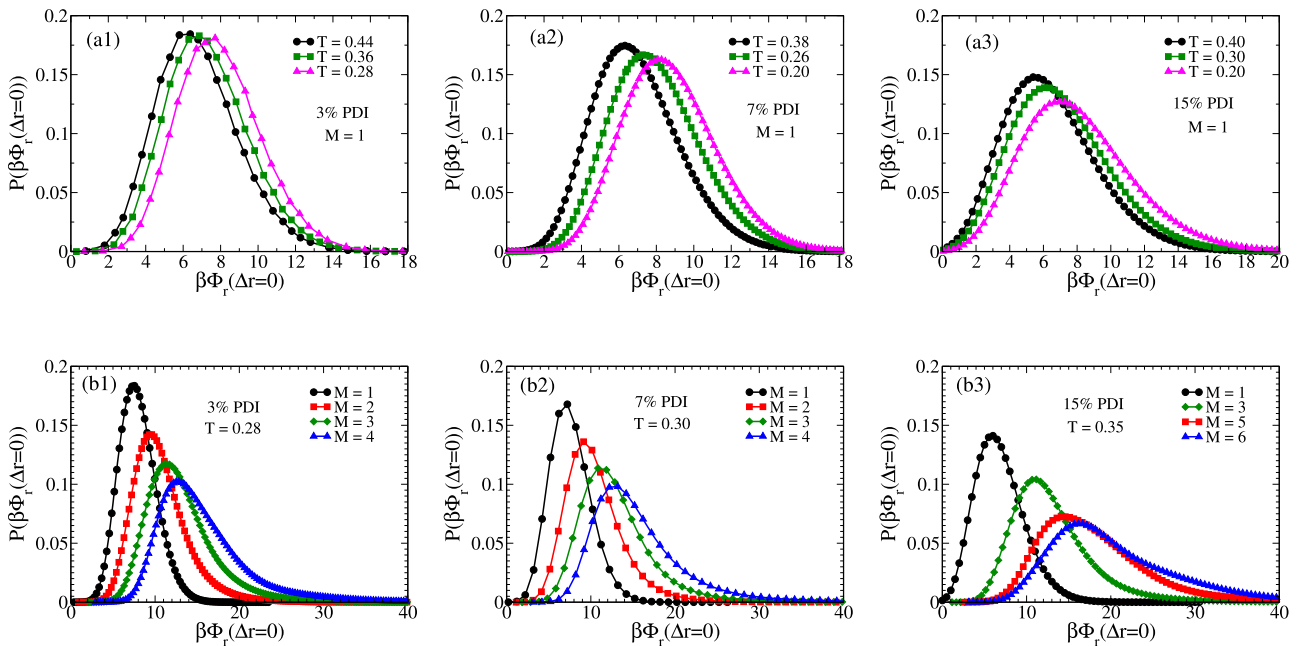


**FIG. 2.** Distribution of caging potential. Top panel: Different temperatures for a fixed  $M = 1$ . Bottom panel: Different  $M$  values. (a1) and (b1): 3% PDI and  $T = 0.28$ ; (a2) and (b2): 7% PDI and  $T = 0.30$ ; (a3) and (b3): 15% PDI and  $T = 0.35$ . As expected, the caging potential increases with decreasing  $T$ . The caging potential also increases with increasing  $M$ . The temperatures are chosen such that the relaxation times are similar for all the systems.

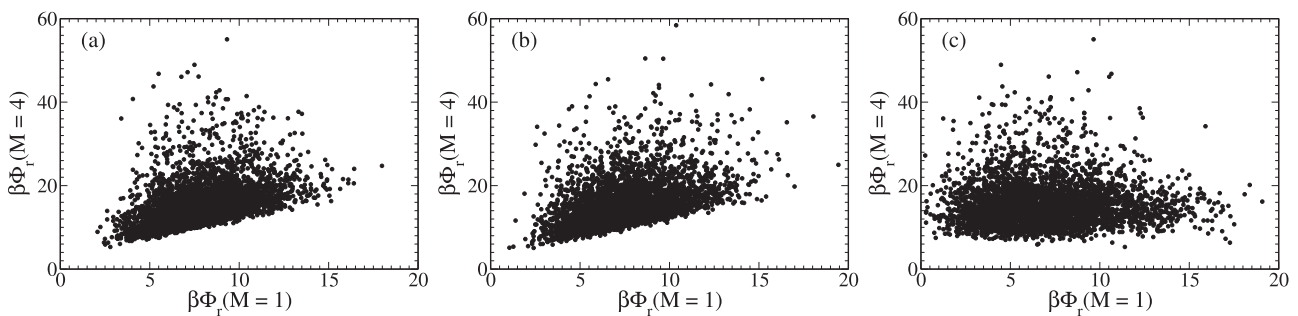


**FIG. 3.** Scatter plot between  $\beta\Phi_r$  at  $M = 1$  and  $M = 4$  at different PDIs: (a) 3% PDI at  $T = 0.28$ ; (b) 7% PDI at  $T = 0.30$ ; (c) 15% PDI at  $T = 0.35$ . The temperatures are chosen such that the relaxation times are similar for all the systems. It clearly shows that the rank of the structural order parameter of a particle changes with  $M$ . The effect increases with PDI.

is well known in the supercooled liquid literature that only below the onset temperature, where there is a separation between the short and long time dynamics, the particles in the short time feel caged by their neighbors, and this cage becomes longer lived at lower temperatures. Therefore, the crossing of the plots marks the highest temperature where this theory is valid, and beyond that, due to the absence of any well-defined cage, the theoretical formulation breaks down. In addition, at lower temperatures, where the lifetime of the cage increases, the structure becomes a better predictor of the dynamics. We extract the onset predicted by the crossing of the  $P_R(1/\beta\Phi_r)$  vs  $T$  plots. They are plotted in Fig. 5. It clearly shows that the  $T_{onset}$  values have a  $M$  dependence. The value of  $M$ , where it saturates, increases with

the percentage of polydispersity. The saturation temperature is similar to the onset temperature obtained using other methods.<sup>49</sup> This result is similar in spirit to that obtained in our earlier work using two-body excess entropy.<sup>49</sup>

## VII. ANALYSIS OF DYNAMICS OF SOFT AND HARD PARTICLES

Since we have established that, on average, the particles with higher softness have a higher probability of moving, we can expect that if we compare the dynamics (via the overlap function) of a few of the hardest and softest particles, then at short times they will

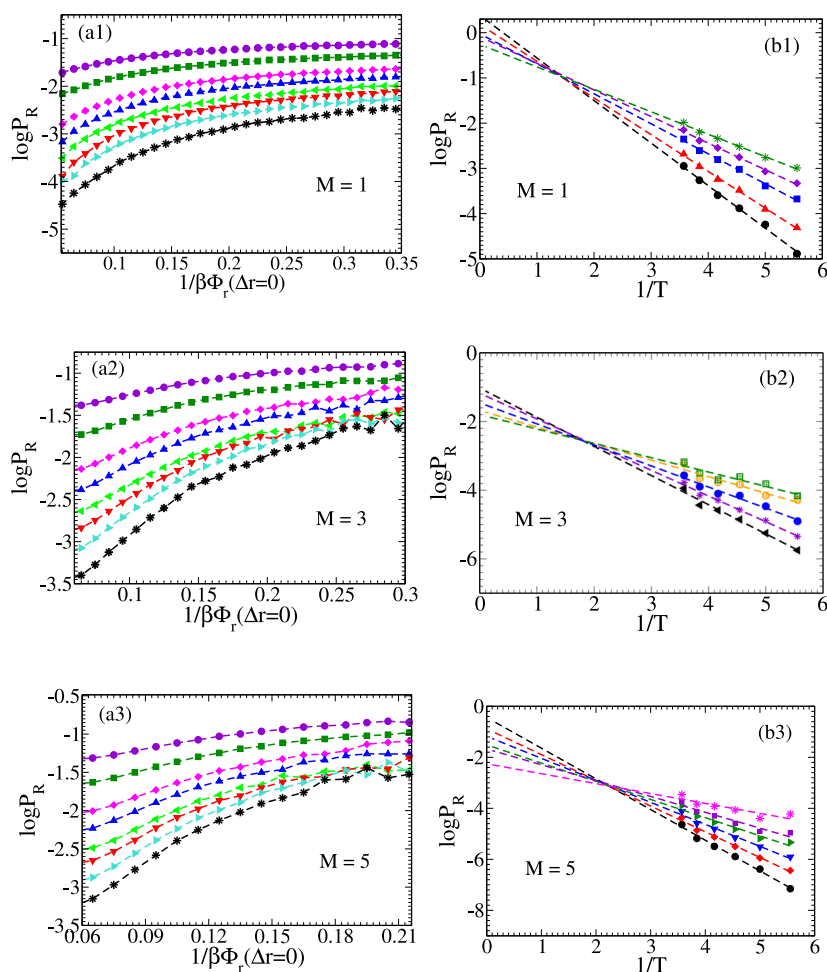


**FIG. 4.** Correlation between structure and dynamics as a function of  $M$ . Left panel: (a1)–(a3) The fraction of particles that underwent rearrangement  $P_R(1/\beta\Phi_r)$  vs the depth of the caging potential,  $1/\beta\Phi_r$ , at different  $T$  [0.4 (violet circle) - 0.2 (black star)]. Right panel: (b1)–(b3)  $P_R(1/\beta\Phi_r)$  as a function of  $1/T$  at different values of the inverse of the caging potential. The results are for a 15% PDI.

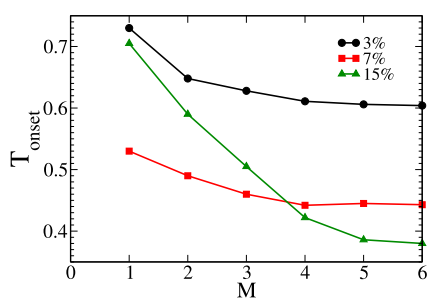


**FIG. 5.** (a)  $T_{onset}$  obtained from the crossing of  $P_R(1/\beta\Phi_r)$  vs  $1/T$  plots (Fig. 4) as a function of  $M$ . The  $T_{onset}$  initially decreases with  $M$  before saturating at higher values of  $M$ . With an increase in polydispersity, the saturation increases to higher  $M$  values.

show a large difference, and eventually due to the evolution of the cage and its softness around the particle, they will decay at the same

time.<sup>20</sup> The dynamics of particles via the overlap function  $[q(t)]$  can be calculated as

$$q(t) = \frac{1}{N} \sum_{i=1}^N \omega(|r_i(t) - r_i(0)|), \quad (9)$$

where function  $\omega(x) = 1$  when  $0 \leq x \leq a$  and  $\omega(x) = 0$  otherwise. The cutoff of the overlap parameter  $a = 0.5$  is chosen such that particle positions separated due to small amplitude vibrational motion are treated as the same.<sup>66</sup> Here, we restrict our study to one temperature for each system. For the 3% PDI system, we choose  $T = 0.28$ , the lowest temperature at which we can run the system before it undergoes crystallization. For the other two systems, we study them at temperatures where the relaxation times are similar to those of the 3% PDI system at  $T = 0.28$ . We pick a few (around 2) of the hardest and softest particles, and the softness parameter is calculated for the same system at different values of  $M$  (Fig. 6).

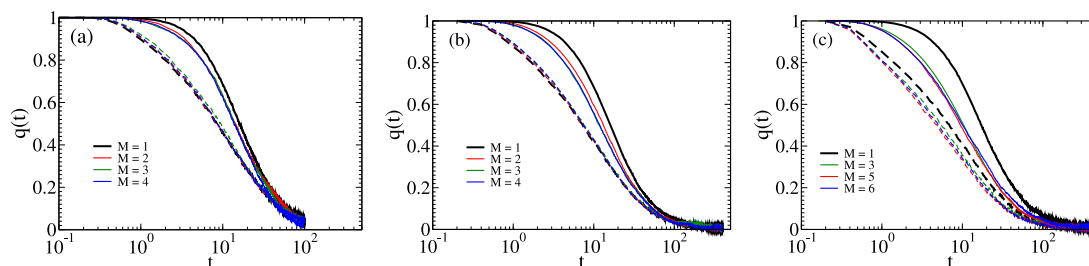


**FIG. 6.** Dynamics of a few softest (high  $1/\beta\Phi_r$  value) (dotted line) and few hardest (low  $1/\beta\Phi_r$  value) (solid line) particles at different  $M$  values. (a) 3% PDI ( $T = 0.28$ ), (b) 7% PDI ( $T = 0.30$ ), and (c) 15% PDI ( $T = 0.35$ ).  $T$  is chosen such that the relaxation times of each system are in the same range. The dark lines are for  $M = 1$ , and with an increase in  $M$ , the plots shift.

We find that the difference in the overlap of the few hardest and softest particles changes with  $M$ . However, beyond a certain value of  $M$ , the overlap functions of the hardest and the softest particles do not change with  $M$ . This suggests that beyond this  $M$  value, the identification of the hardest and softest particles becomes independent of  $M$ . We consider this the optimum value of the species,  $M_0$ , needed to describe the system. For 3% PDI,  $M_0 = 3$ , for 7% PDI,  $M_0 = 4$ , and for 15% PDI,  $M_0 = 6$ . Note that the  $T_{onset}$  values for different PDIs (Fig. 5) also show saturation at similar values of  $M$ . Therefore, the results are consistent. The results obtained also agree with our previous study, where we showed that parameters that need structural input are better determined when the system is described in terms of multiple species,<sup>49</sup> and the optimum number of species increases with polydispersity. Therefore, we can say that the structural order parameter of a system should be calculated by describing the system

in terms of  $M_0$  species. This structural order parameter will provide a true description of the local caging potential and will correlate with the dynamics.

However, although the structure of a system is not well described for  $M = 1$ , the difference in dynamics between the hardest and softest particles is best determined when we treat the system as monodisperse. This is a contradictory result, and it appears that in these systems, apart from the structure, there can be other parameters that drive the dynamic heterogeneity. To understand the result, in Fig. 7, we plot the distribution of the particle diameters of the hardest and the softest particles for different values of  $M$  for all three systems. We also plot the particle size distribution of the whole system,  $P(\sigma)$ . When  $M = 1$ , we find that the distribution of the hardest and softest particles is skewed toward the bigger and smaller-sized particles, respectively. This effect is more prominent

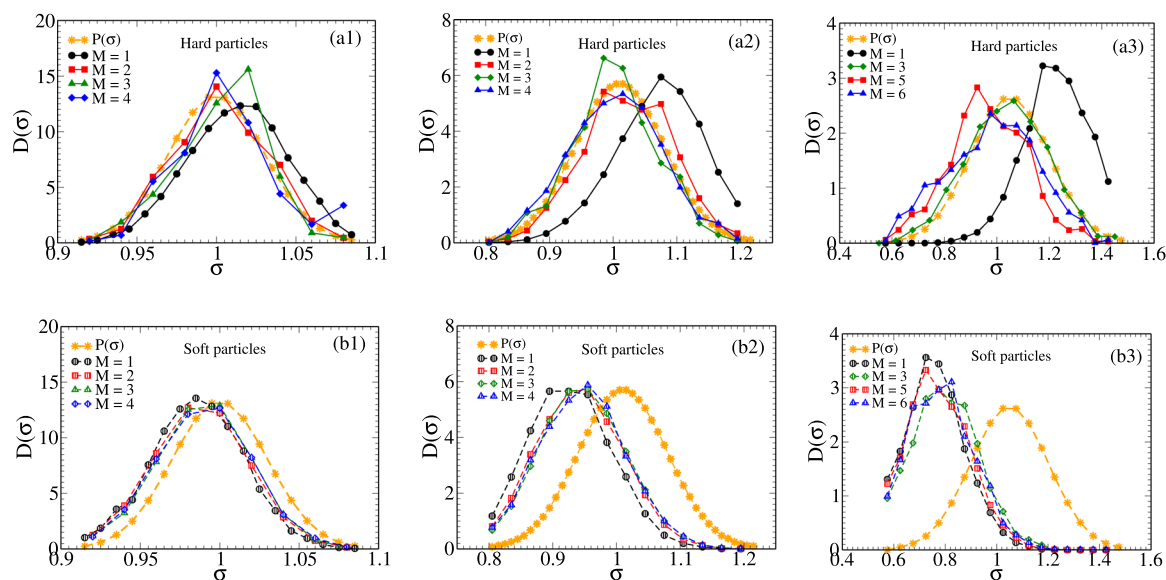


**FIG. 7.** Particle size distribution,  $D(\sigma)$ , of the hardest and softest particles as a function of  $M$  (as defined in Fig. 6). Top panel: (a1)–(a3) Size distribution of all hard particles. Bottom panel: (b1)–(b3) Size distribution of all soft particles. (a1) and (b1) are for 3% PDI, (a2) and (b2) are for 7% PDI, and (a3) and (b3) are for 15% PDI. For comparison, we also plot the size distribution of all the particles,  $P(\sigma)$ .



at higher polydispersity. With an increase in  $M$ , the distribution of the hardest particles moves toward  $P(\sigma)$ . This clearly shows that as we divide particles into species, the cage around smaller particles, which, for  $M = 1$ , is loosely defined, gets better defined at higher  $M$ . This leads to an increase in the depth of the caging potential and, thus, a decrease in the softness of the potential. The distribution of the diameter of the softer particles also shows some change with  $M$ , but differently from the hard particles, it always remains skewed toward smaller particles, which is similar to that observed for granular systems.<sup>67</sup> This implies that the cage around the bigger particles is mostly well-defined, and this effect is again more pronounced at higher polydispersity.

Notice that the shift in the size distribution of the hardest/softest particles (Fig. 7) with  $M$  is also accompanied by a shift in the overlap function of the hardest/softest particles with  $M$  (Fig. 6), suggesting that these shifts are correlated. In both cases (particle size distribution and overlap), the shift is more for the harder particles and also increases with polydispersity. This implies that size also plays a role in the dynamics. In Fig. 8, we plot the dynamics of the two biggest and two smallest particles and compare them with the two hardest and softest particles for  $M = 1$ . We find that for the 3% PDI, the difference in dynamics of the biggest and smallest particles is less than that of the softest and hardest particles. This implies that the heterogeneity in the dynamics is primarily determined by the local structural heterogeneity. With an increase in polydispersity, the scenario reverses. For the 15% PDI system, the difference in dynamics is better described by the size than the local structural order parameter. We know from our earlier study<sup>20</sup> that

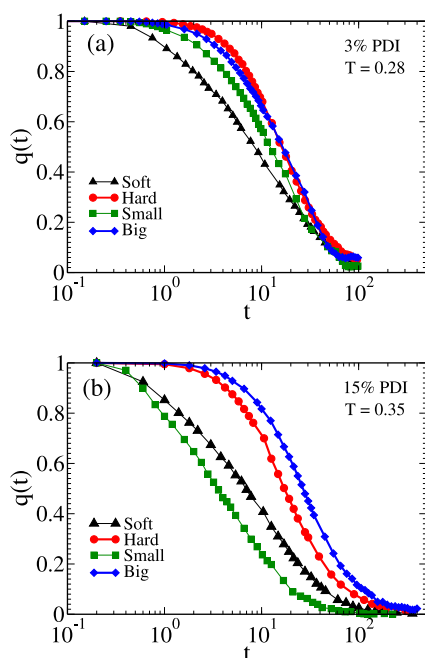


**FIG. 8.** Overlap function of 2 hardest particles (red circle), 2 softest particles (black triangle), 2 biggest particles in size (blue diamond), and 2 smallest particles in size (green square) at different PDIs. The structural order parameter is calculated for  $M = 1$ . (a) 3% PDI and (b) 15% PDI.

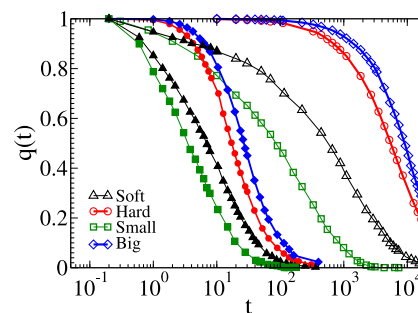


**FIG. 9.** Overlap function for 15% PDI at  $T = 0.35$  (closed symbol) and  $T = 0.22$  (open symbol). Color codes are similar, like in Fig. 8

at lower temperatures, the structure becomes a better predictor of the dynamics. To understand the role of temperature, we choose the 15% PDI system, where size appears to be dominant, and plot the different overlap functions at two different temperatures (Fig. 9). We find that at lower temperatures, although the structure becomes a better predictor of the dynamics, the size still plays a dominant role in determining the dynamics.

## VIII. COMPARATIVE STUDY OF THE ROLE OF PARTICLE SIZE AND LOCAL STRUCTURE ON THE DYNAMICS

The above-mentioned analysis suggests that for polydisperse systems, both size and local structure can play a role in the dynamics. To quantify the dependence of the dynamics on the structure and particle size, we perform isoconfigurational runs (IC). IC is a powerful technique introduced by Harrowell and co-workers to investigate the role of structure in the dynamical heterogeneity of the particles.<sup>12,68–70</sup> Among other factors, a particle's displacement can depend on its structure and its initial momenta. This technique was proposed to remove the uninteresting variation in the particle displacements arising from the choice of initial momenta and extract the role of the initial configuration on the dynamics and its heterogeneity. For each system, five different isoconfigurational runs are carried out for 4000 particles. To ensure that all configurations are different, the configurations are chosen such that the two sets are greater than  $100\tau_\alpha$  apart. We run 100 trajectories for each configuration with different starting velocities randomly assigned from the Maxwell–Boltzmann distribution for the corresponding temperatures. Mobility,  $\mu$  is the average displacement of each particle over these 100 runs and is calculated as  $\mu^j(t) = \frac{1}{N_{IC}} \sum_{i=1}^{N_{IC}} \sqrt{(r_i^j(t) - r_i^j(0))^2}$ . Here,  $\mu^j(t)$  is the mobility of the  $j$ th particle at time  $t$ , and  $N_{IC}$  is the number of trajectories. We calculate the Spearman rank correlation ( $C_R$ ) between different parameters as a function of time (scaled by the  $\alpha$  relaxation time  $\tau_\alpha$ ). We plot  $C_R(\mu, 1/\beta\Phi_r)$  against time for  $M = 1$  and  $M = M_0$ . We find that  $C_R(\mu, 1/\beta\Phi_r)$  decreases with an increase in  $M$ . This result is similar in spirit to that observed for the difference in the overlap functions of the hardest and softest particles (Fig. 6). In Fig. 10, we also plot  $C_R(\mu, \sigma)$ . We find that for all systems, it grows at longer times, and for systems with higher polydispersity, the correlation

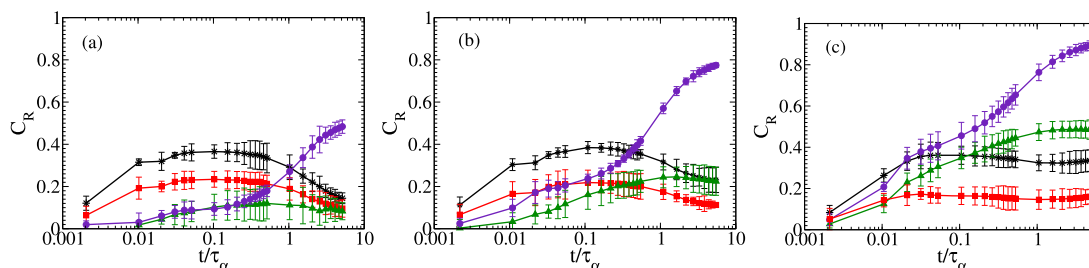


**FIG. 10.** Spearman rank correlation  $C_R$  between mobility and different order parameters at different PDIs: (a) 3% PDI; (b) 7% PDI; and (c) 15% PDI. Color code:  $C_R(\mu, 1/\beta\Phi_r)$   $M = 1$  (black star),  $M = M_0$  (red square),  $C_R(\mu, \Psi)$  (green triangle), and  $C_R(\mu, \sigma)$  (violet circle).  $M_0 = 3, 4,$  and  $6$  for 3%, 7%, and 15% PDI, respectively.

is large, even at shorter times. This supports our earlier conclusion that at higher PDI, the size of the particles plays a greater role in describing the dynamic heterogeneity.

Note that apart from the softness parameter described in this work, other parameters are often used to describe the local static property of a supercooled liquid.<sup>16</sup> We check if size plays any role in an order parameter that does not include the radial distribution function. Earlier studies have shown that Vibrality, the local Debye–Waller Factor,<sup>12,14,16</sup> is a good predictor of dynamics. The analysis is performed on the inherent structure. The Fast Inertial Relaxation Engine (FIRE) algorithm is employed to obtain the inherent structures (IS).<sup>71</sup> Vibrality is written as  $\Psi(i) = \sum_{k=1}^{3N-3} \frac{|\mathbf{v}_k^i|^2}{\omega_k^2}$ , where the sum runs over the entire set of eigenmodes with frequency  $\omega_k$ .  $\mathbf{v}_k^i$  is a vector that has the three components of the eigenvector  $\vec{v}_k$  associated with the  $i$ th particle.  $\Psi(i)$  is the mean square vibrational amplitude of the  $i$ th particle, assuming the vibrational energy is equally distributed to all modes. In Fig. 10, we plot  $C_R(\mu, \Psi)$  and find that it increases with polydispersity, which is similar to  $C_R(\mu, \sigma)$ . It appears that  $C_R(\mu, \sigma)$  affects  $C_R(\mu, \Psi)$  more compared to  $C_R(\mu, 1/\beta\Phi_r)$ .

To quantify the above-mentioned observations, we now use multiple linear regressions to model mobility in terms of  $\Phi$  and  $\sigma$ . To evaluate the predictive power of the model, we use the standard 5-fold cross-validation approach, where the data are randomly split into five equal sets, and a model built on four parts is used to predict mobility on the held-out test set. This is performed five times, with each data point tested exactly once. The mean relative error,  $MRE = \frac{1}{N} \sum_{j=1}^N \frac{|\mu_p^j - \mu_t^j|}{\mu_t^j}$ , and the root mean square deviation,  $RMSD = \sqrt{\frac{1}{N} \sum_{j=1}^N (\mu_p^j - \mu_t^j)^2}$ , are shown along with the error bar computed from the five test sets. Here,  $\mu_p^j$  and  $\mu_t^j$  are the predicted mobility and true mobility of the  $j$ th particle, respectively. The mobility used here is calculated at  $t = 5$ , but the results are independent of  $t$ .

We compare results with simple linear regression, also evaluated in the same manner but using only one of the parameters, i.e., either  $\Phi$  or  $\sigma$ . From the analysis of the errors plotted in Fig. 11, we find that for lower PDI, the caging potential is a good parameter to describe mobility. However, with an increase in PDI, size becomes the dominant variable in prediction. We also do a similar analysis

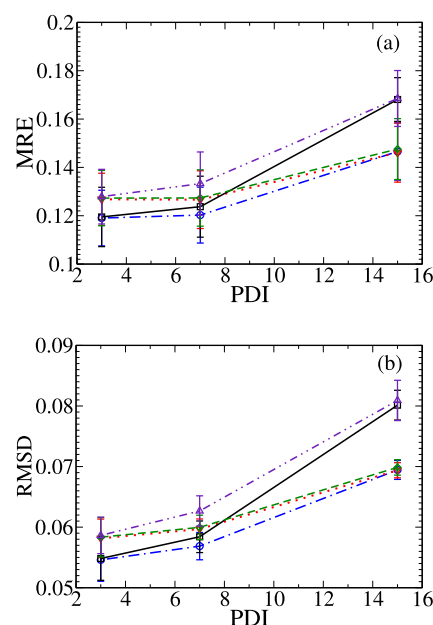


**FIG. 11.** Error between predicted and true values of mobility  $\mu$ . (a) Mean relative error,  $MRE = \frac{1}{N} \sum_{j=1}^N \frac{|\mu_p^j - \mu_t^j|}{\mu_t^j}$ , and (b) root mean square deviation,  $RMSD = \sqrt{\frac{1}{N} \sum_{j=1}^N (\mu_p^j - \mu_t^j)^2}$ . Color code: Independent variables are  $\Phi_r$  and  $\sigma$  (blue, dashed-dotted line), independent variable is  $\Phi$ , (black, solid line), independent variable is  $\sigma$  (green, dashed line), independent variables are  $\Psi$  and  $\sigma$  (red, dotted line), and independent variable is  $\Psi$  (indigo, dashed-double dot line).

using  $\Psi$  and  $\sigma$  and find that between this pair, size always plays a dominant role for all systems. For smaller PDIs where size does not play a strong role, it appears that among the three variables, SOP is the best predictor of the dynamics.

Note that in the above-mentioned analysis, although we have treated  $\Phi$  and  $\Psi$  as independent variables, both have some dependence on size. The dependence of  $\Phi$  on size can be seen in Fig. 7, where we find that soft particles are primarily small and hard par-

**TABLE I.** Spearman rank correlation,  $C_R$  between particle size,  $\sigma$  and local caging potential,  $\beta\Phi_r$  when the system is assumed to be monodisperse,  $M = 1$ , and when the system is described in terms of the optimum number of species,  $M_0$ . We also report the Spearman correlation between  $\sigma$  and Vibrality,  $\Psi$ . The systems are polydisperse with a polydispersity index of 3% at  $T = 0.28$ , 7% at  $T = 0.30$ , and 15% at  $T = 0.35$ .

PDI (%)	$C_R(\sigma, \beta\Phi_r)$ $M = 1$	$C_R(\sigma, \beta\Phi_r)$ $M = M_0$	$C_R(\sigma, \Psi)$
3	0.139	0.082	-0.111
7	0.293	0.129	-0.253
15	0.464	0.195	-0.516

ticles are primarily big in size. The figure also suggests that this dependence increases with PDI and decreases as we increase  $M$ . Note that in the figure, we have taken only the hardest and softest particles. To quantify this observation for all particles, in Table I, we report the Spearman rank correlations between the different parameters, and the correlation values do support the inference drawn from Fig. 7. For all the systems, the correlation between the local structure and size is more for  $M = 1$ . Now since dynamics is also correlated with the size of the particles, the local structure appears to be better correlated with dynamics for  $M = 1$ . This effect increases with polydispersity. We also find that at higher polydispersity, compared to  $\Phi$ ,  $\Psi$  is more correlated with  $\sigma$ . Therefore, at higher polydispersity and longer times, the Vibrality appears to be a better predictor of the dynamics, as seen in Fig. 10. Therefore, for systems with a large PDI, any order parameter that is correlated with the size of the particles will appear to be a good predictor of the dynamics.

## IX. CONCLUSION

In a recent study, we proposed a new structural order parameter that strongly correlates with dynamics.<sup>20</sup> This SOP is the inverse of the depth of the local mean-field caging potential, described in terms of the local liquid structure. We further showed that this correlation between the SOP and dynamics is valid below the onset temperature of the glassy dynamics. Therefore, the validity of the theory can be used to determine the onset of glassy dynamics. Since polydisperse systems are good model systems to study supercooled liquid dynamics, in this work, we study the structural order parameter and its correlation with the dynamics of a few polydisperse systems. Note that this SOP needs information on the local structure. It is well known that describing the structure of a polydisperse system is tricky.<sup>49,52</sup> Treating the system as a monodisperse system leads to artificial softening of the structure. In an earlier study, we had shown that for a polydisperse system, the correct structural description is obtained only when the system is expressed in terms of multiple species,  $M$ .<sup>49</sup> Here, we first show that our earlier method also leads to an increase in mutual information, thus validating the method further.

We find that the distribution of the particle level SOP changes with  $M$ . We also find that this change does not affect all particles similarly. Therefore, if we rank particles in terms of the value of the order parameter, then the rank order changes and finally appears to saturate beyond a certain  $M$  value. We also find that the detection

of the onset temperature from the correlation of the SOP and the dynamics depends on  $M$ . The onset temperature first changes with  $M$ , and at higher values of  $M$ , it saturates. The saturation of the onset temperature and the rank of the particle order parameter allow us to estimate the optimum number of species needed to describe the system. Like in our earlier study,<sup>49</sup> the value of  $M_0$  increases with polydispersity.

However, the most surprising result is that although the structure is not well defined for  $M = 1$ , the correlation between the structure and dynamics is at its maximum when the system is assumed to be monodisperse. Furthermore, analysis using multiple linear regression shows that although at low polydispersity, the local SOP determines the dynamics, at higher polydispersity, the size of the particle plays a dominant role in the dynamics. We also find that for  $M = 1$ , the bigger particles are primarily well-caged, and the smaller particles appear loosely caged. Therefore, there is a high correlation between the local SOP and the size of the particles. However, with an increase in  $M$  and a better description of the structure, the cage is better defined, especially for smaller particles. This reduces the correlation between the SOP and the particle size. Since size plays a dominant role in determining the dynamics, this reduction in the correlation reduces the apparent predictive power of the SOP at higher  $M$  values. To test if order parameter-size correlation is present for other order parameters where the local structural information is not needed, we calculate the Vibrality, which is the local Debye-Waller factor, known to be a good predictor of the dynamics.<sup>14,16</sup> We first show that Vibrality also correlates with size, and this correlation increases sharply with an increase in polydispersity. At lower polydispersity, compared to Vibrality, the SOP is a better predictor of the dynamics. However, at higher polydispersity, the Vibrality performs marginally better. This increase in the predictive power of the Vibrality is due to its stronger coupling with the size of the particle.

Therefore, our study suggests that for a polydisperse system with a high PDI, any order parameter with a strong coupling with the particle size will appear to be a good predictor of the dynamics. However, this may not reflect the true predictive power of the order parameter. Therefore, for a polydisperse system with reasonably high polydispersity, the correlation between dynamics and any static order parameter must be interpreted cautiously, as size can play a role in this correlation and the results may not be generic.

In this paper, we have studied the structure-dynamics correlation at a single particle level, which is an acceptable practice.<sup>12,13,16,18,68</sup> However, the correlation between structure and dynamics is weak when we use single particle information.<sup>15,19,69,70,72</sup> On the other hand, the correlation improves when we consider the collective dynamical property over a certain region<sup>69,70,73</sup> or correlate the coarse grained structural property with longtime dynamics.<sup>15,17,19,72</sup> In a polydisperse system, this coarse graining of the SOP over a static length reduces the coupling between the order parameter and particle size. It can thus be a useful way to study the real correlation between the order parameter and the dynamics.

## ACKNOWLEDGMENTS

P.P. acknowledges the CSIR for the research fellowships. M.S. acknowledges SERB for funding. S.M.B. acknowledges SERB for the

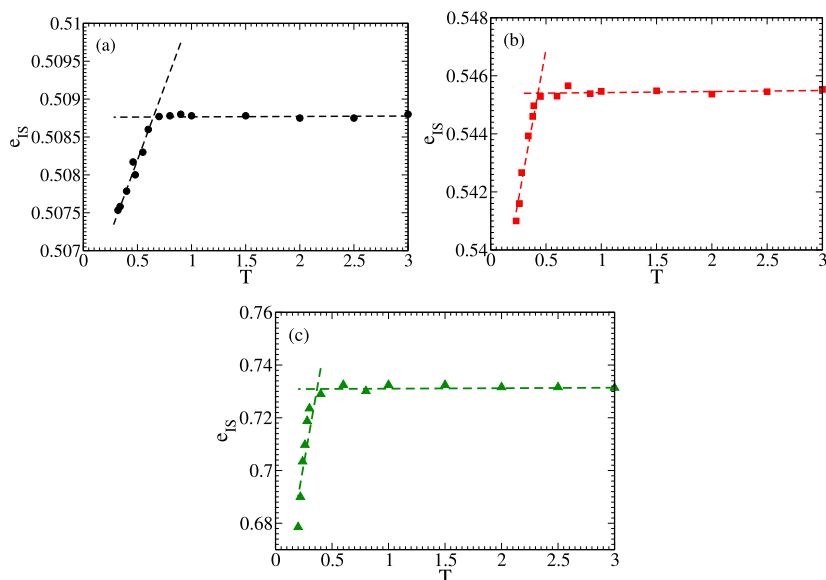


**FIG. 12.** Inherent structure energy ( $e_{IS}$ ) as a function of temperature. (a) 3% PDI; (b) 7% PDI; (c) 15% PDI. Near the onset temperature, the value of IS starts deviating from its high temperature value, thus allowing us to predict the onset.

funding, and S.M.B. acknowledges Chandan Dasgupta for the discussion. The authors would like to acknowledge Leelavati Narlikar for the helpful discussions.

#### AUTHOR DECLARATIONS

##### Conflict of Interest

The authors have no conflicts to disclose.

##### Author Contributions

**Palak Patel:** Data curation (equal); Formal analysis (equal); Methodology (equal); Software (lead); Validation (equal); Visualization (equal); Writing – original draft (equal); Writing – review & editing (equal). **Mohit Sharma:** Formal analysis (equal); Methodology (equal). **Sarika Maitra Bhattacharyya:** Conceptualization (lead); Formal analysis (equal); Funding acquisition (lead); Methodology (equal); Project administration (lead); Resources (lead); Supervision (lead); Validation (lead); Visualization (equal); Writing – original draft (lead); Writing – review & editing (lead).

##### DATA AVAILABILITY

The data that support the findings of this study are available from the corresponding author upon reasonable request.

#### APPENDIX A: DYNAMICS AND EXCESS ENTROPY

To elucidate the temperature range of the system, we first obtain the onset temperature of the glassy dynamics for the systems

by analyzing the temperature dependence of their inherent structures (IS)<sup>61</sup> (Fig. 12). The IS is obtained using the FIRE algorithm.<sup>71</sup> For PDI 3%, 7%, and 15%, the onset temperatures are 0.64, 0.43, and 0.37, respectively. We calculate the relaxation time  $\tau_\alpha$  by examining the overlap function [see Eq. (9)] decay to  $1/e = 0.367$ . The relaxation time vs temperature below the onset temperature is plotted in Fig. 13. The temperature dependence of the relaxation time is fitted to the well known Vogel–Fulcher–Tammann (VFT) equation,<sup>74</sup> and the resulting VFT temperatures for the different systems are as follows: 3% - 0.073, 7% - 0.117, and 15% - 0.154. However, as mentioned in the main text, the system with 3% PDI crystallizes at a reasonably high temperature (below  $T = 0.28$ ) compared to its VFT temperature.

Excess entropy,  $S_{ex}$ , is a loss of entropy due to the interaction between particles. Excess entropy is calculated via the temperature

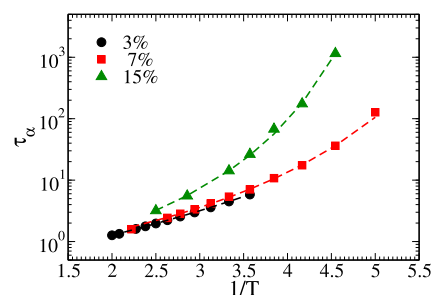


**FIG. 13.** The temperature dependence of the  $\alpha$  relaxation time at different PDIs. The dashed lines are the VFT fits.

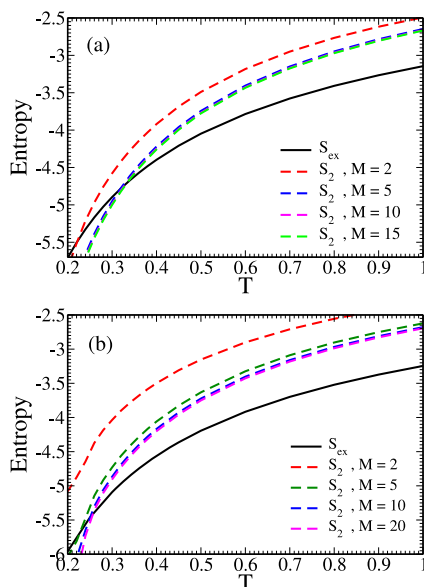


**FIG. 14.** Temperature dependence of  $S_2$  changes with  $M$ , and this also changes the  $T_{cross}$  values (a) 7% PDI and (b) 15% PDI.

integration (TI) method.<sup>56,75</sup> As discussed in the main text pair excess entropy,  $S_2$  takes into account the excess entropy due to the two-body correlation.  $S_2$  and  $S_{ex}$  cross each other at a temperature  $T_{cross}$ , which is similar to the onset temperature.<sup>60</sup> In Fig. 14, we plot the temperature dependence of  $S_{ex}$  and  $S_2$  for 7% and 15% PDI, where  $S_2$  is calculated at different values of  $M$ . Both  $S_2$  and  $T_{cross}$  change with  $M$ . Initially, they vary strongly, and then the variation is weaker with  $M$ .

#### APPENDIX B: CALCULATION OF LOCAL CAGING POTENTIAL USING $C_{uv}$ AND $C_{uv}^{approx}$

The potential energy depth calculation using this direct correlation function is given in Eq. (6). The expression of  $C_{uv}(r)$

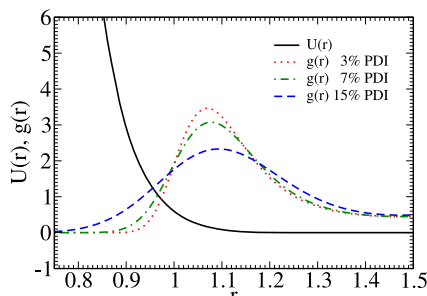


**FIG. 15.** Inverse power law potential,  $U$ , and radial distribution function,  $g(r)$ , for different PDIs at  $M = 1$ .

according to the Hypernetted chain (HNC) approximation<sup>5</sup> is given in Eq. (7). At higher PDI, when the system is described by one species, the rdf shows a large softening and is non-zero at very small values of “ $r$ ” compared to the interaction potential (as shown in Fig. 15). In experimental systems where the interaction potential is not known, it is often assumed that the potential of mean force is the same as the interaction potential, i.e.,  $-\beta U_{uv}(r) = \ln[g_{uv}(r)]$ . Under this assumption, the expression of the direct correlation function,  $C_{uv}^{approx}(r) \approx [g_{uv}(r) - 1]$ . Here, we present an analysis that shows that using  $C(r)$  and  $C^{approx}(r)$  primarily shifts the distribution of the potential energy depth but does not affect the correlation between the structural order parameter and the dynamics. In Fig. 16(a), we show a scatter plot of  $\beta\Phi(r)$  calculated using  $C_{uv}(r)$  vs that using  $C_{uv}^{approx}(r)$  and find that they are strongly correlated. Averaged over 1000 frames, the Spearman rank correlation between  $(C_{uv}, C_{uv}^{approx}) = 0.948$  and the Pearson correlation is 0.955. This confirms that the use of the approximate direct correlation function primarily shifts the distribution of  $\beta\Phi(r)$  as shown in Fig. 16(b). We also plot the distribution of the softness for the fast particles, and it shows that in both cases, more than 80% of the fast particles have a softness value higher than the average softness. In Fig. 16(c), we plot the onset temperature obtained when  $\beta\Phi(r)$  is calculated using  $C(r)$  and  $C^{approx}(r)$  (details of onset temperature calculation are given in Sec. VI), and interestingly, both results are identical. The dynamics of a of the few hardest and a few of the softest particles are plotted in Fig. 16(d). It clearly shows that using an approximate direct correlation function does not reduce the predictive power of the structural order parameter.

#### APPENDIX C: IDENTIFICATION OF FAST PARTICLES

There are many ways of identifying fast particles.<sup>11,64,65,76,77</sup> Here, we use the method proposed by Candelier *et al.*<sup>64,65</sup> In that method, for each particle in a certain time window  $W = [t_1, t_2]$ , they calculated the quantity  $p_{hop}(i, j)$ . When the average position of a particle changes rapidly, a cage jump happens. Expression for  $p_{hop}(i, j)$  is

$$p_{hop}(i, t) = \sqrt{\langle (r_i - \langle r_i \rangle_U)^2 \rangle_V \langle (r_i - \langle r_i \rangle_V)^2 \rangle_U}, \quad (10)$$

where  $\Delta t$  timescale over which the particles can rearrange,  $U = [t - \Delta t/2, t]$ , and  $V = [t, t + \Delta t/2]$ . For a time window  $W$ , a small value of  $p_{hop}$  means the particle is within the same cage, and a large  $p_{hop}$  means that within that time window, the particle has moved between two distinct cages. With the help of  $p_{hop}$ , fast particles are defined in this work. If  $p_{hop}$  is greater than  $p_c$ , then we identify that as a fast particle.<sup>18,20</sup>  $p_c$  is the value of the mean square displacement at time  $t_{max}$ , where  $t_{max}$  is the time at which the non-Gaussian parameter is at its maximum. Although we are working with a polydisperse system, we have kept the  $p_c$  value fixed for all particles. For more details, refer to Ref. 20.



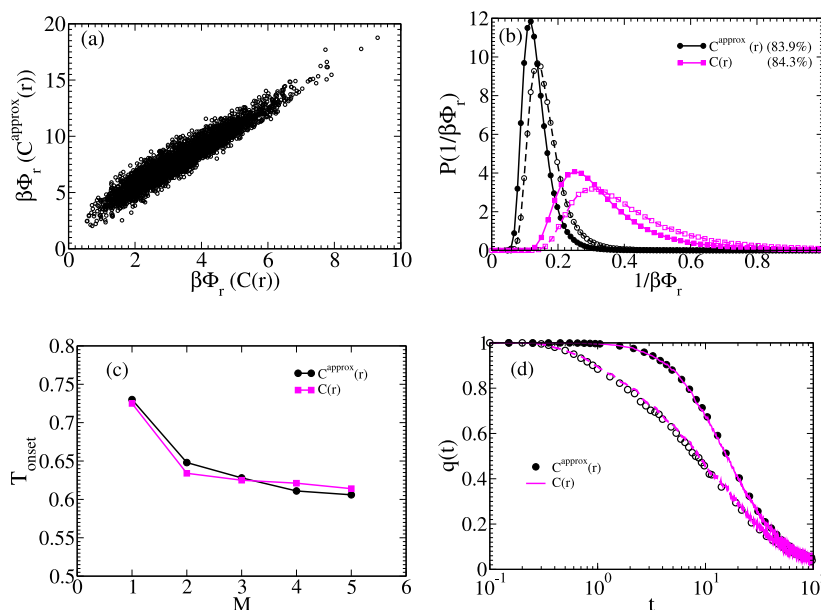


**FIG. 16.** Different parameters for justification of  $1/\beta\Phi_r$  can be calculated from  $C_{uv}(r)$  and  $C_{uv}^{approx}(r)$  both. This analysis is performed at 3% PDI. (a) Single frame scatter plot from  $C_{uv}(r)$  and  $C_{uv}^{approx}(r)$  at  $T=0.28$ . (b) Distribution of the inverse of  $\beta\Phi_r$  of all particles  $P(1/\beta\Phi_r)$  in the system (solid line with filled symbol) and of those which are about to rearrange (dotted line with open symbol) at  $T=0.28$ , from  $C(r)$  (black) and  $C^{approx}(r)$  (magenta). (c) Onset temperature obtained from  $C(r)$  (square) and  $C^{approx}(r)$  (circle). (d) Overlap function of few particles that has the highest (solid line [ $C(r)$ ] or closed symbol [ $C^{approx}(r)$ ]) and the lowest value of  $\beta\Phi(r)$  {dotted line [ $C(r)$ ] or open symbol [ $C^{approx}(r)$ ]} at  $T=0.28$ .

## REFERENCES

- <sup>1</sup> P. G. Debenedetti and F. H. Stillinger, *Nature* **410**, 259 (2001).
- <sup>2</sup> C. Angell, *J. Non-Cryst. Solids* **102**, 205 (1988).
- <sup>3</sup> W. Gotze and L. Sjogren, *Rep. Prog. Phys.* **55**, 241 (1992).
- <sup>4</sup> V. Lubchenko and P. G. Wolynes, *Annu. Rev. Phys. Chem.* **58**, 235 (2007).
- <sup>5</sup> J. P. Hansen and I. R. McDonald, *The Theory of Simple Liquids* 2nd ed. (Academic, London, 1986).
- <sup>6</sup> A. Banerjee, S. Sengupta, S. Sastry, and S. M. Bhattacharyya, *Phys. Rev. Lett.* **113**, 225701 (2014).
- <sup>7</sup> S. L. Glashow, D. Guadagnoli, and K. Lane, *Phys. Rev. Lett.* **114**, 091801 (2015).
- <sup>8</sup> M. K. Nandi and S. M. Bhattacharyya, *Phys. Rev. Lett.* **126**, 208001 (2021).
- <sup>9</sup> M. D. Ediger, *Annu. Rev. Phys. Chem.* **51**, 99 (2000).
- <sup>10</sup> M. M. Hurley and P. Harrowell, *Phys. Rev. E* **52**, 1694 (1995).
- <sup>11</sup> W. Kob, C. Donati, S. J. Plimpton, P. H. Poole, and S. C. Glotzer, *Phys. Rev. Lett.* **79**, 2827 (1997).
- <sup>12</sup> A. Widmer-Cooper, H. Perry, P. Harrowell, and D. R. Reichman, *Nat. Phys.* **4**, 711 (2008).
- <sup>13</sup> S. S. Schoenholz, E. D. Cubuk, D. M. Sussman, E. Kaxiras, and A. J. Liu, *Nat. Phys.* **12**, 469 (2016).
- <sup>14</sup> R. L. Jack, A. J. Dunleavy, and C. P. Royall, *Phys. Rev. Lett.* **113**, 095703 (2014).
- <sup>15</sup> H. Tong and H. Tanaka, *Phys. Rev. Lett.* **124**, 225501 (2020).
- <sup>16</sup> D. Richard *et al.*, *Phys. Rev. Mater.* **4**, 113609 (2020).
- <sup>17</sup> J. Paret, R. L. Jack, and D. Coslovich, *J. Chem. Phys.* **152**, 144502 (2020).
- <sup>18</sup> F. P. Landes, G. Biroli, O. Dauchot, A. J. Liu, and D. R. Reichman, *Phys. Rev. E* **101**, 010602 (2020).
- <sup>19</sup> T. Hua and T. Hajime, *Nat. Commun.* **10**, 5596 (2019).
- <sup>20</sup> M. Sharma, M. K. Nandi, and S. M. Bhattacharyya, *Phys. Rev. E* **105**, 044604 (2022).
- <sup>21</sup> T. S. Ingebrigtsen and H. Tanaka, *J. Phys. Chem. B* **119**, 11052 (2015).
- <sup>22</sup> P. G. Bolhuis and D. A. Kofke, *Phys. Rev. E* **54**, 634 (1996).
- <sup>23</sup> T. Kawasaki, T. Araki, and H. Tanaka, *Phys. Rev. Lett.* **99**, 215701 (2007).
- <sup>24</sup> M. A. Bates and D. Frenkel, *J. Chem. Phys.* **109**, 6193 (1998).
- <sup>25</sup> M. Leocmach, J. Russo, and H. Tanaka, *J. Chem. Phys.* **138**, 12A536 (2013).
- <sup>26</sup> J. Russo and H. Tanaka, *Proc. Natl. Acad. Sci. U. S. A.* **112**, 6920 (2015).
- <sup>27</sup> P. Sampedro Ruiz, Q.-I. Lei, and R. Ni, *Commun. Phys.* **2**, 70 (2019).
- <sup>28</sup> M. R. Stapleton, D. J. Tildesley, and N. Quirke, *J. Chem. Phys.* **92**, 4456 (1990).
- <sup>29</sup> D. J. Lacks and J. R. Wienhoff, *J. Chem. Phys.* **111**, 398 (1999).
- <sup>30</sup> S. R. Williams, I. K. Snook, and W. van Meegen, *Phys. Rev. E* **64**, 021506 (2001).
- <sup>31</sup> P. Chaudhuri, S. Karmakar, C. Dasgupta, H. R. Krishnamurthy, and A. K. Sood, *Phys. Rev. Lett.* **95**, 248301 (2005).
- <sup>32</sup> S. Sarkar, R. Biswas, M. Santra, and B. Bagchi, *Phys. Rev. E* **88**, 022104 (2013).
- <sup>33</sup> A. Ninarello, L. Berthier, and D. Coslovich, *Phys. Rev. X* **7**, 021039 (2017).
- <sup>34</sup> S. E. Abraham, S. M. Bhattacharyya, and B. Bagchi, *Phys. Rev. Lett.* **100**, 167801 (2008).
- <sup>35</sup> M. Yiannourakou, I. G. Economou, and I. A. Bitsanis, *J. Chem. Phys.* **133**, 224901 (2010).
- <sup>36</sup> D. J. Shaw, *J. Disper. Sci. Technol.* **15**, 119 (1994).
- <sup>37</sup> R. P. Murphy, K. Hong, and N. J. Wagner, *J. Colloid Interface Sci.* **501**, 45 (2017).
- <sup>38</sup> J. Roller, J. D. Geiger, M. Voggenreiter, J.-M. Meijer, and A. Zumbusch, *Soft Matter* **16**, 1021 (2020).
- <sup>39</sup> M. Voggenreiter *et al.*, *Langmuir* **36**, 13087 (2020).
- <sup>40</sup> J. Roller, A. Laganapan, J.-M. Meijer, M. Fuchs, and A. Zumbusch, *Proc. Natl. Acad. Sci. U. S. A.* **118**, e2018072118 (2021).
- <sup>41</sup> T. Eckert, M. Schmidt, and D. de las Heras, *J. Chem. Phys.* **157**, 234901 (2022).
- <sup>42</sup> T. S. Grigera and G. Parisi, *Phys. Rev. E* **63**, 045102 (2001).
- <sup>43</sup> D. Gazzillo and G. Pastore, *Chem. Phys. Lett.* **159**, 388 (1989).
- <sup>44</sup> D. Coslovich, M. Ozawa, and L. Berthier, *J. Phys.: Condens. Matter* **30**, 144004 (2018).
- <sup>45</sup> M. Ozawa and L. Berthier, *J. Chem. Phys.* **146**, 014502 (2017).

- <sup>46</sup>M. Ozawa, G. Parisi, and L. Berthier, *J. Chem. Phys.* **149**, 154501 (2018).
- <sup>47</sup>L. Berthier, D. Coslovich, A. Ninarello, and M. Ozawa, *Phys. Rev. Lett.* **116**, 238002 (2016).
- <sup>48</sup>L. Berthier *et al.*, *Proc. Natl. Acad. Sci. U. S. A.* **114**, 11356 (2017).
- <sup>49</sup>P. Patel, M. K. Nandi, U. K. Nandi, and S. M. Bhattacharyya, *J. Chem. Phys.* **154**, 034503 (2021).
- <sup>50</sup>N. Kiriushcheva and P. H. Poole, *Phys. Rev. E* **65**, 011402 (2001).
- <sup>51</sup>T. S. Ingebrigtsen and J. C. Dyre, *J. Phys. Chem. B* **127**, 2837 (2023).
- <sup>52</sup>M. J. Pond, J. R. Errington, and T. M. Truskett, *J. Chem. Phys.* **135**, 124513 (2011).
- <sup>53</sup>D. L. Majure, R. W. Haskins, N. J. Lee, R. M. Ebeling, R. S. Maier, C. P. Marsh, A. J. Bednar, R. A. Kirgan, and C. R. Welch, "Large-scale atomic/molecular massively parallel simulator (LAMMPS) simulations of the effects of chirality and diameter on the pullout force in a carbon nanotube bundle," *IEEE* **201**, 1 (2008).
- <sup>54</sup>R. Gutiérrez, S. Karmakar, Y. G. Pollack, and I. Procaccia, *Europhys. Lett.* **111**, 56009 (2015).
- <sup>55</sup>S. Sastry, *PhysChemComm* **3**, 79 (2000).
- <sup>56</sup>U. K. Nandi *et al.*, *J. Chem. Phys.* **156**, 014503 (2022).
- <sup>57</sup>R. E. Nettleton and M. S. Green, *J. Chem. Phys.* **29**, 1365 (1958).
- <sup>58</sup>T. Goel, C. N. Patra, T. Mukherjee, and C. Chakravarty, *J. Chem. Phys.* **129**, 164904 (2008).
- <sup>59</sup>A. Baranyai and D. J. Evans, *Phys. Rev. A* **40**, 3817 (1989).
- <sup>60</sup>A. Banerjee, M. K. Nandi, S. Sastry, and S. Maitra Bhattacharyya, *J. Chem. Phys.* **147**, 024504 (2017).
- <sup>61</sup>S. Sastry, P. G. Debenedetti, and F. H. Stillinger, *Nature* **393**, 554 (1998).
- <sup>62</sup>P. M. Piaggi, O. Valsson, and M. Parrinello, *Phys. Rev. Lett.* **119**, 015701 (2017).
- <sup>63</sup>M. Sharma, M. Kumar Nandi, and S. M. Bhattacharyya [arXiv:2306.16149](https://arxiv.org/abs/2306.16149).
- <sup>64</sup>R. Candelier *et al.*, *Phys. Rev. Lett.* **105**, 135702 (2010).
- <sup>65</sup>A. Smessaert and J. Rottler, *Phys. Rev. E* **88**, 022314 (2013).
- <sup>66</sup>S. Sengupta, F. Vasconcelos, F. Affouard, and S. Sastry, *J. Chem. Phys.* **135**, 194503 (2011).
- <sup>67</sup>C. David, A. Emilien, S. Philippe, and R. Farhang, *Phys. Rev. E* **98**, 052910 (2018).
- <sup>68</sup>A. Widmer-Cooper, P. Harrowell, and H. Fynewever, *Phys. Rev. Lett.* **93**, 135701 (2004).
- <sup>69</sup>A. Widmer-Cooper and P. Harrowell, *Phys. Rev. Lett.* **96**, 185701 (2006).
- <sup>70</sup>L. Berthier and R. L. Jack, *Phys. Rev. E* **76**, 041509 (2007).
- <sup>71</sup>J. Guérolé *et al.*, *Comput. Mater. Sci.* **175**, 109584 (2020).
- <sup>72</sup>H. Tong and H. Tanaka, *Phys. Rev. X* **8**, 011041 (2018).
- <sup>73</sup>A. J. Dunleavy, K. Wiesner, R. Yamamoto, and C. P. Royall, *Nat. Commun.* **6**, 6089 (2015).
- <sup>74</sup>L. S. Garca-Coln, L. F. del Castillo, and P. Goldstein, *Phys. Rev. B* **40**, 7040 (1989).
- <sup>75</sup>Appendix k—small research projects, *Understanding Molecular Simulation*, 2nd ed., edited by D. Frenkel and B. Smit (Academic Press, San Diego, 2002), pp. 581–585.
- <sup>76</sup>K. Vollmayr-Lee, W. Kob, K. Binder, and A. Zippelius, *J. Chem. Phys.* **116**, 5158 (2002).
- <sup>77</sup>A. Widmer-Cooper and P. Harrowell, *J. Phys.: Condens. Matter* **17**, S4025 (2005).

# Effect of the presence of pinned particles on the structural parameters of a liquid and correlation between structure and dynamics at the local level

Palak Patel<sup>1,2</sup> and Sarika Maitra Bhattacharyya<sup>1,2, a)</sup>

<sup>1)</sup>*Polymer Science and Engineering Division, CSIR-National Chemical Laboratory, Pune-411008, India*

<sup>2)</sup>*Academy of Scientific and Innovative Research (AcSIR), Ghaziabad 201002, India*

Pinning particles at the equilibrium configuration of the liquid is expected not to affect the structure and any property that depends on the structure while slowing down the dynamics. This leads to a breakdown of the structure dynamics correlation. Here, we calculate two structural quantities, the pair excess entropy,  $S_2$ , and the mean field caging potential, the inverse of which is our structural order parameter (SOP). We show that when the pinned particles are treated the same way as the mobile particles, both  $S_2$  and SOP of the mobile particles remain the same as that of the unpinned system, and the structure dynamics correlation decreases with an increase in pinning density, “ $c$ ”. However, when we treat the pinned particles as a different species, even if we consider that the structure does not change, the expression of  $S_2$  and SOP changes. The microscopic expressions show that interaction between a pinned and mobile particle affects  $S_2$  and SOP more than the interaction between two mobile particles. We show that a similar effect is also present in the calculation of the excess entropy and the primary reason for the well-known vanishing of the configurational entropy at high temperatures. We further show that contrary to common belief, the pinning process does change the structure. When these two effects are considered, both  $S_2$  and SOP decrease with an increase in “ $c$ ”, and the correlation between the structural parameters and the dynamics continues even for higher values of “ $c$ ”.

## I. INTRODUCTION

When a glass forming liquid is cooled fast enough, it avoids the crystallization process, and the viscosity/relaxation timescale shows a dramatic increase<sup>1,2</sup>. There have been debates about the origin of this increase in viscosity/relaxation time. There are theories suggesting that the slowing down of the dynamics is purely kinetic in nature<sup>3</sup>. However, phenomenological Adam-Gibbs (AG) theory predicts a relation between the relaxation time,  $\tau$ , and configurational entropy,  $S_c$ ,  $\tau = \tau_0 \exp \frac{A}{TS_c}$  where  $A$  is a system dependent constant and  $\tau_0$  is the high temperature relaxation time. As predicted by Kauzman many years ago,  $S_c$  vanishes at the Kauzmann temperature,  $T_K$ , which is a finite temperature below the glass transition temperature<sup>4</sup>. For many systems, the AG relation is found to be valid, and the predicted temperature where the dynamics diverges is found to be the same as  $T_K$ <sup>5-13</sup>. The random first-order transition theory (RFOT), suggests that the slowing down of the dynamics is related to a growing length scale in the system<sup>14-16</sup> which in turn is related to the configurational entropy,  $S_c$  of the system thus suggesting a generalized AG relationship<sup>17,18</sup>. However, the ideal glass transition temperature  $T_K$  can be obtained only via extrapolating the temperature dependence of  $S_c$  to low temperatures.

In order to access the ideal glass transition temperature,  $T_K$ , a novel model system was proposed where some fraction of particles in their equilibrium liquid configuration are pinned<sup>19-23</sup>. It was predicted<sup>19</sup> and also shown in numerical simulations<sup>20,21</sup> that as the fraction of pinned

particles increases, the  $T_K$  increases, and eventually, at high enough pinning, the ideal glass transition moves to high enough temperature where the system can be equilibrated. Interestingly, the pinned system can also be experimentally realized by laser pinning some particles<sup>24</sup> or via soft pinning<sup>25</sup>.

Studies showed that for these pinned systems, although the configurational entropy vanishes at high temperatures, the dynamics continues and there is a breakdown of the AG relationship<sup>20,22,26</sup>. It was later shown that in the calculation of the vibrational entropy, when anharmonic contributions are considered, the configurational entropy remains positive<sup>27</sup>. However, even with this anharmonic contribution, the AG relationship was shown to break down<sup>22</sup>. It was also shown that the RFOT theory, which leads to a generalized AG relationship, is valid if it is assumed that the configurational entropy of the pinned system is related to the unpinned system by a multiplicative factor where the factor decreases with increasing pinning<sup>21,28</sup>. All these studies showed that the correlation between dynamics and entropy of the pinned system differs from that of the unpinned systems.

The correlation between local pair excess entropy, which depends on the structure and the local dynamics of the pinned system, was also studied<sup>24</sup>. It was shown that since the pinning process is expected not to affect the structure, the local pair excess entropy remains the same as the unpinned system, whereas the dynamics slows down due to pinning. Thus, there is a decorrelation between pair excess entropy and dynamics even at the microscopic level.

From the above discussion, it appears that both at macroscopic and microscopic levels, the dynamics and the entropy are not correlated. However, at the macro-

<sup>a)</sup>Electronic mail: mb.sarika@ncl.res.in



scopic level, pinning decreases the configurational entropy more than slowing down the dynamics<sup>20</sup>, whereas, at the microscopic level, the pinning process does not alter the pair excess entropy but slows down the dynamics. Thus, the decorrelation between entropy and dynamics observed at the macroscopic and microscopic levels is just the opposite. Note that for the unpinned system, the macroscopic pair excess entropy,  $S_2$  contributes to 80% of the excess entropy<sup>29</sup>. The configurational entropy  $S_c = S_{id} + S_{ex} - S_{vib}$  has a contribution from three terms: the ideal gas entropy  $S_{id}$ , the excess entropy,  $S_{ex}$  and the vibrational entropy,  $S_{vib}$ . Since pair excess entropy does not change due to pinning, we can expect the excess entropy, which is usually obtained using thermodynamic integration (TI) method<sup>30,31</sup> also not to change. In that case, we may expect that the other terms are responsible for the observed decrease in the configurational entropy of the pinned systems.

In this paper, we first revisit the calculation of the configurational entropy. We show that the decrease in the excess entropy is primarily responsible for the decrease in the configurational entropy. We further show that in the calculation of the excess entropy, the pinned particles should be treated as a different species, and the analytical expression shows that compared to the interaction with another mobile particle, the interaction with a pinned particle contributes twice in decreasing the excess entropy of a mobile particle. We next show that when we use a similar methodology in the calculation of the pair excess entropy, both at macroscopic and microscopic levels, it decreases with pinning. The expression of the pair excess entropy shows that this decrease again comes from the stronger interaction between the pinned and mobile particles.

We then extend the recently developed theoretical formulation, where we describe that each particle in a mean field caging potential for the pinned system. Note that, as shown before, this mean field caging potential is obtained from the structure of the liquid<sup>32-34</sup>. We find that even the mean field potential, both at microscopic and macroscopic levels, shows that the pinned particles have a stronger interaction with the mobile particles, thus increasing the depth of the caging potential and confining the mobile particles. We refer to the inverse depth of the caging potential as the structural order parameter (SOP). Interestingly, a similar confinement effect of the pinned particles was observed in the elastically collective nonlinear equation (ECNLE) theory<sup>35,36</sup>. In ECNLE theory, the dynamics of the system was obtained using Langevin dynamics on the dynamic free energy surface. The studies showed that with pinning, the depth of the free energy barrier increases, and the particles are more confined. In the ECNLE theory, while treating the system, the Authors considered that the pinned particles do not change the structure, but the pinned particles are considered to be a different species. Thus, it appears that in any formulation to obtain the stronger confinement effect by the pinned particles, the pinned particles should be treated

as a different species.

We next show that contrary to the common belief, the pinning process does change the structure, which can be observed only when the partial radial distribution functions are calculated, assuming the pinned particles are a different species. Our study reveals that with an increase in pinning, it is a combined effect of the change in structure and the stronger contribution of pinned particles in decreasing the potential energy of the mobile particles that reduces both  $S_2$  and SOP, the latter effect playing a more dominant role. Finally, we show that the correlation between the local structural parameters ( $S_2$  and SOP) and local dynamics increases when the above mentioned two effects are taken into consideration in the calculation of  $S_2$  and SOP.

The rest of the paper is organized as follows: section II contains the simulation details. The analysis at the macroscopic level is presented in section III with excess entropy,  $S_{ex}$ , in section III A, pair excess entropy,  $S_2$ , in section III B, the depth of local caging potential,  $\beta\Phi_r$ , in section III C and the numerical results in section III D. The analysis at the microscopic level is presented in section IV with microscopic  $S_2$  in section IV A, microscopic  $\beta\Phi_r$  in section IV B and numerical results in section IV C. In section V, we analyze the structure dynamics correlation at the microscopic level. The paper ends with a brief conclusion in section VI. This paper contains six Appendix sections at the end.

## II. SIMULATION DETAILS

In this study, we work with the well-known Kob-Andersen<sup>37</sup> 80:20 binary Lennard-Jones mixture. The shifted and truncated Lennard-Jones interaction potential in the KA model is given by,

$$u(r_{\alpha\gamma}) = \begin{cases} u^{(LJ)}(r_{\alpha\gamma}; \sigma_{\alpha\gamma}, \epsilon_{\alpha\gamma}) - u^{(LJ)}(r_{\alpha\gamma}^{(c)}; \sigma_{\alpha\gamma}, \epsilon_{\alpha\gamma}), & r \leq r_{\alpha\gamma}^{(c)} \\ 0, & r > r_{\alpha\gamma}^{(c)} \end{cases} \quad (1)$$

where  $u^{(LJ)}(r_{\alpha\gamma}; \sigma_{\alpha\gamma}, \epsilon_{\alpha\gamma}) = 4\epsilon_{\alpha\gamma}[(\frac{\sigma_{\alpha\gamma}}{r_{\alpha\gamma}})^{12} - (\frac{\sigma_{\alpha\gamma}}{r_{\alpha\gamma}})^6]$  and  $r_{\alpha\gamma}^{(c)} = 2.5\sigma_{\alpha\gamma}$ . Where  $\alpha, \gamma \in \{A, B\}$  and  $\epsilon_{AA} = 1.0$ ,  $\epsilon_{AB} = 1.5$ ,  $\epsilon_{BB} = 0.5$ ,  $\sigma_{AA} = 1.0$ ,  $\sigma_{AB} = 0.80$ ,  $\sigma_{BB} = 0.88$ . Length, energy, and time scales are measured in units of  $\sigma_{AA}$ ,  $\epsilon_{AA}$  and  $\sqrt{\frac{\sigma_{AA}^2}{\epsilon_{AA}}}$ , respectively. We use three-dimensional, LAMMPS-based molecular dynamics simulation<sup>38</sup>. The Nosé-Hoover thermostat is used to simulate NVT molecular dynamics in a cubic box with  $N = 4000$ ,  $\rho = (N/V) = 1.2$ , integration time step  $\Delta t = 0.005$ . The system is equilibrated for a period longer than  $100 \tau_\alpha$ , where  $\tau_\alpha$  is the system's relaxation time.

The following pinning procedure is applied to create the pinned system. The pinned particles are chosen randomly from an equilibrium configuration of the KA system at the target temperature<sup>21,39</sup>. In this process, we make sure that the ratio of mobile A and mobile B parti-

cles in the pin sub-population is the same as the regular KA system (80:20). Note that we ensure that two pin particles are not close to each other. The simulations are performed assuming that there is no interaction between two pinned particles ( $u_{PP} = 0$ ). After pinning, we perform NVT molecular dynamics simulation with an integration time step  $\Delta t = 0.005$ . We equilibrate the system for  $t = 100$ . For this work, we generate three different pinning concentrations “c”, i.e., 0.05, 0.10, and 0.15.

In this work, to characterize the dynamics, we consider the self part of the overlap function,  $q(t)$ , defined as;

$$q(t) = \frac{1}{N} \sum_{i=1}^N \omega(|r_i(t) - r_i(0)|) \quad (2)$$

where function  $\omega(x) = 1$  when  $0 \leq x \leq a$  and  $\omega(x) = 0$  otherwise. The overlap parameter cutoff ( $a$ ) = 0.3 is taken such that particle positions separated due to small amplitude vibrational motion are treated as the same<sup>40</sup>. We calculate the  $\alpha$  relaxation time  $\tau_\alpha$  by examining the time where the overlap function decays to  $1/e = 0.367$ .

### III. ENTROPY AND MEAN FIELD CAGING POTENTIAL AT MACROSCOPIC LEVEL

#### A. Macroscopic excess entropy

The excess entropy of a system is the loss of entropy due to the interaction between particles. The excess entropy of pinned systems has been calculated before, and it was also shown that compared to the unpinned system, the configurational entropy of the system disappears at a higher temperature<sup>20,22</sup>. As discussed in the Introduction, this disappearance of the configurational entropy at a temperature where the dynamics continues has been a topic of intense research<sup>20–22,26,41</sup>. The configurational entropy,  $S_c = S_{id} + S_{ex} - S_{vib}$  is obtained from the ideal gas entropy,  $S_{id}$ , excess entropy,  $S_{ex}$  and the vibrational entropy,  $S_{vib}$  of the system. All these three terms change due to pinning. Here, we first revisit the configurational entropy calculation and find out which terms are primarily responsible for the vanishing of the configurational entropy of the pinned system at a higher temperature<sup>19,20</sup>. As shown in Appendix II we find that as we increase the pinning concentration, the per particle ideal gas entropy increases. However, the per particle excess entropy and per particle vibrational entropy decrease. The decrease in the excess entropy appears to be stronger than the vibrational entropy. We make a comparative analysis of the excess entropy of the pinned and the unpinned systems to understand what leads to this substantial decrease in the excess entropy.

The excess entropy per particle level is expressed as<sup>30,31</sup>;

$$S_{ex}(\beta') = \beta' \langle U \rangle - \int_0^{\beta'} d\beta \langle U \rangle \quad (3)$$

where  $\langle U \rangle$  is per partial potential energy.

In the case of a regular binary system, the per particle potential energy in terms of the radial distribution function,  $g(r)$ , can be expressed as<sup>42</sup>:

$$\begin{aligned} \langle U_B \rangle &= 2\pi\rho \int_0^\infty \sum_{i=1}^2 \sum_{j=1}^2 \frac{N_i}{N} \frac{N_j}{N} u_{ij}(r) g_{ij}(r) r^2 dr \\ &= 2\pi\rho \int_0^\infty \sum_{i=1}^2 \sum_{j=1}^2 \chi_i \chi_j u_{ij}(r) g_{ij}(r) r^2 dr \end{aligned} \quad (4)$$

where,  $\chi_i = \frac{N_i}{N}$  is the fraction of particles in type  $i$ .  $N$  is the total number of particles in the system.

Note that when we pin particles in a binary system, we actually create a quaternary system of two types of mobile particles and two types of pinned particles. We refer to the first type of mobile particles as species 1, the second type of mobile particles as species 2, the first type of pinned particles as species 3, and the second type of pinned particles as species 4. The potential energy per particle for a regular quaternary system can be expressed as follows:

$$\begin{aligned} \langle U_Q \rangle &= 2\pi\rho \int_0^\infty \sum_{i=1}^4 \sum_{j=1}^4 \frac{N'_i}{N} \frac{N'_j}{N} u_{ij}(r) g_{ij}(r) r^2 dr \\ &= 2\pi\rho \int_0^\infty \sum_{i=1}^4 \sum_{j=1}^4 \chi'_i \chi'_j u_{ij}(r) g_{ij}(r) r^2 dr \end{aligned} \quad (5)$$

Now if we assume that a fraction,  $c$  of particles are pinned then  $N'_1 = (1 - c)N_1$ ,  $N'_2 = (1 - c)N_2$ ,  $N'_3 = cN_1$ ,  $N'_4 = cN_2$ ,  $\chi'_i = \frac{N'_i}{N}$ . The number of mobile particles can be written as  $M = (1 - c)N$ . In our model system, the pinned particles do not interact with each other<sup>20</sup>; thus,  $u_{PP} = u_{33} = u_{34} = u_{43} = u_{44} = 0$ . We also know that the interaction between pinned and mobile particles is symmetric, for example,  $u_{13} = u_{31}$ . These conditions modify the quaternary expression and reduce the first summation in Eq. 5 only over types 1 and 2. Moreover, for a system with pinned particles, the excess entropy,  $S_{ex}^M$ , is calculated only for the mobile particles, and the total potential energy is divided only between the  $M$  mobile particles. This further modifies the quaternary expression (Eq. 5), and the potential energy at per mobile particle level for the pinned system, which we now also refer to as the modified quaternary system,  $\langle U_M \rangle = \frac{N}{M} \times \langle U_Q(u_{PP} = 0) \rangle$  can be written as;

$$\begin{aligned}
\langle U_M \rangle &= 2\pi\rho \int_0^\infty r^2 dr \sum_{i=1}^2 \frac{N'_i}{M} \left[ \sum_{j=1}^2 \frac{N'_j}{N} u_{ij}(r) g_{ij}(r) \right. \\
&\quad \left. + 2 \times \sum_{j=3}^4 \frac{N'_j}{N} u_{ij}(r) g_{ij}(r) \right] \\
&= 2\pi\rho \int_0^\infty r^2 dr \sum_{i=1}^2 \frac{(1-c)N_i}{(1-c)N} \left[ \sum_{j=1}^2 \frac{N'_j}{N} u_{ij}(r) g_{ij}(r) \right. \\
&\quad \left. + 2 \times \sum_{j=3}^4 \frac{N'_j}{N} u_{ij}(r) g_{ij}(r) \right] \\
&= 2\pi\rho \int_0^\infty r^2 dr \sum_{i=1}^2 \chi_i \left[ \sum_{j=1}^2 \chi'_j u_{ij}(r) g_{ij}(r) \right. \\
&\quad \left. + 2 \times \sum_{j=3}^4 \chi'_j u_{ij}(r) g_{ij}(r) \right]
\end{aligned} \tag{6}$$

The above expression of the potential energy, when replaced in Eq. 3, provides us with the excess entropy of the mobile particles in the pinned system,  $S_{ex}^M(\beta')$ . The first and second terms in Eq. 6 describe the potential energy of a mobile particle due to the interaction with other mobile particles and pinned particles, respectively. The expression of the first and second term are identical except for the fact that the 2nd term has a factor of 2. This implies that compared to a mobile particle, a pinned particle has a stronger effect in decreasing the potential energy of a mobile particle. In Appendix II, we show that if we neglect this stronger effect of the pinned particles on the mobile particle *i.e.* remove the factor 2 in the second term of  $\langle U_M \rangle$  (Eq. 6) then the excess entropy shows a marginal change and the per particle configurational entropy increases with an increase in pinning density. This is because, with the increase in pinning density, the increase in the ideal gas entropy is more than the decrease in the vibrational entropy. This result is not physical, but it clearly shows that the vanishing of the configurational entropy at higher temperatures is due to the stronger effect of the pinned particles in confining the mobile particles and thus decreasing the excess entropy. We will show in section III B and III C that this effect of the pinned particles plays an important role in the two body excess entropy and the mean field caging potential.

## B. Macroscopic pair excess entropy

The excess entropy,  $S_{ex}$  can be written in terms of an infinite series via the Kirkwood factorization method<sup>43,44</sup>,

$$\begin{aligned}
S_{ex} &= S_2 + S_3 + S_4 \dots \\
&= S_2 + \Delta S
\end{aligned} \tag{7}$$

While  $S_{ex}$  represents the loss of entropy due to total interaction, the pair excess entropy,  $S_2$  describes the loss of entropy due to interaction described by the two-body correlation.  $\Delta S$  is the loss of entropy due to many body correlations (beyond pair correlation). The per particle pair excess entropy, which contributes to 80% of the total excess entropy<sup>29</sup> can be written as<sup>44</sup>;

$$\frac{S_2^B}{k_B} = -2\pi\rho \int_0^\infty \sum_{i=1}^2 \sum_{j=1}^2 \chi_i \chi_j \{g_{ij}(r) \ln g_{ij}(r) - (g_{ij}(r) - 1)\} r^2 dr \tag{8}$$

Pair excess entropy per particle level for the quaternary system is expressed as;

$$\frac{S_2^Q}{k_B} = -2\pi\rho \int_0^\infty r^2 dr \sum_{i=1}^4 \sum_{j=1}^4 \chi'_i \chi'_j \{g_{ij}(r) \ln g_{ij}(r) - (g_{ij}(r) - 1)\} \tag{9}$$

To obtain the pair excess entropy of the pinned system,  $S_2^M$ , we make similar modifications to the pure quaternary system as is done for the calculation of the excess entropy given in the previous system. First, we assume that there is no structure between the pinned particles, *i.e.*  $g_{PP} = g_{33} = g_{44} = g_{34} = g_{43} = 1$ . This assumption is justified as  $u_{33} = u_{34} = u_{43} = u_{44} = 0$ , and we can also neglect any higher order correlation between the pinned particles, thus assuming that the potential of mean force between the pinned particles also vanishes. We also assume that the partial rdf between mobile and pinned particles is symmetric. Thus, the first summation in Eq. 9 is only over the mobile particles, types 1 and 2. Next, in the modified system, we calculate the entropy of only the mobile particles. The total pair excess entropy,  $N * S_2^Q(g_{PP} = 1)$  is divided only amongst the mobile particles, and the per particle pair excess entropy of the mobile particles,  $S_2^M = \frac{N}{M} * S_2^Q(g_{PP} = 1)$ . Thus, in the first summation  $\chi'_i$  is replaced by  $\chi_i$  like in Eq. 6. The pair excess entropy per particle level of the mobile particles in the pinned system,  $S_2^M$  can be written as,

$$\begin{aligned}
\frac{S_2^M}{k_B} &= \\
&- 2\pi\rho \int_0^\infty r^2 dr \sum_{i=1}^2 \chi_i \left[ \sum_{j=1}^2 \chi'_j \{g_{ij}(r) \ln g_{ij}(r) - (g_{ij}(r) - 1)\} \right. \\
&\quad \left. + 2 \times \sum_{j=3}^4 \chi'_j \{g_{ij}(r) \ln g_{ij}(r) - (g_{ij}(r) - 1)\} \right]
\end{aligned} \tag{10}$$

From Eq. 10, we find that similar to that discussed for excess entropy, when we treat the pinned system as this modified quaternary system, the effect of the pinned particles in determining the entropy of the mobile particles is stronger (factor of 2) compared to other mobile particles.

When we pin the particles at their equilibrium position, the structure/rdf of the system is not expected to

change. Thus, pinning is believed to keep the equilibrium of the system the same<sup>24,45,46</sup>. If the structure/rdf remains the same, then treating the system as quaternary or binary in the calculation of the two body excess entropy gives us identical results,  $S_2^Q = S_2^B$  (see Appendix III). However, note that for the pinned system, the pair excess entropy is not given by  $S_2^Q$  (Eq. 9) but by  $S_2^M$  (Eq. 10). In the expression of  $S_2^M$ , even if we assume there is no change in structure due to pinning, the pair excess entropy of the system,  $S_2^M$  is different from that of a binary system and can be written as,

$$\begin{aligned} \frac{S_2^{M'}}{k_B} &= -2\pi\rho \int_0^\infty r^2 dr \\ &\left[ \chi_1(\chi'_1 + 2\chi'_3)\{g_{11}(r) \ln g_{11}(r) - (g_{11}(r) - 1)\} \right. \\ &\quad + \chi_1(\chi'_2 + 2\chi'_4)\{g_{12}(r) \ln g_{12}(r) - (g_{12}(r) - 1)\} \\ &\quad + \chi_2(\chi'_1 + 2\chi'_3)\{g_{21}(r) \ln g_{21}(r) - (g_{21}(r) - 1)\} \\ &\quad \left. + \chi_2(\chi'_2 + 2\chi'_4)\{g_{22}(r) \ln g_{22}(r) - (g_{22}(r) - 1)\} \right] \\ &= \frac{S_2^B}{k_B} - 2\pi\rho \int_0^\infty r^2 dr \sum_{i=1}^2 \sum_{j=1}^2 \chi_i \chi'_{(j+2)} \\ &\quad \{g_{ij}(r) \ln g_{ij}(r) - (g_{ij}(r) - 1)\} \end{aligned} \quad (11)$$

Note that in writing the last equality, we have applied the relation,  $\chi_1 = \chi'_1 + \chi'_3$  and  $\chi_2 = \chi'_2 + \chi'_4$ . Thus, it shows that even if the pinning process does not change the structure, the pair excess entropy for mobile particles in the pinned system is lower than that in the unpinned system. This implies that the pinned particles have a stronger confinement effect on the mobile particle. In the next section, we will show that this stronger confining effect of the pinned particles is present not only in entropy but also in other quantities.

### C. Macroscopic mean field caging potential

The time evolution of the density, under mean-field approximation, can be written in terms of a Smoluchowski equation in an effective mean field caging potential, which is obtained from the Ramakrishnan-Yussouff free energy functional<sup>32,33,47</sup>. Following our earlier studies, the caging potential is calculated by assuming that the cage is static when the particle moves by a distance  $\Delta r$ <sup>32</sup>. The mean field caging potential is expressed in terms of the static structure factor/radial distribution function of the liquid<sup>33</sup>. In this section, we obtain a pinned system's mean field caging potential. Previous work by some of us showed that the depth of caging potential is coupled to the dynamics<sup>32,33</sup>. Thus, in this study, instead of dealing with the whole potential, we deal with the absolute magnitude of the depth of the caging potential as we view the depth of the caging potential as an energy barrier. We first start with the binary

system, where the average depth of mean field caging potential can be expressed as<sup>33</sup>;

$$\beta\Phi_r^B(\Delta r = 0) = -4\pi\rho \int r^2 dr \sum_{i=1}^2 \sum_{j=1}^2 \chi_i \chi_j C_{ij}(r) g_{ij}(r) \quad (12)$$

Here  $r$  is the separation between the tagged particle and its neighbors and  $\beta = 1/k_B T$ ,  $k_B = 1$ ,  $\rho$  is the density.  $\Delta r$  is the tagged particle's distance from its equilibrium position. According to Hypernetted chain approximation, the direct correlation function,  $C_{ij}(r)$ , can be represented as;

$$C_{ij}(r) = -\beta u_{ij}(r) + [g_{ij}(r) - 1] - \ln[g_{ij}(r)]. \quad (13)$$

For a regular quaternary system, the caging potential can be expressed as;

$$\beta\Phi_r^Q(\Delta r = 0) = -4\pi\rho \int r^2 dr \sum_{i=1}^4 \sum_{j=1}^4 \chi_i \chi'_j C_{ij}(r) g_{ij}(r) \quad (14)$$

Next, for the calculation of the mean field caging potential for the pinned system, we apply similar conditions as discussed before for the calculation of the excess and pair excess entropies. Under these conditions the average depth of mean field caging potential of the mobile particles in the pinned system,  $\beta\Phi_r^M$  can be written as;

$$\begin{aligned} \beta\Phi_r^M(\Delta r = 0) &= -4\pi\rho \int r^2 dr \sum_{i=1}^2 \chi_i \left[ \sum_{j=1}^2 \chi'_j C_{ij}(r) g_{ij}(r) \right. \\ &\quad \left. + 2 \times \sum_{j=3}^4 \chi'_j C_{ij}(r) g_{ij}(r) \right] \end{aligned} \quad (15)$$

Note that similar to excess and pair excess entropy, the depth of the mean field caging potential of mobile particles in this modified quaternary system is affected more by the pinned particles (factor of 2) than by other mobile particles. Also, if the structure does not change due to pinning, the expression of the caging potential for a quaternary and binary system is identical, but that is not the case for the modified quaternary system. The expression for the depth of the mean field caging potential under the assumption that the structure does not change due to pinning can be written as,

$$\begin{aligned}
\beta\Phi_r^{M'}(\Delta r = 0) &= -4\pi\rho \int r^2 dr \left[ \chi_1(\chi'_1 + 2\chi'_3)C_{11}(r)g_{11}(r) \right. \\
&\quad + \chi_1(\chi'_2 + 2\chi'_4)C_{12}(r)g_{12}(r) \\
&\quad + \chi_2(\chi'_1 + 2\chi'_3)C_{21}(r)g_{21}(r) \\
&\quad \left. + \chi_2(\chi'_2 + 2\chi'_4)C_{22}(r)g_{22}(r) \right] \\
&= \beta\Phi_r^B(\Delta r = 0) - 4\pi\rho \int r^2 dr \sum_{i=1}^2 \sum_{j=1}^2 \chi_i \chi'_{(j+2)} C_{ij}(r) g_{ij}(r)
\end{aligned} \tag{16}$$

In the last equality we have applied the relation that  $\chi_1 = \chi'_1 + \chi'_3$  and  $\chi_2 = \chi'_2 + \chi'_4$ . The above expression suggests that even when we assume that the structure does not change due to pinning, the depth of the caging potential for the pinned system is deeper compared to the unpinned system. This higher confinement effect comes due to the stronger interaction with the pinned particles. Interestingly, a similar effect of the pinned particles has been discussed while studying the nonlinear Langevin equation on a dynamic free energy surface<sup>35,36</sup>. Note that our mean field caging potential is obtained from the functional derivative of the static version of this dynamic free energy<sup>47,48</sup>. Similar to the methodology used here, their study<sup>35,36</sup> on a monoatomic liquid treats the pinned system as a binary system, thus considering the pinned particle as a different species. They also consider the dynamic free energy of only the mobile particles. Under these conditions, they show that the free energy barrier and confinement of the mobile particles increase with pinning density.

#### D. Numerical results for the macroscopic pair excess entropy and mean field caging potential

Note that the two body excess entropy and the mean field caging potential are both functions of the radial distribution function (rdf) given by,

$$g_{ij}(r) = \frac{V}{N_i N_j} \left\langle \sum_{\alpha=1}^{N_i} \sum_{\beta=1, \beta \neq \alpha}^{N_j} \delta(r - r_\alpha + r_\beta) \right\rangle \tag{17}$$

where  $V$  is the system's volume,  $N_i$ ,  $N_j$  are the number of particles of the  $i$  and  $j$  types, respectively.  $r_\alpha$ ,  $r_\beta$  are the  $\alpha^{th}$  and  $\beta^{th}$  particle's position in the system respectively.

In Fig. 1, we plot the partial rdfs of the system where we do not differentiate between the pinned and unpinned particles and we find that, as expected, the rdf remains the same as the unpinned regular KA model ( $c=0$ ).

In the rest of the article when we refer to the unpinned binary KA system, following the usual norm, we refer to the particles as A and B types. However, as discussed in the previous sections, when we pin particles in a binary system, we actually create a quaternary system. We refer

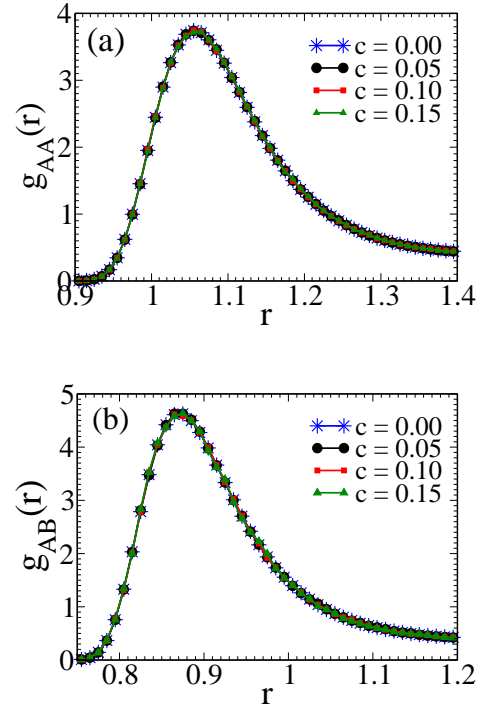


FIG. 1: Radial distribution function,  $g(r)$  while treating the pinned system as a binary system, at  $T = 0.68$  (a)  $g_{AA}$  as a function of  $r$  (b)  $g_{AB}$  as a function of  $r$ . Here  $A$  and  $B$  are the bigger and smaller sizes of particles respectively.

to the mobile A type of particles as 1, mobile B type of particles as 2, pinned A type of particles as 3, and pinned B type of particles as 4.

We next plot some representative partial rdfs assuming the system to be quaternary at different pinning concentrations (Fig. 2). We find that with increased pinning density, the partial rdfs start deviating from the  $c=0$  system. With an increase in “ $c$ ”, there is a drop in the peak value of the rdfs between two mobile particles ( $g_{11}$ ,  $g_{12}$ ). On the other hand, the first peak height of the partial rdfs between mobile and pinned particles ( $g_{13}$ ,  $g_{14}$ ) grows with “ $c$ ”. To ensure that this is not an artifact of choosing the pinned particles as a different species, in the  $c=0$  system, we randomly choose 15% of the particles and treat them as a different species. In Fig. 3, we show that in that case,  $g_{11} = g_{13} = g_{AA}$ . A similar result is also observed for other partial rdfs (not shown here). This clearly shows that when we pin a certain fraction of particles, contrary to the common belief, there is a structural change.

We observe that this structural change happens quickly, immediately after the pinning process. We calculate  $g(r)$ , averaged from  $t = 0 - 100$  and  $t = 101 - 200$ , where the pinning is performed at  $t=0$ . We find that both rdfs overlap (Appendix IV, Fig. 13). In Appendix IV, Fig. 14, we also show that  $\chi_1 g_{11} + \chi_3 g_{13}$  is the same



as  $\chi_{AGAA}$  and  $\chi_2'g_{12} + \chi_4'g_{14}$  is the same as  $\chi_{BGBB}$ . This is precisely why we do not see a change in structure when the pinned particles are not treated as a different species (Fig. 1). Note that this change in the partial rdfs is independent of the integration timestep and system size (Fig. 16).

Thus, from this analysis, it is clear that the structure of the system does change when particles are pinned. However, this change is significant at higher pinning densities only when we treat the pinned particles as a different species. In Fig. 4, we plot the pair excess entropy,  $S_2^{M'}$  (Eq. 11) and the caging potential,  $\beta\Phi_r^{M'}$  (Eq. 16) of the pinned systems where we assume that the structure does not change due to pinning. We also plot  $S_2^M$  (Fig. 4 (a)) and  $\beta\Phi_r^M$  (Fig. 4 (b)), where we consider that the structure changes due to pinning. We find that, even when we consider that the structure does not change, the pair excess entropy of the pinned system differs from that of the binary system and decreases with increasing pinning density. This decrease in entropy is due to the stronger effect of the pinned particles in confining the mobile particles. When we consider that the structure changes due to pinning, as shown in Fig. 2, then the entropy further decreases, and like the structure, this decrease is significant at higher pinning densities. The plot of the mean field caging potential shows a similar effect. The caging potential depth increases with pinning, even if the change in the structure due to pinning is ignored. There is a further increase in the depth when the change in the structure is taken into account.

Thus, we find that both the pair excess entropy and the mean field caging potential for the pinned system differ from that of the unpinned system, and this difference comes due to two factors. Firstly, compared to the interaction between two mobile particles, the interaction between a mobile and a pinned particle is stronger, leading to a decrease in entropy and an increase in the caging potential. Secondly, due to pinning, the structure of the liquid changes, and this further decreases the entropy and increases the mean field caging potential. As seen from Fig. 4, the first effect is stronger and plays a dominant role.

In Appendix III, we show that the well-known crossover<sup>49</sup> between the excess entropy and the pair excess entropy takes place at a physically meaningful temperature only when we take into consideration these two effects in the calculation of the entropy.

#### IV. PAIR EXCESS ENTROPY AND MEAN FIELD CAGING POTENTIAL AT THE MICROSCOPIC LEVEL

In the previous section, we developed the protocol for calculating the caging potential and pair excess entropy at the macroscopic level for the pinned system. However, our primary goal is to understand how these two order parameters can describe the dynamics at the local level. We clearly demonstrate that the pinned system should be

treated as a modified quaternary system. In this section, we make a comparative analysis of these two structural quantities, when the pinned system is treated as a binary system and a modified quaternary system. First, we start with the microscopic expressions, which are obtained from the macroscopic expressions. The bigger ‘‘A’’ particles, which are larger in number, are the ones for which all microscopic calculations are performed. This is done to make sure that there is no size inhomogeneity, which we know also affects the dynamics<sup>50</sup>.

##### A. Microscopic pair excess entropy

Calculation of the pair excess entropy at the macroscopic level ( $S_2$ ) is given in section III.

In the binary system, the pair excess entropy of each mobile ‘‘A’’ particle, which is type ‘‘1’’ in our notation, can be expressed by removing the first summation in Eq. 8;

$$\frac{S_2^B(A)}{k_B} = -2\pi\rho \int_0^\infty r^2 dr \sum_{j=1}^2 \chi_j \{g_{1j}(r) \ln g_{1j}(r) - (g_{1j}(r) - 1)\} \quad (18)$$

Similarly, in the modified quaternary system, the pair excess entropy of each mobile ‘‘A’’ particle (type 1) can be expressed by removing the first summation in Eq. 10;

$$\begin{aligned} \frac{S_2^M(A)}{k_B} = & -2\pi\rho \int_0^\infty r^2 dr \left[ \sum_{j=1}^2 \chi_j' \{g_{1j}(r) \ln g_{1j}(r) - (g_{1j}(r) - 1)\} \right. \\ & \left. + 2 \times \sum_{j=3}^4 \chi_j' \{g_{1j}(r) \ln g_{1j}(r) - (g_{1j}(r) - 1)\} \right] \end{aligned} \quad (19)$$

Note that the differences between the binary and modified quaternary are the following. In the binary expression, when treating the neighbors, we do not differentiate between the mobile and pinned particles; however, in the quaternary expression, we do. Thus, in the binary expression, the effect of the mobile neighbors on the tagged particle is the same as that of the pinned neighbors. However, in the quaternary expression, the effect of the pinned neighbors on the tagged particle is twice that of the mobile neighbors. As shown in the macroscopic calculation (Fig. 4), it is this second effect that plays a dominant role in differentiating between the binary and the modified quaternary values of the entropy.

##### B. Microscopic mean field caging potential

The macroscopic calculation of the depth of the caging potential ( $\beta\Phi_r$ ), the inverse of which we refer to as the

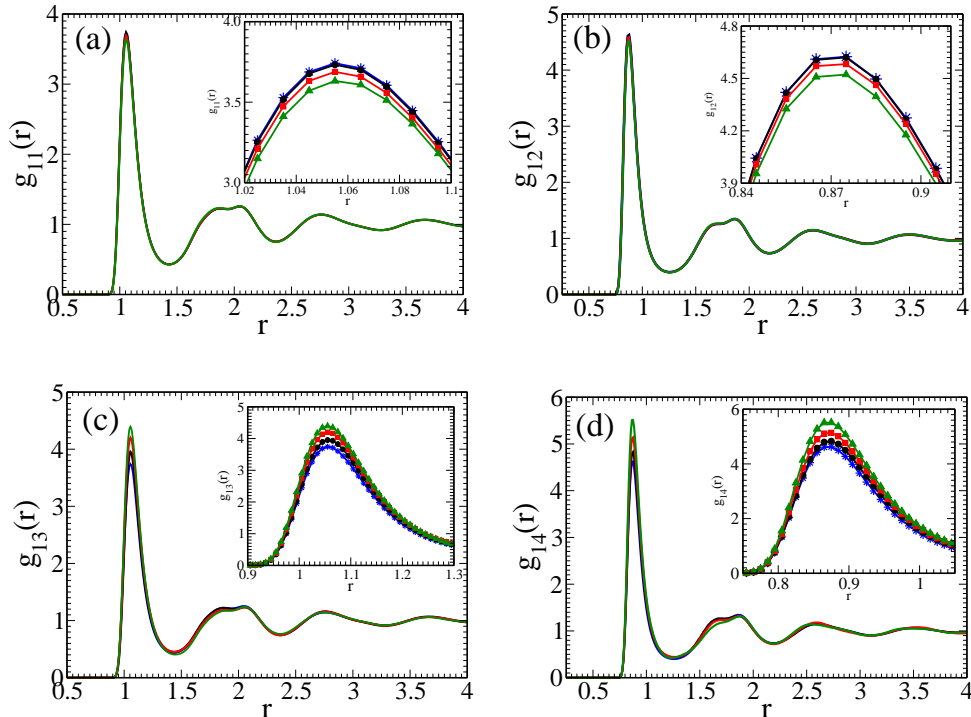


FIG. 2: Radial distribution function,  $g(r)$  while treating the pinned system as a quaternary system, at  $T = 0.68$ . (a)  $g_{11}$  as a function of  $r$  (b)  $g_{12}$  as a function of  $r$  (c)  $g_{13}$  as a function of  $r$  (d)  $g_{14}$  as a function of  $r$ . Inset: We have zoomed onto the first peak of the respective figures, which clearly shows the difference in the radial distribution functions. Note that color coding is similar to Fig. 1. Here, we refer to the mobile A type of particles as 1, mobile B type of particles as 2, pinned A type of particles as 3, and pinned B type of particles as 4.

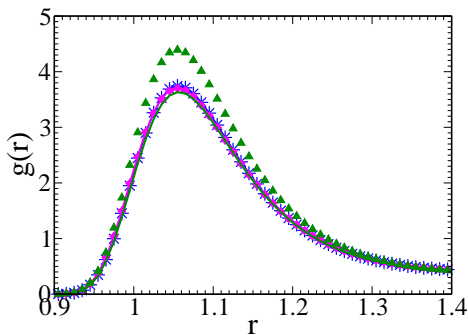


FIG. 3: Comparison between radial distribution functions,  $g(r)$ s by randomly picking 15% particles in the KA system and treating them as different species (magenta, diamond =  $g_{13}$ , magenta solid line =  $g_{11}$ ) and pinning 15% of particles position during the simulation and treating the pinned particles as different species (green, triangle =  $g_{13}$ , green solid line =  $g_{11}$ ). We also plot the  $g(r)$  for a regular KA ( $c=0$ ) system for comparison (blue, star). The plots are shown only for the big particles.

structural order parameter (SOP), is given in section III C. At the microscopic level for a binary system, the

caging potential of a mobile “A” type of particle can be written by removing the first summation in Eq. 12;

$$\beta\Phi_r^B(A, \Delta r = 0) = -4\pi\rho \int r^2 dr \sum_{j=1}^2 \chi_j C_{1j}(r) g_{1j}(r) \quad (20)$$

The mean field caging potential for a mobile “A” type of particle in a modified quaternary system can be written by removing the first summation in Eq. 15,

$$\beta\Phi_r^M(A, \Delta r = 0) = -4\pi\rho \int r^2 dr \left[ \sum_{j=1}^2 \chi_j' C_{1j}(r) g_{1j}(r) + 2 \times \sum_{j=3}^4 \chi_j' C_{1j}(r) g_{1j}(r) \right] \quad (21)$$

Thus, note that similar to that discussed for the pair excess entropy, in the modified quaternary expression, compared to the mobile neighbors, the pinned neighbors have a stronger effect in confining the tagged particle.

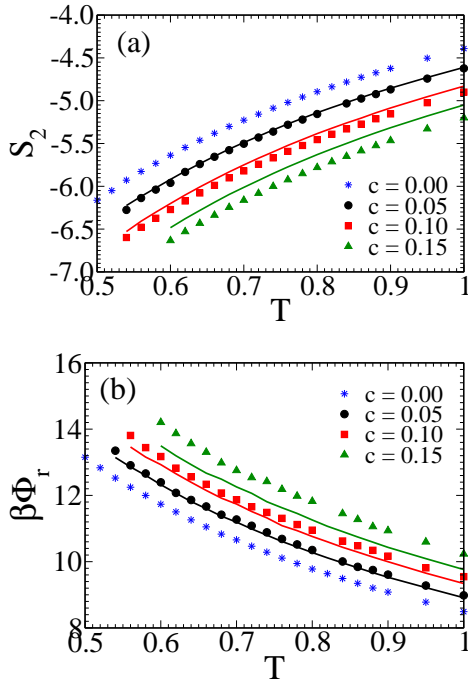


FIG. 4: (a) Macroscopic  $S_2$  as a function of  $T$ , (b) macroscopic  $\beta\Phi_r$  as a function of  $T$ . Solid line represents  $S_2^{M'}$  (Eq. 11) or  $\beta\Phi_r^{M'}$  (Eq. 16) and symbol represents  $S_2^M$  (Eq. 10) or  $\beta\Phi_r^M$  (Eq. 15).

### C. Numerical results for the microscopic pair excess entropy and mean field caging potential

To perform the microscopic investigation, we determine  $\beta\Phi_r(\Delta r = 0)$  and  $S_2$  for every snapshot at the single particle level that requires the partial rdf to be calculated at a single particle level. In this calculation, the sum of Gaussian can be used to express the single particle partial rdf in a single frame, and it is calculated as follows<sup>51</sup>;

$$g_{ij}^\alpha(r) = \frac{1}{4\pi\rho r^2} \sum_{\beta} \frac{1}{\sqrt{2\pi\delta^2}} \exp\left[-\frac{(r-r_{\alpha\beta})^2}{2\delta^2}\right] \quad (22)$$

where “ $\alpha$ ” is the particle index,  $\rho$  is the density. The Gaussian distribution’s variance ( $\delta$ ) is employed to transform the discontinuous function into a continuous form. We use  $\delta = 0.09\sigma_{AA}$  for this work. Single particle rdf is used to derive the direct correlation function at the single particle level from Eq. 13.

We can determine caging potential (Eq. 12, 14, 15) by combining the direct correlation function (Eq. 13) and particle level rdf (Eq. 22). This leads to a term that is a product of the interaction potential and the rdf. As shown in an earlier work<sup>33</sup>, at distances shorter than the average rdf, the particle level rdf generated by the Gaussian approximation has finite values. At small “ $r$ ” due to this finite value of the rdf, its product with the interaction

potential, which diverges at small “ $r$ ”, leads to a large unphysical contribution from this range. To get around this problem, we use an approximate expression of the direct correlation function,  $C_{ij}^{approx}(r) = [g_{ij}(r) - 1]$  where we assume that the interaction potential is equal to the potential of mean force  $-\beta u_{ij}(r) = \ln(g_{ij}(r))$ . It has also been shown earlier that using  $C_{ij}^{approx}(r)$  marginally improves the theoretical prediction of structure-dynamics correlation<sup>34,50</sup>. In the rest of the microscopic calculation, we will use  $C_{ij}^{approx}(r)$  in place of  $C_{ij}(r)$ .

In Fig. 5, we plot the distribution of pair excess entropy and local caging potential by describing the pinned system as binary. Note that for all the cases, the quantities are calculated only for the mobile “A” particles. We find that the distribution remains similar to the unpinned system (KA model at  $c=0$ ). This is because the expressions are identical for pinned and unpinned systems, and even for  $c=0.15$ , there are enough mobile “A” particles to give the correct statistics. However, when we calculate the quantities assuming the pinned system as a modified quaternary system (Eq. 15 and 10), we observe that as “ $c$ ” increases, the depth of the caging potential increases and the pair excess entropy decreases. Distribution of  $\beta\Phi_r^M$ , and  $S_2^M$  are shown in Fig. 5. This analysis clearly shows that the entropy and the SOP (inverse depth of the caging potential) are higher when the system is treated as binary compared to when it is treated as a modified quaternary. In the next section, we will show that the correlation between the dynamics and structural quantities differs when we treat the pinned system as binary or modified quaternary.

## V. CORRELATION BETWEEN STRUCTURE AND DYNAMICS AT MICROSCOPIC LEVEL

In the following section, we study the correlation between two structural order parameters, namely the  $S_2$  and SOP, with the dynamics using different techniques. To make a comparative analysis, while calculating the structural quantities, we treat the pinned system both as binary and modified quaternary systems.

### A. Correlation between structure and dynamics using isoconfiguration runs

In this section, we study the correlation between structure and dynamics using isoconfiguration runs (IC). IC is a powerful technique developed by Harrowell et al.<sup>52–55</sup> to examine the role the structure plays in the dynamics (details are given in Appendix V).

We calculate the Spearman rank correlation,  $C_R(X, Y) = 1 - \frac{6 \sum d_i^2}{m(m^2 - 1)}$  (where  $d_i^2 = R(X_i) - R(Y_i)$  is the difference between the ranks,  $R(X_i)$  and  $R(Y_i)$  of the raw data  $X_i$  and  $Y_i$  respectively, and  $m$  denotes the number of data), between the mobility,  $\mu$  and the pair excess entropy ( $C_R(\mu, S_2)$ ), and between



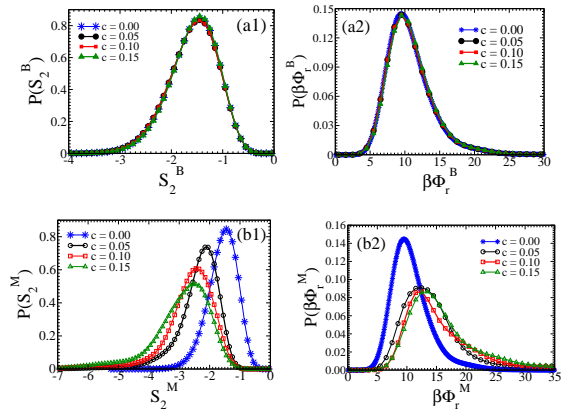


FIG. 5: Distribution of pair excess entropy ( $S_2$ ) and depth of mean field caging potential ( $\beta\Phi_r$ ) in different pinned systems at  $T = 0.68$ . (a1) - Distribution of  $S_2$  treating pinned system as binary, (a2) Distribution of  $\beta\Phi_r$  treating pinned system as binary (b1) - Distribution of  $S_2$  treating pinned system as modified quaternary, (b2) Distribution of  $\beta\Phi_r$  treating pinned system as modified quaternary. The distribution remains the same for binary treatment, while for the modified quaternary treatment, the caging potential increases with increasing  $c$ , and pair excess entropy decreases, with increasing  $c$ .

the mobility,  $\mu$  and the SOP  $C_R(\mu, 1/\beta\Phi_r)$ . In Figs. 6(a) and 6(b), we plot  $C_R(\mu, S_2)$  and  $C_R(\mu, 1/\beta\Phi_r)$  respectively, for the pinned systems as a function of scaled time. We observe that when considering the system as a binary system, the correlations,  $C_R(\mu, S_2^B)$  and  $C_R(\mu, 1/\beta\Phi_r^B)$  decrease as the pinning concentration increases (Fig. 6). This observation is concurrent with the findings of Williams *et al.*<sup>24</sup>. However, when the system is treated as a modified quaternary system, we observe an increase in  $C_R(\mu, S_2^M)$  and  $C_R(\mu, 1/\beta\Phi_r^M)$  compared to when the system is treated as binary. This suggests that treating the system as binary does not capture the full complexity of the structure-dynamics relationship. In the modified quaternary treatment of the system, the pinning decreases the pair excess entropy and the SOP, which is commensurate with the slowing down of the dynamics.

Between the SOP and the pair excess entropy, we find that the SOP can predict the dynamics better and  $C_R(\mu, 1/\beta\Phi_r^M) > C_R(\mu, S_2^M)$ . This is similar to that observed in an earlier study where, for attractive systems compared to entropy, the SOP is a better predictor of the dynamics<sup>34</sup>. Also note that for all values of “ $c$ ”, the peak height of the  $C_R(\mu, 1/\beta\Phi_r^M)$  almost remains constant, whereas the peak height of  $C_R(\mu, S_2^M)$  drops with an increase in “ $c$ ”. Thus the difference between  $C_R(\mu, 1/\beta\Phi_r^M)$  and  $C_R(\mu, S_2^M)$  increases with “ $c$ ”. This drop in the value of  $C_R(\mu, S_2^M)$  with an increase in “ $c$ ” may be connected to the breakdown of the AG relation-

ship at the macroscopic level. However, we cannot calculate the configurational entropy at the microscopic level, but we do find from Fig. 5 that the shift in the distribution of the pair excess entropy with pinning density is stronger than the shift in the distribution of SOP.

We also find that with increasing pinning concentration, the peak height of  $C_R(\mu, 1/\beta\Phi_r^B)$  moves to smaller values of  $t/\tau_\alpha$ . A similar observation was made while comparing the more fragile Lennard-Jones (LJ) and the less fragile Weeks-Chandler-Anderson (WCA) models<sup>34</sup>. Note that in the case of pinned systems, the fragility decreases with increasing “ $c$ ”<sup>21</sup>. Thus, it appears that for more fragile systems, the correlation between structure and dynamics continues for longer times. However, at this point, this is only a conjecture, and to make more concrete statements, further investigations are needed, which is beyond the scope of the present study.

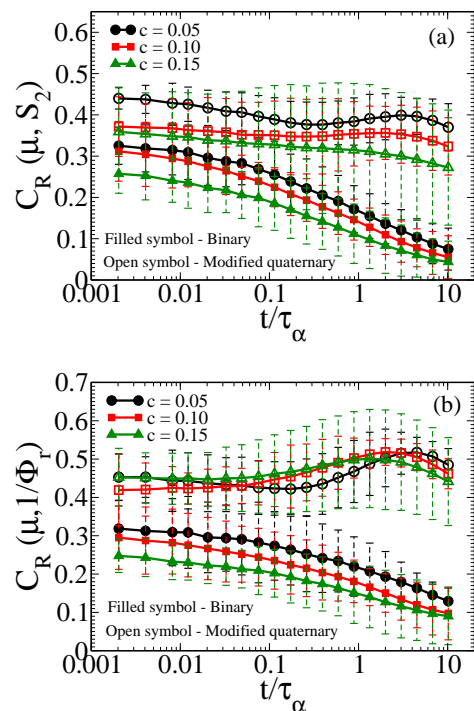


FIG. 6: Spearman rank correlation,  $C_R$  between different parameters, while treating the pinned system as binary (filled symbol) and modified quaternary (open symbol) (a) Spearman rank correlation ( $C_R$ ) between mobility ( $\mu$ ) and pair excess entropy ( $S_2$ ) (b) Spearman rank correlation ( $C_R$ ) between mobility ( $\mu$ ) and inverse depth of caging potential ( $1/\beta\Phi_r$ ). Working temperature for  $c = 0.05, 0.10$  and  $0.15$  is  $0.52, 0.60$ , and  $0.68$  respectively. Note that  $T$  is chosen such that all the pinned systems have approximately the same  $\tau_\alpha \approx 10^3$ .

## B. Analysis of dynamics of particles belonging to the softest and hardest regions

Since we show that the inverse of the mean field caging potential, SOP, is a better predictor of the dynamics, in the next two subsections, we will present the study of the structure-dynamics correlation using only the SOP. At short timescales, we expect to observe a significant difference in the dynamics of the hardest (in a deep cage) and softest (in a shallow cage) particles. The hardest particles, less likely to escape their local cages, will exhibit slower dynamics. On the other hand, the softest particles, with a higher probability of moving, will display faster dynamics. However, over a longer time, as the cage evolves, the separation in dynamics between the hardest and softest particles diminishes<sup>32,33,50</sup>. We average over a few (approximately 2-3) hardest and softest particles and compare their dynamics via the overlap function (Eq. 2). Note that the identity of the soft and hard particles depends on how the SOP is calculated, *i.e.* assuming the system to be binary or modified quaternary.

The dynamics of the hardest and softest particle for different concentrations of the pinning is shown in Fig. 7. When we calculate the SOP treating the system as a modified quaternary system, the difference in dynamics between the hard and the soft particles is wider compared to the case where the system is treated as binary (Fig. 7). Note that the difference is greater for the hard particles. This is because our analysis reveals that the identity of the softest particles does not change when we treat the system as binary or modified quaternary. However, the identity of the hardest particles completely changes because, in the binary treatment, we neglect the stronger interaction between the pinned and the mobile particles, which is present in the modified quaternary treatment. Due to this effect in the modified quaternary treatment, the hardest particles are the ones that have pinned particles as their neighbors. As shown in Fig. 7, the hardest particles, as identified by the modified quaternary treatment, are slower than those identified by the binary treatment. This is precisely the reason why the modified quaternary treatment of the system shows higher value of  $C_R(\mu, 1/\beta\Phi_r^M)$  compared to the binary treatment of the system.

## C. Correlation between structure and dynamics and prediction of onset temperature

In this section, we use the structure dynamics correlation to identify the onset temperature of the glassy dynamics, a methodology used in earlier studies<sup>33,56</sup>.

We identify fast particles using a well-documented method<sup>33,57,58</sup> (details are given in Appendix VI). In Fig. 8 we plot  $P_R(1/\beta\Phi_r)$  as a function of temperature for different  $1/\beta\Phi_r$  values and find that it can be expressed in an Arrhenius form,  $P_R(1/\beta\Phi_r) = P_0(1/\beta\Phi_r) \exp(\Delta E(1/\beta\Phi_r)/T)$ , where activation energy,

$\Delta E$  is a function of  $1/\beta\Phi_r$ , and is higher for smaller  $1/\beta\Phi_r$  values. The plots cross at a certain temperature, which describes the limiting temperature where the theory is valid<sup>33</sup> and has been identified earlier as the onset temperature of the supercooled liquid<sup>33,50,56</sup>.

In this analysis, we find that when we treat the system as binary, the onset temperature remains similar for all pinning concentrations. However, when we treat the system as a modified quaternary system, the onset temperature increases with increasing pinning concentration<sup>19</sup>. As we show in Appendix I, this predicted onset temperature is similar to the onset temperature predicted from the well known inherent structure energy method (Fig. 9 and Table I)<sup>59</sup>.

## VI. CONCLUSION

As discussed in the Introduction, earlier studies on the pinned system have shown that both at macroscopic and microscopic levels, the correlation between the dynamics and entropy breaks down. However, the nature of the breakdown at the microscopic and macroscopic levels is not similar but just the opposite. At the macroscopic level, with pinning, the configurational entropy disappears, whereas the dynamics continues<sup>20,22,26</sup>. At the microscopic level, the pair excess entropy remains high and the same as the unpinned system, whereas the dynamics slows down with an increase in pinning density<sup>24</sup>. This is possible only when the macroscopic configurational entropy and the microscopic pair excess entropy are uncorrelated. However, it is well known that for the unpinned systems, the pair excess entropy contributes to about 80% of the excess entropy, which in turn contributes to the configurational entropy<sup>29</sup>. Thus, to understand the different results at the macroscopic and microscopic levels, we revisit the excess entropy calculation of the pinned system.

We show that when we pin particles in a binary system, we should treat this pinned system as a quaternary system under the assumption that there is no interaction between pinned particles (an assumption we use while simulating the system) and the potential energy is only distributed amongst the mobile particles. The excess entropy of this modified quaternary system predicts that the effect of a pinned particle in stabilizing a mobile particle by decreasing the potential energy is a factor of two more than the effect of another mobile particle. We show that this effect leads to the well documented vanishing of configurational entropy at higher temperatures<sup>19</sup> and the breakdown of the Adam-Gibbs relationship in a pinned system<sup>20,22</sup>.

We follow the same methodology to calculate the pair excess entropy and the mean field caging potential at macroscopic and microscopic levels. We first show that the expression of  $S_2$  and SOP (inverse depth of the mean field caging potential) differ when the system is treated as binary and modified quaternary. In the binary treatment,

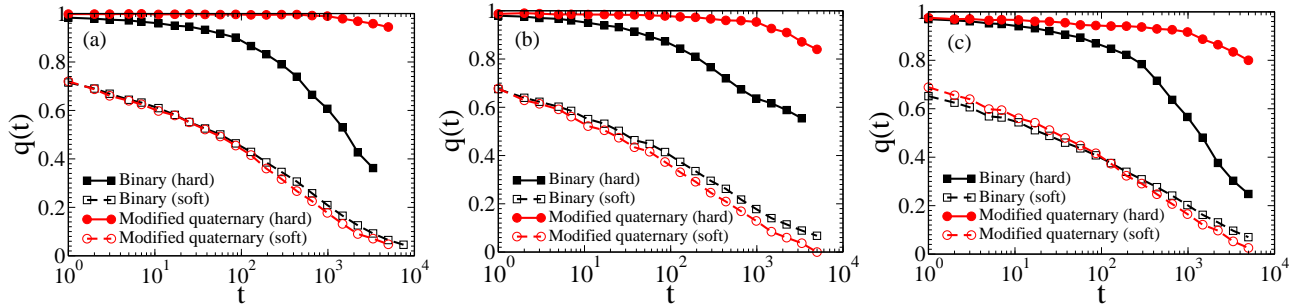


FIG. 7: Comparison of the dynamics of a few hardest (filled symbol) and a few softest (open symbol) particles at different pinning concentrations while treating the pinned system as binary (Black), and modified quaternary (Red) (a)  $c = 0.05$  (at  $T = 0.52$ ), (b)  $c = 0.10$  (at  $T = 0.60$ ) (c)  $c = 0.15$  (at  $T = 0.68$ ). Note that  $T$  is chosen such that all pinned system has approximately the same  $\tau_\alpha$ .

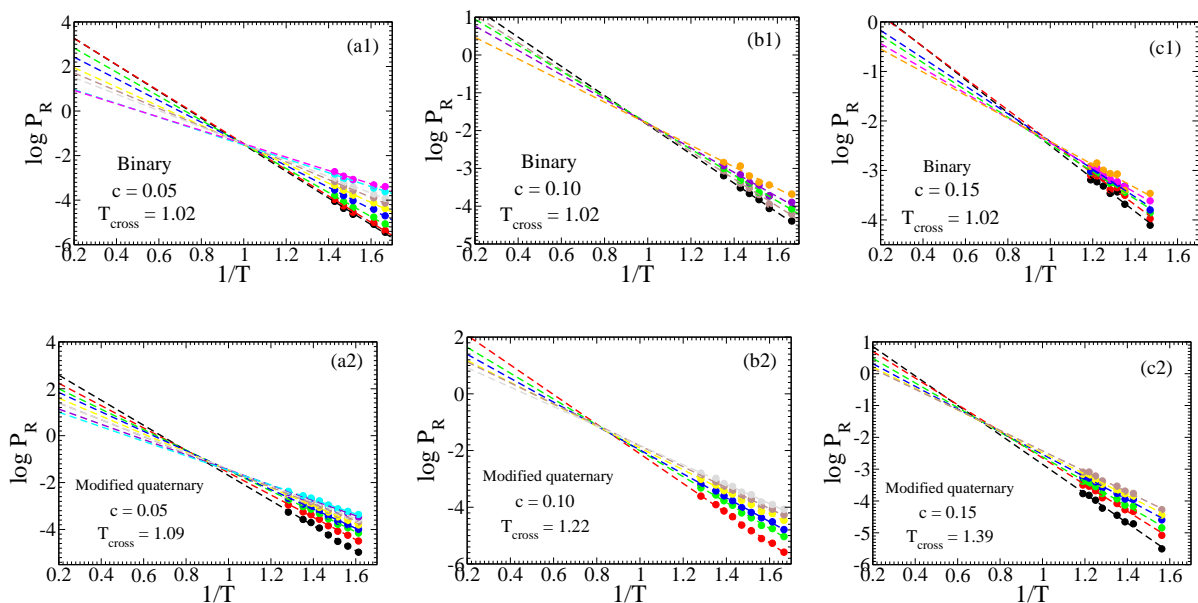


FIG. 8:  $\log P_R(1/\beta\Phi_r)$  as a function of  $1/T$  at different values of the SOP ( $1/\beta\Phi_r$ ). Top panel - In the calculation of the SOP, the pinned system is treated as a binary system (a1)  $c = 0.05$ , (b1)  $c = 0.10$ , and (c1)  $c = 0.15$ . Bottom panel - In the calculation of the SOP, the pinned system is treated as a modified quaternary system (a2)  $c = 0.05$ , (b2)  $c = 0.10$ , (c2)  $c = 0.15$ .

the effect of a pinned particle on the mobile particle is identical to that of another mobile particle. However, in modified quaternary treatment, similar to that observed in the calculation of the excess entropy, the pinned particles have a stronger effect on the mobile particles than other mobile particles. We next show that contrary to the common belief that if pinned at the equilibrium position, the properties of the system do not change, pinning changes the structure of the liquid, which can be observed only when we treat the pinned particles as a different species. We then show that when we treat the system as a modified quaternary system, the entropy and the SOP are much lower than that obtained by treating the system as a binary system. The analysis reveals that more than

the change in structure, the stronger effect of the pinned particles on the mobile particles plays a dominant role in confining the mobile particles by decreasing the entropy and the SOP. Interestingly, a similar confinement effect of the pinned particles was discussed in an earlier study of a monotonic system, where it was shown that the free energy barrier of the mobile particles increases with pinning density<sup>35,36</sup>. Note that similar to the the present study in these earlier studies<sup>35,36</sup>, the pinned particles were treated as a different species.

We further study the correlation between structure and dynamics using different techniques. In all cases, we show that compared to the case where the pinned system is treated as a binary system, there is an increased corre-

lation between structural order parameters and the dynamics when the pinned system is treated as a modified quaternary system. This is because, unlike in the binary case, in the modified quaternary case, the pinned particles affect not only the dynamics but also the structural properties. We also show that compared to the entropy, the SOP can predict the dynamics better. The correlation between fast particles and the SOP can only predict the correct onset temperature when the SOP is calculated, assuming the pinned system is a modified quaternary system.

In Summary, our study reveals two important points. The pinning affects not only the bulk macroscopic quantities but also the microscopic quantities. The effect of the pinned particles can be expressed by treating the pinned particles as a different species, which then shows that a pinned particle confines the mobile particle more than another mobile particle which then alters the microscopic expression of the quantities that depend on the structure. Thus, pinning not only slows down the dynamics of the mobile particle but also changes the structural parameters. Along with this, the pinning process also affects the structure of the liquid. In future studies, these two effects should be considered when calculating different properties of the pinned system. Also, note that, like local pair excess entropy, the local mean field caging potential depends on the local structure. This allows us to apply it to experimental colloidal systems where, both for quiescent and sheared systems, we find a good structure dynamics correlation<sup>60</sup>. Thus, the mean field caging potential can be applied to study the structure-dynamics correlation even in experimental pinned systems<sup>24,25</sup>.

### Appendix I: Onset temperatures of the pinned systems from inherent structure energy

To estimate the temperature range of the system, we first obtain the onset temperature of the supercooled. In Fig. 9, we plot the inherent structure energy,  $e_{IS}$  as a function of  $T$  to calculate the onset temperature ( $T_{onset}$ ) from the inherent structure (IS)<sup>59</sup>.  $T_{onset}$  at different pinning concentrations is given in Table I. The IS is obtained using the FIRE algorithm<sup>61</sup>. From this analysis, we observe that the onset temperature increases with increasing pinning concentration, “ $c$ ”<sup>19</sup> (see Table I).

TABLE I: Onset temperature,  $T_{onset}$  at different pinning concentrations, “ $c$ ”

$c$	$T_{onset}$
0.00	0.80
0.05	0.89
0.10	1.01
0.15	1.27

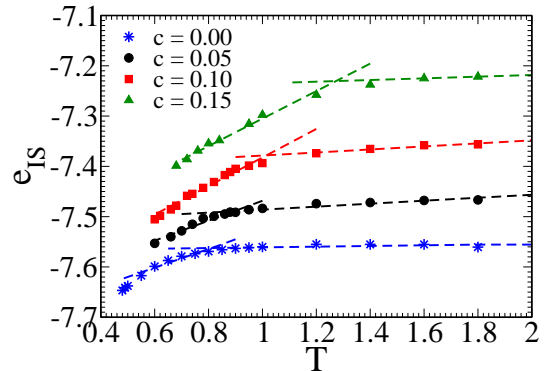


FIG. 9: Inherent structure energy,  $e_{IS}$  as a function of temperature ( $T$ ). The onset temperature is the temperature where  $e_{IS}$  starts to drop from its high-temperature value. Onset temperature increases as  $c$  increases.

### Appendix II: Various forms of entropy in pinned systems

The various forms of entropy in pinned systems are discussed here.

- Ideal gas entropy: The ideal gas entropy in pinned systems only comes from the moving particle. The pinned system’s ideal gas entropy is calculated as<sup>20</sup>;

$$MS_{id} = \frac{3M}{2} - 3M \ln \Lambda + M(1 - \ln \frac{M}{V}) - \sum_{i=1}^2 N'_i \ln \frac{N'_i}{M} \quad (23)$$

where  $M$  is the total number of particles that are moving and  $\Lambda = \sqrt{\frac{\beta h^2}{2\pi m}}$  is the de Broglie thermal wavelength and  $h$  is the Planck constant. We plot the per particle ideal gas entropy of pinned systems at various pinning concentrations in Fig. 10. As the pinning increases, we see an increase in ideal gas entropy. The decrease in the density (as  $M < N$ ) and the increase in the mixing entropy contribute to the increase in the per particle ideal gas entropy.

- Vibrational entropy: We consider a weakly vibrating system around an inherent structure (IS). If we indicate by  $r_i$  the displacement of the  $i^{th}$  particle from its point in the IS, then the potential energy can be approximated well by the following formula<sup>20</sup>,

$$U \approx U_{IS}(S) + \frac{1}{2} \sum_{i,j} \frac{\delta^2 U}{\delta r_i \delta r_j} \delta r_i \delta r_j \quad (24)$$

It is important to realize that only the derivative of the potential energy with respect to the coordinates of unpinned particles should be taken into



account, not including the ones of pinned particles. (However, of course  $U$  will depend on the positions of the pinned and unpinned particles). Thus, the size of the Hessian matrix is  $3M \times 3M$ . Introducing the eigenvalues  $\lambda_1, \lambda_2, \dots, \lambda_{3M}$  of the Hessian, the harmonic vibrational entropy of the given inherent structure with a given pinned particle configuration can be written as<sup>20</sup>;

$$MS_{vib} = 3M(1 - \ln \Lambda) + \frac{1}{2} \sum_{\alpha=1}^{3M} \ln \frac{2\pi}{\beta m \omega_{\alpha}^2} \quad (25)$$

We plot the vibrational entropy of pinned systems at various pinning concentrations in Fig. 10. As the pinning increases, we see a drop in vibrational entropy.

- Excess entropy: We employ the thermodynamic integration approach to determine entropy from simulations. At the target temperature  $\beta'$ , the entropy of the system with the pinned particles  $S$  can be written as<sup>20,22,31</sup>;

$$S_{ex}^M(\beta') = \beta' \langle U_M \rangle - \int_0^{\beta'} d\beta \langle U_M \rangle \quad (26)$$

where  $\langle U_M \rangle$  is a thermal average of the potential energy. Details of excess entropy calculation are discussed in section III A. We plot the excess entropy of pinned systems at various pinning concentrations in Fig. 10. As the pinning increases, we see a drop in excess entropy. We also plot the excess entropy for the pinned system where we ignore the stronger effect of the pinned particles on the mobile particles by removing the prefactor 2 in the second term of  $\langle U_M \rangle$  (Eq. 6), which we now denote as  $\langle U_M^I \rangle$  and express as;

$$\langle U_M^I \rangle = 2\pi\rho \int_0^{\infty} r^2 dr \sum_{i=1}^2 \chi_i \left[ \sum_{j=1}^2 \chi_j' u_{ij}(r) g_{ij}(r) + \sum_{j=3}^4 \chi_j' u_{ij}(r) g_{ij}(r) \right] \quad (27)$$

In this case, the excess entropy can be written as;

$$S_{ex}^I = \beta' \langle U_M^I \rangle - \int_0^{\beta'} d\beta \langle U_M^I \rangle. \quad (28)$$

We find that the excess entropy,  $S_{ex}^I$ , does not decrease with pinning. Rather, it shows a marginal increase. This analysis clearly shows that the decrease in the excess entropy with pinning is due

to the higher potential energy contribution of the pinned particles, which leads to a stronger confinement of the mobile particles.

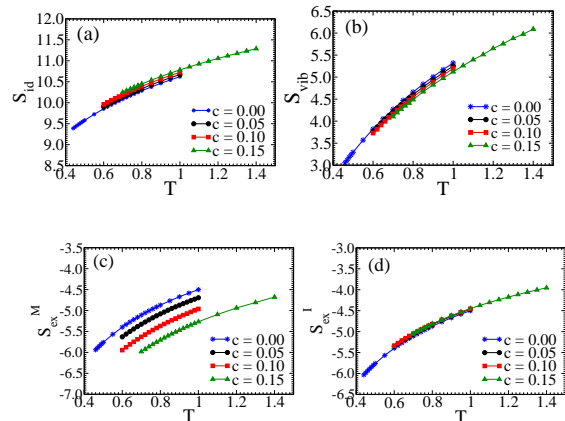


FIG. 10: Various forms of entropy as a function of temperature,  $T$  (a) Ideal gas entropy,  $S_{id}$ , (b) Vibrational entropy  $S_{vib}$ , (c) Excess entropy,  $S_{ex}^M$  (Eq. 26). (d) Excess entropy,  $S_{ex}^I$  (Eq. 28).

In Fig. 11 we plot the configurational entropy,  $S_c^M = S_{id} + S_{ex}^M - S_{vib}$  and  $S_c^I = S_{id} + S_{ex}^I - S_{vib}$  at different pinning concentrations. We observe that the Kauzmann temperature,  $T_K$ , where the extrapolated entropy vanishes, increases when excess entropy is calculated using the modified quaternary expression of the potential energy,  $\langle U_M \rangle$  and the Adam-Gibbs relation between the dynamics and entropy is not valid. However, when we ignore the stronger effect of the pinned particles on the mobile particle, *i.e.* use  $\langle U_M^I \rangle$  in the calculation of the excess entropy, then  $T_K$  decreases with increasing pinning and the Adam-Gibbs relation between the dynamics and entropy is valid. This, as discussed in the main paper, is not a physically correct picture, but this analysis clearly shows that in the pinned system, the vanishing of the entropy at higher temperatures is due to the stronger confinement effect of the pinned particles on the mobile particles.

### Appendix III: Pair excess entropy

In section III B, we show that the pair excess entropy can have different expressions when the system is treated as binary, quaternary, and modified quaternary. We also show that the rdf is different when the system is treated as binary and quaternary (section III D).

If the structure (rdf) does not change, then treating the system as quaternary or binary in the calculation of the  $S_2$  gives us identical results. This can be easily seen when comparing Eq. 8 and Eq. 10. If we assume that in the rdfs we can replace 3 by 1 and 4 by 2 then Eq. 9 can

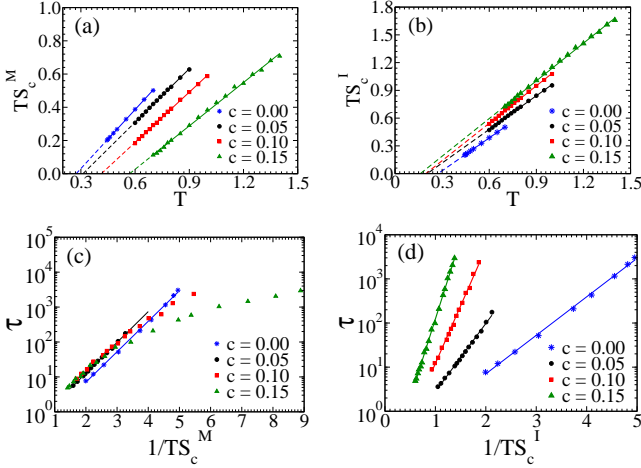


FIG. 11: (a)  $TS_c^M = T(S_{id} + S_{ex}^M - S_{vib})$ , as a function of T (b)  $TS_c^I = T(S_{id} + S_{ex}^I - S_{vib})$ , as a function of T (c)  $\tau$  vs.  $1/TS_c^M$ . The solid lines show the Adam-Gibbs fitting. (d)  $\tau$  vs.  $1/TS_c^I$ . The solid lines show the Adam-Gibbs fitting.

be rewritten as,

$$\begin{aligned}
 \frac{S_2^Q}{k_B} &= -2\pi\rho \int_0^\infty r^2 dr \\
 &\left[ (\chi'_1\chi'_1 + 2\chi'_1\chi'_3 + \chi'_3\chi'_3)\{g_{11}(r) \ln g_{11}(r) - (g_{11}(r) - 1)\} \right. \\
 &+ (\chi'_1\chi'_2 + \chi'_1\chi'_4 + \chi'_3\chi'_2 + \chi'_3\chi'_4) \\
 &\quad \left. \{g_{12}(r) \ln g_{12}(r) - (g_{12}(r) - 1)\} \right. \\
 &+ (\chi'_2\chi'_1 + \chi'_2\chi'_3 + \chi'_4\chi'_1 + \chi'_4\chi'_3) \\
 &\quad \left. \{g_{21}(r) \ln g_{21}(r) - (g_{21}(r) - 1)\} \right. \\
 &+ (\chi'_2\chi'_2 + 2\chi'_2\chi'_4 + \chi'_4\chi'_4)\{g_{22}(r) \ln g_{22}(r) - (g_{22}(r) - 1)\} \left. \right] \\
 &= -2\pi\rho \int_0^\infty r^2 dr \left[ (\chi'_1 + \chi'_3)^2 \{g_{11}(r) \ln g_{11}(r) - (g_{11}(r) - 1)\} \right. \\
 &+ (\chi'_1 + \chi'_3)(\chi'_2 + \chi'_4)\{g_{12}(r) \ln g_{12}(r) - (g_{12}(r) - 1)\} \\
 &+ (\chi'_2 + \chi'_4)(\chi'_1 + \chi'_3)\{g_{21}(r) \ln g_{21}(r) - (g_{21}(r) - 1)\} \\
 &+ (\chi'_2 + \chi'_4)^2 \{g_{22}(r) \ln g_{22}(r) - (g_{22}(r) - 1)\} \left. \right] \\
 &= -2\pi\rho \int_0^\infty r^2 dr \sum_{i,j=1}^2 \chi_i\chi_j \{g_{ij}(r) \ln g_{ij}(r) - (g_{ij}(r) - 1)\}
 \end{aligned} \tag{29}$$

The last equality can be written because  $\chi_1 = \chi'_1 + \chi'_3$  and  $\chi_2 = \chi'_2 + \chi'_4$ .

In Fig. 12 we plot  $S_2^M$  where the change in structure due to the pinned particles is considered. We find that at high temperatures  $S_2^M$  is larger than  $S_{ex}^M$ , and at low temperatures, the scenario is reversed.

The temperature where these two entropies cross each other is the  $\Delta S = 0$  (Eq. 7) point. For the KA model ( $c=0$ ) and other systems, it was earlier shown

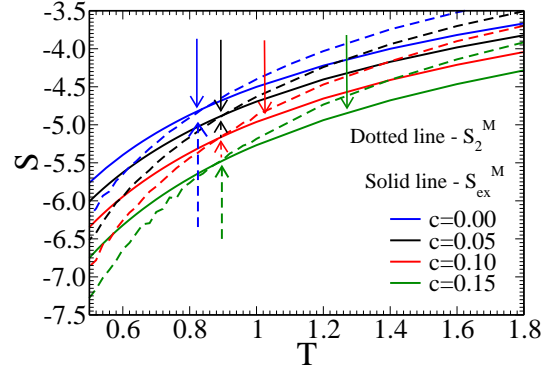


FIG. 12: The crossing between pair excess entropy  $S_2^M$  (Eq. 10) and excess entropy  $S_{ex}^M$  (Eq. 26). The  $S_2$  and  $S_{ex}$  crosspoint are indicated by a dotted upward arrow, while the onset temperature from the inherent structure (Fig. 9) is shown by a solid downward arrow.

that the temperature where these two entropies cross is similar to the onset temperature of glassy dynamics<sup>49,62</sup>. However, it has also been found that in systems with mean field like characteristics, the temperature where  $\Delta S = 0$  is lower than the onset temperature<sup>63,64</sup>. The latter scenario is similar to what we find for pinned systems. We find that with the increase in pinning, the difference between the onset temperature and the temperature where the two entropies cross increases. Interestingly, a similar difference between the freezing point and  $\Delta S = 0$  was observed for higher dimensional systems<sup>65</sup> and Gaussian core model (GCM)<sup>66</sup>. Note that if the pair excess entropy is calculated assuming the pinned system to be a binary system, then the cross over between the pair excess entropy and the total entropy will take place at unphysically low temperatures.

#### Appendix IV: Radial distribution function

In Fig. 2 (assuming the pinned particles are of a different species) we find that with increased pinning density, the partial rdfs start deviating from the  $c=0$  system. With an increase in “ $c$ ”, there is a drop in the peak value of the rdfs between two mobile particles ( $g_{11}$ ,  $g_{12}$ ). On the other hand, the height of the first peak of the partial rdfs between mobile and pinned particles ( $g_{13}$ ,  $g_{14}$ ) grows with “ $c$ ”.

We observe that this structural change happens quickly, immediately after the pinning process. In Fig. 13, we plot  $g(r)$ , averaged from  $t = 0 - 100$  and  $t = 101 - 200$ , where the pinning is done at  $t=0$ . We find that both rdfs overlap. This is shown for the  $c=0.15$  system where the difference is maximum.

We also show that  $\chi'_1 g_{11} + \chi'_3 g_{13}$  is the same as  $\chi_A g_{AA}$  and  $\chi'_2 g_{12} + \chi'_4 g_{14}$  is the same as  $\chi_B g_{BB}$  (Fig. 14). This is precisely why we do not see a change in structure when the pinned particles are not treated as a different

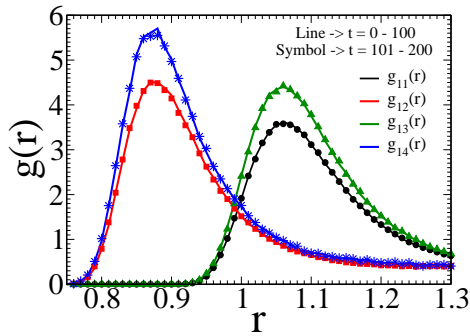


FIG. 13: Radial distribution function,  $g(r)$  at different time intervals for  $c = 0.15$  system. The solid line and symbol represent the radial distribution function at time  $t = 0 - 100$  and  $t = 100 - 200$ , respectively.

species (Fig. 1).

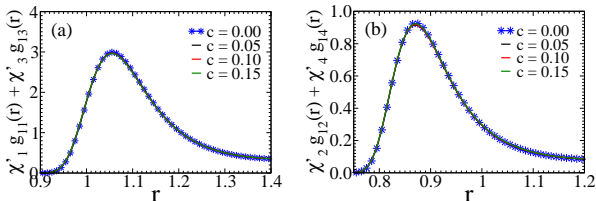


FIG. 14: (a)  $(\chi_1'g_{11} + \chi_3'g_{13})$  of the pinned system and  $\chi_{A9AA}$  of the KA system as a function of  $r$  (b)  $(\chi_2'g_{12} + \chi_4'g_{14})$  of the pinned system and  $\chi_{B9AB}$  of the KA system as a function of  $r$ .

To check the system size dependence, in Fig. 15, we plot the rdfs for a 4000 particle and 1000 particle system. We find that change in the rdf with pinning is almost independent of the system size, with the difference between the rdfs of the unpinned and pinned systems increasing marginally for larger system sizes.

We also check the dependence of the rdf on the integration time  $\Delta t$  (Fig. 16). From this plot, we observe that rdf is independent of the integration time step.

### Appendix V: Isoconfiguration run (IC)

To quantify the dependence of the dynamics on the structure and particle size, we perform isoconfigurational runs (IC). IC is a powerful technique introduced by Harrowell and co-workers to investigate the role of structure in the dynamical heterogeneity of the particles<sup>52-55</sup>. Among other factors, a particle's displacement can depend on its structure and also its initial momenta. This technique was proposed to remove the uninteresting variation in the particle displacements arising from the choice of initial momenta and extract the role of the initial configuration on the dynamics and its heterogeneity. For each system, five different isoconfigurational runs are carried out for 4000 particles. To ensure that all configurations are different, the configurations are chosen such that the

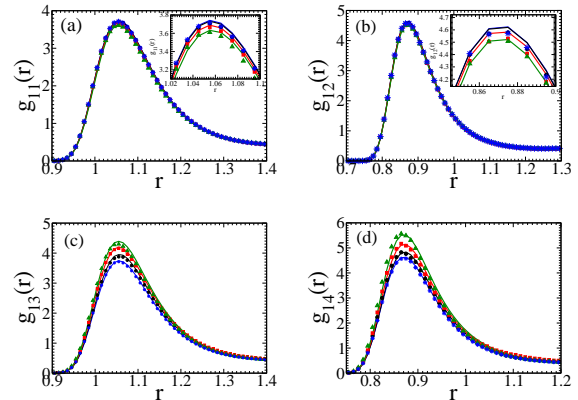


FIG. 15: System size dependence in radial distribution function,  $g(r)$  while treating the pinned system as a quaternary system, at  $T = 0.68$  (a)  $g_{11}$  as a function of  $r$  (b)  $g_{12}$  as a function of  $r$  (c)  $g_{13}$  as a function of  $r$  (d)  $g_{14}$  as a function of  $r$ . Inset: We have zoomed onto the first peak of the respective figures, which clearly shows the difference in the radial distribution functions. Note that color coding is similar to Fig. 1. Here we refer to the mobile A type of particles as 1, mobile B type of particles as 2, pinned A type of particles as 3, and pinned B type of particles as 4. The solid line represents the 4000 particle system and the symbol represents the 1000 particle system.

two sets are greater than  $100\tau_\alpha$  apart. All these five IC has different structure as well as contain different pin particle position. Note that since we have shown in section IIID that after pinning, the structure changes; thus after we pin the equilibrium position of the mobile particles, we run the system for  $t=100$  timestep and then consider that as our initial configuration. We run 100 trajectories for each configuration with different starting velocities randomly assigned from the Maxwell-Boltzmann distribution for the corresponding temperatures.

Mobility,  $\mu$  is the average displacement of each particle over these 100 runs and is calculated as<sup>54</sup>,

$$\mu^j(t) = \frac{1}{N_{IC}} \sum_{i=1}^{N_{IC}} \sqrt{(r_i^j(t) - r_i^j(0))^2} \quad (30)$$

where  $j^{th}$  particle's mobility at time  $t$  is represented by the term  $\mu^j(t)$ . The position of the  $j^{th}$  particle in the  $i^{th}$  trajectory at time  $t$  is denoted by the term  $r_i^j(t)$ , and its initial position is denoted by the term  $r_i^j(0)$ . The sum of the values is calculated over each of the  $N_{IC}$  trajectories that were carried out during the isoconfiguration runs. We determine the average displacement or mobility for the  $j^{th}$  particle at time  $t$  by averaging these displacements over all trajectories.

### Appendix VI: Identification of fast particles

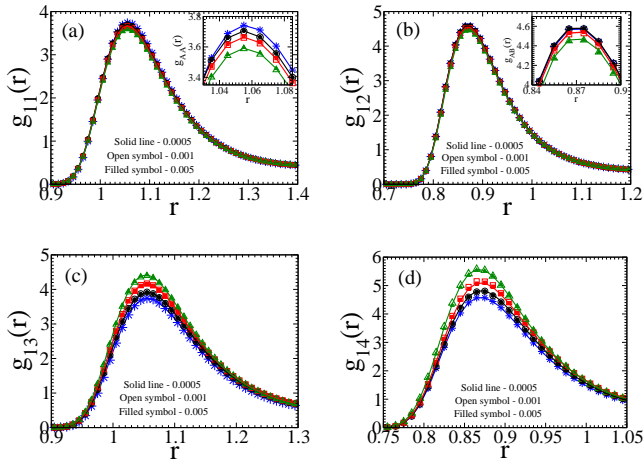


FIG. 16: Effect of integration time step,  $\Delta t$  on radial distribution function,  $g(r)$  while treating the pinned system as a quaternary system, at  $T = 0.68$  (a)  $g_{11}$  as a function of  $r$  (b)  $g_{12}$  as a function of  $r$  (c)  $g_{13}$  as a function of  $r$  (d)  $g_{14}$  as a function of  $r$ . Inset: We have zoomed onto the first peak of the respective figures, which clearly shows the difference in the radial distribution functions. Note that color coding is similar to Fig. 1. Here we refer to the mobile A type of particles as 1, mobile B type of particles as 2, pinned A type of particles as 3, and pinned B type of particles as 4.

There are various methods available for identifying fast particles in the literature<sup>57,58,67–69</sup>. In our study, we employ the approach proposed by Candelier et al.<sup>57,58</sup>. This method involves the calculation of a quantity called  $p_{hop}(i, t)$  for each particle within a specified time window  $W = [t_1, t_2]$ .

The  $p_{hop}(i, t)$  quantity captures the rate of change in the average position of a particle, indicating the occurrence of a cage jump. The expression for  $p_{hop}(i, t)$  is given as follows<sup>56</sup>:

$$p_{hop}(i, t) = \sqrt{\langle (r_i - \langle r_i \rangle_U)^2 \rangle_V \langle (r_i - \langle r_i \rangle_V)^2 \rangle_U} \quad (31)$$

here,  $r_i$  represents the position of particle  $i$ , and  $\langle \cdot \rangle$  denote the averages over the time. The time window  $W$  is divided into two intervals,  $U = [t - \Delta t/2, t]$  and  $V = [t, t + \Delta t/2]$ . By calculating  $p_{hop}(i, t)$  for each particle, we can determine whether a particle experiences a significant change in its average position, indicating its involvement in cage jumps and enhanced dynamics. In our analysis, we compare the calculated  $p_{hop}(i, t)$  values to a threshold value  $p_c$ , which is determined as the mean square displacement,  $\langle \Delta r(t)^2 \rangle$  at a specific time  $t_{max}$  where the non-Gaussian parameter,  $\alpha_2 = \frac{3\langle \Delta r(t)^4 \rangle}{\langle \Delta r(t)^2 \rangle^2} - 1$  is maximized. If  $p_{hop}(i, t)$  exceeds  $p_c$ , we identify the particle as

a fast particle<sup>33,62,70</sup>.

It is important to note that in our study, we specifically analyze the structure and dynamics of the mobile A particles. Therefore, we calculate the Mean Square Displacement (MSD) and the non-Gaussian parameter specifically for the mobile A particles. For a more comprehensive understanding of the method and its application in our study, we refer readers to Reference<sup>33,56,62,70</sup>.

## ACKNOWLEDGMENT

P. P. Thanks, CSIR, for the research fellowships. S. M. B. thanks, SERB, for the funding. The authors would like to thank Chandan Dasgupta, Smarajit Karmakar, and Mohit Sharma for the discussions.

## AVAILABILITY OF DATA

The data that supports the findings of this study is available from the corresponding author upon reasonable request.

## VII. REFERENCE

- <sup>1</sup>P. G. Debenedetti and F. H. Stillinger, *Nature* **410**, 259 (2001).
- <sup>2</sup>K. Binder and W. Kob, *Glassy Materials and Disordered Solids*, Revised ed. (WORLD SCIENTIFIC, 2011).
- <sup>3</sup>D. Chandler, D. Wu, and P. Chandler, *Introduction to Modern Statistical Mechanics* (Oxford University Press, 1987).
- <sup>4</sup>W. Kauzmann, *Chemical Reviews* **43**, 219 (1948).
- <sup>5</sup>C. A. Angell, *J Res Natl Inst Stand Technol.* **102**, 171 (1997).
- <sup>6</sup>R. Richert and C. A. Angell, *The Journal of Chemical Physics* **108**, 9016 (1998).
- <sup>7</sup>J. H. Magill, *The Journal of Chemical Physics* **47**, 2802 (1967).
- <sup>8</sup>T. M. Shuichi Takahara, Osamu Yamamuro, *The Journal of Physical Chemistry* **99**, 9589 (1995).
- <sup>9</sup>K. L. Ngai, *The Journal of Physical Chemistry B* **103**, 5895 (1999).
- <sup>10</sup>C. Alba-Simionesco, *Comptes Rendus de l'Académie des Sciences - Series IV - Physics-Astrophysics* **2**, 203 (2001).
- <sup>11</sup>C. M. Roland, S. Capaccioli, M. Lucchesi, and R. Casalini, *The Journal of Chemical Physics* **120**, 10640 (2004).
- <sup>12</sup>D. Cangialosi, A. Alegría, and J. Colmenero, *Europhysics Letters* **70**, 614 (2005).
- <sup>13</sup>E. Masiewicz *et al.*, *Scientific Reports* **5**, 2045 (2015).
- <sup>14</sup>T. R. Kirkpatrick, D. Thirumalai, and P. G. Wolynes, *Physical Review A* **40**, 1045 (1989).
- <sup>15</sup>G. Biroli and J.-P. Bouchaud, *The Random First-Order Transition Theory of Glasses: A Critical Assessment* (John Wiley and Sons, Ltd, 2012), chap. 2, pp. 31–113.
- <sup>16</sup>V. Lubchenko and P. G. Wolynes, *The Journal of Chemical Physics* **119**, 9088 (2003).
- <sup>17</sup>C. Cammarota, A. Cavagna, G. Gradenigo, T. S. Grigera, and P. Verrocchio, *The Journal of Chemical Physics* **131**, 194901 (2009).
- <sup>18</sup>A. Cavagna, T. S. Grigera, and P. Verrocchio, *The Journal of Chemical Physics* **136**, 204502 (2012).
- <sup>19</sup>C. Cammarota and G. Biroli, *Proceedings of the National Academy of Sciences* **109**, 8850 (2012).
- <sup>20</sup>M. Ozawa, W. Kob, A. Ikeda, and K. Miyazaki, *Proceedings of the National Academy of Sciences* **112**, 6914 (2015).



- <sup>21</sup>S. Chakrabarty, S. Karmakar, and C. Dasgupta, *Scientific Reports* **5**, 12577 (2015).
- <sup>22</sup>U. K. Nandi *et al.*, *The Journal of Chemical Physics* **156**, 014503 (2022).
- <sup>23</sup>C. Brito, G. Parisi, and F. Zamponi, *Soft Matter* **9**, 8540 (2013).
- <sup>24</sup>I. Williams *et al.*, *Journal of Physics: Condensed Matter* **30**, 094003 (2018).
- <sup>25</sup>R. Das, B. P. Bhowmik, A. B. Puthirath, T. N. Narayanan, and S. Karmakar, *PNAS Nexus* **2**, pgad277 (2023).
- <sup>26</sup>S. Chakrabarty, S. Karmakar, and C. Dasgupta, *Proceedings of the National Academy of Sciences* **112**, E4819 (2015).
- <sup>27</sup>M. Ozawa, A. Ikeda, K. Miyazaki, and W. Kob, *Physical Review Letter* **121**, 205501 (2018).
- <sup>28</sup>S. Chakrabarty, R. Das, S. Karmakar, and C. Dasgupta, *The Journal of Chemical Physics* **145**, 034507 (2016).
- <sup>29</sup>T. Goel, C. N. Patra, T. Mukherjee, and C. Chakravarty, *The Journal of Chemical Physics* **129**, 164904 (2008).
- <sup>30</sup>D. Frenkel and B. Smit, Appendix k - small research projects, in *Understanding Molecular Simulation (Second Edition)*, pp. 581–585, Academic Press, San Diego, , second edition ed., 2002.
- <sup>31</sup>M. Ozawa, Numerical Study of Glassy Systems: Fragility of Supercooled Liquids, Ideal Glass Transition of Randomly Pinned Fluids, and Jamming Transition of Hard Spheres, Thesis (2015).
- <sup>32</sup>M. K. Nandi and S. M. Bhattacharyya, *Physical Review Letter* **126**, 208001 (2021).
- <sup>33</sup>M. Sharma, M. K. Nandi, and S. M. Bhattacharyya, *Physical Review E* **105**, 044604 (2022).
- <sup>34</sup>M. Sharma, M. K. Nandi, and S. Maitra Bhattacharyya, *The Journal of Chemical Physics* **159**, 104502 (2023).
- <sup>35</sup>A. D. Phan and K. S. Schweizer, *The Journal of Chemical Physics* **148**, 054502 (2018).
- <sup>36</sup>A. D. Phan, *Journal of Physics: Condensed Matter* **34**, 435101 (2022).
- <sup>37</sup>W. Kob and H. C. Andersen, *Physical Review E* **51**, 4626 (1995).
- <sup>38</sup>D. Majure *et al.*, Large-Scale Atomic/Molecular Massively Parallel Simulator (LAMMPS) Simulations of the Effects of Chirality and Diameter on the Pullout Force in a Carbon Nanotube Bundle, *IEEE*, 201 (2008).
- <sup>39</sup>W. Kob and L. Berthier, *Physical Review Letter* **110**, 245702 (2013).
- <sup>40</sup>S. Sengupta, F. Vasconcelos, F. Affouard, and S. Sastry, *The Journal of Chemical Physics* **135**, 194503 (2011).
- <sup>41</sup>M. Ozawa, W. Kob, A. Ikeda, and K. Miyazaki, *Proceedings of the National Academy of Sciences* **112**, E4821 (2015).
- <sup>42</sup>J. P. Hansen and I. R. McDonald, *The Theory of Simple Liquids*, 2nd ed., Academic, London (1986).
- <sup>43</sup>J. G. Kirkwood and E. M. Boggs, *The Journal of Chemical Physics* **10**, 394 (1942).
- <sup>44</sup>R. E. Nettleton and M. S. Green, *The Journal of Chemical Physics* **29**, 1365 (1958).
- <sup>45</sup>C. P. Royall, F. Turci, S. Tatsumi, J. Russo, and J. Robinson, *Journal of Physics: Condensed Matter* **30**, 363001 (2018).
- <sup>46</sup>P. Scheidler, W. Kob, and K. Binder, *Journal of Physical Chemistry B* **108**, 6673 (2004).
- <sup>47</sup>M. K. Nandi, A. Banerjee, C. Dasgupta, and S. M. Bhattacharyya, *Physical Review Letter* **119**, 265502 (2017).
- <sup>48</sup>K. S. Schweizer, *The Journal of Chemical Physics* **123**, 244501 (2005).
- <sup>49</sup>A. Banerjee, M. K. Nandi, S. Sastry, and S. Maitra Bhattacharyya, *The Journal of Chemical Physics* **147**, 024504 (2017).
- <sup>50</sup>P. Patel, M. Sharma, and S. Maitra Bhattacharyya, *The Journal of Chemical Physics* **159**, 044501 (2023).
- <sup>51</sup>P. M. Piaggi, O. Valsson, and M. Parrinello, *Physical Review Letter* **119**, 015701 (2017).
- <sup>52</sup>A. Widmer-Cooper, P. Harrowell, and H. Fynewever, *Physical Review Letter* **93**, 135701 (2004).
- <sup>53</sup>A. Widmer-Cooper and P. Harrowell, *Physical Review Letter* **96**, 185701 (2006).
- <sup>54</sup>A. W. Cooper, H. Perry, P. Harrowell, and D. R. Reichman, *Nature Physics* **4**, 711 (2008).
- <sup>55</sup>L. Berthier and R. L. Jack, *Physical Review E* **76**, 041509 (2007).
- <sup>56</sup>S. S. Schoenholz, E. D. Cubuk, D. M. Sussman, E. Kaxiras, and A. J. Liu, *Nature Physics* **12** (2016).
- <sup>57</sup>R. Candelier *et al.*, *Physical Review Letter* **105**, 135702 (2010).
- <sup>58</sup>A. Smessaert and J. Rottler, *Physical Review E* **88**, 022314 (2013).
- <sup>59</sup>S. Sastry, P. G. Debenedetti, and F. H. Stillinger, *Nature* **393**, 554 (1998).
- <sup>60</sup>R. Sahu, M. Sharma, P. Schall, S. M. Bhattacharyya, and V. Chikkadi, Under preparation .
- <sup>61</sup>J. Guérolé *et al.*, *Computational Materials Science* **175**, 109584 (2020).
- <sup>62</sup>P. Patel, M. K. Nandi, U. K. Nandi, and S. M. Bhattacharyya, *The Journal of Chemical Physics* **154**, 034503 (2021).
- <sup>63</sup>M. K. Nandi and S. Maitra Bhattacharyya, *The Journal of Chemical Physics* **148**, 034504 (2018).
- <sup>64</sup>U. kumar Nandi, Connecting real glasses to mean-field models: A study of structure, dynamics and thermodynamics, Thesis (2021).
- <sup>65</sup>W. P. Krekelberg, V. K. Shen, J. R. Errington, and T. M. Truskett, *The Journal of Chemical Physics* **128**, 161101 (2008).
- <sup>66</sup>D. Coslovich, A. Ikeda, and K. Miyazaki, *Physical Review E* **93**, 042602 (2016).
- <sup>67</sup>W. Kob, C. Donati, S. J. Plimpton, P. H. Poole, and S. C. Glotzer, *Physical Review Letter* **79**, 2827 (1997).
- <sup>68</sup>K. Vollmayr-Lee, W. Kob, K. Binder, and A. Zippelius, *The Journal of Chemical Physics* **116**, 5158 (2002).
- <sup>69</sup>A. Widmer-Cooper and P. Harrowell, *Journal of Physics: Condensed Matter* **17**, S4025 (2005).
- <sup>70</sup>F. P. Landes, G. Biroli, O. Dauchot, A. J. Liu, and D. R. Reichman, *Physical Review E* **101**, 010602 (2020).